



An Investigation Into the Limitations of Myocardial Perfusion Imaging

Submitted for the Degree of Doctor of Philosophy

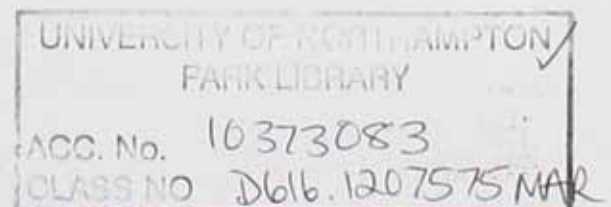
At the University of Northampton

2011

Johan Marais

© Johan Marais February 2012.

This thesis is copyright material and no quotation from it may be published without proper acknowledgement.



Acknowledgments

The author would like to thank the following individuals for their assistance and support during the course of this project. First and foremost, I thank my wife, Olena, for her unwavering love and support. I also thank my daughter, Nicole, for her constant presence and joy. I am grateful to my friends and family for their encouragement and advice. I would also like to thank the following individuals for their assistance in the collection and analysis of data: [names]. I am also indebted to the following organizations for their financial support: [names]. Finally, I thank the anonymous reviewers for their helpful comments and suggestions.

To my wife Olena and my daughter, the very "noisy" 4½ year old Nicole!

Acknowledgments

I would like to thank all my supervisors for their friendly advice and encouragement throughout the time leading to the submission of this thesis:

- Prof Carol Philips, Associate Dean (Research and Knowledge Transfer), School of Health, University of Northampton for her guidance and assistance.
- Prof Philip Picton, Divisional Leader in Engineering Science and Technology – Computing, University of Northampton for his suggestions and assistance.
- Dr Antony Denman, former Head of Medical Physics, Northampton General Hospital, and former Visiting Professor, University of Northampton for all the hours spent proof reading and correcting the grammatical problems in the thesis, as well as his advice on various aspects of the thesis and its contents. Furthermore I want to thank him for making it possible for me to do the work required to complete the thesis.
- Dr David Taylor, formerly Project Leader, Department of Medical Physics, Northampton General Hospital, Northampton for the subject related assistance and advice given to me throughout the time I was working on the various research projects.

I would also like to record my gratitude to the following people:

- Prof Jackie Campbell, Principal Lecturer, Health - Administration, University of Northampton for her help and advice on the statistical analysis.
- Mr Paul Strike, Research Design Service Statistician, Research & Development, Salisbury District Hospital, Salisbury for his input and advice on the statistical analysis
- David Monk, Physicist at the Department of Nuclear Medicine, Leicester General Hospital, Leicester, for providing me with the data I required, without it the completion of many parts of the thesis would have been impossible.

On a more practical note, I am indebted to the Strategic Health Authority of the NHS East Midlands for their continued funding of my studies.

Abstract

Myocardial Perfusion Imaging (MPI) plays a very important role in the management of patients with suspected Coronary Artery Disease and its use has grown despite the shortcomings of the technique. Significant progress has been made in identifying the causes of these shortcomings and many solutions been suggested in the literature but the clinical sensitivity and specificity of the technique is still well below optimum.

Monte Carlo Simulation is a very useful tool in identifying and guiding the understanding of the existing problems in MPI and this present study utilised this method to establish the basis of the simulations to be used and the way to analyse the results so that many of the causes of the attenuation defects, when using MPI, could be identified. This was achieved by investigating the effect that the different anatomical parts of the thorax have on the attenuation defects caused. A further aspect investigated was the impact that self-absorption in the heart has on these defects. The variability of these defects were further investigated by altering the position and orientation of the heart itself within the thorax and determining the effect it has on the attenuation defects caused. Results indicate that the attenuation caused is a very complicated process, that the self-absorption of the heart plays an extremely important role and the impact of the different positions and orientation of the heart inside the thorax are also significant. The distortion caused on the images by these factors was demonstrated by the intensity losses in the basal part and an over-estimation in the apical parts, which were clearly observable on the final clinical images, with the potential to affect clinical interpretation.

Attenuation correction procedures using transmission sources, have been available for some time, but have not been adopted widely, amidst concern that they introduce additional artefacts. This study determined the effectiveness of these methods by establishing the level of correction obtained and whether additional artefacts were introduced. This included the effectiveness of the compensation achieved with the use of the latest commercially available comprehensive correction techniques. The technique investigated was "Flash3D" from Siemens providing transmission based attenuation correction, depth-dependent resolution recovery and scatter correction. The comparison between the defects and intensity losses predicted by the Monte Carlo Simulations and the corrections provided by this commercial correction technique revealed that solution is compensating almost entirely for these problems and therefore do provide substantial progress in overcoming the limitations of MPI. As a result of the improvements gained from applying these commercially available techniques and the accuracy established in this study for the mentioned technique it is strongly recommended that these new techniques be embraced by the wider Nuclear Medicine community so that the limitations in MPI can be reduced in clinical environment.

Non-withstanding the above gains made there remains room for improvement by overcoming the of use transmission attenuation correction techniques by replacing them with emission based techniques. In this study two new related emission based attenuation correction techniques have been suggested and investigated and provide a promising prospect of overcoming these limitations.

Contents

Acknowledgments.....	i
Abstract	ii
Contents	iii
List of Figures	iv
List of Tables	vii
Chapter 1 - Introduction	1
Chapter 2 - Limitations of Myocardial Perfusion Imaging: a Literature Study	4
2.1 Myocardial Perfusion Imaging (MPI).....	4
2.2 Quantitative Myocardial Perfusion SPECT Scintigrams	7
2.2.1 ECG-Gating of Myocardial Perfusion SPECT Scintigrams	8
2.2.2 Absolute Quantification	9
2.3 Reported Sensitivity and Specificity of SPECT MPI.....	9
2.4 Permutations in Emission Tomography	9
2.4.1 The Problem of Photon Attenuation in Emission Tomography	10
2.4.2 The Problem of Photon Scatter in Emission Tomography	10
2.4.3 The Problem of the Partial Volume Effect in Emission Tomography	12
2.4.4 The Problem of Depth-Dependent Collimator Response	15
2.4.5 Commercially Available Correcting Systems	16
A. SIEMENS - FLASH 3D	17
B. PHILIPS - Astonish	17
C. GE Healthcare - Evolution	18
D. ULTRASPECT - Wide Beam Reconstruction	18
E. Hermes Medical Solutions – Hybrid Reconstruction	19
2.5 Attenuation Correction Strategies in Emission Tomography	19
2.5.1 Import and Register Maps from Another Modality	20
2.5.2 Radionuclide Transmission Methods	23
2.5.3 The Implementation of Transmission Based Methods	24
2.5.4 Reducing the Time for the Transmission Scan and Emission Based Methods	24
2.5.5 The Method of Inferred Anatomy and Derived Anatomy	26
2.6 New Hardware for the Optimisation of MPI.....	27
2.6.1 DIGIRAD - CARDIUS 3 XPO	27
2.6.2 CardiArc	28
2.6.3 Spectrum Dynamics – D-SPECT	28
2.6.4 Multi-Pinhole Collimation Approach	28
2.6.5 GE Healthcare - Ultra Fast Cardiac (UFC) Camera	29
2.6.6 SIEMENS - IQ•SPECT	29
2.7 Conclusions.....	30

Chapter 3 - Monte Carlo Simulations to Determine the Limitations of Myocardial Perfusion Imaging.....	32
3.1 Introduction	32
3.2 Monte Carlo Simulations	33
3.3 Computer Phantoms in Medical Imaging Simulation Techniques.....	34
3.4 Simulation of SPECT Acquisitions	34
3.4.1 Validation of SimSET	35
3.5 Choosing the Number of Seeded Events.....	36
3.6 Image Reconstruction.....	36
3.7 Image Interpretation	37
3.8 Statistical Analysis	39
3.8.1 Regression as a Statistical Model	40
A. The Line of Best Fit	40
B. Deciding Which Model to Use	40
C. Using the Models	41
3.8.2 Comparing Two Means as a Statistical Model	42
A. Calculating the effect size	42
3.9 Patient Selection for Monte Carlo Simulations	42
3.10 Conclusion	44
Chapter 4 - Attenuation and Scatter From Individual Anatomical Parts in the Thorax.....	46
4.1 Introduction	46
4.2 Methods	50
4.2.1 Data Simulations and Analysis	50
4.2.2 Evaluation Criteria	52
A. Uniformity of the Polar Map (PMU) Over the 9 Segments	52
B. Fraction Absolute Difference in Intensities	53
4.2.3 Investigation of the Perfusion Losses in the Left Ventricle When not Applying Any Corrections	53
4.2.4 Comparison Between the Basal and Apical Regions of the Perfusion Distortion Found	54
4.2.5 Investigating the Relative Distortion in the Basal and Apical Parts	55
4.2.6 Investigation Into the Contribution to This Distortion by Each Anatomical Part	56
4.2.7 Investigating the Effect of Scatter on the Perfusion Distribution in the Left Ventricle	56
4.2.8 Fractional Intensity Losses in the Final Ventricular Images	57
4.2.9 Investigating the Differences in Perfusion Losses Experienced Between Males and Females	58
4.3 Results.....	58
4.3.1 Tests to Ensure That a Parametric Model Will be Valid	58
4.3.2 The Distortion in the Left Ventricle	58

4.3.3	Comparison Between the Basal and Apical Regions	61
4.3.4	Under Estimation of the Basal Regions and Over Estimation of the Apical Regions of the Left Ventricle	63
4.3.5	The Contribution of the Different Anatomical Parts to This Distortion	65
	A. The PMUD's of the Individual Parts for the 9 Segments	65
	B. The Contribution of the Body	66
	C. The Contribution of the Heart	67
	D. The Contributions of the Individual Parts as a Percentage	70
4.3.6	The Contribution of Scatter	72
4.3.7	Fractional intensity Loss in the Final Ventricular Images	74
4.3.8	Comparison Between the Simulated Male and Female Patients	76
4.4	Discussion and Conclusion.....	82
4.4.1	The Distortion in the Left Ventricle When Not Applying Any Corrections	82
4.4.2	Comparison Between the Basal and Apical Regions of the Non-Uniformities Experienced	83
4.4.3	The Relative Non-Uniformities in the Basal and Apical Parts	83
4.4.4	The Contribution to This Distortion by Each Anatomical Part	83
4.4.5	The Effect of Scatter on the Intensity Distribution in the Left Ventricle	84
4.4.6	Fractional Intensity Losses in the Final Ventricular Images	84
4.4.7	Investigating the Differences in Intensity Losses Experienced Between Males and Females	84
4.4.8	Summary	84
Chapter 5 - Attenuation Variations as a Result of Different Orientations and Positions of the Myocardium in the Thorax.....		86
5.1	Introduction	86
5.2	Methods	87
	5.2.1 Images Required for the Monte Carlo Simulations	91
	5.2.2 Statistical Analysis	94
5.3	Results	94
	5.3.1 Results of the Linear Regression	95
	5.3.2 Results of the Cubic Regression	104
	5.3.3 Comparison Between the Linear and Cubic Regression	114
	5.3.4 Final Outcome of the Analysis	116
5.4	Discussion and Conclusion.....	117
	5.4.1 Deciding Which Model to Use	117
	5.4.2 Variation Studies	118
	5.4.3 Summary	118
Chapter 6 - Determination of the Extent of Attenuation Correction in Patients by Using a Commercially Available Correction Solution		121
6.1	Introduction	121
6.2	Methods	123
	6.2.1 Patient Selection and Analysis	123
	6.2.2 Analysing the "Distortion" on the Left Ventricle	124
	6.2.3 Comparing the Basal and Apical Portions for Both Genders	124

6.2.4	Comparing the Results of the Male Patients Against Those of the Female Patients	124
6.2.5	Comparing the Results of the Patients Against Those Predicted by the Monte Carlo Simulations	125
6.3	Results	125
6.3.1	Tests to Ensure that a Parametric Model Will be Valid for the Attenuation Corrected Patient Studies on the Commercial System	125
6.3.2	The "Distortion" in the Left Ventricle in the Attenuation Corrected Patient Studies	125
6.3.3	Comparing the Basal Against the Apical Regions of the Attenuation Corrected Patient Studies	127
6.3.4	Under Estimation of the Basal Regions and Over Estimation of the Apical Regions of the Left Ventricle of the Attenuation Corrected Images on the Commercial System	129
6.3.5	Fraction Intensity Losses in the Final Ventricular Images of the Attenuation Corrected Patient Studies on the Commercial System	130
6.3.6	Comparing Attenuation Corrected Male Against Female Patients on the Commercial System	132
6.3.7	Comparing the Results of the Attenuation Corrected Patients on the Commercial System Against Those Predicted by the Monte Carlo Simulations	136
6.4	Discussion and Conclusion	143
6.4.1	Attenuation Correction in Attenuation Corrected Male Patients on the Commercial System	143
6.4.2	Attenuation Correction in Female Patients on the Commercial System	143
6.4.3	Comparing the Correction in Male to That in Female Patients on the Commercial System	143
6.4.4	Comparing the Attenuation Correction Obtained in Patients on the Commercial System Against the Attenuation Losses Predicted by the Monte Carlo Simulations	144
A.	Significant Inferior Wall Attenuation	144
B.	The Effect of the Heart Itself as Attenuation Medium	144
C.	Under Estimation of the Basal Regions of the Left Ventricle	144
D.	The Overestimation and "Correction" of the Apical Region	144
E.	The Intensities Gained by Implementation of TBAR	145
F.	Summary	145
Chapter 7 - The Proposed Methods of Inferred & Derived Anatomy for Attenuation Correction in the Thorax		147
7.1	Introduction	147
7.2	Creation of the Source Object	149
7.3	Creation of the Target Object	149
7.3.1	Segmentation of the Body Outline	150
7.3.2	Segmentation of the Left Ventricle	152
7.3.3	Determination of the Patient Data Slices	155
7.4	Registration of the Source Object to the Relevant Target Object	156
7.5	Testing of the segmentation and Registration	160
7.5.1	Patient with a Hot Gall Bladder	161
7.5.2	Patient with Substantial Gut Uptake	164
7.5.3	Patient with Substantial Liver Uptake	166
7.5.4	Patient with Substantial Intensity Loss in the Inferior Wall	169
7.5.5	Cardiomyopathy with Very Severe Defects	171

7.6 The method of derived anatomy	174
7.6.1 Mid-Myocardial Surface Extraction and Fit	174
7.6.2 Testing the Mid-Myocardial Surface Extraction and Fit	175
7.7 Conclusion	176
7.8 Future Work.....	177
Chapter 8 - Conclusions and Further Work.....	180
8.1 Conclusions.....	180
8.2 Future Work.....	184
Appendix A – Source Code used for the Reconstruction of the Simulated Studies	185
References	212

List of Figures

Figure 2-1:	Illustrating the partial volume effect with the real image (a) and the displayed image (b) as a result of the PVE.....	13
Figure 2-2:	Illustrating the effect of distance on the shape of the PSF.....	16
Figure 2-3:	The inferred-anatomy algorithm. The preliminary reconstruction of the patient (a), the atlas consisting out of both the anatomically and functionality parts (b). The registration of the functionality part to the preliminary reconstruction (c) and after applying the result of the registration to the anatomical part of the atlas (d).....	26
Figure 3-1:	The polar maps created from reconstructed simulation outputs. The polar map itself (a), the regions displaying the 5-segment model (b).....	38
Figure 3-2:	Polar maps displaying the 5-segment model. The polar map and the related values for the air simulation (a) and the polar map and the related values for the real life simulation (b).	39
Figure 4-1:	The non-attenuated (air simulation) (NA) images and attenuation (A) images displays the typical effect of attenuation in (a). The images in (b) show the "shortening" of the ventricular cavity. The sagittal images in (c) shows the effect attenuation has on the anterior and inferior wall, with the inferior wall clearly experiencing a bigger loss of intensities.....	49
Figure 4-2:	The individual body parts which acted as attenuation media, as well as "Everything", i.e. the whole thorax, which represents the attenuation map in patients, as well as the activity map.	51
Figure 4-3:	The 9-segment cardiac model which was used to analyse the data in this study.....	51
Figure 4-4:	Images to illustrate the PMUD.....	53
Figure 4-5:	The means (as displayed above each bar) of the PMUD's as a result of the Whole Thorax together with the 95% confidence intervals for each of the 9 segments for the male and female simulated patients.....	59
Figure 4-6:	The PMUD's when comparing the difference between the basal and apical regions of the anterior, lateral, inferior and septal walls in the male and female simulated patients.	62
Figure 4-7:	The PMUD's when using the whole thorax as attenuation media in both the male and female simulated patients and the PMDUI to determine the under- and over-estimation of different regions.....	64
Figure 4-8:	The means of the PMUD's (as displayed above each bar) as a result of the body (remainder and skeleton) together with their 95% confidence intervals for each of the 9 segments for both genders.	67
Figure 4-9:	The means of the PMUDs (as displayed above each bar) as a result of the heart (myocardium, pericardium and bloodpool) together with their 95% confidence intervals for each of the 9 segments for both genders.	68
Figure 4-10:	The means of the PMUDs (as displayed above each bar) comparing the heart (myocardium, pericardium and bloodpool) and the body (remainder and skeleton) together with their 95% confidence intervals for each of the 9 segments for both genders.	70
Figure 4-11:	The percentage contribution to the intensity losses experienced in the final images as a result of the different anatomical parts for both genders (the y-axis represent the % contribution).....	71
Figure 4-12:	Illustrating the effect of scatter, reconstructed images of only the scatter component (top row), reconstructed images of only the primary photons (middle row) and the non-attenuated reconstructed images (bottom row). Note that each image set is normalised to the maximum in that specific image set and that the maximum in the scatter reconstructed images is significant lower than the maximum in the other two sets.....	72
Figure 4-13:	The scatter fraction (as a percentage) in the 9 segments as a result of scatter for the female simulated patients.....	73
Figure 4-14:	Fractional Index (FI) of the "Whole Thorax" as attenuation medium for the 9 segments.....	75

Figure 4-15: The means of the PMUD's of "Everything" for the Male and Female patient selection, presenting the differences between these two population groups (the y-axis represents the PMUD's).....	77
Figure 4-16: The means of the PMUD's of the Heart for the Male and Female patient selection, presenting the differences between these two population groups (the y-axis represents the PMUD's).....	79
Figure 5-1: The 15 variations in each of the 6 variation studies (a) xz-rotation (phi), (b) xy-rotation (psi), (c) zy-rotation (beta), (d) x-translation, (e) y-translation and (f) z-translation.....	91
Figure 5-2: The simulation input files generated with the NCAT program. The activity distribution and index file (a), the attenuation distribution (b) and the attenuation index file (c).....	92
Figure 5-3: The simulation index input files generated with the NCAT program. The air simulation with the empty attenuation index file and the activity index file (a) and the real life simulation with the attenuation index file and the activity index file (b).	93
Figure 5-4: Linear regression results showing the percentage intensity losses on the y-axis and indicating the 95% confidence and prediction intervals.....	103
Figure 5-5: Cubic regression results showing the percentage intensity losses on the y-axis and indicating the 95% confidence and prediction intervals.....	113
Figure 6-1: PMUD of the 9 segments of male and female patients as a result of transmission attenuation corrections using Gd-153 line sources.	126
Figure 6-2: The PMUD's when comparing the difference between the basal and apical regions of the anterior, lateral, inferior and septal walls in the male and female patients.....	128
Figure 6-3: Showing the PMUDI values to determine the amount of under estimation in the basal regions.....	130
Figure 6-4: The fraction indexes in the 9 segments to indicate the intensity gain in each segment.....	131
Figure 6-5: Comparison of percentage intensity gain in the 9 segments between male and female patients as a result of transmission attenuation corrections using Gd-153 line sources (in each graph the y-axis represents the % intensities gained from the attenuation correction).....	133
Figure 6-6: Comparing the FI's of the male population to the female population.	134
Figure 6-7: Comparing the PMUD's when comparing the difference obtained after attenuation correction for the basal and apical regions of the male population against that of the female population.....	135
Figure 6-8 a: A comparison between the uniformities gained by using TBAR to the uniformity losses predicted by the Monte Carlo simulations – Male patients.....	137
Figure 6-8 b: A comparison between the uniformities gained by using TBAR to the uniformity losses predicted by the Monte Carlo simulations – Female patients.	138
Figure 6-9: A comparison between the intensity gained by using TBAR to the intensity losses predicted by the Monte Carlo simulations.....	141
Figure 7-1: A typical slice from the attenuation object created out of the NCAT phantom (a), the functional image of this slice (b) and a slice from the target object created from the patient data (c).....	148
Figure 7-2: The provided NCAT attenuation map (a) and functional map (b) which need to be modified to adhere to the spatial representation of the patient under investigation.	149
Figure 7-3: The same patient data set reconstructed by using filtered backprojection (fbp) (a) and the Maximum Likelihood Expectation Maximisation (MLEM) reconstruction method (b) showing the reduced background produced by the iterative reconstruction method in (b).....	150
Figure 7-4: The originally binary image (a), the binary image of the body outline after applying thresholding (b), the body outline after erosion (c) and the outline after masking (d). ...	152
Figure 7-5: Segmentation of the body outline. The images after the initial reconstruction of a patient dataset (a) and the body outline of the same data set after application of the body outline segmentation steps (b).....	152
Figure 7-6: The original and final source objects of the first part of the registration. The body outline before (a) and after (b) registration. The attenuation map before (c) and after (d) registration.....	159

Figure 7-7: Quality control of the registration process. Adjusting the Intensity and Contrast allow the verification of the registration of the left ventricle (a) as well as the body (b).....	160
Figure 7-8: The images obtained for a patient with an extremely hot gall bladder. (a) Raw images illustrating the "masking" effect of this situation. (b) The original reconstructed images (c) The body and LV segmented images (d) Images illustrating the removal of all the non-LV pixels (e) Overlay of this images over the final attenuation map illustrating the successful outcome of the registration parts and (f) The final attenuation map.....	163
Figure 7-9: Set of images from a patient with substantial gut uptake.	166
Figure 7-10: Set of images from a patient with substantial liver uptake.....	168
Figure 7-11: Set of images from a patient with substantial intensity loss in the inferior wall.	171
Figure 7-12: Set of images from a patient with a dilated heart with very severe defects.....	173
Figure 7-13: The fit (mesh) fitted to the extracted data points of the mid-myocardial surface.....	176
Figure 7-14: Determination of the angles required by the NCAT parameter file.....	176

List of Tables

Table 3-1:	Male Patient Selection for the Monte Carlo Simulations	43
Table 3-2:	Female Patient Selection for the Monte Carlo Simulations	44
Table 4-1:	Summary of the PMUD values for both male and female simulated patients as a result of using the whole thorax as attenuation medium	60
Table 4-2:	Paired Samples t-test to determine the significance between the PMUD values	60
Table 4-3:	r-values to quantify the PMUD (Values in red indicate that it is significant)	61
Table 4-4:	2-tailed dependent t-test to determine the equality of the means of the intensity losses differences between the basal and apical regions of the anterior, lateral, inferior and septal walls in male and female simulated patients	62
Table 4-5:	r-values to quantify the PMUD (Values in red indicate that it is significant)	63
Table 4-6:	The PMUDI's for the male and female simulated patients. The values in red indicates negative PMUD's and which indicates an over estimation in that segment and the ones in orange a PMUD higher than the index and therefore a severe under estimation	65
Table 4-7:	A summary of the PMUD's in all the segments for all the anatomical parts for both the male and female simulated patients	65
Table 4-8:	Dependent sampled t-test to determine whether the mean of the percentage loss in apical parts are significant different from those in the basal parts for the scattered photons and primary photons as well as a comparison between the means of the scatter fractions of the basal and apical regions	73
Table 4-9:	Results of the 2-tailed independent t-test to determine the equality of the means of the PMUD's when comparing the basal and apical regions of the anterior, lateral, inferior and septal walls for the male and female simulated patients	82
Table 5-1:	The 15 variations for the 6 variation studies	88
Table 5-2:	Model summary for the linear regression model	95
Table 5-3:	ANOVA results for the linear regression model. For all non-significant values the p-value are shown in red	96
Table 5-4:	Coefficients for the linear regression model. For all non-significant values the p-value are shown in red	97
Table 5-5:	Model summary for the cubic regression model	104
Table 5-6:	ANOVA results for the cubic regression model. The non-significant p-value is shown in red and therefore the significant p-values are those not marked in red	105
Table 5-7:	Coefficients for the cubic regression model. The non-significant p-value is shown in red and therefore the significant p-values are those not marked in red	106
Table 5-8:	Comparison of the mean standard error between the linear and cubic regressions. The non-significant p-value is shown in red and therefore the significant p-values are those not marked in red	114
Table 5-9:	Comparison of models of the linear regression against that of the cubic regressions. When the R Squares are compared, the best (highest) values are shown in green	115
Table 5-10:	F and t values and their significance	116
Table 5-11:	Percentage intensity losses at the reference orientation of the Visible Human and the percentage unit intensity losses when deviating from it when using the linear regression model	116
Table 5-12:	The maximum intensity losses found for the variation ranges used in this study	117
Table 6-1:	Summary of the means of the PMUD values for both male and female patients as well as the PMUDI	127
Table 6-2:	Comparing the PMUD's between the apical and basal parts	128
Table 6-3:	The r-values when comparing the PMUD's between the apical and basal parts	129
Table 6-4:	PMUD and PMUDI values to determine the amount of under estimation in the basal regions and over estimation in the apical regions	130
Table 6-5:	Comparing the uniformity gains (PMUD) between the two genders in the 9 segments	132
Table 6-6:	Comparing the FI's of the male population to the female population	134
Table 6-7:	The mean and 95% confidence intervals for the percentage intensity gain in the 9 segments for the male patients	139

Table 6-8:	2-tailed paired t-tests to compare the means of the attenuation gain in each of the 9 segments against each other in the male population	139
Table 6-9:	A comparison between the intensity gained by using TBAR to the intensity losses predicted by the Monte Carlo simulations.....	142
Table 6-10:	Summary of the MFI values of the patients and the Monte Carlo simulations	142
Table 6-11:	Comparing the MFI between the genders and the Monte Carlo simulations	142
Table 7-1:	Results of the segmentation and registration	161

Chapter 1 - Introduction

Coronary artery disease (CAD) is the most important cardiac pathology in the adult population of the Western world (and therefore in the UK as well) and therefore makes it the most common form of heart disease¹. CAD and its complications, like angina pectoris, arrhythmia and heart attack, are the leading causes of death in the Western world². Coronary artery disease (CAD) is the UK's biggest killer, around one in five men and one in seven women die from the disease. CAD is the leading cause of death in women in the USA and more than twice as many women die from cardiovascular disease as from all forms of cancer combined³. Coronary Heart Disease (CHD) causes around 94,000 deaths in the UK each year⁴.

CAD is a complex degenerative disease that causes reduced or absent blood flow in one or more of the arteries that encircle and supply the heart. CAD may affect just a small branch vessel far from the aortic root (distal) or a larger vessel near its origin (proximal). CAD may affect any or all three of the major supply arteries to the heart, - the left anterior descending (LAD) artery, the left circumflex artery (LCX), and the right coronary artery (RCA). Thus, a simple ranking of disease severity is noted as 1-, 2-, or 3-vessel disease.

During the last 30 years, scintigraphy, ultrasonography, computed tomography, and magnetic resonance imaging have emerged as invaluable tools to delineate abnormalities in the cardiovascular system. The optimal roles of the various methods of noninvasive evaluation continue to evolve as refinements are developed. Faster, stronger, and more efficient hardware and associated faster and more flexible digital processing are now providing faster scan times, as well as nearly real-time physiologic information. Quantitative and semiquantitative analysis and the development of new contrast and radiopharmaceutical agents have further improved the accuracy of anatomic and physiologic noninvasive testing.

The protocol that has been used in Nuclear Medicine to determine abnormalities in the blood supply to the myocardium, and therefore CAD, is called Myocardial Perfusion Imaging (MPI). The effectiveness of MPI in detecting blood supply abnormalities to the heart associated with CAD has been the subject of many studies^{5,6,7}. Most have assessed the sensitivity and specificity of the technique using coronary angiography as the gold standard.

Although Myocardial Perfusion Imaging is a well-established approach for the assessment of Coronary Artery Disease and Myocardial Viability, there still exists uncertainty in different areas and therefore the need to address these uncertainties exists. This study will address the most visible of these uncertainties to further enhance the assessment of CAD and Myocardial Viability.

The study will provide a thorough evaluation of current practices and identification of their limitations. These will include Attenuation Correction, Scatter Correction, Partial Volume Effect and Resolution Recovery. The remainder of this study consists of addressing the limitations of the current practises of MPI as well as a proposal to address those limitations.

Chapter 2 looks at the limitations of Myocardial Perfusion Imaging as described in the literature. The most substantial limitations are considered, and their impact on the final reconstructed images reviewed. Corrections for the limitations are suggested, some of which have been developed commercially, and their suitability and acceptance in clinical use considered.

Chapter 2 also indicates that although a vast amount of investigation has been done into the subject of attenuation in the thorax substantial areas still exist where there is still no clear understanding of the effect of attenuation on the final reconstructed images. In this study Monte Carlo simulation studies were used to investigate certain areas and chapter 3 describes in more detail how these techniques can be used to study the effects of non-uniform thoracic attenuation.

Chapter 4 describes how these techniques can be used to discover the effect of the different anatomical parts on the total attenuation caused in the final reconstructed images, something that has not been reported in the literature and will represent new and original work. The distortion of these final reconstructed images has also been investigated in much more detail to highlight aspects of attenuation which are not that well known or has not been highlighted yet.

Chapter 5 looks at the effect on the final reconstructed images for variations in the orientation and positioning of the heart within the thorax. The position and orientation of the heart varies substantially from patient to patient and this can have a potentially substantial impact on the amount of attenuation in the final reconstructed images but this aspect has not been reported or analysed by others.

A wide range of commercially available solutions have become available in recent times. The extent of the correction achieved by such a commercially available attenuation correction technique, together with the correction for scatter and depth-dependent collimator blurring of the gamma camera, is the topic of chapter 6.

Chapter 2 shows that real progress has been made with dealing with the inherent limitations of Myocardial Perfusion Imaging with the exception of attenuation correction. A lot of work has been done on this subject and commercially available systems are in use today but the use of attenuation correction has not obtained universal acceptance. There are still widespread resistance to its implementation. In view of the findings in Chapters 4 and 5, it is clear that there is a real need for an accurate universally accepted attenuation correction

technique to ensure accurate and improved reporting. The technique of inferred anatomy seemed a very attractive alternative method which can be implemented with the use of software only. This method has been introduced for brain studies in the literature but in this study it has been developed specifically to cover the thorax as well. Chapter 7 describes the image manipulation and segmentation techniques necessary for such an implementation. Chapter 7 also touches slightly on another possibility of an emission based attenuation correction technique, referred to as derived anatomy.

Chapter 8 summarises the results obtained in the previous chapters and the contribution made in this study to get a better understanding of the limitations in Myocardial Perfusion Imaging, as well as the new and original work introduced. It also summarises the possibility of methods for improving the areas where there is not a universally accepted method of correcting for these limitations and how further work can contribute to get a complete universally accepted correction for all the described limitations.

This study was conducted during a period when the institution was planning and commissioning a nuclear cardiology suite, but were not conducting clinical studies. With the approval of the Local Ethics Committee data were obtained from another institution and software was developed in-house by the candidate so that this project could be developed. The exception to this is the data and analysis described in chapter 6 when MPI studies were performed at the research institution when the hardware and software for performing, reconstructing and analysing these images became available.

Chapter 2 - Limitations of Myocardial Perfusion Imaging: a Literature Study

2.1 Myocardial Perfusion Imaging (MPI)

Myocardial Perfusion Imaging (MPI), a Nuclear Medicine imaging technique using radioisotopes, is most frequently performed in symptomatic patients with low to intermediate probability for CAD⁸. It is also useful in patients with non-diagnostic ECGs as well as in patients unable to exercise sufficiently to get an accurate picture of the heart under stress. The effectiveness of myocardial perfusion scintigraphy in detecting perfusion abnormalities associated with Coronary Artery Disease (CAD) has been the subject of many studies^{5,6,7}. Most have assessed the sensitivity and specificity of the technique using coronary angiography as the standard.

The words "sensitivity" and "specificity" have their origins in screening tests for diseases. When a single test is performed, the person may in fact have the disease or the person may be disease free. The test result may be positive, indicating the presence of disease, or the test result may be negative, indicating the absence of the disease.

Test Result	Presence of Disease	
	Yes	No
Positive	True positive (TP)	False positive (FP)
Negative	False negative (FN)	True negative (TN)

Statistical terms

False Positive: A false positive occurs when the test reports a positive result for a person who does not have the specific disease that the test is designed to detect. Ideally this value should be zero.

False Negative: A false negative occurs when the test reports a negative result for a person who actually has specific disease that the test is designed to detect.

Sensitivity measures the proportion of patients who actually have the disease which are correctly identified as such (e.g. the percentage of patients with CAD who are correctly identified as having CAD). **Specificity** measures the proportion of patients who do not have the disease which are correctly identified (e.g. the percentage of patients without CAD who are correctly identified as not having CAD).

Before Single Photon Emission Computerized Tomography (SPECT) technology became widely available, two-dimensional planar imaging was used for blood pool and all myocardial perfusion imaging⁹. The MUGA (multigated acquisition) scan has been used for decades to evaluate global and regional wall motion, to calculate the excursion of blood from the left or right ventricles, determine ventricular volumes and to obtain a stroke volume ratio. Until the advent of gated myocardial SPECT, physicians relied on the MUGA scan to get valuable ventricular function data on patients with any number of heart conditions but important technical limitations remain, including the relatively restricted spatial resolution of standard Anger cameras, precluding precise evaluation of regional LV abnormalities, and overlap of atria and ventricles during equilibrium studies, even in the standard left anterior oblique view, limiting precision in measuring LV and RV volumes exists. New developments in radiopharmaceuticals, as well as in imaging hardware and computer technology, have contributed substantially to the development of gated SPECT¹⁰. The technetium-99m based perfusion tracers, because of their higher count rates and stable myocardial perfusion with time, permit evaluation of regional wall motion and wall thickening throughout the cardiac cycle. The development of automatic algorithms to quantitatively measure left ventricular volume and ejection fraction, and even regional myocardial wall motion and thickening from gated SPECT rapidly and accurately, with minimal operator interaction, has contributed to its widespread use.

As stated before, the clinical evaluation of these SPECT myocardial perfusion scans are usually compared with the results of coronary angiography^{11, 12, 13}. However, angiography does have some important limitations raising the question of whether coronary angiography is the best reference method available.

First, coronary angiography does not show myocardial perfusion but, rather, the morphology of coronary blood vessels providing a silhouette view of the vessel, showing luminal irregularities and discrete obstructions, but not actual atherosclerosis in coronary arterial walls. This does not include information on the possible malfunction of endothelial cells, which leads to perfusion defects¹⁴. The presence of endothelial dysfunction may therefore reduce the specificity of MPI as compared with coronary angiography. Another drawback of performing coronary angiography routinely is the risk of the procedure¹⁵. A mortality of 1 per 1000 and myocardial infarction in 1 per 2000 were reported. Vascular complications and

contrast reactions occurred in 1 per 250 patients, while cerebrovascular accident occurred in 1 per 1400 patients.

On the other hand, myocardial perfusion might be preserved even in supply areas of coronary vessels with major stenosis if collateral blood flow is present¹⁶. In this case, MPI will appear to have a reduced sensitivity. Furthermore, due to the variability of the supply areas of coronary vessels and due to the possible stenosis of secondary coronary branches, perfusion defects are sometimes assigned to the wrong coronary artery.

Despite these limitations, coronary angiography remains the best practical reference standard due to its availability, proven utility, and the ability to guide revascularisation when required.

MPI uses the technique of Single photon Emission Tomography (SPECT) and has been used extensively in the non-invasive study of myocardial perfusion and viability. The current techniques rely generally on the visual interpretation of the tracer studies as well as relative quantification of the tracer uptake but the ultimate goal is to achieve absolute quantification - that is, to make an absolute measurement of Becquerels of tracer per gram of tissue in a specified region which will overcome the problems with balanced triple vessel disease as discussed in section 2.2.

The original cardiac scintigraphic studies utilise ²⁰¹Thallium as tracer. The major limitation of ²⁰¹Tl scintigraphy is the high false-positive rate observed which is predominantly attributed to attenuation artefacts and variants of normal that are interpreted as defects¹⁷. Although quantification of ²⁰¹Tl images improves specificity, the false-positive rate remains problematic, particularly in women and in obese patients because the low photon energy of the thallium gamma ray gets rapidly attenuated by tissue. Breast attenuation artefacts in women are sometimes difficult to distinguish from perfusion abnormalities secondary to inducible ischemia or myocardial scar¹⁸.

The introduction of ^{99m}Tc-labeled perfusion agents (energy of 140 keV, half-life of 6 hours, etc.) into clinical practice enhanced the specificity of MPI and provided additional information regarding regional and global left ventricular systolic function via ECG gating of images¹⁹. The quality of images obtained with ^{99m}Tc-labeled radionuclides is superior to that of images obtained with ²⁰¹Tl because of the more favourable physical characteristics of ^{99m}Tc imaging with a gamma camera. With ^{99m}Tc, patient injected activities of ~10 to 20 times higher than those that are feasible with ²⁰¹Tl can be administered, yielding images with higher count density for the same patient radiation dose. ^{99m}Tc images demonstrate less scatter and attenuation than ²⁰¹Tl, and there are fewer image artefacts using ^{99m}Tc in patients with no underlying CAD²⁰. More importantly, ^{99m}Tc-sestamibi or ^{99m}Tc-tetrofosmin²¹ imaging allows easy gated acquisition, permitting the simultaneous evaluation of regional systolic thickening,

global left ventricular function, and myocardial perfusion²². Sestamibi is a coordination complex of the radioisotope technetium-99m with the ligand methoxyisobutylisonitrile (MIBI) which, when injected intravenously into a patient, distributes in the myocardium proportionally to the myocardial blood flow. Tetrofosmin is the ether functionalized diphosphine ligand 1,2-bis[bis(2-ethoxyethyl)phosphino]ethane and is chelated by two 1,2-bis[di-(2-ethoxyethyl)phosphino]ethane ligands which belong to the group of diphosphines and which are referred to as tetrofosmin. Tetrofosmin is rapidly taken up by myocardial tissue.

Regardless of the radiopharmaceutical used, SPECT imaging is performed at rest and during stress to produce images of myocardial regional uptake that reflect relative regional myocardial blood flow in each case. During maximal exercise or vasodilator stress, myocardial blood flow is typically increased three- to fivefold compared to rest. In the presence of a substantial coronary stenosis, myocardial perfusion will not increase as expected in the stress study. In patients who are unable to undergo physical exercise, either one of the two coronary vasodilatory drugs, adenosine or dipyridamole, may be used to stimulate the required increase in blood flow.

Several ^{99m}Tc labelled agents have been developed, including teboroxime (A MIBI variant), tetrofosmin, and sestamibi. Sestamibi is the most studied of these agents, and is currently the most widely used. Tetrofosmin was developed after sestamibi and has been the subject of far fewer studies. Both tetrofosmin and sestamibi distribute to the myocardium in relation to blood flow. Their uptake requires a viable myocardial cell and an intact cell membrane.

2.2 Quantitative Myocardial Perfusion SPECT Scintigrams

With the use of planar ²⁰¹Tl imaging and visual assessment to interpret myocardial scintigrams, sensitivity and specificity for detection of CAD averaged 82% and 88%, respectively, in ~4000 patients combined from multiple published series. When quantitative analysis, instead of qualitative analysis, was used the sensitivity and specificity of planar ²⁰¹Tl scintigraphy were significantly higher at 91% and 89%, respectively, in 682 patients from studies published in the literature²³. The overall sensitivity and specificity for planar ^{99m}Tc exercise MPI studies were 90% and 70% respectively²⁴. Qualitative and quantitative methods of interpreting planar ^{99m}Tc images after stress showed similar results²⁵.

Quantitative SPECT perfusion imaging could be considered as one of the most important advances in MPI and significant higher sensitivities of 89% were obtained at the expense of specificity (76%) for studies performed with ²⁰¹Tl²⁶. In the case of ^{99m}Tc agents the introduction of SPECT imaging has not appreciably improved these measures in two studies^{19, 27} performed on a total of 157 patients, using both quantitative and qualitative methods. The sensitivity was 85% and the specificity was 79% for the detection of CAD.

Other studies did find the sensitivity of exercise MPI to be comparable to that of ^{201}Tl ^{28,29}. These equivalent (and occasionally reduced) specificities compared to ^{201}Tl planar and SPECT images are most likely attributed to a referral bias in which patients with abnormal scans are more likely to be referred for coronary angiography than patients with normal scans in more recent studies³⁰.

It is of interest that the sensitivity of SPECT remains high (85%) for CAD detection in patients without prior myocardial infarction. As expected, the sensitivity for detection of single-vessel disease with SPECT ^{201}Tl imaging averaged 83% compared with 93% for patients with angiographic 2-vessel disease and 95% for patients with 3-vessel disease²³. In the case of 3-vessel disease there is a reduction of intensity in all the regions which can be interpreted as reduced intensities in the study or by adjusting the intensity levels such a study can be interpreted as normal.

The lower specificity for myocardial perfusion imaging is mostly related to false-positive defects on the inferior wall³¹. This phenomenon is created by a loss in depth-dependent resolution and by attenuation of the signal.

2.2.1 ECG-Gating of Myocardial Perfusion SPECT Scintigrams

The simultaneous assessment of myocardial function together with myocardial perfusion from a single procedure became available with the introduction of ECG-gated (electrocardiographically-gated) myocardial perfusion SPECT imaging³². It is currently one of the most commonly performed cardiology procedures in a nuclear medicine department replacing the SPECT only MPI studies. Automation of the image processing and quantification has made this technique highly reproducible, practical and user friendly in the clinical setting. It is now routinely used to assess, in addition to myocardial perfusion, global and regional left ventricular function^{33,34}. The main parameter of global function that is measured is left ventricular ejection fraction. Other important parameters of global function that are measured are end-diastolic volume, end-systolic volume, stroke volume and myocardial mass. For assessment of regional LV function both myocardial wall motion and wall thickening is determined. Incorporating ECG-gating as a routine during SPECT cardiac perfusion scintigraphy is appropriate for at least four reasons: there is an extensive peer-reviewed literature^{35,36,37} attesting to its value; the practice is now widespread; practitioners in diverse settings (academia and private practice) regularly employ it; and the hardware and software requirements are widely available.

2.2.2 Absolute Quantification

The ultimate goal in myocardial SPECT is to achieve absolute quantification - that is, to make an absolute measurement of Becquerels of tracer per gram of tissue in a specified region of the left ventricular myocardium. Unfortunately, photon attenuation, scatter radiation, partial-volume errors, and other complications compromise absolute quantification of the radionuclide uptake from SPECT^{38,39,40}. According to a study which has been done on a porcine model without any corrections, the measured in vivo activity concentration in the porcine myocardium was only 10% of the true value⁴¹. Correcting for object-specific attenuation improved the accuracy of this measurement but resulted in values that were still only 42% of the true value. By correcting for both attenuation and partial-volume errors, they were able to achieve absolute quantification with an accuracy error near 10%.

2.3 Reported Sensitivity and Specificity of SPECT MPI

SPECT MPI has important prognostic value and sensitivity in the region of 85%. However, the specificity of SPECT has been commonly reported to be as 65% low indicating a number of false-positive readings in studies^{42, 43, 44}.

Among several physical factors that degrade image quality and quantitative accuracy in SPECT, photon attenuation is believed to be the major cause of false-positive cardiac SPECT perfusion images^{45, 46, 47, 48}.

2.4 Permutations in Emission Tomography

There are several factors that degrade the image quality and the quantitative accuracy of emission tomography reconstructions and these factors have to be addressed for the optimisation of the reconstruction process. These factors include the following^{41,49, 50}:

- ▶ Attenuation of the photons travelling toward the detector,
- ▶ The detection of scattered as well as primary photons,
- ▶ Depth-dependent collimator response correction (frequency-distance principle),
- ▶ The finite spatial resolution of the imaging systems or partial-volume effect.
- ▶ Patient motion during the scan.

Whereas all of these effects limit practical quantitative emission tomography, the most important effects are the photon absorption in the object and the contribution in the images of events arising from photons scattered in the patient (the object)^{40,51,52}. Both absorption and scattering are components of the general process of photon attenuation and in order to improve quantitative assessment, these factors have to be addressed. Extensive work has been done to reduce the effect of these factors and solutions have been provided but there is still a need to improve these techniques because the current specificity of the technique is still too low causing a significant number of false-positive reports. This means that about 20%

of patients will be diagnosed as having a positive scan and will undergo additional testing but they will not be suffering from CAD. This places unnecessary stress to the patients involved and has a substantial impact on cost. As an example, for a District General Hospital doing on average 1500 MPI studies per year, about 300 patients without CAD will undergo additional testing incurring an extra cost to the hospital. False negative MPI studies are uncommon⁵³, but include the difficult to diagnose 'balanced triple vessel disease' where perfusion to all myocardial territories is equally reduced and therefore no normal myocardium exists for comparison. Sometimes no identifiable explanation exists for a false negative result but it can also be as a result of the existence of collated circulation, also known as "collaterals", which restore a substantial amount of blood flow but the person is not disease free.

2.4.1 *The Problem of Photon Attenuation in Emission Tomography*

Photons emitted by the radiopharmaceutical will interact with tissue and other materials as they pass through the body. This forms the physical basis of photon attenuation. For photon energies encountered in nuclear medicine (i.e., from 68–80 keV for ²⁰¹Tl to 511 keV for positron emitters), photons emitted by radiopharmaceuticals can undergo photoelectric interactions and Compton incoherent scattering within the patient. In the case of photoelectric interactions the incident photon is completely absorbed. In the case of Compton scattering, the primary radionuclide photon interacts with loosely bound electrons in the surrounding material and is scattered. The scattered photons have a trajectory which generally carries it in a different direction than that of the primary photon. The energy of the scattered photon can be lower than, in the case of Compton incoherent scattering, or be the same as, in the case of coherent scattering, than that of the incident photon. The more medium in the trajectory of the photon, the bigger the chance for it to be stopped or scattered.

Many solutions have been proposed to compensate for the effect of photon attenuation and this will be discussed in detail in section 2.4.5.

2.4.2 *The Problem of Photon Scatter in Emission Tomography*

Another source of degradation inherent in SPECT imaging which distorts the projection data is the inclusion of scatter in the projections and although Compton scatter is part of the attenuation process, scatter is normally considered to be a separate problem and can be treated as such. Scattered photons are diverted from their original path with some loss in energy. Due to scatter, the photons reaching the Gamma Camera will have energies with a broad band ranging from close to zero to the maximum energy of the isotope. Most of the photons with energy lower than the maximum energy can be eliminated with the use of an energy window. This will discriminate the photons based on their energy and only photons

close to the maximum energy will be detected reducing the number of scattered events that are detected. Making the window too small will lead to extensive scanning times which will limit the usefulness of the test. Therefore, although the window size can be used to limit the number of scattered photons, its size cannot be reduced to a value which will completely remove all scattered photons and approximately 30% of the scattered photons will still be detected and these can lead to artefacts in the reconstruction as well as loss of contrast. The problem with scatter is that photons originating from a position which would not have been detected can be scattered in a different direction so they will be detected. Sohlberg et al suggest that scatter appears to be a greater problem when attenuation correction is performed⁵⁴. This leads to the inclusion of photons in the projections that normally would not have been detected. The ratio of scattered to primary photons in the photopeak energy window (scatter fraction) is typically 0.34 for ^{99m}Tc ⁵⁵ and 0.95 for ^{201}Tl ⁵⁶ when using a 20% energy window.

Scatter correction results in improvement in image contrast and it is essential if absolute quantification is desired. In cardiac studies, performing attenuation correction alone tends to result in reduction of contrast compared with results without attenuation correction (in fact the apparent contrast is artificially high without attenuation correction due to the errors in reconstruction). As a result some form of scatter correction is desirable to restore visual contrast.

There have been many methods of scatter correction suggested and this is still a topic for continuing research. Unfortunately there is no single method that is universally accepted. Generally, the methods of scatter correction can be divided into two different categories^{57,58}. The first category, referred to as scatter estimation, consists of those methods that estimate the scatter contributions to the projections based on the acquired emission data. The data used may be information from the energy spectrum or a combination of the photopeak data and an approximation of scatter Point Spread Functions (PSFs). The scatter estimate can be used for scatter correction before, during, or after reconstruction. The second category consists of those methods that model the scatter PSFs during the reconstruction process. The second approach will be called reconstruction-based scatter compensation.

Whereas attenuation and collimator blurring can nowadays be corrected in clinically acceptable computation times, accurate and efficient scatter correction has been proven to be a more difficult problem.

In the triple-energy window scatter compensation method⁵⁹ the count of scattered photons is subtracted from that acquired with a photopeak window at each pixel in each planar image of single-photon emission computed tomography (SPECT). The subtraction is carried out using two sets of data: one set is acquired with a main window centered at photopeak energy and the other is acquired with two subwindows on both sides of the main window. The scattered

photons included in the main window are estimated from the counts acquired with the subwindows and then they are subtracted from the count acquired with the main windows.

One very promising recently presented scatter compensation method is the Monte Carlo (MC)-based scatter correction⁶⁰. In this method, a MC simulator is used as a forward-projector for scatter in the ordered subset expectation maximization (OS-EM) algorithm. MC-based scatter modelling is expected to be especially advantageous in areas where the attenuating media is highly non-uniform such as the thorax because it can faithfully produce the complex shape of the scatter response function. The MC-based scatter compensation has been shown to outperform the common triple-energy window scatter compensation method in terms of contrast and myocardial lesion detectability⁶¹. Unfortunately, despite the considerable advances made in MC based scatter compensation its widespread utilisation in clinical practice can still be limited by long computation times.

To overcome this limitation two simple and effective acceleration methods⁶² for reconstruction-based scatter compensation have been presented. The first of these approaches is the coarse grid scatter modelling method, which calculates the scatter contribution using sparser grid than is used in the actual reconstruction. The second approach is the intermittent scatter modelling method, where scatter is modelled only during the first couple of OS-EM iterations and then held as a constant additive factor for the later iterations. Both of these approaches are based on the assumption that the scatter response contains mainly low-frequency components and can thus be modelled with a relatively large voxel size and not during the last OS-EM iterations.

In a study⁶³ to implement the coarse grid and intermittent scatter modelling methods for MC-based scatter compensation a substantial reduction in the reconstruction time has been achieved making both the coarse grid and the intermittent scatter modelling methods suitable for everyday accelerating MC-based scatter compensation, and with these methods MC-based scatter compensation is available for routine use in clinical cardiac SPECT today.

2.4.3 The Problem of the Partial Volume Effect in Emission Tomography

The spatial resolution in the reconstructed images in SPECT is limited (about 12 to 16 mm at FWHM (Full Width Half Maximum))⁶⁴, especially in small structures which results in the underestimation of peak activity in small structures. This finite spatial resolution is also called the partial-volume effect.

The partial volume effect is part of a set of effects which occur due to the finite size of the detection elements or resolution elements (voxels which are the pixel size in 3 dimensions). When the object varies rapidly over distances comparable or less than the spatial resolution,

the image value will reflect the mean value over the resolution element. This partial volume averaging is also called the partial volume effect and is illustrated in figure 2.1.

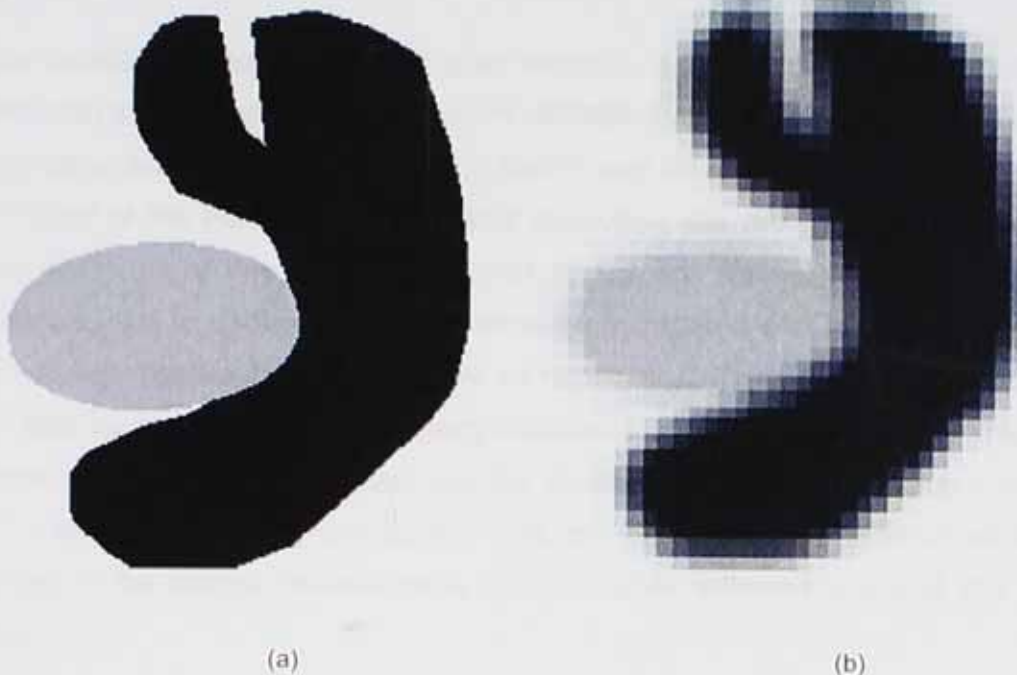


Figure 2-1: Illustrating the partial volume effect with the real image (a) and the displayed image (b) as a result of the PVE.

In SPECT a point source of radioactivity yields a blurred image. The PSF is an index of this blur, which limits the ability to resolve small objects. This intrinsic blur also limits the quantitative accuracy of SPECT measurements and results in an incorrect estimate of radioactivity concentration in small structures⁶⁵. The observed radioactivity concentration in small structures differs from the true concentration because of "spillover" effects between regions, i.e. blurring of counts out of the structure ("spill-out") and blurring of counts into the structure from surrounding radioactivity ("spill-in").

To correct for the partial volume effect (PVE) in SPECT data sets is an important though complex issue. Two main approaches for PVE correction can be distinguished: a voxel-based⁶⁶ and a region-of-interest (ROI) based method⁶⁷. Although other methods have been proposed, they either represent a combination of the above techniques⁶⁸, or have not been fully validated⁶⁹. Although the ROI-based approach is of interest on a theoretical basis, it does not allow actual mapping of the resulting PVE-corrected data sets, so the voxel-based approach would have wider applications despite its limitations.

Different methods have been proposed that use well defined information from either MR and/or CT data together with the SPECT data to correct for the partial volume effect^{50,70}. The accuracy of SPECT is limited by the relatively poor resolution compared to these anatomy-oriented systems.

Correction for PVEs must account for both the signal loss from the limited extent of the region observed compared to the spatial resolution of the tomographic system, and the "spillover" or signal contamination from surrounding tissue with different tracer uptake and kinetics.

A simple convolution model⁷¹ can be used where a 1-dimensional square wave can be convolved with a 1-dimensional Gaussian of Full Width Half Maximum (FWHM) to predict the underestimation associated with the PVE in the LV wall for spatial resolutions (characterized by the FWHM of the PSF). For each spatial resolution, the ratio \max_{obs}/\max between the observed maximum of the square wave after convolution (\max_{obs}) and its true maximum (\max) can be used to deduce the underestimation associated with the PVE in the LV wall, and the recovery coefficient is then defined as \max/\max_{obs} . The activity measured in the LV wall can then be multiplied by this recovery coefficient for PVE compensation. This recovery component can then be incorporated into the iterative reconstruction for each iteration as $\text{Image}^{k+1} = \text{Image}^k \times \text{recovery component}$. This provides a practical solution which can be incorporated in the routine reconstruction of MPI studies without the use of any additional hardware.

Resolution element and sampling

The Nyquist–Shannon sampling theorem, named after Harry Nyquist and Claude Shannon, is a fundamental result in the field of information theory. Sampling is the process of converting a signal (for example, a function of continuous time or space) into a numeric sequence (a function of discrete time or space). Shannon's version of the theorem states:⁷² If a function $x(t)$ contains no frequencies higher than N hertz, it is completely determined by giving its ordinates at a series of points spaced $1/(2N)$ seconds apart. The theorem is commonly called the Nyquist sampling theorem and it is often referred to simply as the sampling theorem.

The sampling process

The theorem describes two processes in signal processing: a sampling process, in which a continuous time signal is converted to a discrete time signal, and a reconstruction process, in which the original continuous signal is recovered from the discrete time signal.

The continuous signal varies over space in a digitised image and the sampling process is performed by measuring the continuous signal's value every T units of space, which is called the sampling interval. Sampling results in a sequence of numbers, called samples, to represent the original signal. Each sample value is associated with the instant in time when it was measured. The reciprocal of the sampling interval ($1/T$) is the sampling frequency denoted f_s , which is measured in samples per unit of space.

The theorem gives an upper bound for frequency components, $N < f_s/2$, of the signal to allow for perfect reconstruction. This upper bound is the Nyquist frequency, denoted f_N . The sampling theorem provides a sufficient condition, but not a necessary one, for perfect reconstruction.

Nyquist sampling and band limited images

Convolution by a point spread function in an image space is equivalent to multiplication by the Fourier transform of the PSF in Fourier space. PSF Fourier transforms are generally low-pass filters: they reduce the high frequency components of the image. If a PSF completely removes all frequencies higher than some μ_c , then the PSF (and any images convolved by the PSF) are band limited at μ_c .

The sampling of an image determines which Fourier frequencies can be measured from the image. If all frequencies lower than the band limit can be extracted, the image is said to be critically sampled. If the image is oversampled, then it is sampled more frequently than necessary.

If we oversample the image, we might preserve noise that otherwise would be lost, but no signal.

Under sampling the image (preserving too few pixels to measure all Fourier components out to the band limit) has the same result as multiplying the Fourier transform by a square function. The Fourier transform of a square function is a sinc, and a multiplication in Fourier space is a convolution in image space, so this resampling results in a convolution by a sinc function.

Of all the limitations mentioned in 2.4, the one outstanding point is correcting for the partial volume effect. There is no very good and easy "global" solution for the partial volume effect available yet⁷³. Collimator modelling reduces the partial volume effect, but does not fully correct for it. Reconstruction with anatomical prior information could also reduce the partial volume effect, but incorporating anatomical information is not always so easy (there are several reconstruction methods available which can do this⁷⁴), but clinically there still are a lot of problems (e.g. accurate alignment, respiratory and cardiac motion, etc).

2.4.4 The Problem of Depth-Dependent Collimator Response

Because collimator holes are not infinitely narrow, the photons that traverse the collimator will not all come from a direction that is exactly aligned with the holes. This leads to a substantial loss of resolution in the gamma-camera images and in the reconstructions. The amount of resolution also depends on the distance of the camera head from the patient, the further away the detector are, the worse the resolution as depicted in figure 2.2. The acceptance angle of a collimator is defined by the length of the collimator and the hole

diameter. Although decreasing the acceptance angle would decrease the collimator blurring, it would also greatly decrease the sensitivity of the collimator. It can be shown that a twofold increase of the collimator resolution (typical collimated planar resolution is from 7 to 10 mm at FWHM⁶⁴) would decrease the sensitivity by a factor of about 4⁷⁵.

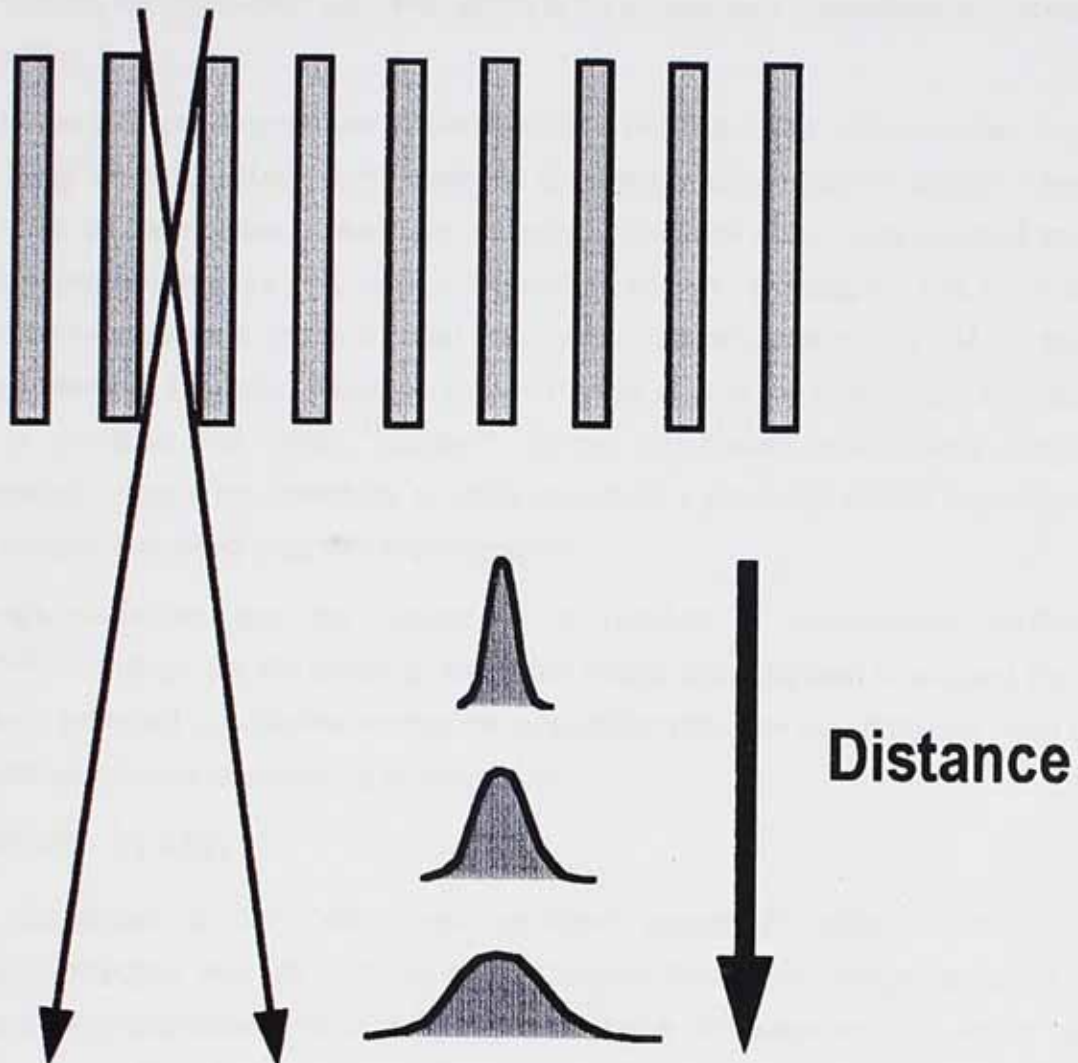


Figure 2-2: Illustrating the effect of distance on the shape of the PSF.

Correcting for this distance dependent blurring is possible as a result of accurate mathematical descriptions of collimator blurring^{76,77}. The distance dependent blurring can be incorporated into the Fourier transform of the sinogram, making use of the frequency-distance principle⁷⁸. In iterative reconstruction it is possible to incorporate the detector response into the projector/back-projector pair to compensate for the distance dependent detector response during the acquisition to achieve a 2-fold improvement⁷⁹.

2.4.5 Commercially Available Correcting Systems

A range of commercially available solutions are available which integrate scatter correction, attenuation correction and resolution recovery compensation techniques into an iterative

reconstruction algorithm to simultaneously address these problems by modelling the camera and collimator and imaging parameters used for a specific application so that the degrading physical effects can be eliminated and to suppress noise in the image reconstruction process. Several such systems are now commercially available and will be briefly discussed. All these methods achieved this by modifying the Ordered Subset Expectation Maximization (OSEM) iterative reconstruction algorithm which is an accelerated Expectation Maximization (EM) algorithm.

Most of these systems incorporate noise reduction methods. The reconstructed images obtained using the MLEM (Maximum Likelihood Expectation Maximization) algorithm tend to become noisy as the number of iterations increases, because noisy reconstructed images may yield projections that are very close to the measured noisy projections. The introduction of a priori knowledge as a constraint that may favour convergence of the EM process is called regularisation. The prior, based on an assumption of what the true image is, is usually chosen to penalise the noisy images⁷⁴. Some of these commercially available implementations include the possibility of using maximum a posteriori (MAP) reconstruction methods such as penalised weighted least-squares⁸⁰.

These implementations are the subject of a number of independent verification studies^{81,82,83,84,85}, which are still ongoing, and initial results would appear to suggest that the improvement achieved is sufficient so that the acquisition time can be halved (or even be a quarter) without the loss of sensitivity or specificity.

A. SIEMENS - FLASH 3D

Siemens introduced a 3D OSEM reconstruction algorithm⁸⁶ utilising Transmission Attenuation Correction with 3D Collimator and Detector Response Compensation in both forward and back-projection directions by implementing a 3D Gaussian PSF which varies with the distance from the collimator. Scatter compensation are achieved with Energy Window-based Scatter Correction techniques, i.e. Dual Energy Window (DEW) and Triple Energy Window (TEW)-based scatter projection images which are applied additively in the forward projection. It utilises multiple-peak isotope acquisitions and each photopeak is reconstructed separately with attenuation correction maps and scatter images for each peak where the peak reconstructions are summed post acquisition.

The acquisition time can be reduced to between 33% and 50% from the expected 20 minutes, as compared to acquisition protocols with Filtered Back Projection reconstruction⁸⁶.

B. PHILIPS - Astonish

Astonish has been developed by Philips Healthcare and is a fast SPECT reconstruction algorithm based on the OSEM reconstruction method that includes corrections for photon

scatter, photon attenuation, and variations in spatial resolution. It also uses built-in noise reduction methods during the iterative process.

By measuring the changes in spatial resolution with distance from the collimator corrections for variations in spatial resolution are achieved but it is necessary to obtain calibrations for each of the collimators initially by the manufacturer. This collimator information is then incorporated into both the back projection and the forward projection parts of the reconstruction. Resolution Recovery correction can be performed with or without attenuation and scatter corrections.

The corrections for the photon scatter are performed by the Effective Scatter Source Estimation (ESSE) method⁶². It can perhaps be best described briefly by quoting from the authors' abstract: "The method requires 3 image space convolutions and an attenuated projection for each viewing angle. Implementation in a projector-backprojector pair for use with an iterative reconstruction algorithm would require 2 image space Fourier transforms and 6 image space inverse Fourier transforms per iteration." The corrections for the photon scatter are performed prior to the Transmission Attenuation Correction in each iterative OSEM step. Corrections for attenuation are performed during the forward projection process.

To be able to implement it for clinical use this technique has been tested⁶⁷ and interpretative certainty and diagnostic accuracy were the same for standard FBP reconstruction, full-time imaging and half-time imaging.

C. GE Healthcare - Evolution

Evolution for Cardiac has been introduced by GE Healthcare which uses a modification of the OSEM algorithm to incorporate resolution recovery. By modelling the integrated collimator and detector response function image resolution recovery⁸⁸ based on a number of parameters are achieved. These parameters are collimator hole and septa dimensions, collimator to detector gap, intrinsic detector resolution, crystal thickness and projection-angle specific centre-of-rotation to collimator face distances⁸⁹. This is achieved by either using look-up tables or obtained directly from the raw projection data. Additionally noise suppression is incorporated, which is required to prevent hot spots because of the amplification of noise. MAP (Maximum a Posteriori estimation) technique is incorporated to control image noise.

D. ULTRASPECT - Wide Beam Reconstruction

A company in Haifa, Israel, UltraSpect has developed a standalone workstation which utilises the patented Wide Beam Reconstruction (WBR) algorithm⁸¹. This system is available as an additional workstation and can reconstruct data from most existing gamma cameras with standard collimators. WBR is based on an accurate physical description of the emission detection process and on its reconstruction, utilising iterative optimisation methods with no post-filtering applied. It is designed to simultaneously suppress noise and improve image

resolution by eliminating the line spread function limitations from the system resolution. During the iterative reconstruction it uses the information regarding the collimator's geometry (such as the dimensions and shape of holes or the septa thickness) and the detector's distance from the patient. WBR applies statistical modelling of the expected photon emission and Fourier analysis of projection data to determine the approximate noise level that is present in the acquired data. Therefore selection of an optimal noise model to yield the appropriate balance between resolution and noise is possible.

A preliminary study of WBR demonstrated equivalent image quality and defect characterisation with simulated fast imaging with times as low as one-fourth of standard imaging time as compared to full-time standard imaging⁹⁰.

E. Hermes Medical Solutions – Hybrid Reconstruction

The company Hermes Medical Solutions is a long standing provider of standalone workstations for the processing and analysis of Nuclear Medicine images. A recent development is the Hybrid Reconstruction algorithm. This system can reconstruct data from most existing gamma cameras with standard collimators. It utilises the Coarse Grid and Intermittent Scatter Modelling method to obtain scatter correction⁶³ together with Transmission Attenuation Correction and uses Incremental Gaussian Diffusion⁹¹ to obtain compensation for depth-dependent collimator blurring. The use of MAP reconstruction is also available.

2.5 Attenuation Correction Strategies in Emission Tomography

The determination of an accurate, patient-specific attenuation map, which represents the spatial distribution of linear attenuation coefficients for the region of the patient's anatomy that is included in the radionuclide imaging study, is fundamental to performing attenuation compensation. The methods for generating the attenuation map generally can be described as falling within these strategies:

- ▶ Import and register maps from another modality, i.e. Computerised Tomography (CT) and Magnetic Resonance Imaging (MRI);
- ▶ Obtain transmission data to construct the attenuation maps using the gamma camera employed for emission imaging; and
- ▶ Estimate the attenuation map from solely the emission data, i.e. emission based methods.

The first two classes include correction methods based on transmission scanning while the third class includes transmissionless correction methods based on assumed distribution and boundary of attenuation coefficients (calculated methods), statistical modelling for simultaneous estimation of attenuation and emission distributions or consistency conditions criteria. The reconstructed attenuation coefficients are energy dependent and therefore the

reconstructed attenuation coefficients need to be transformed to the coefficients of the appropriate isotope energy by using suitable techniques.

After the attenuation map is generated it can be used to compensate for photon attenuation. The attenuation correction process can be done before reconstruction⁹², after reconstruction⁹³, or it can be integrated within the transition matrix of an iterative reconstruction algorithm⁹⁴.

The iterative reconstruction algorithm uses the fact that the attenuation map accurately delineates the contours of structures in the body and contains information about the distribution of its linear attenuation coefficients. It uses this information to calculate the attenuation to the boundary of each attenuating region for each pixel along the ray between the points of emission and detection in SPECT, before the resulting values are summed to estimate the projected or back-projected pixel values. If an accurate patient-specific attenuation map is available, then non-homogeneous attenuation can be easily implemented in the image reconstruction process.

2.5.1 Import and Register Maps from Another Modality

It is well known that x-ray computed tomography (CT) can provide a patient-specific map of attenuation coefficients that can be used to compensate radionuclide data from PET or SPECT for the effects of photon attenuation^{95,96}. This is a natural observation since the CT image inherently represents the three-dimensional spatial distribution of attenuation coefficients of the patient. In addition, CT scanners are widely available and can produce cross-sectional images quickly with low noise and excellent spatial resolution in comparison to transmission images produced with external radionuclide sources and Nuclear Medicine Imaging generally. Overall, x-ray transmission techniques offer practical advantages for producing attenuation coefficient maps in terms of high photon output and short procedure times, excellent decay, lack of physical decay with a source that can be turned off between scans and that can be discarded easily at the end of its useful operating life.

Appropriately scaled CT scans can be acquired either independently on separate CT Scanners^{97,98,99,100} or simultaneously on multimodality imaging systems^{101,102,103}. These image sets are then co-registered with the emission data to provide the attenuation map that can then be used in the reconstruction algorithm to compensate for the attenuation of the patient's anatomy.

The integration of SPECT and CT systems into a single imaging unit sharing a common imaging table provides a substantial advance in technology because this combination permits the acquisition of SPECT and CT data sequentially in a single patient study with the patient in a fixed position. Thus, the 2 datasets can be acquired in a registered format by

appropriate calibrations, permitting the acquisition of corresponding slices from the 2 modalities and avoiding the complications of aligning the two datasets acquired on different machines at different times, with slight positional differences. The CT data can then be used to correct for tissue attenuation in the SPECT scans on a slice-by-slice basis. Because the CT data are acquired in a higher-resolution matrix than the SPECT data, it is necessary to decrease the resolution of the CT data to match that of SPECT. In other words, the CT data are blurred to match the SPECT data. From the attenuation coefficient data acquired with CT, correction factors can then be determined, which can then be used to correct the SPECT data for attenuation, yielding the attenuation-corrected SPECT data.

There are numerous advantages in the use of CT data for attenuation correction of emission data. First, the CT scan provides a high photon flux that substantially reduces the statistical noise associated with the correction in comparison to other techniques (i.e., radionuclides used as transmission sources). Also, because of the fast acquisition speed of CT scanners, the total imaging time is substantially reduced by using this technology. Another advantage related to the high photon flux of CT scanners is that attenuation measurements can be made in the presence of radionuclide distributions with negligible contributions from photons emitted by the radionuclides (i.e., postinjection CT measurements can be performed). And of course the anatomic images acquired with CT can be fused with the emission images to provide functional anatomic maps for accurate localization of radiopharmaceutical uptake.

The benefits of using CT for attenuation correction as opposed to a radionuclide transmission source include less noise, faster acquisition, no influence on CT data by the SPECT radionuclide, and no need to replace decayed transmission sources¹⁰⁴.

Unfortunately, a potential disadvantage is that there is sequential acquisition of CT data and then SPECT data; therefore, misregistration can occur, with patient movement leading to an artefact on the corrected scintigraphic images.

Several artefacts can be encountered with SPECT/CT. Patient movement between acquisition of the SPECT and CT images will lead to misregistration¹⁰⁵, which can produce an incorrect attenuation map, causing defects on the attenuation-corrected images. Movement can result from respiratory¹⁰⁶ and cardiac motion, sagging of the emission table, and patient motion between SPECT and CT acquisitions. It is essential that any SPECT/CT system use a coregistration program and associated quality control phantom on a regular basis to ensure correct alignment between the SPECT and CT scanners, in addition to routine quality control for both SPECT and CT. It is also beneficial to have a quality control program to realign the SPECT/CT data before attenuation-corrected SPECT image reconstruction, to correct for patient motion.

Other sources of error¹⁰⁷ include CT truncation, metal artefacts, and beam-hardening artefacts. Truncation, which occurs because the smaller CT field of view compared with that of SPECT may not account for part of the patient beyond the field of view, can result in an inaccurate attenuation correction map and reduce image quality, particularly in large patients. Artefacts from metal or beam hardening can also affect CT image quality and may lead to "false positive" focal uptake on attenuation-corrected SPECT images, which is caused by incorrect scaling of the Hounsfield units into the SPECT attenuation map.

Physiological misregistration artefacts¹⁰⁸ occur when the SPECT emission image scan is displaced relative to the CT scan used for attenuation correction when involuntary physiological motion is present. This is not only relevant when CT attenuation maps are used but can also be relevant when attenuation correction is done with rotating radioactive sources emitting gamma rays. CT data are obtained at a speed much faster than a respiratory cycle, they depict images in a specific phase of the respiratory and cardiac cycles. The much longer SPECT data acquisition averages over all respiratory and the cardiac positions. SPECT depict the average tidal breathing position of the diaphragm but in CT imaging the diaphragm may be caudally displaced relative to this position when the CT is acquired with the patient close to end-inspiration or in end-inspiration breath-hold. Such a CT-image used for attenuation correction will erroneously place lung tissues in the cranial abdominal regions, where on co-registered SPECT there is soft tissue. As the lung CT pixel values are low and result in a low attenuation correction, this region will appear as having less activity than it actually has. The cranial areas of the liver and the spleen thus appear as if they would be part of the lung on the SPECT scans.

It is well known that patient motion may cause image artefacts in myocardial SPECT images and affect clinical diagnosis^{109,110,111,112}. Patient motion can be grouped into two categories, voluntary and involuntary motions. Voluntary motion includes unpredictable movements of the patients during data acquisition. Involuntary motion involves movements of the organs such as upward creep in stress perfusion study and respiratory motion. Upward creep is probably related to a transient increase in mean total lung volume early following exhaustive exercise, resulting in a mean lower position of the diaphragm (and thus the heart) at the beginning of imaging¹¹³. However, these motion artefacts are often masked by more serious effects generated by other image degrading factors, such as attenuation, collimator-detector blurring and scatter. Recently, quantitative reconstruction methods are available to reduce the effects of these image degrading factors. As a result, motion artefacts and their compensation are become increasingly important in quantitative myocardial SPECT imaging.

Upward creep and respiratory motion can produce substantial artefacts¹¹⁴ in myocardial SPECT images. Due to changes in attenuation effects from movement of the heart and diaphragm and blur from respiratory motion, the artefacts are shown as regional decrease of

count density in the inferior wall. The magnitudes of the artefacts increase with the extent of the motion. The artefacts cannot be reduced by correction. This implies that motion corrections are important in myocardial SPECT image reconstruction to obtain quantitatively accurate reconstructed images. Upward creep can be corrected simply by appropriate translation of the projection data. To correct for respiratory motion, however, respiratory gating may be needed.

2.5.2 Radionuclide Transmission Methods

The earlier systems used either ^{99m}Tc or ^{201}Tl transmission sources to produce accurate attenuation maps¹¹⁵. More recently the use of either line or point sources with ^{153}Gd , ^{133}Ba or ^{139}Ce has been developed to compute the attenuation map, depending on practical and cost effectiveness issues¹¹⁶.

This section considers the use of radionuclide sources to produce the attenuation map. This method acquires transmission data for use in conjunction with conventional emission scanning. In a clinical environment, the most widely used attenuation correction techniques use transmission data acquired before (preinjection)¹¹⁷, during (simultaneous)^{118,119}, or after (postinjection)¹²⁰ of the emission scan. Technically it is easier to perform sequential emission–transmission scanning rather than simultaneous scanning, but it increases the imaging time and patient misalignment or motion can cause errors in the image registration process. On the other hand, simultaneous acquisition requires no additional time for the emission and transmission measurements, which can be an important factor for routine clinical use but errors may be introduced due to cross talk between the transmission and emission data. A range of approaches have been proposed to minimise or eliminate the effects of contamination of emission data by transmission photons and to reduce spillover of emission data into the transmission energy window^{118,121}. The attenuation coefficients and activity concentrations have been shown to be not significantly different when estimated with sequential and simultaneous emission transmission imaging¹²². The accuracy of the transmission and emission maps produced using different transmission–emission source combinations has been the subject of many debates and studies¹²³. Different transmission-scanning geometries have emerged for clinical implementation in SPECT¹²⁴.

Uncollimated flood or sheet sources have been used in the early designs of transmission systems for SPECT cameras. This design has certain advantages, for example, the source fully irradiates the opposite head and requires no motion of the source other than that provided by the rotation of the camera gantry. Such sources also have drawbacks in that the high proportion of scattered photons in the transmission data due to the broad-beam imaging conditions. As a result, the attenuation map estimates an effective linear attenuation coefficient rather than the value that would be calculated from narrow-beam geometry.

Collimation of the transmission source can overcome this difficulty in part¹²⁵ to produce a geometry that more accurately represents narrow-beam transmission geometry.

The main radionuclide-based configurations include¹²⁶:

- ▶ a stationary line source fixed at the collimator's focus with convergent collimation on a triple-detector system¹²²,
- ▶ scanning line sources with parallel-hole collimation⁷⁶,
- ▶ a multiple line source array with parallel-hole collimation¹²⁷,
- ▶ scanning point sources using either fanbeam and offset fanbeam geometry¹²⁸, or
- ▶ an asymmetric fanbeam geometry acquired by using a high-energy source that emits transmission photons capable of penetrating the septa of a parallel-hole collimator¹²⁹.

The scanning line source geometry has emerged as the most widely implemented configuration for commercial transmission acquisition. However, each configuration has its unique advantages and drawbacks, and camera manufacturers are still optimising the apparatus used to acquire the transmission data.

2.5.3 *The Implementation of Transmission Based Methods*

The majority of clinical attenuation compensation techniques use maps reconstructed from data obtained in transmission scans. Such patient-specific compensation methods, based on experimentally measured maps, should create substantially improved images, but serious problems with the technique created distrust and leading to heated debates about the value of attenuation correction¹³⁰. Several reviews have shown that attenuation correction methods that are currently available on clinical cameras can introduce artefacts that may be difficult to identify and might inadvertently alter diagnoses and study outcomes¹³¹. As a result, the attenuation correction option is often avoided in clinical practice, even in those centres that have all the necessary equipment relying instead on the feeling that an expert reporter will observe and correctly identify any artefacts.

2.5.4 *Reducing the Time for the Transmission Scan and Emission Based Methods*

Transmission imaging is achieved at substantial costs: increased imaging time, increased hardware complexity, and increased financial cost.

Several attempts have been made to overcome these limitations. One such attempt uses estimates of tissue density to provide an attenuation map without increasing scan time¹³². Attempts to provide attenuation maps that are based on fast transmission scans, simultaneous emission-transmission scans^{122,76}, or exploiting the consistency conditions of the attenuated radon transform¹³³ are also examples. The fast and simultaneous transmission scan methods were developed to minimise both scan time and the artefacts

associated with errors in scatter and attenuation correction caused by misaligned emission and transmission data¹³⁴. A method has been developed to extrapolate complete attenuation maps from truncated transmission scans¹³⁵. However, transmission imaging still suffers the penalty of requiring extra hardware.

In principle, the attenuation maps containing detailed information about density distribution in the body can be computed using only emission data¹²⁶, but this approach is still too complex and time consuming for routine use^{136, 137}. Algorithms in this class of methods either assume a known body contour in which a (uniform) distribution of attenuation coefficients is assigned or try to derive the attenuation map directly from the measured emission data.

Attenuation correction is straightforward in imaging the brain and abdominal areas. In these areas soft tissues are the dominant constituent allowing use of a uniform attenuation correction. In regions such as the thorax, which are more heterogeneous, and include low density air spaces, the attenuation coefficients have a wide range and vary rapidly over very short distances. In the brain and abdomen, it is possible to determine the body contour from the emission data, then the region within the contour is assigned a uniform linear attenuation coefficient value corresponding to that of water or soft tissue to generate the corresponding attenuation map. Automatic edge-detection methods can be used to determine the body contour or it can be done manually.

In some of the earliest work on emission based methods alternating iterations of the reconstruction algorithm were used¹³⁸ to reconstruct emission tomograms and attenuation maps from a set of emission data alone. Many researchers, who applied various optimisation techniques, have also used similar philosophies in generating emission tomograms and attenuation maps¹²⁹. The problem can be formulated as an optimisation task in which the objective function is a combination of the likelihood and an a priori probability¹³⁹. The latter uses a Gibbs prior distribution to encourage local smoothness and a multimodal distribution for the attenuation coefficients. Other methods included the use of the expectation maximization (EM) algorithm¹⁴⁰ or penalty functions^{141, 142}.

An attractive alternative for the estimation of attenuation maps from emission data alone is called "inferred anatomy"¹³³. Earlier attempts to infer anatomy include fitting ellipses to photopeak- or Compton-window sinograms or thresholding preliminary reconstructions¹⁴³.

An inferred anatomy method for brain SPECT using attenuation distributions inferred from a head atlas¹⁴⁴ has been proposed. This method requires a digitised head atlas and a registration program. It is simple to implement, because no customised software is required, and is computationally feasible on modern desktop computers, requiring only slightly more computation time than a typical tomographic reconstruction.

2.5.5 The Method of Inferred Anatomy and Derived Anatomy

The above mentioned inferred-anatomy algorithm requires a preliminary reconstruction of the patient as shown in figure 2.3(a) and an atlas (a brain atlas in the case described by Stodilka et. al.) and shown in figure 2.3(b). This preliminary reconstruction does not include scatter and attenuation correction. The atlas consists of a functional component (colour) and an anatomical component (gray scale). The functional component is then spatially registered to the preliminary reconstruction as shown in figure 2.3(c), and this optimal transformation is recorded. The patient's anatomy is then inferred by applying the same transformation to the anatomical component of the head atlas, figure 2.3(d).

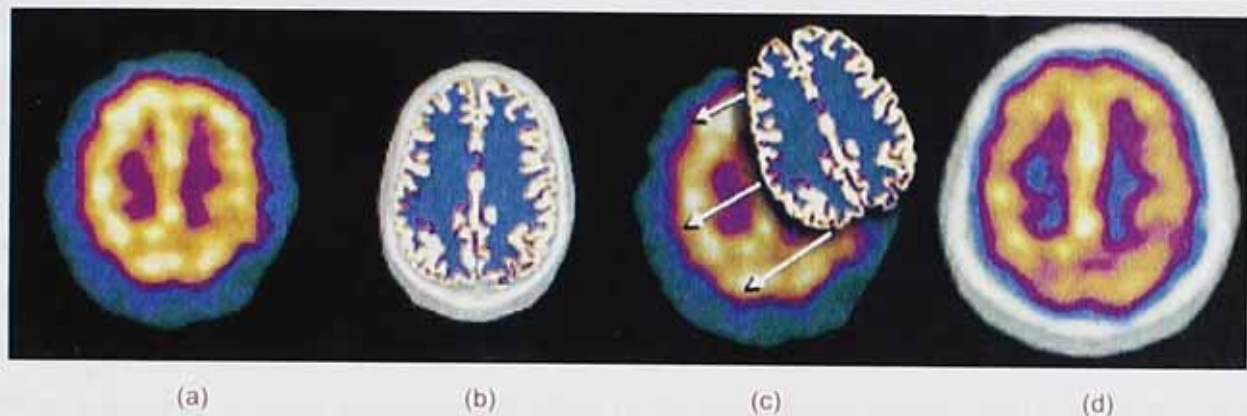


Figure 2-3: The inferred-anatomy algorithm. The preliminary reconstruction of the patient (a), the atlas consisting out of both the anatomically and functionality parts (b). The registration of the functionality part to the preliminary reconstruction (c) and after applying the result of the registration to the anatomical part of the atlas (d).

The brain is a much more homogeneous part of the human anatomy compared to other areas such as the thorax but it should be feasible to extend the method of inferred anatomy to provide non-uniform attenuation correction in the thorax.

Extending the method of inferred anatomy to the thorax by overcoming the obstacles caused by the non-uniform nature of the thorax has not yet been reported. This has been achieved in this study and will be the subject of chapter 7. In this instance the 4-dimensional NCAT-phantom¹⁴⁵ was used as the atlas to produce the anatomical and functional components. This process consisted of an initial reconstruction of a patient, not including attenuation and scatter correction. The reconstructed image was spatially registered to the functional component of the NCAT-phantom and after applying this transformation to the patient's anatomy the desired attenuation map was obtained.

The above mentioned method of inferred anatomy in the thorax required various image manipulation and segmentation techniques which can be extended to develop another emission based method, termed "Derived Anatomy". This is a unique approach, never attempted before, which uses the results of the image segmentation to create a patient specific NCAT parameter file. This parameter file can then be used to produce a NCAT-phantom relating exactly to the anatomy of the patient under investigation and therefore can

be used as the attenuation map for that specific patient. This implementation will also be discussed in much more detail in chapter 7. It provides a very promising solution for the implementation of emission based attenuation correction algorithms.

2.6 New Hardware for the Optimisation of MPI

This chapter would not be complete without looking at developments to improve the performance of Gamma Cameras and address the issues which affect Nuclear Medicine Imaging generally and address many of the problems discussed in this chapter, as most gamma cameras are still using the same design principles introduced with the first angler cameras in the 1960's. There have also been substantial recent efforts to develop new imaging systems with increased sensitivity by addressing the main limitations of MPI by combining several approaches such as changing the detector geometry and optimising tomographic sampling of the field of view for myocardial imaging, improving the detector material and collimator design¹⁴⁶.

A range of new dedicated hardware camera systems with optimised acquisition geometry, collimator design, and associated reconstruction software have been recently introduced by different vendors. This include innovative designs of the gantry and detectors which have been proposed to allow increased sampling of the myocardial region, and thus allow better local sensitivity. These systems combine an improvement in spatial resolution and sensitivity. As a consequence of faster imaging times and more comfortable patient positioning, these systems have the additional benefit of reducing patient motion during a scan¹⁴⁶.

These new developments include:

- ▶ Solid state detectors such as pixilated CsI(Tl) or cadmium zinc telluride (CZT) pixilated detectors.
- ▶ Photodiodes instead of photo multiplier tubes.
- ▶ Region-of-interest (ROI) or organ-of-interest centred acquisition scanning.
- ▶ No visibly moving parts.
- ▶ Digital logic and software.
- ▶ List mode acquisitions.
- ▶ Multi-pinhole or astigmatic collimator design.
- ▶ Dual isotope imaging.

2.6.1 DIGIRAD - CARDIUS 3 XPO

The Cardius XPO camera dedicated to fast cardiac imaging has been developed by Digirad and it uses indirect, solid-state detectors consisting of pixilated CsI(Tl) detectors and photodiodes. Digital logic, instead of analog systems, is used to process the signals. Data acquisition is typically accomplished in 7½ minutes as compared to 20 minutes on a standard angler camera. When comparing its performance to that of a standard dual-headed camera it

was found that the similar quality could be obtained with 38% reduction in the acquisition time¹⁴⁷.

2.6.2 *CardiArc*

CardiArc has developed a dedicated nuclear cardiology SPECT camera in which the detector and collimation are redesigned and optimised specifically for cardiac imaging. This device has no visibly moving parts and has a single internally moving part which is hidden from the patient. Scan times reported by the company are as short as 2 minutes. An independent evaluation concluded that the CardiArc system appears to gain image quality by a factor of 5-10 when compared to the conventional dual-head camera in these scans¹⁴⁸.

2.6.3 *Spectrum Dynamics – D-SPECT*

Spectrum Dynamics introduced a system using pixilated CZT detector arrays (with a superior energy resolution of ~1.7 better than a standard Anger camera at 140 keV), called D-SPECT, where acquisition time as short as 2 minutes has been reported¹⁴⁹. It utilises region-of-interest (ROI)-scanning where a 10-second pre-scan is performed to identify the location of the region of interest. Scan limits and timings are then set and the final scan are performed. The myocardial count rate was 7 to 8 times higher for D-SPECT¹⁴⁹ as compared with a standard gamma camera and it has also been demonstrated that, by taking advantage of the improved energy resolution of CZT¹⁵⁰, simultaneous dual isotope SPECT MPI is feasible using ²⁰¹Tl and ^{99m}Tc, and therefore raise the possibility of obtaining the results from both the rest and stress study in a single study.

2.6.4 *Multi-Pinhole Collimation Approach*

Multi-pinhole collimation has been introduced by some vendors to provide an alternative approach to parallel-hole rotational tomography on current Gamma Cameras. Useful results have been demonstrated in small animal imaging with multi-pinhole SPECT providing improved spatial resolution and detection efficiency in comparison to parallel-hole collimation^{151,152,153}. This approach allows many views to be acquired simultaneously throughout the entire image acquisition period without the need for motion of the detector, collimator or patient.

The approach may be prone to greater formation of artefacts because it inherently produces an incomplete tomographic dataset and it acquires images from only limited views¹⁵⁴. Background activity from other organs may not be seen by all of the views, which could lead to inconsistencies in the reconstructed data. It is also known that the resolution and sensitivity of pinhole collimators decreases with the distance from the collimator¹⁵⁵ and these issues need to be addressed for this technique to have clinical value.

This approach has been introduced by a company called Eagle Heart Imaging who integrated multi-pinhole methodology with the Emory Reconstruction Toolbox to provide a commercial multi-pinhole upgrade product which they called MP-SPECT to be used on existing dual-head SPECT gamma cameras.

A 9-pinhole collimator using 8 mm diameter pinholes was investigated¹⁵⁴ and it was found that the spatial resolution was 30% less than that achieved by standard parallel-hole collimation but the detection efficiency was increased 10-fold predicting a 5-fold increase in sensitivity and would provide comparable resolution to that of a standard gamma camera. Another issue addressed¹⁵⁴ is regarding the minimal number of views and the optimal viewing geometry required for clinical cardiac SPECT. There are both advantages and disadvantages to having fewer views. As the number of views present in the SPECT data set is decreased, the geometric appearance of the heart is visibly altered. This aspect must be weighed against the fact that the increased statistical content and simultaneity of these views improves the comparability of the stress versus rest data sets acquired on the same patient. The improved statistical content of multi-pinhole SPECT images is also a key factor in supporting the ability to image multiple isotopes simultaneously. The clinical utility of this approach has been demonstrated clinical comparability¹⁵⁶ between a three detector 18-pinhole SPECT system and a conventional rotational SPECT gamma camera.

2.6.5 GE Healthcare - Ultra Fast Cardiac (UFC) Camera

The multi-pinhole design was also introduced by GE Healthcare in the UFC camera using an array of cadmium zinc telluride (CZT) pixilated detectors. Energy and spatial resolution improved with the use of CZT detectors. The detectors and collimators do not move during acquisition and views from all angles are acquired simultaneously through the proprietary multi-pinhole collimator which utilises a large number of pinholes which lead to an improved overall sensitivity. It was possible to obtain a 30% reduction of the scatter component as a result of the asymmetric CZT energy response¹⁵⁷. The improved energy resolution obtained with CZT detectors alone was further improved with the combination of CZT and a pinhole collimator¹⁵⁸. This may facilitate new applications such as simultaneous dual isotope imaging. An improvement of 1.65-fold in energy resolution was demonstrated and an improvement of 1.7-2.5 fold in spatial resolution and 5-7 fold in sensitivity with UFC energy resolution of 5.70% and spatial resolution in the 4.3-4.9 mm range¹⁵⁹ when compared to a standard gamma camera.

2.6.6 SIEMENS - IQ•SPECT

Siemens recently introduced IQ•SPECT, which consists of three components: an astigmatic collimator, an optimized organ-of-interest centred acquisition, and iterative reconstruction.

The collimator is based on a previously developed astigmatic (cardiofocal) collimator concept¹⁶⁰. The collimator is designed so that the centre of the field-of-view magnifies the heart both in the axial as well as in the trans-axial direction, while the edges sample the entire body to avoid truncation artefacts common to single focal collimators when imaging the torso. With an appropriate orbit this variable-focus collimator increases the number of detected events from the heart by more than a factor of two in each direction compared to that of a parallel-hole collimator with equivalent resolution, and magnifying the heart while imaging the rest of the torso under traditional conditions¹⁶⁰.

In IQ-SPECT this organ centric orbit acquisition technique is combined with a new proprietary iterative reconstruction algorithm based on Flash3D⁸⁶ which models the astigmatic geometry of these collimators. IQ-SPECT reconstruction also includes state-of-the-art distant dependent isotropic (3D) resolution recovery, CT-based attenuation correction, and energy window-based scatter correction. The reported image acquisition time of this system can be as short as 4 minutes.

2.7 Conclusions

The application of depth-dependent resolution recovery, attenuation correction using external source devices, and scatter correction has been proposed to resolve the lack of specificity for myocardial perfusion imaging and an improvement in its sensitivity. Substantial advances had been made in implementing these solutions. The introduction of new hardware designs could also have a substantial impact on the improvement of the sensitivity and specificity of MPI but as these are all recent introductions, no published results are available yet. There is also currently a fairly large equipment base using the older technology using general gamma cameras rather than dedicated cardiac cameras is unlikely to be replaced in the near future that would benefit substantially from improved attenuation correction. In addition, an improved attenuation correction method is also likely to work on the new equipment, therefore increasing the accuracy still further.

Part of these solutions is the application of attenuation correction. The benefits of an accurate attenuation correction are universally accepted but it still lacks widespread implementation. Some of the reasons for the lack of acceptance of transmission based attenuation correction are that it seems to introduce additional artefacts (which will be referred to again in later chapters) and its cost and complexity. In contrast, the implementation of correction techniques for the other permutations, i.e. scatter, finite resolution response and depth-dependent collimator response, seems to be met with far less resistance. It is interesting to note that these implementations are all software based as compared to the attenuation corrections technique, which is a hardware implementation. The lack of the universal implementation of attenuation correction in many cases can also be

contributing to a lack of understanding of the complexity of attenuation despite the amount of research which has been done on the topic, as well as understanding the real impact current available attenuation methods can have on improving the outcome of clinical studies. Resolving the issues of attenuation correction, so that it becomes universally accepted should be a priority.

To add to the understanding of attenuation artefacts and the effect it can have on the interpretation of clinical studies this project includes two studies which were devoted to studying less well known and some unknown aspects of attenuation to build up a better understanding and appreciation of the impact of not applying attenuation correction, as well as highlighting the complexity of attenuation artefacts. The hope is that a better understanding of the complexity and unpredictability of attenuation will inspire the wider implementation of correcting for it.

Although transmission based attenuation correction is viewed with a great deal of scepticism, it is current commercially available on most systems. It is often combined with correction methods for both depth-dependent collimator blurring and scatter. This project includes a study of the evaluation of such a commercially available solution that uses transmission scanning, scatter correction and depth-dependent resolution recovery, to determine the level of compensation achieved with it despite the reservation about using transmission scanning. This will be important because its implementation could substantially improve the outcome of Myocardial Perfusion Imaging. Further, it will take a substantial time to develop and verify alternative emission based methods which may be able to provide a complete solution without the draw backs of transmission scanning.

This project will also introduce two emission based methods to overcome the limitations and drawbacks of transmission based attenuation correction methods that can contribute substantially to obtaining a more accurate and more universally acceptable attenuation correction solution. These methods are software based and will remove the burden of substantial additional cost, radiation dose and scan time of many of the other solutions and will work on the current generation of Gamma Cameras and will hopefully accept much wider acceptance.

It is postulated that these methods of inferred and derived anatomy, together with the implementations for scatter, finite resolution response and depth-dependent collimator response, can provide a complete solution for the permutations in Myocardial Perfusion Imaging which can achieve wide spread implementation.

Chapter 3 - Monte Carlo Simulations to Determine the Limitations of Myocardial Perfusion Imaging

3.1 Introduction

As described in the previous chapter the full clinical potential of Myocardial Perfusion Imaging (MPI) has not been realised because of numerous factors producing artefacts that degrade image quality and result in misinterpretation of the results¹⁶¹. Photon attenuation, scatter radiation, partial-volume errors, and other perturbations compromise the accuracy obtainable with MPI⁴⁹.

The range of natural variability in size, shape and position of many organs in the thorax may contribute to such artefacts. To gain a better understanding of the effect of these above mentioned limitations on the percentage intensity losses and the amount and position of defects caused by these intensity losses it was decided to perform two Monte Carlo simulation studies to investigate these effects.

The first simulation study was to investigate the contribution of the different individual anatomical parts in the thorax and how the amount of intensity losses are caused by the heart itself compared to the rest of the anatomical parts in the thorax. This study was performed on both male and female patients

The second study was to investigate the percentage of intensities lost, as well as their location in the image of left ventricle when the orientation and position of the heart changes relative to the thorax. Difference is to be expected between male and female patients and therefore this study should be done for both male and female patients. Unfortunately the study involves a substantial number of simulations and therefore using both genders is impractical. For this reason only male patients were simulated in the second study. Although it is possible that this fact somehow limits the usefulness of the study, enough information could be gained regarding the influence of all the different anatomical parts on the overall attenuation caused.

These studies will provide a much clearer picture of intensity losses in the image of the left ventricle caused by attenuation, scatter and other contributors and will illustrate the need for corrections to be done when performing MPI and the potential effect these corrections can have.

3.2 Monte Carlo Simulations

The term Monte Carlo as a mathematical method was coined in the 1940s by physicists working on nuclear weapon projects in the Los Alamos National Laboratory¹⁶². The name was popularised by physics researchers Stanislaw Ulam, Enrico Fermi, John von Neumann, and Nicholas Metropolis, among others; the name is a reference to a famous casino in Monaco where Ulam's uncle gambled with borrowed money¹⁶³. The use of randomness and the repetitive nature of the process are analogous to the activities conducted at a casino.

Monte Carlo simulation is a method for iteratively evaluating a deterministic model using sets of random numbers as inputs. It is a class of computational algorithms that rely on repeated random sampling to compute their results. Monte Carlo methods are often used when simulating physical and mathematical systems. It is well suited to situations where a large number of events with variable probability make up the situation that is being modelled.

Perhaps the most famous early use was by Enrico Fermi in 1930, when he used a random method to calculate the properties of the newly-discovered neutron. Monte Carlo methods were central to the simulations required for the Manhattan Project, though were severely limited by the computational tools at the time. Therefore, it was only after electronic computers were first built (from 1945 on) that Monte Carlo methods began to be studied in depth.

Monte Carlo simulation is also an important technique in nuclear medicine. It is well adapted to nuclear medicine with its particle emission, propagation and detection random processes. Each photon trajectory can be processed separately. The photon is propagated through the 3 dimensional volume under consideration where it can be absorbed or scattered conforming to suitable random events the likelihood of which depends on the local environment. Various Monte Carlo computer codes have been developed and used by various researchers for years to simulate and study a wide range of nuclear medicine applications.

In this study Monte Carlo simulations were used to assess the amount of attenuation caused by the different organs and body parts in the thorax region as well as variation in attenuation as a result of different orientations of the myocardium in the thorax which are found in patients.

3.3 Computer Phantoms in Medical Imaging Simulation Techniques

Simulation involves computer generated "patients", models of the imaging process, and fast computational methods. Computer phantoms provide a model of the subject's anatomy and physiology. Given a model of the physics of the imaging process, acquired data of a computer phantom can be generated using the computational methods. A major advantage of using computer-generated phantoms in simulation studies, rather than using patient studies, is that the exact anatomy and physiological functions of the phantom are known, thus providing a gold standard from which to evaluate and improve medical imaging devices and image processing and reconstruction techniques. Using computer phantoms has the advantage that they are always available and are easy to alter to model different anatomies and medical situations providing a large population of subjects from which to perform research. A further advantage is that a single factor can be changed so that the change can be unambiguously analysed. In addition, it is difficult both ethically and practically to test every combination of parameters on large groups of patients under clinical conditions to achieve the same ends.

A vital aspect of simulation is to have a realistic phantom or model of the subject's anatomy. Without this, the results of the simulation may not be indicative of what would occur in actual patients and could, therefore, have limited practical value. The availability of such a realistic phantom will make Monte Carlo a valuable first test for this project, but it will still require some verification by human studies.

Such a realistic phantom is the four-dimensional (4D) NURBS-based cardiac-torso (NCAT) digital phantom¹⁴⁵ which was developed at the Department of Biomedical Engineering at the University of North Carolina to provide a realistic and flexible model of the human anatomy and physiology to be used in nuclear medicine imaging research. The organ models are based on NURBS, non-uniform rational B-splines, as used in computer graphics and the phantom can easily be adjusted for patient size, and size and orientation of the heart to cover a wide range of potential simulated patients to match the known variability in patients.

In this study the NCAT phantom will be used to generate the necessary activity and attenuation image sets.

3.4 Simulation of SPECT Acquisitions

The Photon History Generator (PHG)¹⁶⁴ is a software application designed to perform Monte-Carlo simulations of photon creation and transport through heterogeneous attenuators for both SPECT and PET. The "Simulation System for Emission Tomography" (SimSET) was developed by The University of Washington Imaging Research Laboratory¹⁶⁵ and the

package uses Monte Carlo techniques to model the physical processes and instrumentation used in emission imaging to simulate a realistic scintillation camera system.

In this study the simulated camera included a Low Energy High Resolution (LEHR) collimator, a 9.35 mm NaI(Tl) crystal and a 20% energy window, centred on 140 keV. An acquisition using 64 SPECT projections was simulated with a circular 180° orbit with acquisition steps of 2.8° starting at the Left Anterior Oblique (LAO) angle at 315° and ending at the Right Posterior Oblique (RPO) angle, i.e. 135°. Photon attenuation was also included in the simulations. The SPECT projections were stored as 128 x 128 matrices with a pixel size of 0.49 cm x 0.49 cm which matches the usual settings for patient imaging.

In the simulation studies the percentage intensity losses in different parts of the left ventricle will be calculated under different simulated physical conditions. To be able to do that a dual simulation will be performed for every condition. The first simulation will be made assuming no attenuation by the body tissues, by setting all tissue density to that of air. This will provide the result that is obtained in the absence of any attenuation medium, and is known as the "air simulation", and represents the ideal situation when no attenuation occurs. The second simulation assumes normal tissue densities, so that attenuation occurs results in intensity losses which will exist in that specific patient anatomy, this will be the "real life simulation".

The output of the SIMSET simulation program provides a sinogram, which is an image representation of raw data obtained, therefore each set of simulations produces 2 sinograms which need to be reconstructed.

3.4.1 Validation of SimSET

The software was obtained as source code written in the C language. It was compiled into a binary file by the author of the thesis for use with the Microsoft Windows® operating systems by using MS Visual Studio 6.0®

To validate the software the advice from the providers was followed. The first form of validation was to verify the compilation process by ensuring that no errors or warnings were received from the compiler.

The second form of validation came from the sample data provided in a "samples" directory where a simulation called fastTest resides and this simulation was run and the results analysed. This simulation has been chosen because it provides a test of a wide range of the features of SimSET. The parameter file and benchmark results were also provided. The successful completion of this simulation indicates that the installation performs as expected but more subtle problems could still be present. For this reason, all data produced by SimSET were approached with a critical eye.

3.5 Choosing the Number of Seeded Events

The choice of the number of events was based on a literature search because the goal was to create a simulation as close to a real scan as possible. A publication by El Fakhri et. al.¹⁶⁶ was chosen because they also used SimSET and similar analysis techniques as what was used in these studies. Furthermore, they also acquired a physical phantom scan to determine the amount of events that will mimic a real scan.

Therefore simulations with different number of seeded events were initially run to produce results which could be used to determine the amount of photons detected in the final images. The final choice of events seeded was determined from the studies which provided similar amounts of detected photons as in the published work, i.e. 41 million photons detected in the "air" simulation and 8 million in a 20% energy window for their "real life" simulations for the whole simulated phantom.

The choice was made to use the same number of events in this study for both the "air" and "real life" simulations because the goal was to detect how many events get "lost" as a result of the attenuation media, scatter and the other effects mentioned in 2.4. This was the case for all the simulation studies where the same amount of events seeded were used.

The fact that the OSEM reconstruction will reconstruct images on the basis of local statistical accuracy in the image was unfortunately not considered in any of the comparison studies and could be included in any further similar studies in the future.

3.6 Image Reconstruction

As is standard practice in Nuclear Cardiology image processing and interpretation, all the images will be reconstructed with an iterative ML-EM (Maximum-Likelihood Expectation-Maximization) algorithm which implements Ordered Subsets. This was done by code written by the author (Johan Nuyts) in the Iterative Data Language (IDL)¹⁶⁷ which included reconstruction routines obtained from Johan Nuyts¹⁶⁸ at the Medical Imaging Research Center, Katholieke Universiteit Leuven, Belgium. The source code of these routines is provided in Appendix A.

The non-attenuation correction reconstructions will be done with the equivalent of 32 full ML-EM iterations as suggested by the original author¹⁶⁸ of the software routines. Using fewer iterations with more subsets results in much faster reconstruction, at the cost of slightly increased noise levels and is suitable for the non-attenuation corrected reconstructions. When doing attenuation corrected reconstructions, decreasing the number of subsets is applied to avoid excessive noise propagation, leading to an increase in the number of iterations and therefore the equivalent to 42 full ML-EM iterations were used to ensure suitable image quality, again as suggested by the author of the software routines.

Unlike Filtered Back Projection, where noise, in the absence of attenuation correction, is constant across the reconstructed field, noise in studies reconstructed using EM is correlated with the signal: i.e. the noise amplitude is lower in regions of low counts but as the iteration number increases, noise increases.

3.7 Image Interpretation

This study makes extensive use of polar maps (or bull's eye displays) to do quantitative analysis and therefore the origin and use of polar maps are described below.

The advances in camera technology in the late 80s allowed SPECT to be used routinely. By the use of reconstruction algorithms, it was possible to estimate and produce transaxial, sagittal and coronal sectional images, creating 3D volumes or stacks of short-axis images that served as input to the quantitative software. The complexity of the problem when using SPECT substantially increased with the myocardium represented as a 3D volume rather than planar images.

The first effort to address this problem¹⁶⁹ was to carry out a quantitative analysis by assessing the circumferential profile curves of the three short-axis (apical, middle and basal) of the left ventricle (LV). To assess the apical region, the most central long-axis cutting through the apex was also selected. From these images, circumferential maximal count profiles of myocardial distribution were obtained.

This method was extended to the entire SPECT volume by introducing the polar map, or bull's eye displays, for viewing circumferential profiles¹⁷⁰. The polar maps allow a quick and comprehensive overview of the circumferential samples from all slices by combining them into a single colour-coded image. The points of each circumferential profile are assigned a colour based on count values and the coloured profiles are shaped into concentric rings as displayed in figure 3.1(a). The slice closest to the apex processed with circumferential profiles defined the center of the polar map, and each successive profile from each successive short-axis slice is displayed as a new ring surrounding the previous. The slice nearest the base of the LV makes up the outermost ring of the polar map.

To be able to get more meaningful results different models can be applied to these polar maps. There are a range of models available, a vascular model, which aims to divide the polar maps into regions with different arteries which supply oxygen to the left ventricle, a 5-segment model (Figure 3.1(b)) and a 9-segment model. There are also 17, 19 and 20-segment models available.

In this study polar maps of regional myocardial tracer uptake will be generated using commercially available software (4DMSPECT; University of Michigan, USA). Figure 3.1(a) shows a polar map (for an "air" simulation). Ideally the polar map will be 100% uniform but in

most practical situations that will not be the case as a result of the factors such as the non-uniform thickness of the myocardium, inclusion of the papillary muscle, etc., but it will closely resemble an even distribution, which are normal variations within patients.

The choice of models in the studies to follow will be mainly determined by the practicality of using a specific model. Using more segments is desirable because it will provide a far more detailed analysis and therefore produce a more accurate localisation than what will be obtained with fewer segments. The downside of using more segments is that it results in fewer counts per segments and the statistical variation associated with such low counts means that the clinical significance of intensity variations cannot be identified. The choice of number of segments is therefore a trade off of these two factors. The raw (un-normalised) intensities will be displayed in the polar maps and for each of these models and the average tracer uptake calculated by the 4DMSPECT software for each segment.

In the simulation studies un-normalised average tracer uptake will be measured in either a 5-segment model (anterior, septal, inferior, lateral and apical) or 9-segment model (basal-anterior, apical-anterior, basal-septal, apical-septal, basal-inferior, apical-inferior, basal-lateral, apical-lateral and apical) for both the "air" and "real life" simulations.

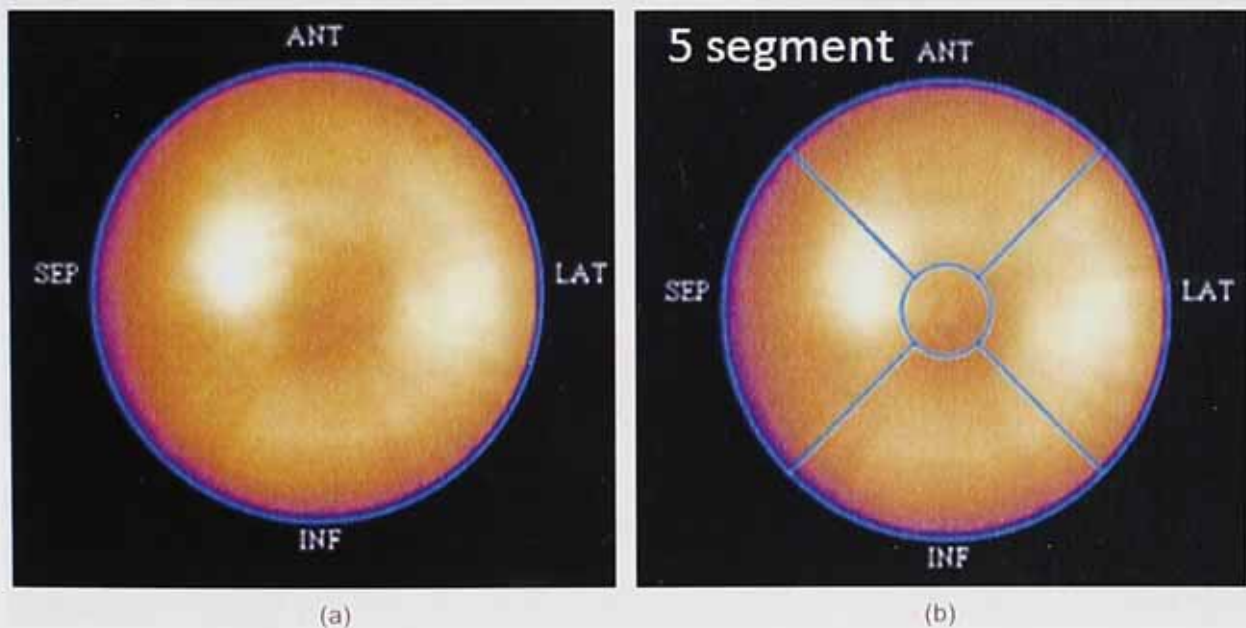


Figure 3-1: The polar maps created from reconstructed simulation outputs. The polar map itself (a), the regions displaying the 5-segment model (b).

The percentage intensity loss in each segment will be determined from the polar maps as displayed in Figure 3.2 for the 5-segment model. By comparing the value of the "real life" simulation to the "air" simulation, one can calculate the percentage intensity loss as illustrated below:

$$\% \text{ Intensity Loss} = \frac{ATU_{air} - ATU_{reallife}}{ATU_{air}} \times 100$$

where ATU_{air} is the un-normalised average tracer uptake in a specific segment for the air simulation and $ATU_{reallife}$ is the un-normalised average tracer uptake in a specific segment for the real life simulation. Please note that the values used are the average value of a specific segment in the 5 or 9 segment polar map and not a single pixel value.

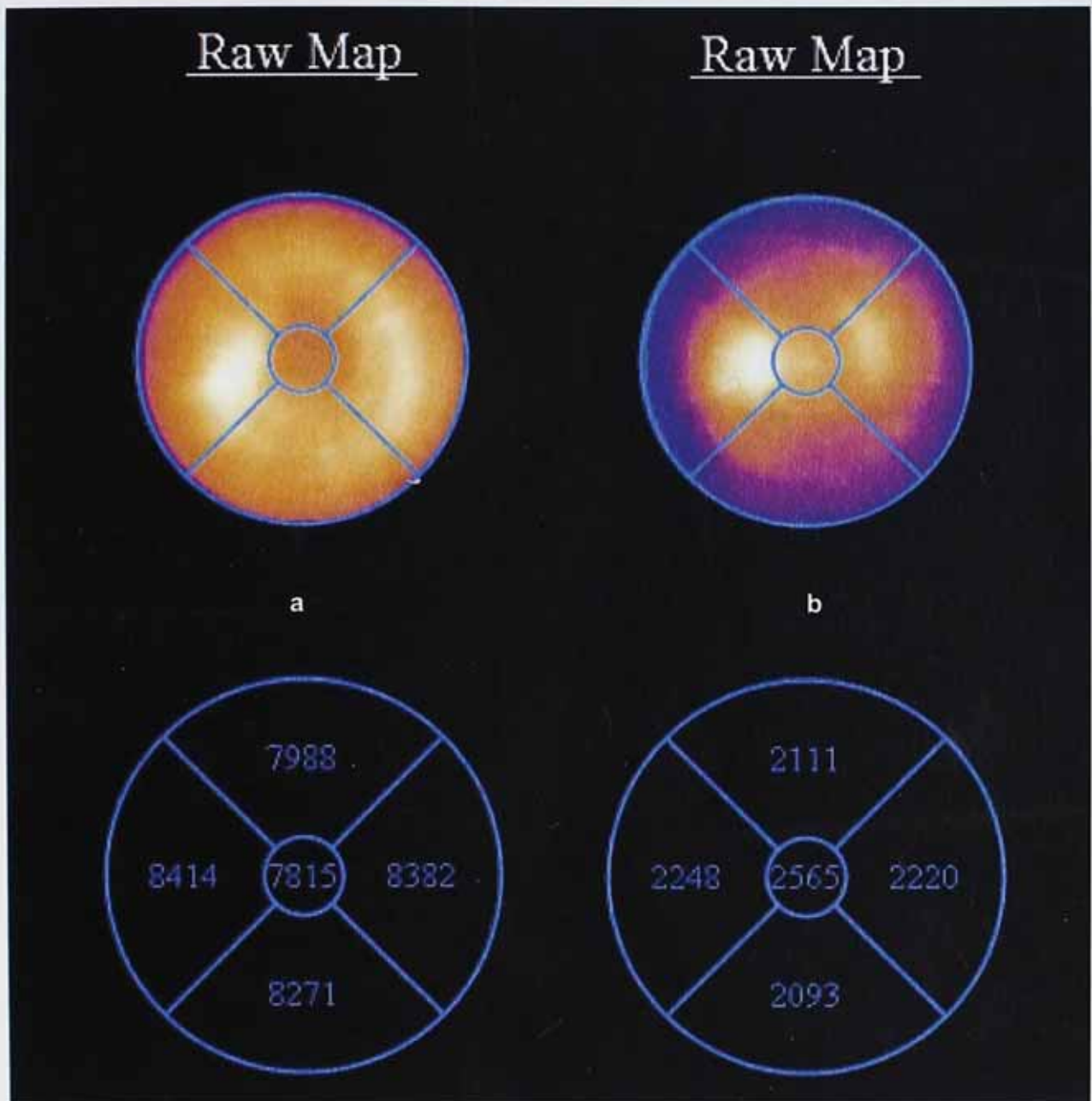


Figure 3-2: Polar maps displaying the 5-segment model. The polar map and the related values for the air simulation (a) and the polar map and the related values for the real life simulation (b).

3.8 Statistical Analysis

Statistical analysis will be performed by either using regression (investigating the effect of orientation and position of the heart in the thorax on the amount of intensity losses in the left ventricle) or by comparing means (calculating the contributions of the different anatomical parts to the amount of intensity losses in the left ventricle), which are both parametric tests.

Most parametric tests based on the normal distribution have four basic assumptions that must be met for the test to be accurate. The assumptions are as follows:

- ▶ **Normally distributed data:** The data must be from one or more normally distributed populations, this can be done by using the Shapiro-Wilk test.
- ▶ **Homogeneity of variance (Homoscedasticity):** The variances should be the same throughout the data and Levene's test will be used for this.
- ▶ **Interval data:** Equal intervals on the scale represent equal differences in the property being measured.
- ▶ **Independence:** This means that the behaviour of one variable does not influence the behaviour of another.

These checks have to be carried out before any statistical analysis involving parametric tests are carried out.

3.8.1 Regression as a Statistical Model

In regression analysis¹⁷¹ one fits a predictive model to the data and uses that model to predict values of the dependent variable from an independent variable. In the following equation:

$$\text{Outcome} = (\text{Model})_i + \text{error}_i$$

the model can be a linear model (which will give a straight line relation between the outcome and the change parameter) or a polynomial model of n degree to predict the outcome (which will give a curve relation) plus some kind of error. Regression analysis also allows for errors generated by the measurements.

A. The Line of Best Fit

The first step in applying a statistical model to data is to find the straight line or curve which fit the data the best. This 'line of best fit' is found by ascertaining which line, of all possible lines, results in the least amount of difference between the observed data points and the line by using a method called the method of least squares¹⁷².

B. Deciding Which Model to Use

After fitting data with one or more models, one should evaluate the goodness of fit. A visual examination of the fitted curve displayed should be the first step. Beyond that, the following methods can be used:

- ▶ Residual analysis
- ▶ Goodness of fit statistics
- ▶ Confidence and prediction bounds

As is common in statistical literature, the term goodness of fit is used here in several senses: A "good fit" might be a model

- ▶ that the data could reasonably have come from, given the assumptions of least-squares fitting
- ▶ in which the model coefficients can be estimated with little uncertainty
- ▶ that explains a high proportion of the variability in the data, and is able to predict new observations with high certainty

A particular application might dictate still other aspects of model fitting that are important to achieving a good fit, such as a simple model that is easy to interpret.

These methods group into two types: graphical and numerical. Plotting residuals and prediction bounds are graphical methods that aid visual interpretation, while computing goodness-of-fit statistics and coefficient confidence bounds yield numerical measures that aid statistical reasoning.

Generally speaking, graphical measures are more beneficial than numerical measures because they allow one to view the entire data set at once, and they can easily display a wide range of relationships between the model and the data. The numerical measures are more narrowly focused on a particular aspect of the data and often try to compress that information into a single number. In practice, depending on the data and analysis requirements, one might need to use both types to determine the best fit.

Note that it is possible that none of the fits can be considered suitable for the data, based on these methods. In this case, it might be necessary to select a different model. It is also possible that all the goodness-of-fit measures indicate that a particular fit is suitable. However, if the goal is to extract fitted coefficients that have physical meaning, but the model does not reflect the physics of the data, the resulting coefficients are useless. In this case, understanding what the data represents and how it was measured is just as important as evaluating the goodness of fit.

C. Using the Models

Should any of these models (linear, quadratic or cubic) hold true it can then be used to make some predictions on the outcome. This can be achieved by using the following equations:

$$\text{(Linear) } \% \text{ Intensity Loss} = b_1 \times (\% \text{UIL}) + b_0$$

$$\text{(Quadratic) } \% \text{ Intensity Loss} = b_2 \times (\% \text{UIL})^2 + b_1 \times (\% \text{UIL}) + b_0$$

$$\text{(Cubic) } \% \text{ Intensity Loss} = b_3 \times (\% \text{UIL})^3 + b_2 \times (\% \text{UIL})^2 + b_1 \times (\% \text{UIL}) + b_0$$

where %UIL represents a unit change in intensity loss.

3.8.2 Comparing Two Means as a Statistical Model¹⁷³

The t-test is well suited to test the difference between two sets of means. There are two different t-tests and the one that is used depends on whether the independent variable was manipulated using the same or different participants.

The purpose of using the t-test is to decide whether the means of two different manipulations differ either a little or a lot and to see whether the difference could happen by chance or whether it is as a result of experimental manipulations. To determine this, the null hypothesis will be tested, meaning, for it to hold true, the experimental manipulation must have no effect on the participants and the sample means will be very similar.

A. Calculating the effect size

Even if one found the t-statistic to be statistically significant, one cannot necessarily conclude that the effect caused by the experiment is important in practical terms. To discover whether the effect size is substantive one need to use what is known as the effect size (r), i.e. a measurement of the effect of the experiment in a standardised way. This is simply an objective and standardised measurement of the magnitude of the observed effect. The fact that the measure is standardised means that the result can be compared across different studies that have measured different variables. Effect sizes are useful because they provide an objective measure of the importance of an effect. The following guidelines can be used to measure the importance of an effect (they are not measured on a linear scale):

- ▶ **$r = 0.10$** (small effect): the effect accounts for 1% of the total variance.
- ▶ **$r = 0.30$** (medium effect): the effect accounts for 9% of the variance.
- ▶ **$r = 0.50$** (large effect): the effect accounts for 25% of the variance.

The following equation can be used to convert a t-value into an r-value¹⁷⁴:

$$r = \sqrt{\frac{t^2}{t^2 + df}}$$

where df is the degrees of freedom.

The threshold for an effect to be large is 0.5 and values greater than that will represent the fact that the effect of the experiment is important in practical terms.

3.9 Patient Selection for Monte Carlo Simulations

By using a parameter file as input to the NCAT phantom software one can “generate” a patient. It is therefore possible by varying different parameters to create a range of patients. The default values in the NCAT are based on the ‘Visible Human’^{175,176}. The NCAT phantom allows for a wide variety of parameters to be set to match the known variability in patients.

In order to generate the patients, the following parameters were altered to create 30 male and 30 female patients:

1. Body long axis to set body transverse axis.
2. Body short axis to set body antero-posterior axis.
3. Body height to set height of phantom.
4. Rib long axis to set ribcage transverse axis.
5. Rib short axis to set ribcage antero-posterior axis.
6. Rib height to set height of ribcage.
7. Setting the weight of the phantom.
8. Number of Counts

so that the a range of patients can be simulated which will match the variations in a normal patient population¹⁷⁷. The values used are shown in Tables 3.1 and 3.2.

Table 3-1: Male Patient Selection for the Monte Carlo Simulations

Set	Body Long Axis (cm)	Body Short Axis (cm)	Rib Long Axis (cm)	Rib Short Axis (cm)	Height (cm)	Weight (kg)	Number Counts
Reference [*]	34.5	27.5	30	22.7	192	95.05	800000000
1	34.5	27.5	30	22.7	192	95.05	800000000
2	32.5	27.5	28	22.7	192	95.05	800000000
3	30.5	27.5	26	22.7	192	95.05	800000000
4	36.5	27.5	32.2	22.7	192	95.05	800000000
5	38.5	27.5	34.2	22.7	192	95.05	800000000
6	34.5	29.5	30	24.7	192	95.05	800000000
7	34.5	31.5	30	26.7	192	95.05	800000000
8	34.5	25.5	30	20.7	192	95.05	800000000
9	34.5	23.5	30	18.7	192	95.05	800000000
10	32.5	25.5	28	20.7	192	95.05	800000000
11	36.5	29.5	32	24.7	192	95.05	800000000
12	36.5	25.5	32	20.7	192	95.05	800000000
13	32.5	29.5	28	24.7	192	95.05	800000000
14	34.5	27.5	30	22.7	194	95.05	800000000
15	34.5	27.5	30	22.7	196	95.05	800000000
16	34.5	27.5	30	22.7	190	95.05	800000000
17	34.5	27.5	30	22.7	188	95.05	800000000
18	34.5	27.5	30	22.7	186	95.05	800000000
19	34.5	27.5	30	22.7	192	90.05	800000000
20	34.5	27.5	30	22.7	192	85.05	800000000
21	34.5	27.5	30	22.7	192	80.05	800000000
22	34.5	27.5	30	22.7	192	100.05	800000000
23	34.5	27.5	30	22.7	192	105.05	800000000
24	34.5	27.5	30	22.7	192	95.05	850000000
25	34.5	27.5	30	22.7	192	95.05	900000000
26	34.5	27.5	30	22.7	192	95.05	950000000
27	34.5	27.5	30	22.7	192	95.05	1000000000
28	34.5	27.5	30	22.7	192	95.05	750000000
29	34.5	27.5	30	22.7	192	95.05	700000000
30	34.5	27.5	30	22.7	192	95.05	650000000

Table 3-2: Female Patient Selection for the Monte Carlo Simulations

Set	Body Long Axis (cm)	Body Short Axis (cm)	Rib Long Axis (cm)	Rib Short Axis (cm)	Height (cm)	Weight (kg)	Number Counts
Reference*	33.0	25.0	28.0	21.0	188	86.00	800000000
1	33.0	25.0	28.0	21.0	188	86.00	800000000
2	31.0	25.0	26.0	21.0	188	86.00	800000000
3	29.0	25.0	24.0	21.0	188	86.00	800000000
4	35.0	25.0	30.0	21.0	188	86.00	800000000
5	37.0	25.0	32.0	21.0	188	86.00	800000000
6	33.0	29.0	28.0	23.0	188	86.00	800000000
7	33.0	29.0	28.0	25.0	188	86.00	800000000
8	33.0	23.0	28.0	19.0	188	86.00	800000000
9	33.0	21.0	28.0	17.0	188	86.00	800000000
10	33.0	23.0	26.0	19.0	188	86.00	800000000
11	35.0	27.0	30.0	23.0	188	86.00	800000000
12	35.0	23.0	30.0	19.0	188	86.00	800000000
13	31.0	27.0	26.0	23.0	188	86.00	800000000
14	33.0	25.0	28.0	21.0	190	86.00	800000000
15	33.0	25.0	28.0	21.0	192	86.00	800000000
16	33.0	25.0	28.0	21.0	186	86.00	800000000
17	33.0	25.0	28.0	21.0	184	86.00	800000000
18	33.0	25.0	28.0	21.0	182	86.00	800000000
19	33.0	25.0	28.0	21.0	188	90.05	800000000
20	33.0	25.0	28.0	21.0	188	85.05	800000000
21	33.0	25.0	28.0	21.0	188	80.05	800000000
22	33.0	25.0	28.0	21.0	188	100.05	800000000
23	33.0	25.0	28.0	21.0	188	105.05	800000000
24	33.0	25.0	28.0	21.0	188	86.00	850000000
25	33.0	25.0	28.0	21.0	188	86.00	900000000
26	33.0	25.0	28.0	21.0	188	86.00	950000000
27	33.0	25.0	28.0	21.0	188	86.00	1000000000
28	33.0	25.0	28.0	21.0	188	86.00	750000000
29	33.0	25.0	28.0	21.0	188	86.00	700000000
30	33.0	25.0	28.0	21.0	188	86.00	650000000

3.10 Conclusion

This chapter provides the groundwork for two studies which will be described in following chapters. In these studies less known and some unknown aspects of attenuation will be investigated to build up a better understanding and appreciation of the impact of not applying attenuation correction, as well as highlighting the complexity of attenuation artefacts. This includes the investigation to find which part of the human anatomy is mostly responsible for the creation of attenuation artefacts and in which regions of the left ventricle they are most likely to occur. Monte Carlo studies of Cardiac Imaging have been used by other workers in the past, but have not been applied in such a systematic way to the wide range of anatomical variations, and individual organs. It is hoped in this way to achieve new insights into the

complexity of attenuation in MPI and the need for accurate attenuation correction. This study will apply methods to aspects which have not been reported in the literature before. It will also highlight the distortion as a result of the non-uniformity of the thorax and will again quantify it. These studies will also highlight and quantify the effect of different positions and orientations of the left ventricle within the thorax. These effects and other effects will be discussed in the next two chapters. These results will then be used to analyse the extent of corrections achieved by a commercially available correction method.

Chapter 4 - Attenuation and Scatter From Individual Anatomical Parts in the Thorax

4.1 Introduction

The purpose of the study described in this chapter is to establish the contribution to the overall intensity losses in the different segments of the left ventricle from the individual anatomical parts in the thorax. This will help to highlight some aspects of the intensity losses experienced in the thorax which are not well known or not known at all so that a better understanding of these intensity losses can be obtained. This understanding should hopefully help to confirm the need for acceptable correction methods, especially attenuation correction, to be implemented on a routine basis when MPI is performed.

Current techniques for assessing myocardial perfusion studies generally rely on visual interpretation and on analysis of relative tracer activity within the myocardial regions defined by an individual SPECT study. Most of these techniques rely on maximal counts derived from radial sectors of reconstructed shortaxis slices (maximum count circumferential profiles) normalised by count values in regions of peak intensity assumed to represent normally perfused regions¹⁷⁸ to determine relative tracer activity at rest and after stress. One serious limitation of these relative quantification techniques is that there is no guarantee that a normally perfused myocardial segment will be present in the patient. Consider patients with multivessel disease; although qualitative and relative quantitative analysis may identify the most severely stenosed coronary artery, less severely stenosed arteries may not be identified without an absolute measure of the radionuclide uptake in the myocardium. In the extreme case of balanced triple-vessel disease¹⁷⁹, an overall reduction in activity may be completely overlooked.

To avoid these problems, the ultimate goal in myocardial SPECT is to achieve absolute quantification - that is, to make an absolute measurement of Becquerels of tracer per gram of tissue in a specified region of the left ventricular myocardium. Unfortunately, photon attenuation, scatter radiation, partial-volume errors, and other perturbations compromise absolute quantification of the radionuclide uptake from SPECT^{38,39,40}.

In a Monte Carlo simulation study investigating the effects of the above mentioned corrections on a simulated human, it was found that for the LV wall, activity was underestimated by 91.8% when using no correction methods¹⁸⁰. According to a study done on a porcine model without any corrections, the measured in vivo activity concentration in the porcine myocardium was only 10% of the true value⁴⁹, indicating a loss of about 90% of the original counts. By correcting for object-specific attenuation, the authors reported an improvement in the accuracy of this measurement but this resulted in values that were still only 42% of the true value. By correcting for both attenuation and partial-volume errors, they were able to achieve absolute quantification with accuracy close to 10%⁴⁹.

It has been reported that the intensity loss experienced is more pronounced in the basal parts of the left ventricle and this can be attributed to the fact that the basal parts of the left ventricle are further away from the body surface and therefore exposed to more attenuation media¹⁸¹.

In a study where the usefulness of using low-dose CT devices to produce attenuation maps was investigated by using perfusion PET as a reference method¹⁸², it was discovered that SPECT overestimates the relative perfusion in the apex and in the anterolateral wall. These authors proposed that the comparably low resolution of the SPECT system leads to a more pronounced partial-volume effect and they concluded that the partial-volume effect might be responsible for the accentuation of the apex in the SPECT studies. In another study using the MCAT phantom, a physical phantom and a patients study it was found that this over estimation could be as high as 20%¹⁸³. These authors postulated that the partial volume effect, interactions between attenuation correction and detector-response blurring, scatter, incomplete detector response compensation and noise may contribute to this but further work is required to explain this effect.

In the study¹⁸² where low-dose CT devices were used to produce attenuation maps it was also reported that the inferior wall is the area of the left ventricle to benefit most from attenuation correction and therefore it is the area that experiences the most attenuation during acquisition. They also reported that they did not find attenuation artefacts in the anterolateral wall in females because of breast attenuation but this may be due to their patient selection.

It has also been reported in numerous studies that breast tissue attenuation in females may produce artifacts in the anterior wall¹⁸⁴. In a phantom study to study breast tissue attenuation¹⁸⁵ it was found that the location of apparent "defects" resulting from attenuation was highly variable, depending on the orientation of the myocardium and the precise positioning of the breast tissue. Furthermore they found that an asymmetric polar map was obtained even without breast tissue due to the nonuniform attenuation of the thorax. The

authors concluded that although anterior "defects" are commonly produced by breast tissue attenuation, false "defects" appear to be possible anywhere in the polar map.

Radioactive tracers are distributed around the body, and emit photons in proportion to their concentration. A gamma camera system will detect the photons and their point of origin and store this information in a matrix that is used to create the required images. The images themselves are displayed as intensities on a computer screen. These intensities reflect the relative perfusion in different parts of the myocardium and are used to decide what the perfusion in the different segments of the myocardium is.

In practice, however, some photons are scattered or absorbed in their passage through the body, and this effect is greater in denser organs and larger patients. Scattered photons have a lower energy than the original photon, and gamma camera systems can be set up to detect only photons in a specific energy range. However, the sensitivity of the gamma camera system is modest, and so the "window" of photon energies detected is sufficiently broad to detect some scattered photons, which the camera system register as being emitted from certain parts of the myocardium while the original photons were actually emitted from a different part. There are other inherent limitations in the imaging and processing system which also affect the final image.

When some of the photons emitted do not reach the gamma camera system, as a result of attenuation, scatter, etc., then the intensity representing that part of the myocardium will be lower than the true value and the relative perfusion will be under estimated. Should it be the case that the intensity values are higher than the true value as a result of the partial-volume effect^{186,187}, non-uniform attenuation, depth-dependent detector response, scatter and statistical noise¹⁸⁷, then the relative perfusion will be over-estimated.

The fact that the intensity losses in the basal parts of the left ventricle is more pronounced and that there could be an over estimation of the apical parts will lead to a distortion of the final reconstructed left ventricular images. This, together with the fact that it has been reported that the inferior wall is more subject to experience intensity losses and that breast tissue can produce attenuation artifacts in female patients will lead to the non-uniform distribution of the intensities in the final images (i.e. artefact or false positive) even if the original activity distribution in the left ventricle were to be uniform.

Typical images of Monte Carlo simulated patients produced by the methods in Chapter 3, section 3.8, can be seen in figure 4.1. This illustrates the fact that attenuation is more pronounced in the basal parts of the left ventricle as indicated by the yellow arrows as well as in the inferior wall as shown by the white arrow.

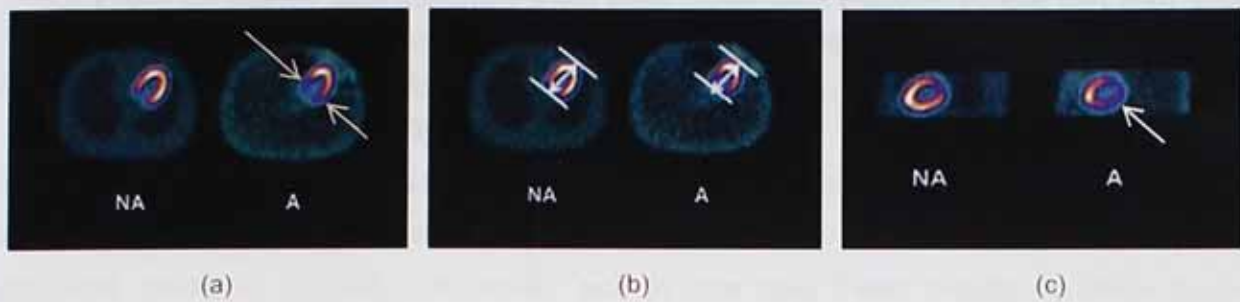


Figure 4-1: The non-attenuated (air simulation) (NA) images and attenuation (A) images displays the typical effect of attenuation in (a). The images in (b) show the "shortening" of the ventricular cavity. The sagittal images in (c) shows the effect attenuation has on the anterior and inferior wall, with the inferior wall clearly experiencing a bigger loss of intensities.

The contribution of the individual anatomical parts in the thorax to the position and perfusion values in the final acquired image in patient studies is not well known. Very little is also known about the amount of scatter caused by the individual anatomical parts in the thorax and the effect that these anatomical parts have on the overall distribution of the photons as a result of this scatter. Therefore there is a need for a systematic study to get a better understanding of the "defects" caused in the left ventricle by these anatomical parts and to investigate the points mentioned above. This study will attempt to answer the following questions:

1. What is the extent of the distortion caused by these problems?
2. Do the basal parts of the final left ventricular images experience substantial intensity losses as compared to the rest of the left ventricle?
3. If found to be true, what is the extent of the intensity losses in the basal parts of the left ventricle as compared to that in the apical regions and how does it contribute to the "distortion" of the images of the reconstructed left ventricle?
4. Is there an over estimation of the apical region in the non-attenuation corrected images and does it contribute to the "distortion" of the images of the reconstructed left ventricle and what is the extent of this "distortion"?
5. What is the contribution of the individual anatomical parts to the overall intensity losses experienced in the final reconstructed images of the left ventricle when no corrections (attenuation, scatter, partial-volume, etc.) are applied?
6. What is the contribution of the heart (myocardium, pericardium and bloodpool of all 4 chambers) to the overall intensity losses experienced and "distortion" caused?
7. Which part or parts of the thorax are responsible for the intensity losses experienced in the regions which are most affected?
8. Which parts of the left ventricular images experience the most substantial intensity losses in males and females?
9. Is there a substantial loss of intensities in the anterior wall of female patients and what is the cause of it?
10. What is the extent of scattered photons in the acquired images and does it contribute to the "distortion" in the images of the reconstructed left ventricle as well?
11. What are the differences in intensity losses experienced between male and female patients?

12. Does the inferior wall experience the most substantial intensity losses and if so, what is the difference of the losses experienced between males and females?
13. What is the fractional intensity losses experienced in the different segments of the final left ventricular images?

This study will investigate these questions by using Monte Carlo simulations and the results will be analysed by using the means (of all the segments for all the anatomical parts) as a statistical model to quantify the results and to see how these results correlate to the published results. Chapter 5 will analyse how these effects are influenced by different orientations and positions of the heart within the thorax. Chapter 6 will investigate the effect of the corrections achieved by a transmission based attenuation correction technique combined with a resolution recovery algorithm and how these results compare to the intensity losses and variations predicted by the Monte Carlo simulations.

4.2 Methods

4.2.1 Data Simulations and Analysis

The input data for the Monte Carlo simulation consisted of an attenuation map and an activity map for every simulation from the NCAT phantom.

Using the NCAT software an attenuation map of a normal patient was created for the whole thorax, referred to as the "whole thorax", or "Everything", map, displayed in figure 4.2 (a), an "air" map with no attenuation, as described in previous chapters, as well as an activity map, displayed in figure 4.2 (b). The purpose of these maps was to study the distortion of the uniformity in the resultant image of the left ventricle which will be presented in later paragraphs and so that questions 1-4 and 9-13 in section 4.1 could be answered.

To study the effect of the different anatomical parts on the overall amount of intensity losses experienced, additional attenuation maps were created by setting the attenuation coefficients to zero for all the anatomical parts in the thorax except for a single anatomical part. For example, assign a non-zero attenuation coefficient to the blood pool and set the coefficients for the rest of the anatomical parts in the thorax to zero, as displayed in figure 4.2(c). This in effect "removed" the remainder of tissue from the thorax and created a result with only the bloodpool creating attenuation. This was repeated for the following anatomical parts, myocardium, pericardium, skeleton, remainder and the lungs, which are displayed in figure 4.2(d)-(h). Attenuation maps were also created for the remainder and skeleton combined (body), as well as the bloodpool, myocardium and pericardium combined (heart) and are displayed in figure 4.2(i)-(j). The same "air" map and activity map as described above were also used. All these attenuation maps were created for the same simulated patient. The purpose of these maps was to study the effect of the different anatomical parts so that questions 5-8 and 10 could be answered.

These simulations were done for the 30 male and 30 female "patients" described in chapter 3, each as a separate study. The reconstructed sinograms were analysed with the 9-segment model, as also described in chapter 3 and displayed again in figure 4.3.

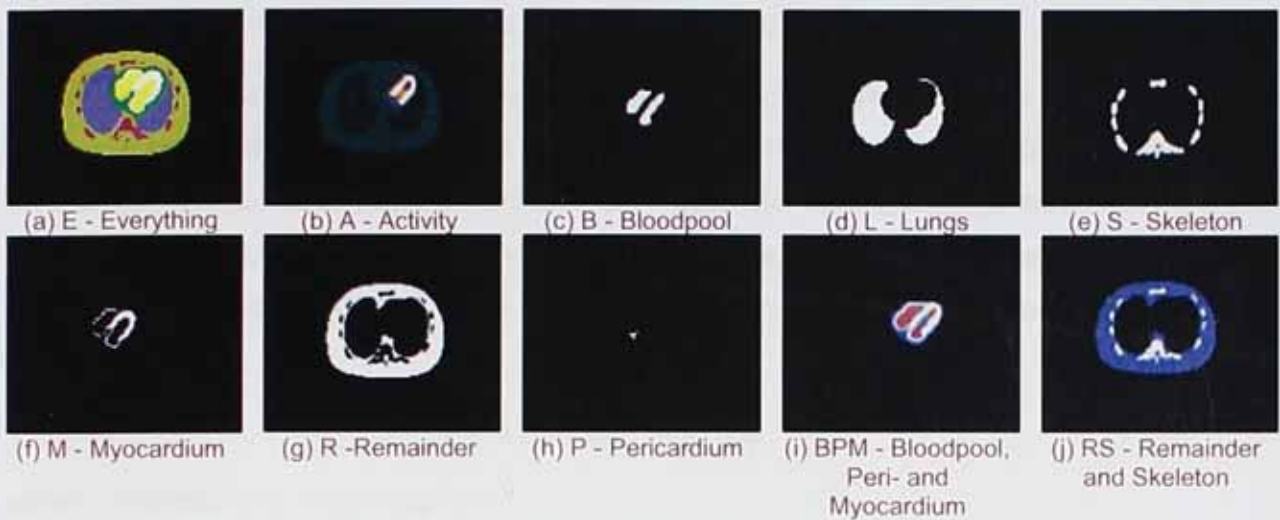
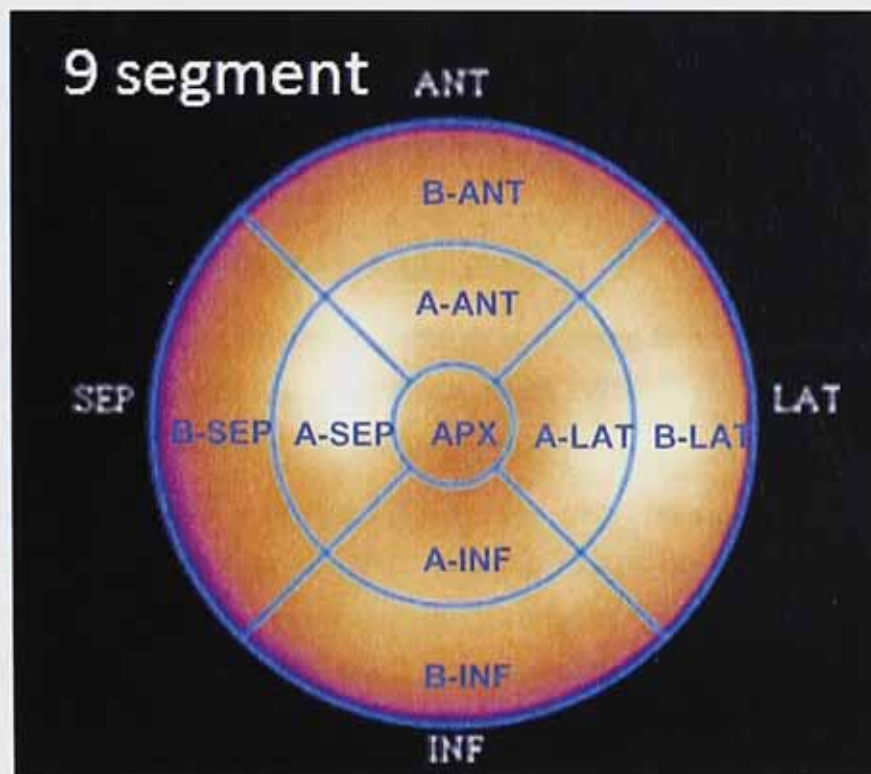


Figure 4-2: The individual body parts which acted as attenuation media, as well as "Everything", i.e. the whole thorax, which represents the attenuation map in patients, as well as the activity map.



where

B-ANT: Basal anterior,	A-ANT: Apical anterior,	B-LAT: Basal lateral
A-LAT: Apical lateral,	B-INF: Basal inferior,	A-INF: Apical inferior
B-SEP: Basal septal,	A-SEP: Apical septal,	APX: Apical

Figure 4-3: The 9-segment cardiac model which was used to analyse the data in this study.

4.2.2 Evaluation Criteria

The effect of the different intensity losses was characterised using the following 2 criteria: (a) uniformity of the polar maps, (b) fractional absolute difference in intensities.

A. Uniformity of the Polar Map (PMU) Over the 9 Segments

When using polar maps to analyse the reconstructed images, intensity losses in these images manifest themselves as lack of uniformity in the polar maps. Each polar map was divided into 9 myocardial regions to create the 9 segment model, and the mean activity m_i in each region was calculated. The maximum m_{max} of these 9 values was used to normalise all 9 values using $(m_i/m_{max}) * 100^{180}$. The polar map uniformity (PMU) was calculated as follows for each segment:

$$PMU = (m_{max} - m_i) / m_{max} * 100$$

where i represents a single segment.

This was expressed as a percentage. This should be 0% if there are no intensity losses because the activity is uniform in the LV wall in the phantom.

The PMU of the "Air" simulation (PMU_{air}) was calculated for each segment and used as the reference. The PMU (PMU_{part}) for all the individual anatomical parts were also calculated for the different segments and the difference expressed as the Polar Map Uniformity Difference (PMUD), see figure 4.4:

$$PMUD = PMU_{air} - PMU_{part}$$

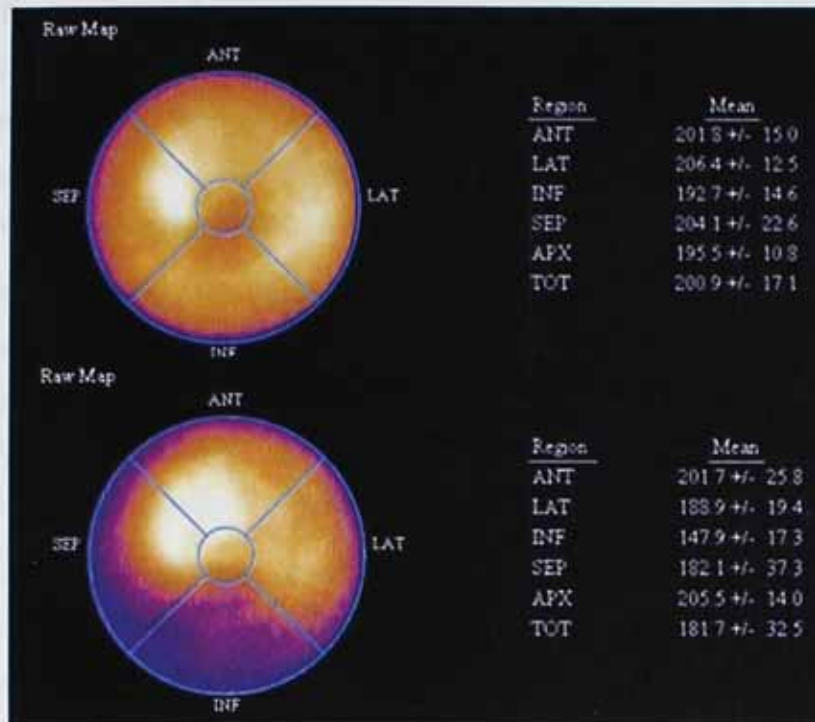
In this study the whole thorax as attenuation medium is referred to as "Everything", meaning it includes all the different individual anatomical parts. When referring to the different anatomical parts, "Everything" is treated in the same way.

The PMU of the "Air" simulation represents the values when no scatter or attenuation is present and any difference between this PMU and the PMU's of the different anatomical parts represents the amount of non-uniformity introduced in that segment by these interactions. These non-uniformities will reflect themselves as "defects" when analysing the polar maps and therefore represent the artefacts, i.e. false positives as defects when analysing patient studies. Although this study does not relate PMUDs to clinically observed defects, the larger the PMUD, the more likely it is to be seen, and be a false positive.

A PMUD index was also defined as the mean of the PMUD's of the 9 segments¹⁸⁰:

$$PMUDI = \text{mean}(PMUD_i)$$

where $PMUD_i$ defines the PMUD values for all the 9 segments. This value should again ideally be 0%.



$$M_{\max} = 206.4$$

$$M_{i-INF(\text{air})} = 192.7$$

$$PMU = \frac{(m_{\max} - m_i) * 100}{m_{\max}}$$

$$= \frac{(206.4 - 192.7) * 100}{206.4}$$

$$= 6.6\%$$

$$M_{\max} = 205.5$$

$$M_{i-INF(\text{part})} = 147.9$$

$$PMU = \frac{(m_{\max} - m_i) * 100}{m_{\max}}$$

$$= \frac{(205.5 - 147.9) * 100}{205.5}$$

$$= 28\%$$

$$PMUD = PMU_{\text{air}} - PMU_{\text{part}} = 6.6\% - 28\% = -21.4\%$$

Figure 4-4: Images to illustrate the PMUD

B. Fraction Absolute Difference in Intensities

As indicated in the introduction, the mean of the intensities in each segment of the "Air" simulations are substantially higher than those for the whole thorax with attenuation. To study the effects of the artefacts introduced during the image acquisition process in more detail, the Fractional Index (FI) for each segment can be calculated:

$$FI = (\text{Mean of intensities in segment})_{\text{air}} / (\text{Mean of intensities in segment})_{\text{everything}}$$

The mean of all the FI's in all the segments is defined as MFI:

$$MFI = \text{mean}(FI\text{'s of all 9 segments})$$

4.2.3 Investigation of the Perfusion Losses in the Left Ventricle When not Applying Any Corrections

To investigate and quantify the degree of non-uniformity of the perfusion in the reconstructed left ventricle (LV) a comparison has been made by using the Whole Thorax ("Everything") as attenuation medium together with the "Air" simulation as reference. The PMUD of "Everything" as the attenuation medium was calculated for all the 9 segments.

If the whole thorax as attenuation medium does not alter the perfusion distribution in the original images as reflected in the polar maps of the simulated patient, the PMUD of each segment will be equal to zero. This was the null hypothesis.

The experimental hypothesis was that effects such as attenuation, scatter, the partial volume effect and the depth dependent collimator response can alter the intensity distribution in the final images by introducing non-uniformities. These can be interpreted as defects by a clinical reporter, and when interpreted as of clinical origin by such a reporter, could lead to the study reported as a false positive. If this hypothesis held true then the extent of these apparent defects were quantified and shown to be statistically significant in this study.

In this case the manipulations were done on the same simulated patient images and therefore the dependent means t-test was used to test the null hypothesis and it was a two-tailed test. If found that the null hypothesis does not hold true, i.e. the experimental hypothesis is valid, the effect size would be calculated and expressed as r-values to calculate the extent of non-uniformity in the final images of the left ventricle.

This hypothesis was used to see whether there are any defects introduced in the LV by the imaging process itself, and if found to be the case, to calculate the extent of these introduced defects. The next hypothesis will investigate any possible differences between the apical and basal parts in these introduced defects in the LV, what the extent of these differences may be.

4.2.4 Comparison Between the Basal and Apical Regions of the Perfusion Distortion Found

When the photons travel from the patient to the imaging system some of them are attenuated (as described in 2.3) and this fact is reflected in the images as lower intensities as compared to what it would have been when no attenuation media is present. Therefore it can be concluded that the imaging system under estimates the real perfusion. As a result of the orientation of the heart, the basal parts of the left ventricle are further away from the imaging system than the apical parts and therefore subject to more attenuation medium. From this it can be concluded that the imaging system will underestimate the relative perfusion in the basal parts more than compared to the apical regions. Under estimation of the real perfusion is reflected as a positive PMUD value.

To quantify any perfusion uniformity difference found between the basal and apical parts of the left ventricle, a comparison has been made between the PMUDs of the basal and apical parts of each of the anterior (ANT), lateral (LAT), inferior (INF) and septal (SEP) regions of the reconstructed left ventricular images. Again the only attenuation medium was the Whole Thorax ("Everything").

The null hypothesis was that there is no difference in the relative perfusion between the basal and apical parts of the LV and therefore no distortion caused in the LV as a result of the imaging process (introduced by effects such as attenuation, scatter, the partial volume

effect and the depth dependent collimator response) and that any defects introduced are of the same extent in both the apical and basal parts and therefore the PMUDs should be zero.

If the null hypothesis did not hold true in a specific segment, the conclusion was made that there are substantial differences between the perfusion uniformities experienced between the apical and basal regions of a specific segment as illustrated in figure 4.5

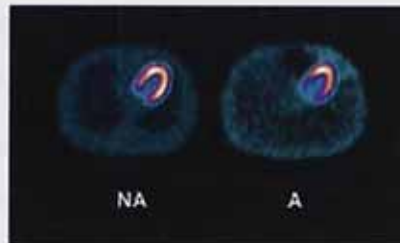


Figure 4-5: Illustrating the differences in intensity losses between the basal and apical parts of the LV

These manipulations were done on the same simulated patient and therefore the dependent t-test was used to test the null hypothesis and it was a two-tailed test. If the hypothesis was true then the effect size was calculated. These effect sizes were used to specify the extent of the differences that contributed to the perfusion non-uniformity in the final images of the left ventricle.

This hypothesis tested to see whether the basal and apical parts experience a different level of intensity loss as a result of the imaging process, i.e. do the basal parts experience a bigger under estimation of the intensities as compared to the apical regions. The next hypothesis will test to see whether the apical parts not only experience a smaller loss in intensities but whether it actually experiences an over estimation of the intensities when no corrections are applied.

4.2.5 Investigating the Relative Distortion in the Basal and Apical Parts

From the previous section it can be concluded that the imaging system will underestimate the relative perfusion in the basal parts more compared to the underestimation in the apical regions. As stated earlier such an under estimation of the real perfusion will be reflected as a positive PMUD value. On the other hand, negative PMUD values will reflect an over estimation by the imaging system of the real perfusion in those segments, i.e. the intensity values in those parts of the images are higher than what it will be expected to be. This would be an unexpected, or unusual, and rarely considered result but this has been reported in the literature where the perfusion in SPECT images of the left ventricle were compared to those obtained by using PET¹⁸⁸, as well as in another Monte Carlo simulation study¹⁸⁹. This will also contribute to the distortion effect on the relative perfusion in left ventricle and actually make it worse. The combined effect of the under estimation of the perfusion in the basal

parts together with the over estimation in the apical parts will have a much bigger distortion effect than would have been the case if the under estimation of the real perfusion in the apical parts had simply been lower than that in the basal parts.

The null hypothesis was that that the apical parts of the LV do not experience an over estimation of the real intensities and therefore all the PMUD values would be positive. If any of these PMUD values were found to be negative then the null hypothesis was not true and the apical parts do experience an over estimation of the real intensities. Once again the PMUDs were calculated for the Whole thorax ("Everything") as attenuation medium.

To determine which regions suffer the most from this an index, as described in 4.2.2, the PMDUI was calculated. Segments with a relative perfusion uniformity higher than this could be classified as experiencing a severe under estimation of their uniformity, which is a reflection of an under estimation of the perfusion in that region.

4.2.6 Investigation Into the Contribution to This Distortion by Each Anatomical Part

The purpose of this part of the investigation was to determine how the different anatomical parts affected the observed perfusion distribution in the final reconstructed left ventricular images. By analysing the reconstructed images when only a specific anatomical part provided attenuation and scatter and comparing that to the "Air" simulation, the contribution of that part to each of the 9 segments could be calculated. The PMUD's of each of the anatomical parts in all the 9 segments were determined. The PMUD's of the heart (myocardium, pericardium and bloodpool together) and the Body (remainder and skeleton combined) were also calculated to see what the effect of these two parts as a combination is.

The effects of all the parts were also added together to give the whole thorax and the contribution of each part was expressed as a percentage of these summed value. This gives the relevant contribution of each part as a percentage and quantifies the contribution of each part.

4.2.7 Investigating the Effect of Scatter on the Perfusion Distribution in the Left Ventricle

It was also an experimental hypothesis that the main contributor to the over estimation of the perfusion of the apical regions, together with the under estimation of the real perfusion in the basal parts, resulting in the "distortion" in the final images, is from scattered photons. Attenuation leads to a reduction of the observed perfusion in a specific segment of the left ventricle while scattered photons from elsewhere can reduce the amount of observed perfusion loss estimated in that segment and this reduction in loss will be visible in the displayed images. This latter is undesirable as the scattered photons will have originated

from outside that part of the left ventricle, this is also known as "in-scatter". This can be reduced by narrowing the energy window during an acquisition but this will also limit the number of primary photons detected, therefore the same window width was used in this study as used in clinical practise. The hypothesis for this work is that this can potentially have serious consequences on the accuracy of quantitative analysis, and potential false positives and negatives, and that correction for attenuation only, and not scatter, will result in an over-estimation of the observed perfusion.

To test the hypothesis that scatter plays a important role in the over estimation of the observed perfusion of the apical regions of images during a SPECT acquisition, 10 female patients were simulated again but in this case the primary and scattered photons were collected in separate sinograms so that the effect of the scattered photons could be analysed.

The percentage of the original photons that reached the target as primary and scattered photons were calculated for each of the 9 segments. For each of the 9 segments the scatter fraction was also calculated, i.e. the fraction of intensities (as compared to the total final intensities) in each segment which is due to scatter and expressed as a percentage.

To test the experimental hypothesis the percentage of the value of the means of the scattered photons in the apical regions were compared to the means of the scattered photons in the basal regions by using the dependent 2-tailed t-test. If the t-value, when comparing a specific apical region to a specific basal region, was significant, it was concluded that the scattered photons in that region contributes to the perfusion over estimation in that specific apical region. The same analysis was also performed on the primary photons. If the t-value is only significant for the scattered photons and not the primary photons the conclusion could be made that the over estimation is mainly due to the scattered photons but if it is also significant for the primary photons, it could only be concluded that the scattered photon partly contributes to the over estimation but there may be other contributing factors.

4.2.8 Fractional Intensity Losses in the Final Ventricular Images

The result of the mentioned permutations can result in up to 90% of the counts being lost and therefore substantially reduce the amount of counts in the final reconstructed left ventricular images. In this section the effect of this reduction was calculated as the FI value, as explained above, so that it can be used as a reference measurement in correction methods in later chapters.

4.2.9 Investigating the Differences in Perfusion Losses Experienced Between Males and Females

It is widely accepted that male and female patients do not display the same losses in intensities in the final reconstructed images as result of differences in anatomy¹⁹⁰. The perception is that male patients experience more losses in the inferior part of the left ventricle, something that is often referred to as "diaphragm attenuation"¹⁹¹ but female patients experience more losses in the anterior parts of the left ventricle as a result of breast attenuation¹⁹². To investigate the actual differences in intensity losses experienced between male and female patients in the final left ventricular images, and what these differences are and how they affect each gender, a comparison has been made between the male and female simulated patients, especially in the region of the anterior wall which are influenced by breast attenuation in females.

To establish these differences, comparisons had been made between the PMUD's of the Whole Thorax, the Heart and the Body as attenuation media and when comparing the basal and apical parts.

These comparisons have been quantified by using the 2-tailed independent samples t-test. These results were used to determine the differences in the polar map uniformities as a result of these parts.

The FI of the total intensity losses were also calculated and compared.

4.3 Results

4.3.1 Tests to Ensure That a Parametric Model Will be Valid

Box-plot methods and z-scores checked for outliers in the data. Levene's tests confirmed the homogeneity of variance (homoscedasticity) and inspection also confirmed that they adhere to the principles of independence and interval data. Using the z-scores for skewness and kurtosis, as well as the Shapiro-Wilk test confirmed the normal distribution of the data.

4.3.2 The Distortion in the Left Ventricle

The PMUDs calculated for all the male and female simulated patients for the 9 different segments when the whole thorax acts as attenuation medium are displayed in figure 4.5 and summarised in table 4.1 and 4.2. The thorax acts as an attenuation medium for every part of the left ventricle and therefore all the segments (representing the whole left ventricle) are expected to show a zero PMUD for the null hypothesis to be true. Should the PMUD's not be zero than the experimental hypothesis holds true and a positive PMUD reflects an under

estimation of the real perfusion and a negative PMUD reflects an over estimation of the real perfusion.

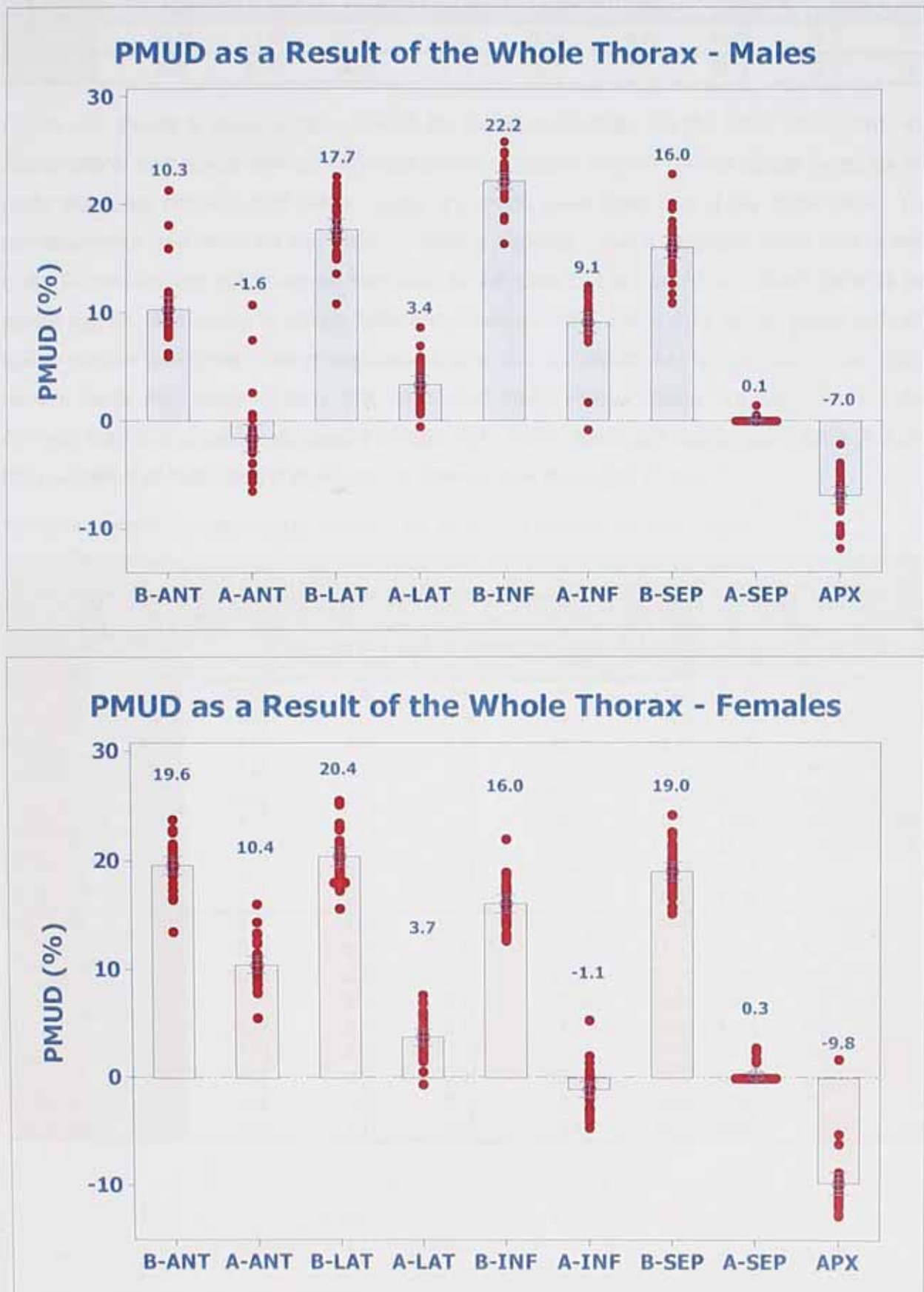


Figure 4-5: The means (as displayed above each bar) of the PMUD's as a result of the Whole Thorax together with the 95% confidence intervals for each of the 9 segments for the male and female simulated patients.

Table 4-1: Summary of the PMUD values for both male and female simulated patients as a result of using the whole thorax as attenuation medium

PMUD as a Result of the Whole Thorax									
	B-ANT	A-ANT	B-LAT	A-LAT	B-INF	A-INF	B-SEP	A-SEP	APX
Male	10.3	-1.6	17.7	3.4	22.2	9.1	16.0	0.1	-7.0
Female	19.6	10.4	20.4	3.7	16.0	-1.1	19.0	0.3	-9.8

Figure 4.5 shows a positive value for all the basal segments. On the other hand, only the apical-lateral and apical-inferior segment show a positive PMUD for the apical parts for the male simulated patients and these values are much lower than that of the basal parts. The apical-anterior and apex for the male simulated patients show a negative value and is very close to zero for the apical-septal segment. In the case of the female simulated patients the apical region also show a visible difference between the basal and apical parts with the apical-inferior and apex having negative values and the apical-septal segment once again have a value very close to zero. The calculated mean PMUD values are displayed in table 4.1 with the t and p values displayed in table 4.2. The r-values are displayed in table 4.3 and the r-values that indicating a significant difference are displayed in red.

Table 4-2: Paired Samples t-test to determine the significance between the PMUD values

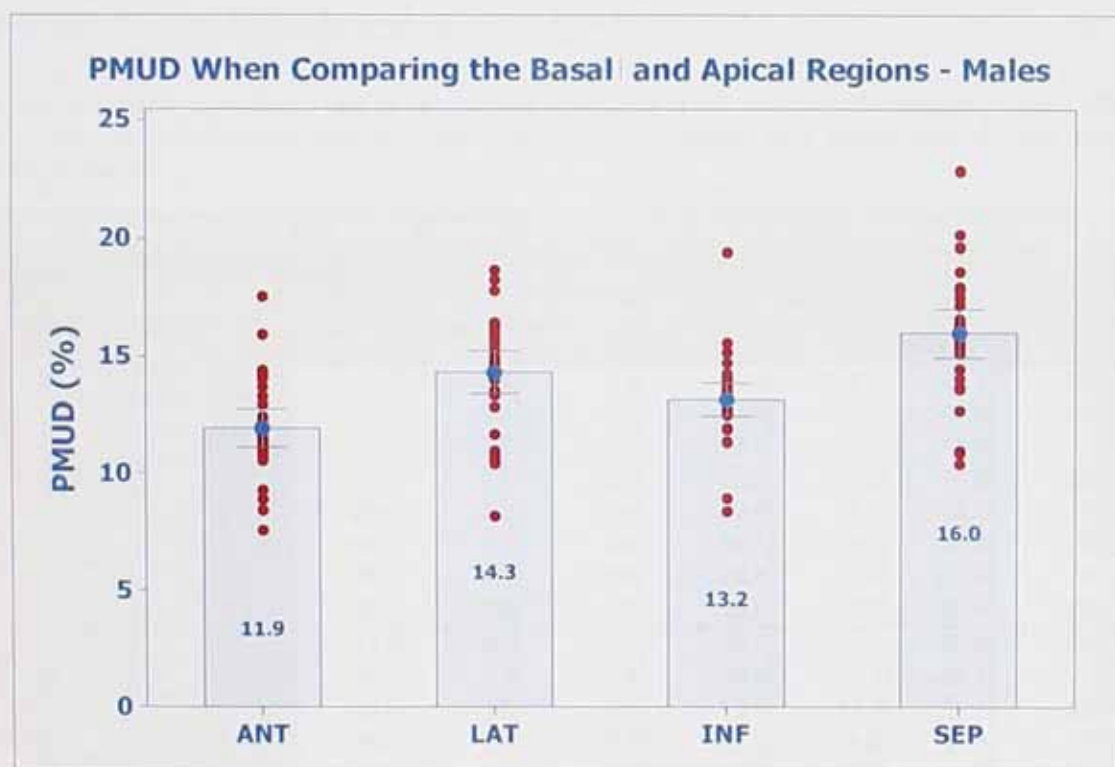
Paired Samples Test - PMUD when using Whole Thorax as Attenuation Medium										
	Segment	Paired Differences						t	df	p (2-tailed)
		PMUD	Std. Deviation	Std. Error PMUD	95% CI of the PMUD					
					Lower	Upper				
Male	B_ANT	10.3	3.3	0.6	9.1	11.5	17.3	29	.000	
	A_ANT	-1.6	3.5	0.6	-2.9	-0.3	-2.6	29	.016	
	B_LAT	17.7	2.6	0.5	16.7	18.7	36.7	29	.000	
	A_LAT	3.4	2.1	0.4	2.6	4.1	8.7	29	.000	
	B_INF	22.2	2.1	0.4	21.4	23.0	57.7	29	.000	
	A_INF	9.1	2.7	0.5	8.0	10.1	18.2	29	.000	
	B_SEP	16.1	2.7	0.5	15.0	17.1	32.6	29	.000	
	A_SEP	0.1	0.3	0.0	0.0	0.2	1.3	29	.206	
	APX	-7.0	2.2	0.4	-7.8	-6.2	-17.1	29	.000	
Female	B_ANT	19.6	2.2	0.4	18.7	20.4	49.1	29	.000	
	A_ANT	10.4	2.1	0.4	9.7	11.2	27.2	29	.000	
	B_LAT	20.4	2.3	0.4	19.5	21.3	47.5	29	.000	
	A_LAT	3.7	2.1	0.4	3.0	4.5	9.7	29	.000	
	B_INF	16.0	2.1	0.4	15.2	16.8	41.0	29	.000	
	A_INF	-1.1	2.0	0.4	-1.9	-0.4	-3.1	29	.005	
	B_SEP	19.0	2.2	0.4	18.1	19.8	46.3	29	.000	
	A_SEP	0.3	0.8	0.1	0.0	0.6	2.0	29	.050	
	APX	-9.8	2.7	0.5	-10.8	-8.8	-19.8	29	.000	

Table 4-3: r-values to quantify the PMUD (Values in red indicate that it is significant)

r-values of the PMUD's										
		B-ANT	A-ANT	B-LAT	A-LAT	B-INF	A-INF	B-SEP	A-SEP	APX
Male	t	17.3	-2.6	36.7	8.7	57.7	18.2	32.6	1.3	-17.1
	df	29	29	29	29	29	29	29	29	29
	r	0.96	0.43	0.99	0.85	1.00	0.96	0.99	0.23	0.95
Female	t	49.1	27.2	47.5	9.7	41.0	-3.1	46.3	2.0	-19.8
	df	29	29	29	29	29	29	29	29	29
	r	0.99	0.98	0.99	0.87	0.99	0.50	0.99	0.36	0.96

4.3.3 Comparison Between the Basal and Apical Regions

The previous graphs indicate that there are substantial differences between the PMUD of the basal and apical parts for both male and female simulated patients. To quantify these differences the basal and apical parts of all the segments were compared and the PMUD's when comparing these differences between the basal and apical regions for the male and female simulated patients are given in figure 4.6 and table 4.4 display the t and p values and table 4.5 the r-values.



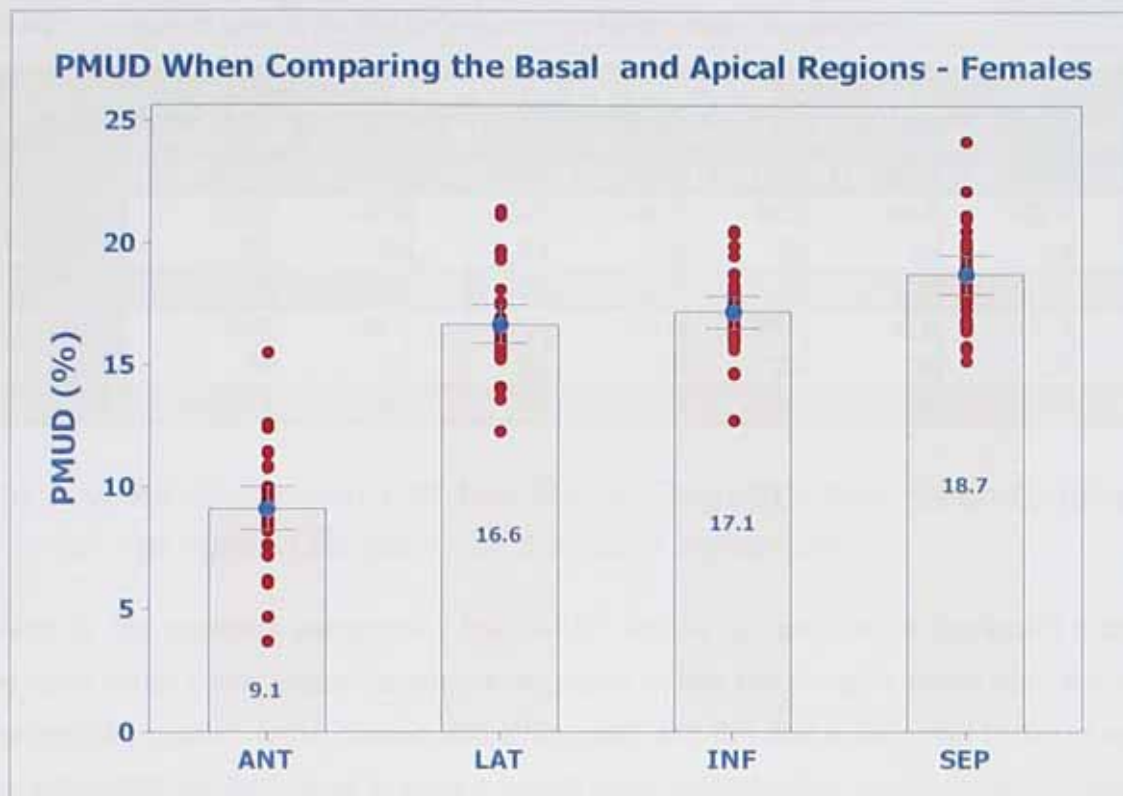


Figure 4-6: The PMUD's when comparing the difference between the basal and apical regions of the anterior, lateral, inferior and septal walls in the male and female simulated patients.

Table 4-4: 2-tailed dependent t-test to determine the equality of the means of the intensity losses differences between the basal and apical regions of the anterior, lateral, inferior and septal walls in male and female simulated patients

Paired Samples Test - PMUD when using Whole Thorax as Attenuation Medium										
	Comparing Segments	Paired Differences					t	df	p (2-tailed)	
		PMUD	Std. Deviation	Std. Error PMUD	95% CI of the PMUD					
					Lower	Upper				
Male	A_ANT - B_ANT	-9.1	2.4	0.4	-10.0	-8.2	-21.1	29	.000	
	A_LAT - B_LAT	-16.6	2.1	0.4	-17.4	-15.8	-42.5	29	.000	
	A_INF - B_INF	-17.2	1.7	0.3	-17.8	-16.5	-55.2	29	.000	
	A_SEP - B_SEP	-18.7	2.1	0.4	-19.5	-17.9	-48.6	29	.000	
	APX - B_ANT	-29.4	2.9	0.5	-30.4	-28.3	-55.2	29	.000	
	APX - B_LAT	-30.2	2.5	0.4	-31.1	-29.2	-67.4	29	.000	
	APX - B_INF	-25.8	2.7	0.5	-26.8	-24.8	-52.4	29	.000	
	APX - B_SEP	-28.8	2.8	0.5	-29.8	-27.7	-55.4	29	.000	
Female	A_ANT - B_ANT	-11.9	2.1	0.4	-12.7	-11.1	-30.6	29	.000	
	A_LAT - B_LAT	-14.3	2.4	0.4	-15.2	-13.4	-32.1	29	.000	
	A_INF - B_INF	-13.2	1.9	0.4	-13.9	-12.4	-37.1	29	.000	
	A_SEP - B_SEP	-16.0	2.8	0.5	-17.0	-14.9	-31.6	29	.000	
	APX - B_ANT	-17.3	4.4	0.8	-18.9	-15.7	-21.7	29	.000	
	APX - B_LAT	-24.7	3.2	0.6	-25.9	-23.5	-42.5	29	.000	
	APX - B_INF	-29.2	2.2	0.4	-30.0	-28.4	-72.0	29	.000	
	APX - B_SEP	-23.0	3.8	0.7	-24.5	-21.6	-32.9	29	.000	

Table 4-5: r-values to quantify the PMUD (Values in red indicate that it is significant)

r-values of the PMUD's									
		A_ANT- B_ANT	A_LAT- B_LAT	A_INF- B_INF	A_SEP- B_SEP	APX- B_ANT	APX- B_LAT	APX- B_INF	APX- B_SEP
Male	t	-21.1	-42.5	-55.2	-48.6	-55.2	-67.4	-52.4	-55.4
	df	29	29	29	29	29	29	29	29
	r	0.97	0.99	1.00	0.99	1.00	1.00	0.99	1.00
Female	t	-30.6	-32.1	-37.1	-31.6	-21.7	-42.5	-72.0	-32.9
	df	29	29	29	29	29	29	29	29
	r	0.98	0.99	0.99	0.99	0.97	0.99	1.00	0.99

4.3.4 Under Estimation of the Basal Regions and Over Estimation of the Apical Regions of the Left Ventricle

As seen in the previous paragraphs the PMUD values do not always represent a positive value as in some cases these values are negative. When the photons travel from the patient to the imaging system some of them are attenuated and this fact is reflected in the images as lower intensities as compared to how it would have looked when no attenuation media are present. Therefore the imaging system under estimates the amount of counts coming from the patient. This fact is reflected as a positive PMUD value. An index, the PMDUI, was earlier defined to determine which segments are subject to the biggest perfusion under estimation. The PMUD's when using the whole thorax as attenuation media in both the male and female simulated patients and the PMDUI to determine the under- and over-estimation of different regions are given in figure 4.7 and the results displayed in table 4.6

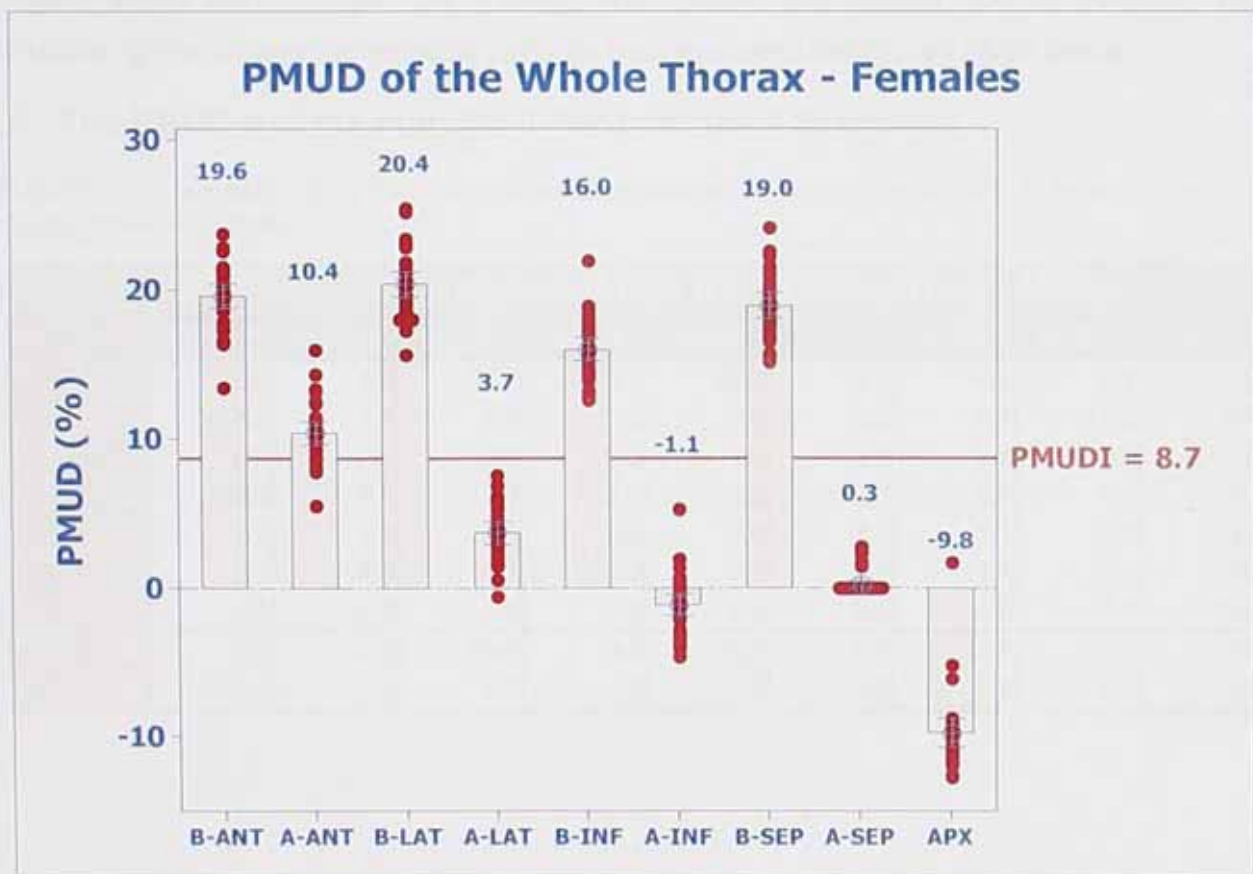
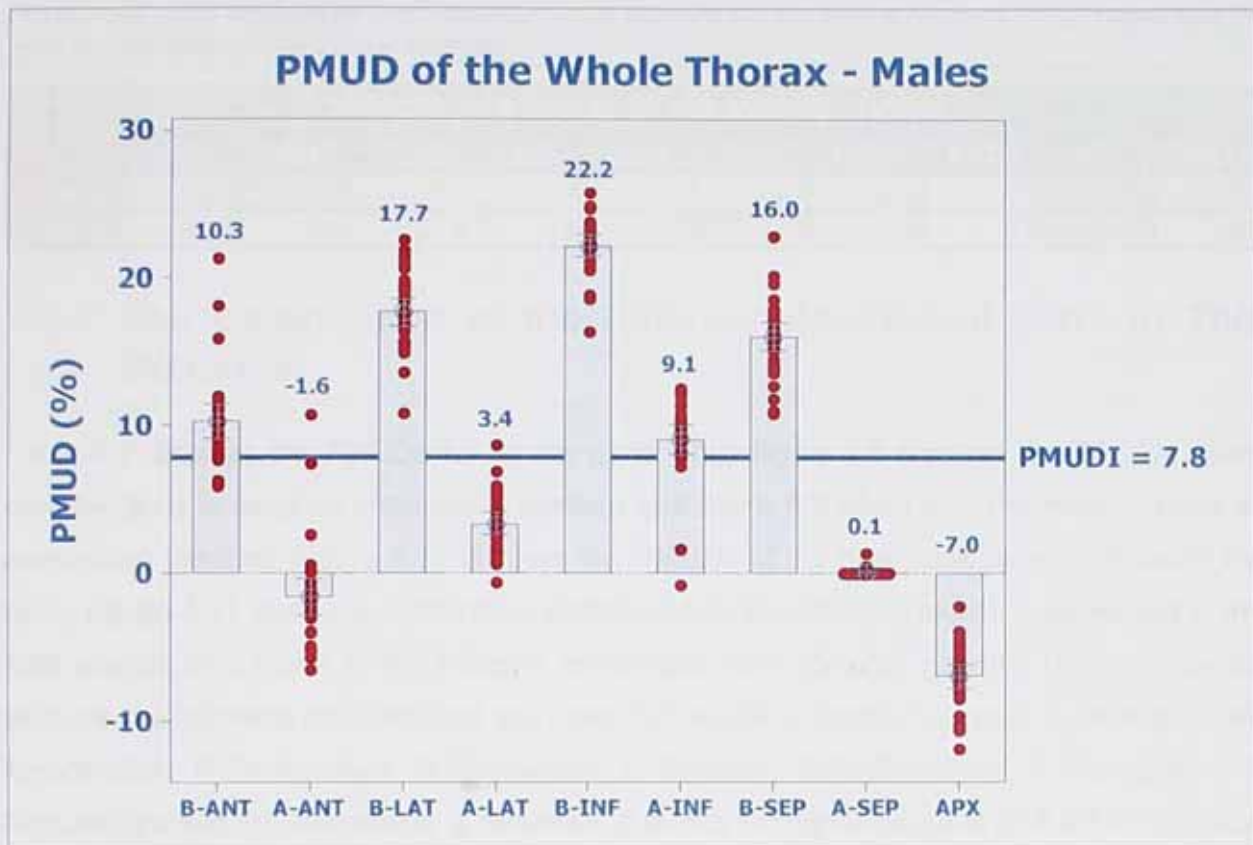


Figure 4-7: The PMUD's when using the whole thorax as attenuation media in both the male and female simulated patients and the PMUDI to determine the under- and over-estimation of different regions.

Table 4-6: The PMUDI's for the male and female simulated patients. The values in red indicates negative PMUD's and which indicates an over estimation in that segment and the ones in orange a PMUD higher than the index and therefore a severe under estimation

PMUDI as a Result of the Whole Thorax										
	B-ANT	A-ANT	B-LAT	A-LAT	B-INF	A-INF	B-SEP	A-SEP	APX	PMUDI
Male	10.3	-1.6	17.7	3.4	22.2	9.1	16.0	0.1	-7.0	7.8
Female	19.6	10.4	20.4	3.7	16.0	-1.1	19.0	0.3	-9.8	8.7

4.3.5 The Contribution of the Different Anatomical Parts to This Distortion

Table 4.7 displays the PMUDs for all the parts while figure 4.8 displays the PMUDs when only the body is used as attenuation medium and figure 4.9 when only the heart is used as attenuation medium. Figure 4.10 displays the PMUDs of the heart compared to those of the body. Figure 4.11 gives the percentage contribution to the intensity losses experienced in the final images as a result of the different anatomical parts for both genders. In the following sections the following abbreviations are used: E-The whole thorax, L-Lungs, B-Bloodpool, M-Myocardium, P-Pericardium, R-Remainder, S-Skeleton, BPM-Bloodpool & Pericardium & Myocardium and RS-Remainder & Skeleton. B stands for the basal parts and A for the Apical region where ANT-Anterior, LAT-Lateral, INF-Inferior, SEP-Septal and APX-Apical. The PMUDs for the different anatomical parts for both male and female are given below.

A. The PMUD's of the Individual Parts for the 9 Segments

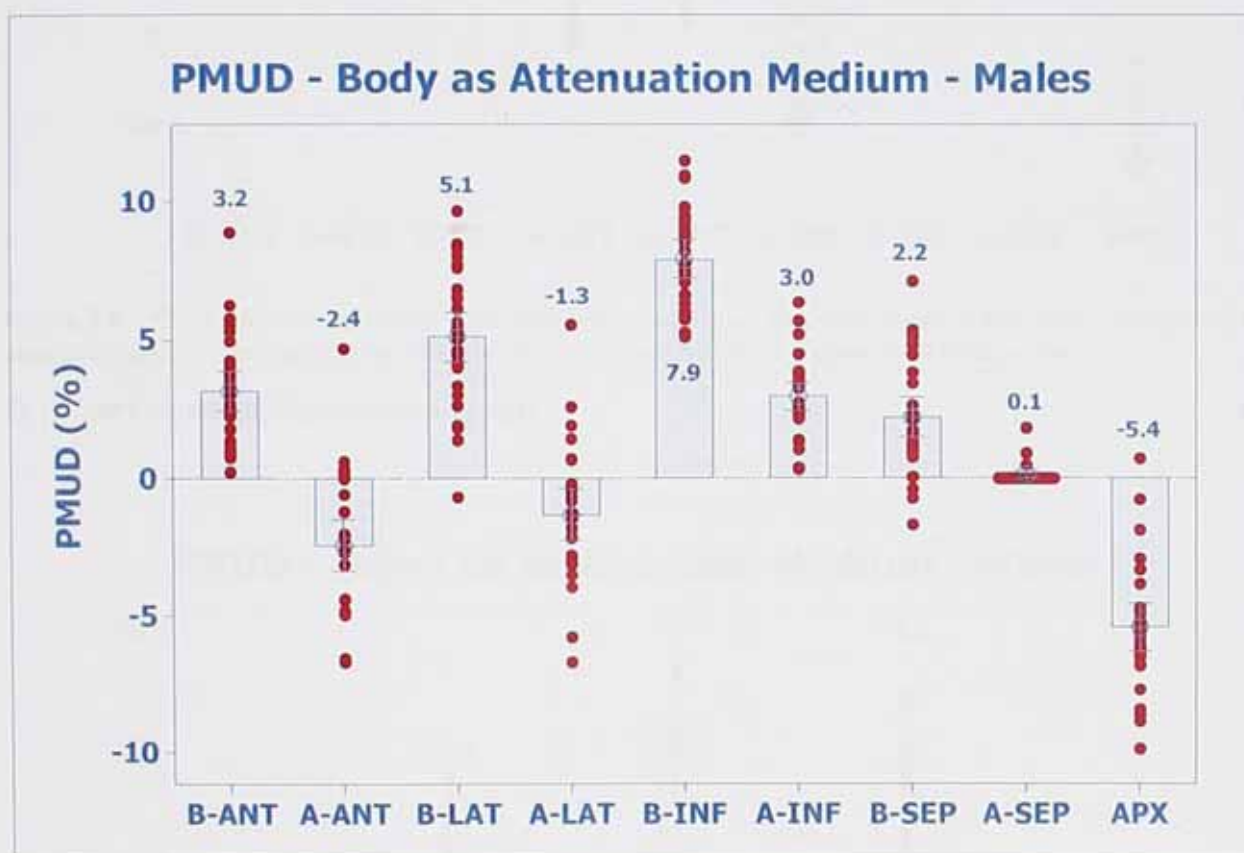
Table 4-7: A summary of the PMUD's in all the segments for all the anatomical parts for both the male and female simulated patients

PMUD for Each Anatomical Part for Each Segment - Males										
	B-ANT	A-ANT	B-LAT	A-LAT	B-INF	A-INF	B-SEP	A-SEP	APX	
E	10.3	-1.6	17.7	3.4	22.2	9.1	16.0	0.1	-7.0	
L	4.4	1.4	4.9	3.2	3.6	2.2	0.7	0.0	0.0	
B	0.5	0.4	3.8	0.0	7.6	2.1	9.6	0.0	2.8	
M	-5.8	-4.1	-2.4	-3.8	6.5	2.5	6.3	0.2	-3.3	
P	8.5	2.6	8.5	5.0	3.0	3.2	1.1	0.0	0.4	
R	2.1	-4.3	1.7	-1.7	3.7	1.9	-1.4	0.4	-6.6	
S	2.0	2.5	4.6	2.4	4.4	2.4	4.0	0.0	2.2	
BPM	3.2	-0.2	10.0	3.4	16.1	8.0	14.2	0.0	0.2	
RS	3.2	-2.4	5.1	-1.3	7.9	3.0	2.2	0.1	-5.4	

PMUD for Each Anatomical Part for Each Segment - Females

	B-ANT	A-ANT	B-LAT	A-LAT	B-INF	A-INF	B-SEP	A-SEP	APX
E	19.6	10.4	20.4	3.7	16.0	-1.1	19.0	0.3	-9.8
L	5.2	2.1	5.5	3.7	4.0	2.2	0.8	0.0	0.4
B	0.3	0.3	3.4	0.0	7.3	2.0	9.6	0.0	2.9
M	0.7	0.0	6.6	2.8	9.5	3.7	6.9	0.0	-2.2
P	0.3	-1.8	-1.4	-1.3	-0.1	1.9	-0.5	0.0	0.1
R	16.0	10.5	7.8	-0.5	-3.3	-8.4	4.7	2.8	-11.1
S	2.4	2.7	5.1	2.2	5.5	2.8	5.3	0.0	2.4
EPM	1.8	-1.0	8.7	2.5	16.6	8.3	15.0	0.0	0.8
RS	15.8	10.1	10.7	-1.5	0.4	-8.6	8.1	1.2	-10.5

B. The Contribution of the Body



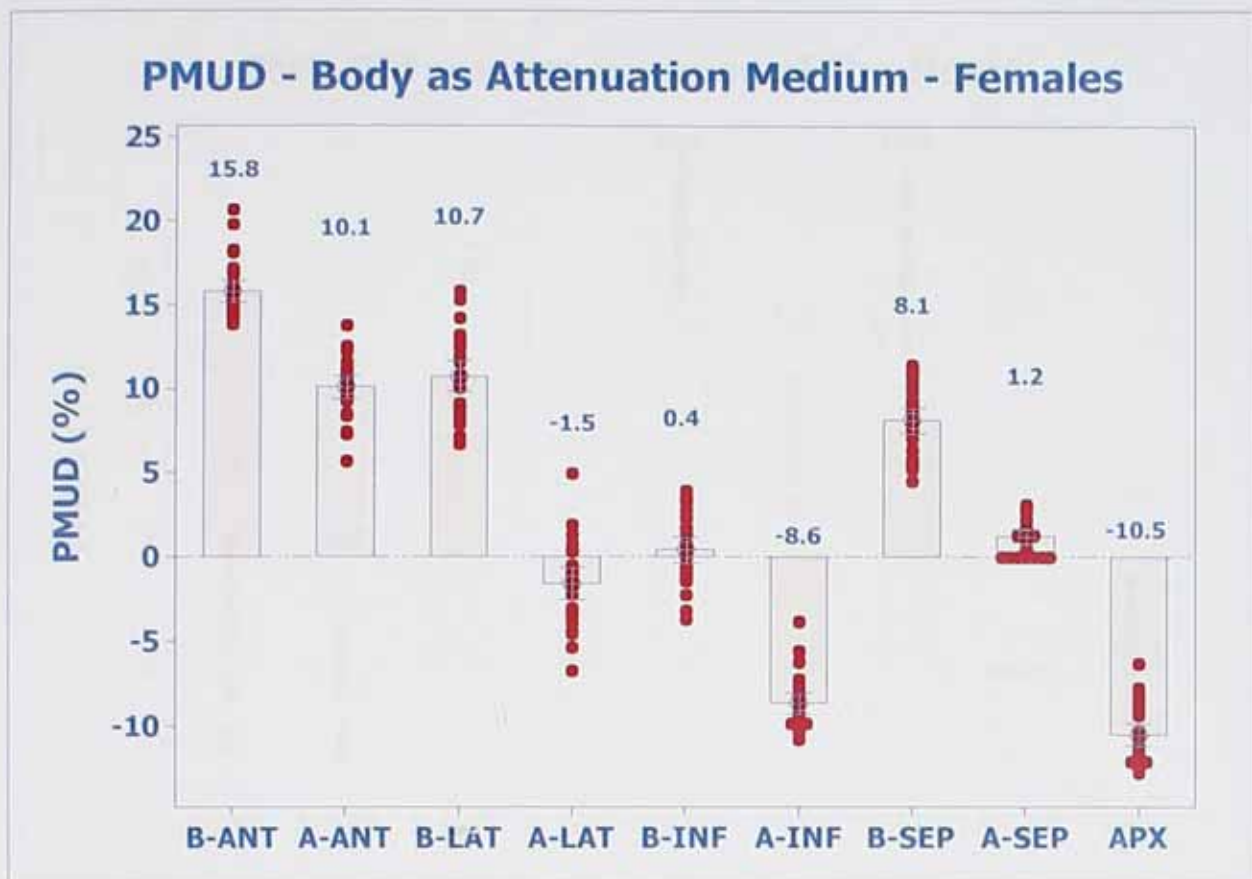
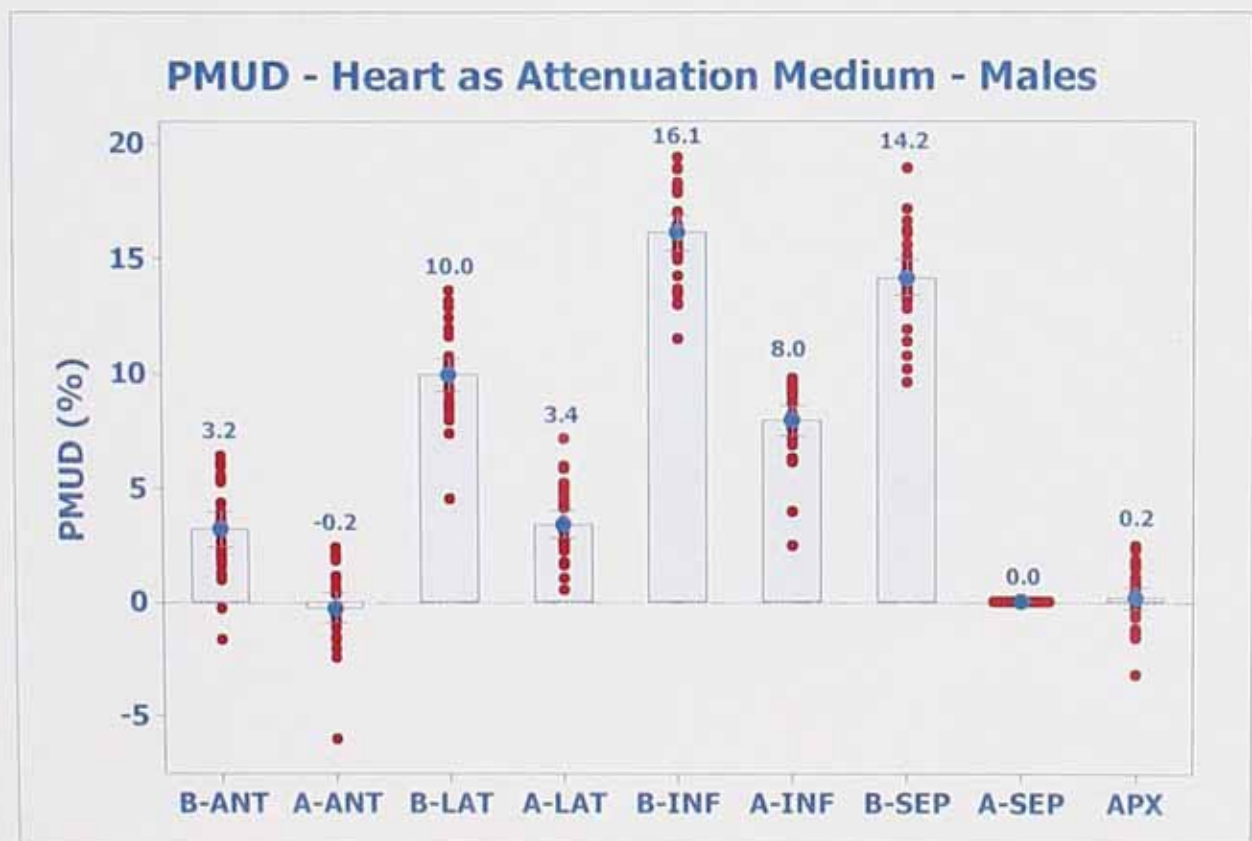


Figure 4-8: The means of the PMUD's (as displayed above each bar) as a result of the body (remainder and skeleton) together with their 95% confidence intervals for each of the 9 segments for both genders.

C. The Contribution of the Heart



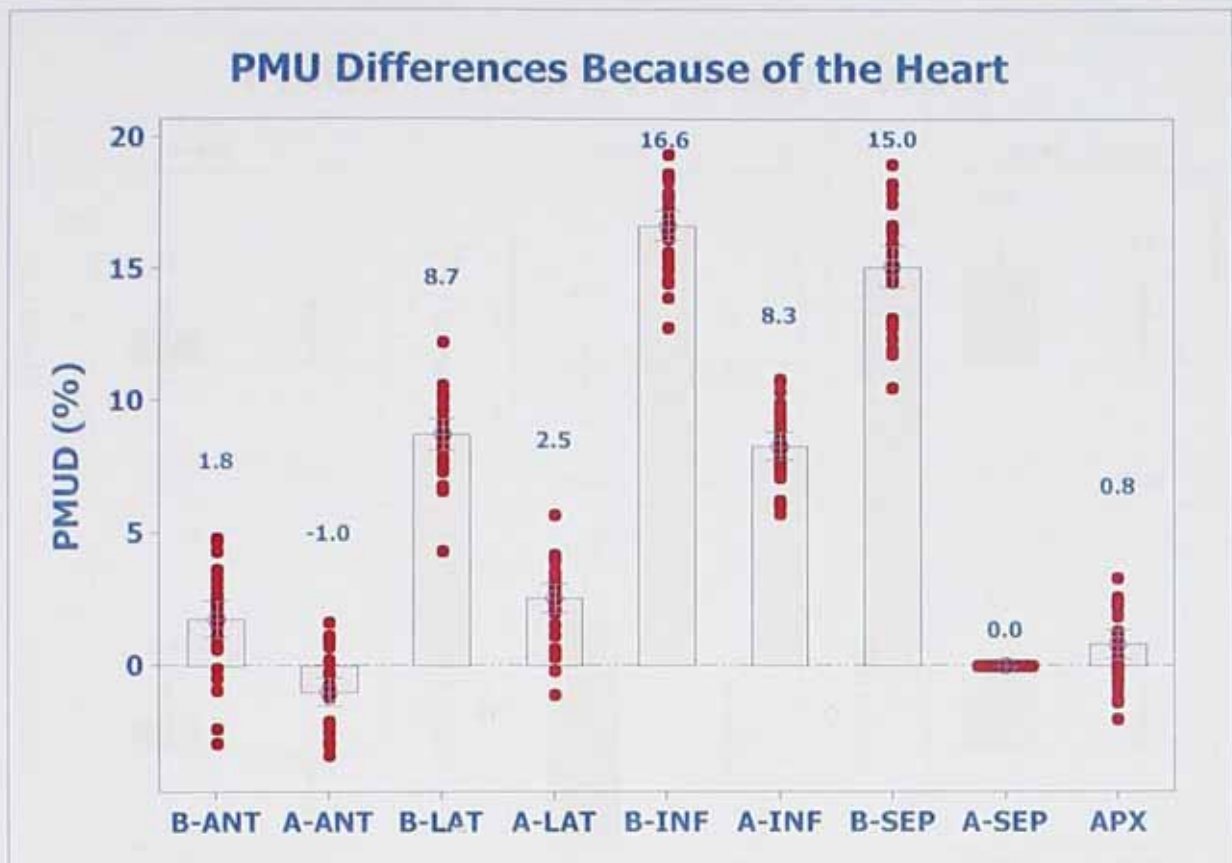
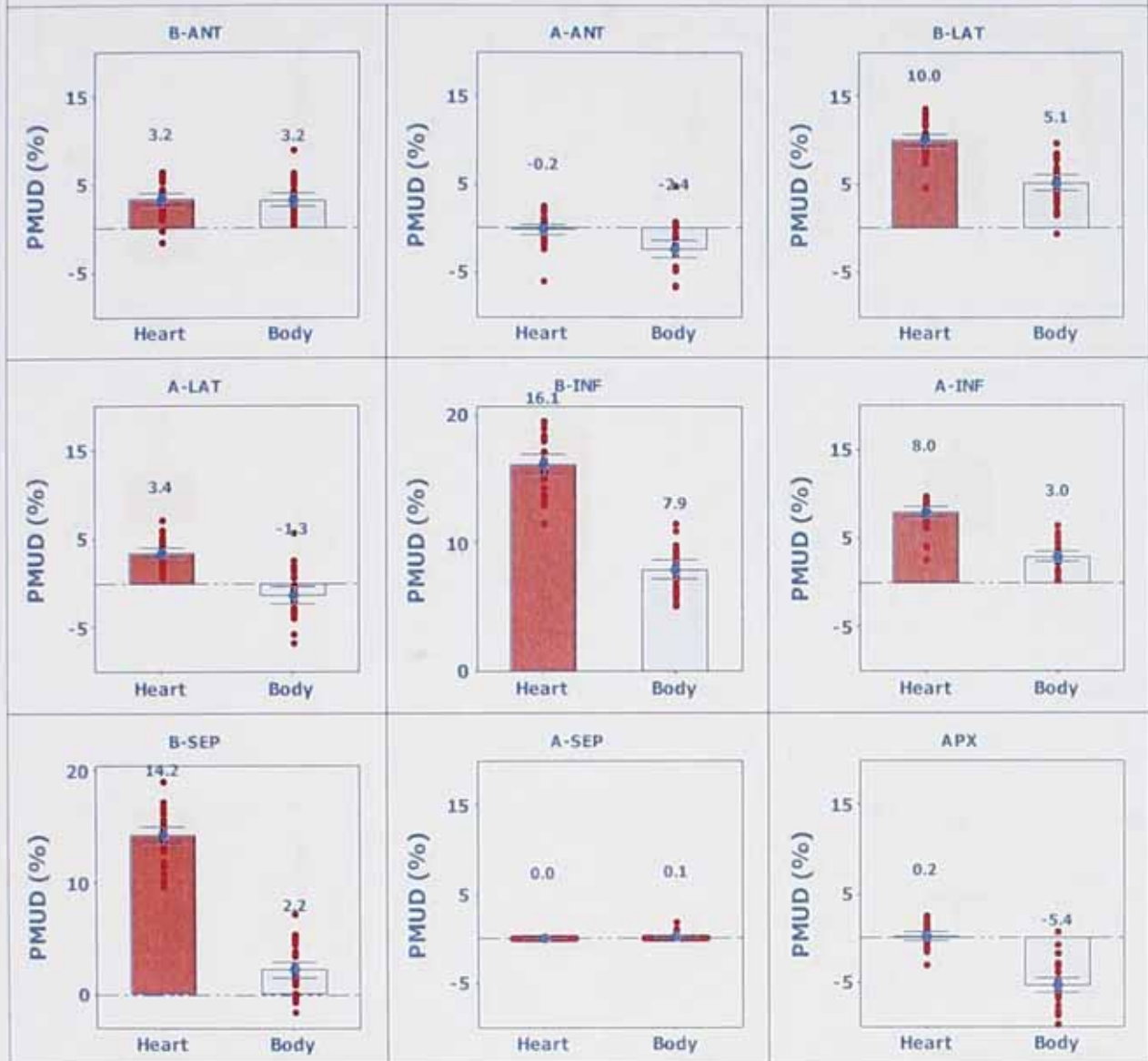


Figure 4-9: The means of the PMUDs (as displayed above each bar) as a result of the heart (myocardium, pericardium and bloodpool) together with their 95% confidence intervals for each of the 9 segments for both genders.

PMUD - Heart vs Body - Male



PMUD - Heart vs Body - Female

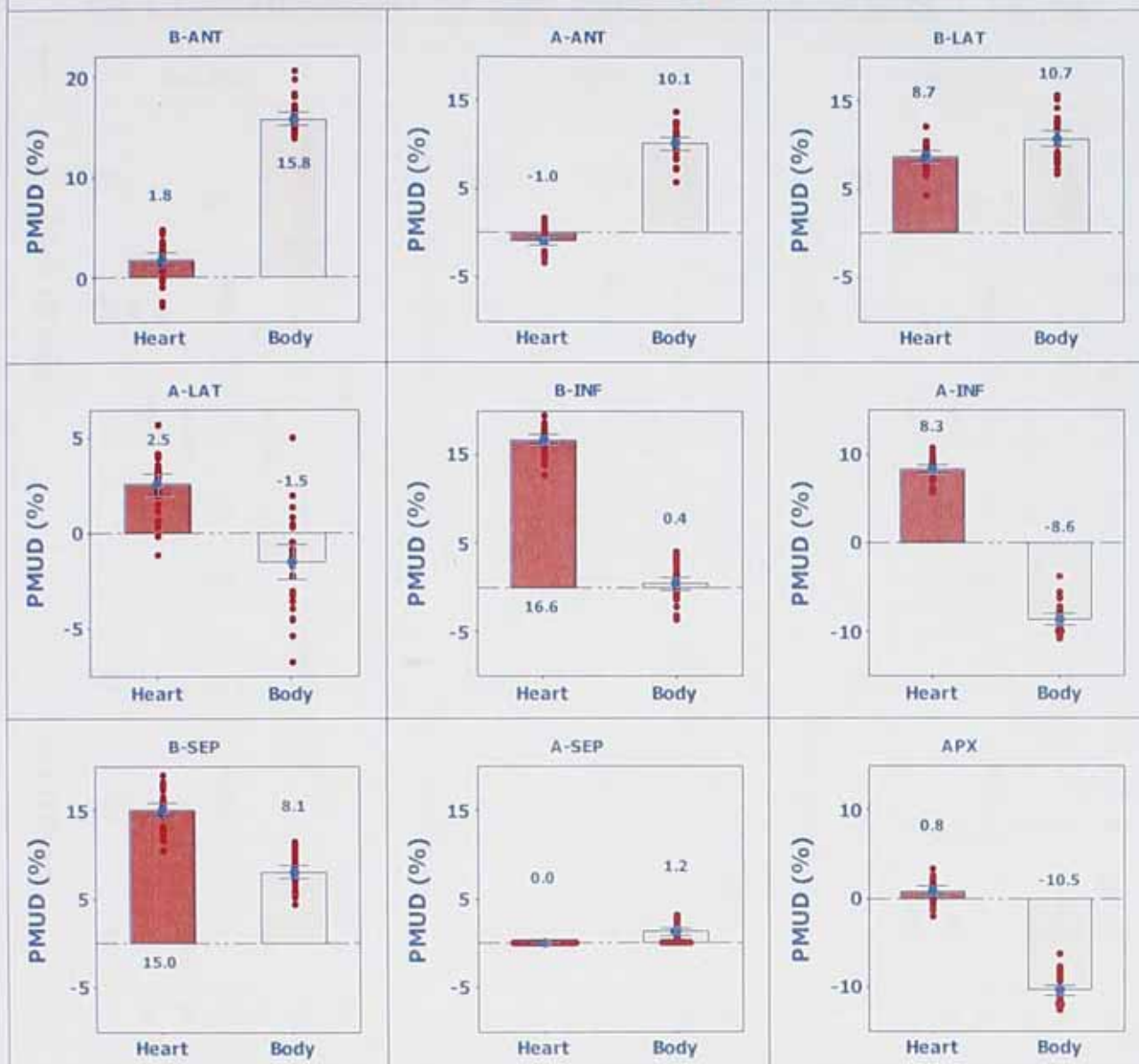


Figure 4-10: The means of the PMUDs (as displayed above each bar) comparing the heart (myocardium, pericardium and bloodpool) and the body (remainder and skeleton) together with their 95% confidence intervals for each of the 9 segments for both genders.

D. The Contributions of the Individual Parts as a Percentage

This section displays the contribution of all the individual parts as percentages in figure 4-11, first for the males, then for the female simulated patients in all 9 segments. This is helpful in illustrating which anatomical parts are the main contributors to the intensity losses experienced as well as the differences between the two genders.

% Contribution of the Anatomical Parts - Male

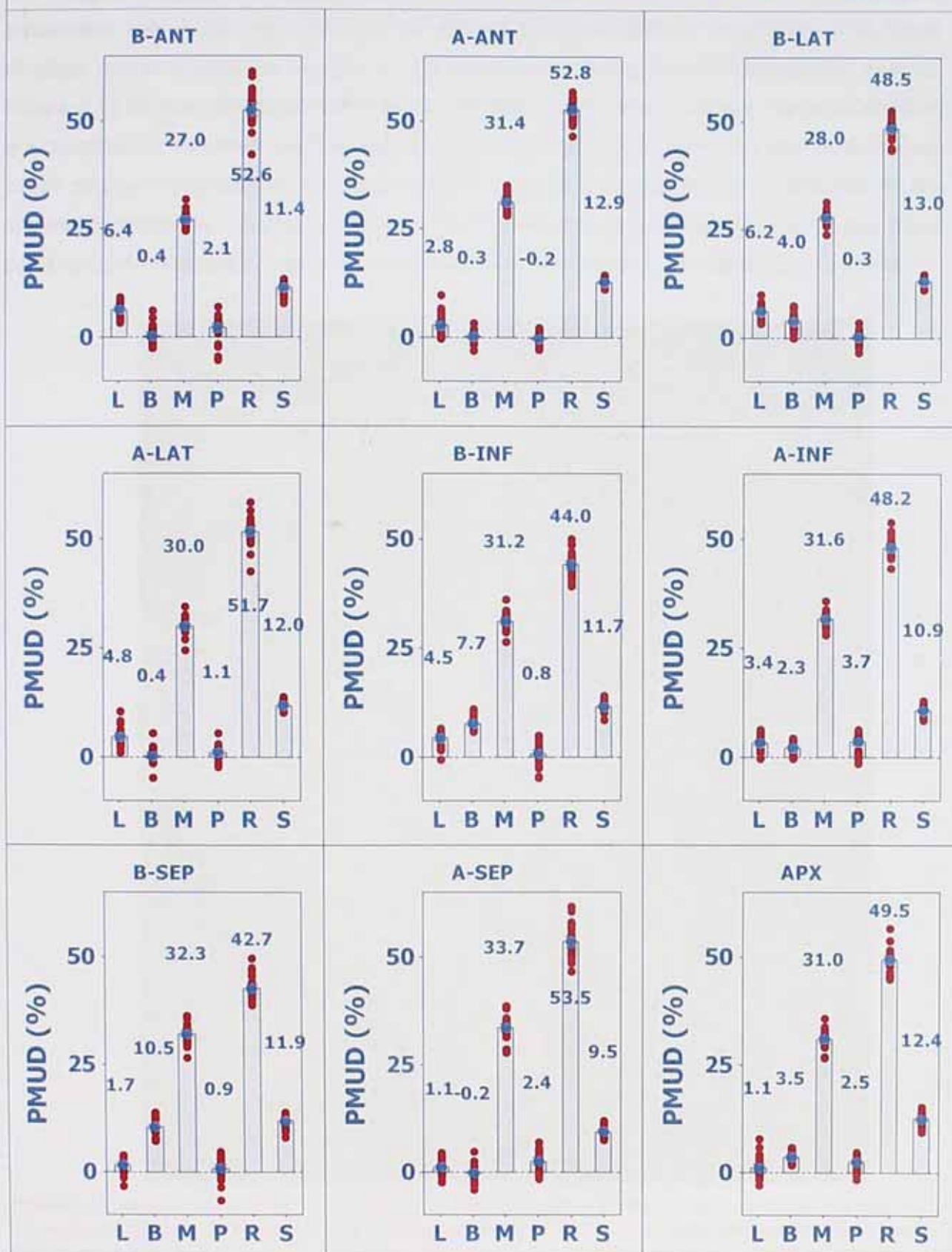


Figure 4-11: The percentage contribution to the intensity losses experienced in the final images as a result of the different anatomical parts for both genders (the y-axis represent the % contribution).

4.3.6 The Contribution of Scatter

The images in figure 4.12 display the result of the test of the hypothesis that scatter plays a substantial role in the non-uniformity of images during a SPECT acquisition. The figure displays the reconstructed images of the scattered, primary and non-attenuated images. Figure 4.13 displays the contribution to the intensity values when only the scattered photons are considered. This is for the nine segments as a percentage so that it is possible to deduce which segment experiences the most scatter. Table 4.8 compares the contribution of the scattered photons to the intensity value of the basal parts as compared to that of the apical parts so that a conclusion can be made that scatter contributes to the distortion observed.

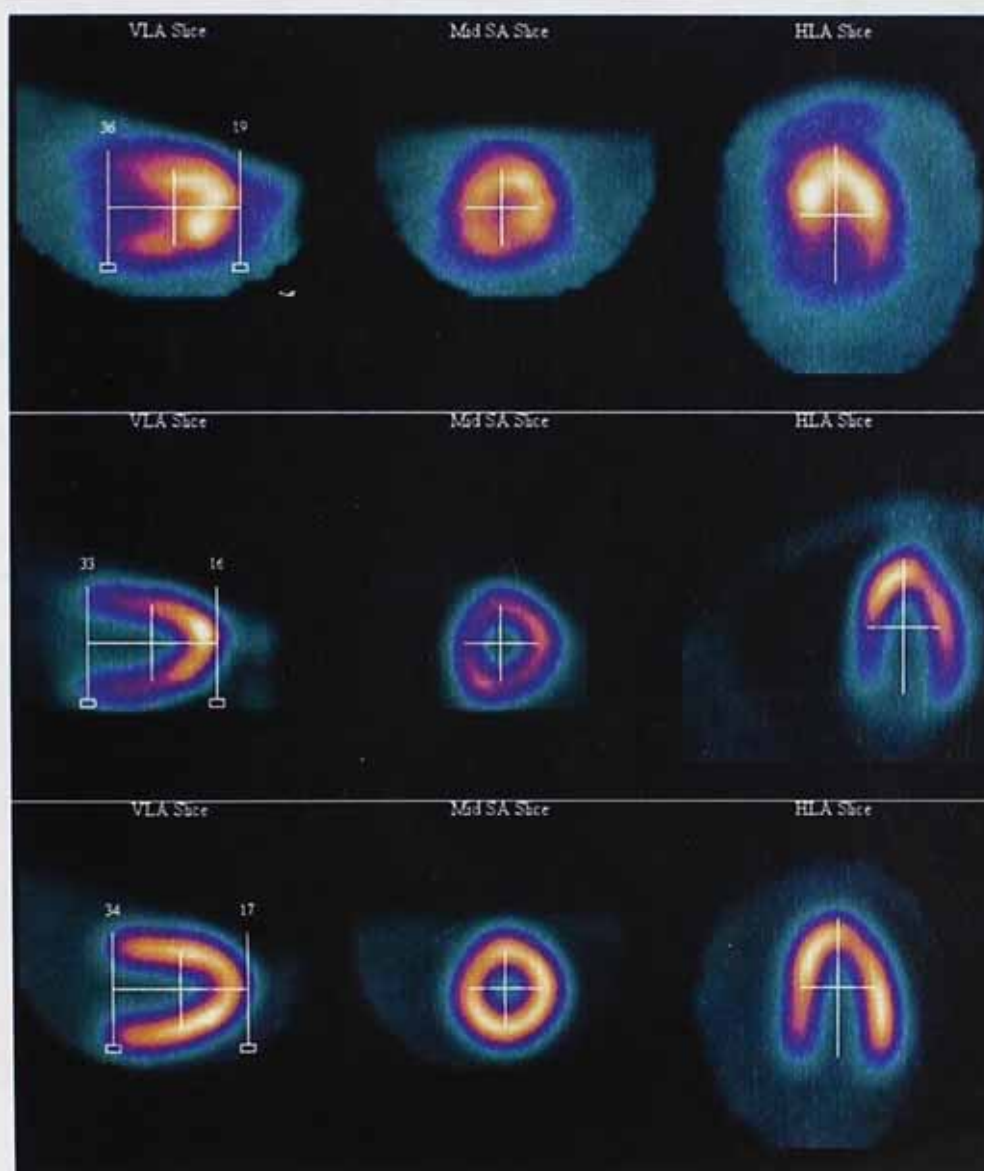


Figure 4-12: Illustrating the effect of scatter, reconstructed images of only the scatter component (top row), reconstructed images of only the primary photons (middle row) and the non-attenuated reconstructed images (bottom row). Note that each image set is normalised to the maximum in that specific image set and that the maximum in the scatter reconstructed images is significant lower than the maximum in the other two sets.

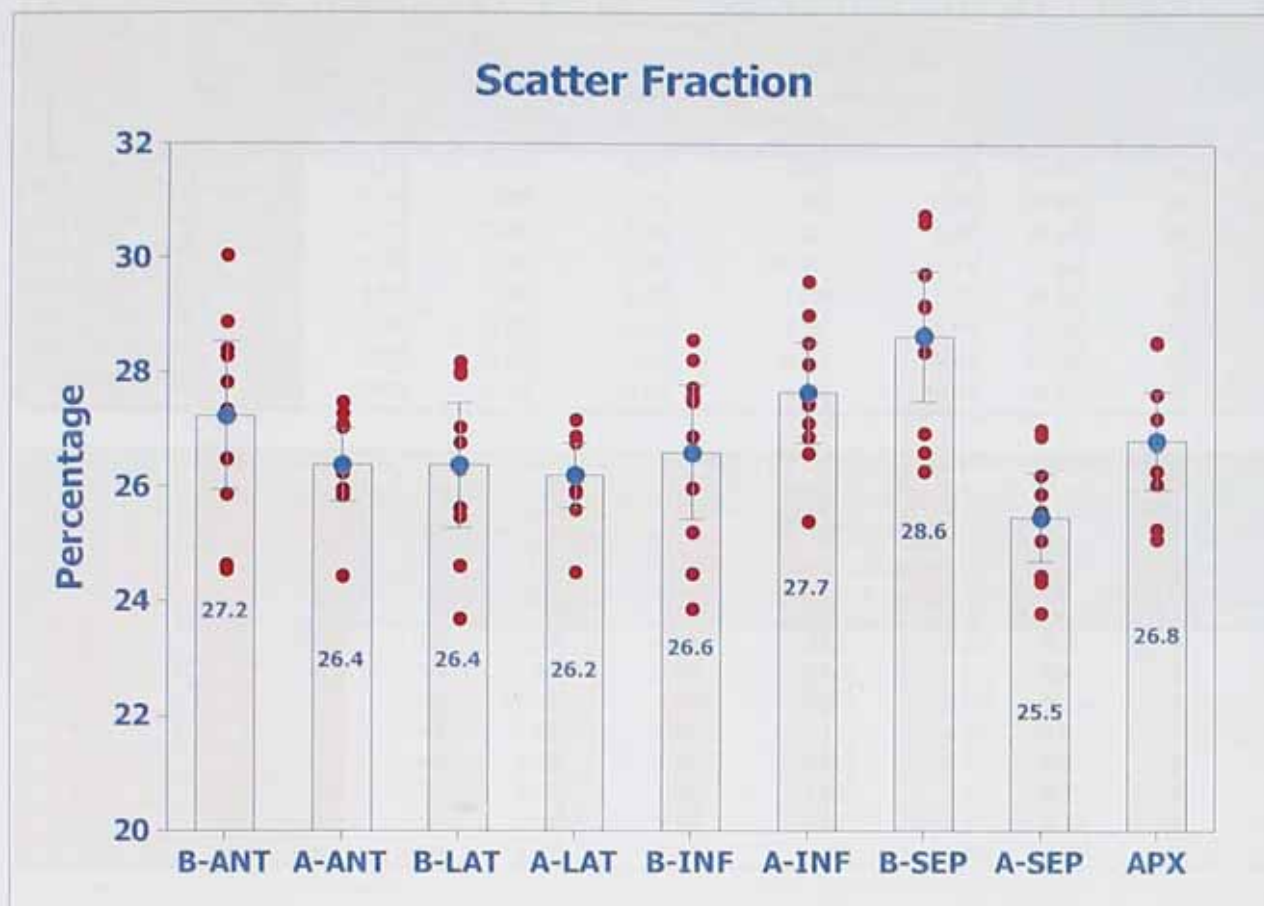


Figure 4-13: The scatter fraction (as a percentage) in the 9 segments as a result of scatter for the female simulated patients.

Table 4-8: Dependent sampled t-test to determine whether the mean of the percentage loss in apical parts are significant different from those in the basal parts for the scattered photons and primary photons as well as a comparison between the means of the scatter fractions of the basal and apical regions

Paired Samples Test – Testing Equality of Means Between Apical and Basal – Scattered

		Paired Differences					t	df	p (2-tailed)
		Mean	Std. Deviation	Std. Error Mean	95% Confidence Interval of the Difference				
					Lower	Upper			
Pair 1	A_ANT - B_ANT	2.30	0.57	0.18	1.89	2.71	12.77	9	.000
Pair 2	A_LAT - B_LAT	2.22	0.44	0.14	1.91	2.53	15.98	9	.000
Pair 3	A_INF - B_INF	2.13	0.42	0.13	1.83	2.43	15.97	9	.000
Pair 4	A_SEP - B_SEP	2.87	0.41	0.13	2.58	3.16	22.08	9	.000
Pair 5	APX - B_ANT	3.00	0.81	0.25	2.42	3.58	11.78	9	.000
Pair 6	APX - B_LAT	3.08	0.79	0.25	2.51	3.65	12.26	9	.000
Pair 7	APX - B_INF	3.29	0.81	0.25	2.71	3.87	12.91	9	.000
Pair 8	APX - B_SEP	3.19	0.78	0.25	2.63	3.75	12.87	9	.000

Paired Samples Test – Testing Equality of Means Between Apical and Basal – Primary

		Paired Differences				t	df	p (2-tailed)	
		Mean	Std. Deviation	Std. Error Mean	95% Confidence Interval of the Difference				
					Lower				Upper
Pair 1	A_ANT - B_ANT	7.19	0.74	0.23	6.66	7.72	30.85	9	.000
Pair 2	A_LAT - B_LAT	6.44	0.56	0.18	6.04	6.84	36.36	9	.000
Pair 3	A_INF - B_INF	4.67	0.49	0.15	4.32	5.02	30.14	9	.000
Pair 4	A_SEP - B_SEP	11.06	1.19	0.38	10.21	11.91	29.44	9	.000
Pair 5	APX - B_ANT	8.60	1.01	0.32	7.88	9.32	26.99	9	.000
Pair 6	APX - B_LAT	8.06	0.75	0.24	7.52	8.60	34.05	9	.000
Pair 7	APX - B_INF	8.80	0.83	0.26	8.20	9.40	33.37	9	.000
Pair 8	APX - B_SEP	10.17	1.13	0.36	9.36	10.98	28.47	9	.000

Paired Samples Test – Testing Equality of Means – Scatter Fraction

		Paired Differences				t	df	p (2-tailed)	
		Mean	Std. Deviation	Std. Error Mean	95% Confidence Interval of the Difference				
					Lower				Upper
Pair 1	A_ANT - B_ANT	-1.65	2.59	0.82	-3.50	0.20	-2.02	9	.074
Pair 2	A_LAT - B_LAT	-0.37	2.37	0.75	-2.06	1.32	-0.49	9	.633
Pair 3	A_INF - B_INF	1.95	2.65	0.84	0.06	3.84	2.33	9	.045
Pair 4	A_SEP - B_SEP	-5.99	1.60	0.51	-7.14	-4.84	-11.82	9	.000
Pair 5	APX - B_ANT	-0.84	4.28	1.35	-3.90	2.22	-0.62	9	.550
Pair 6	APX - B_LAT	0.79	3.30	1.04	-1.57	3.15	0.76	9	.469
Pair 7	APX - B_INF	0.38	3.62	1.14	-2.21	2.97	0.33	9	.747
Pair 8	APX - B_SEP	-3.52	3.87	1.22	-6.28	-0.76	-2.88	9	.018

4.3.7 Fractional intensity Loss in the Final Ventricular Images

In order to investigate the loss of intensity values in the final images the Fractional Index (FI) was introduced in 4.2.2 and 4.2.8. Figure 4.14 illustrates the loss of intensity values for the whole thorax as attenuation medium by displaying the FI for the 9 segments, first for the male simulated patients, then for the female simulated patients. The statistical results are displayed in table 4-9 so that a conclusion can be made whether there are any statistically significant differences.

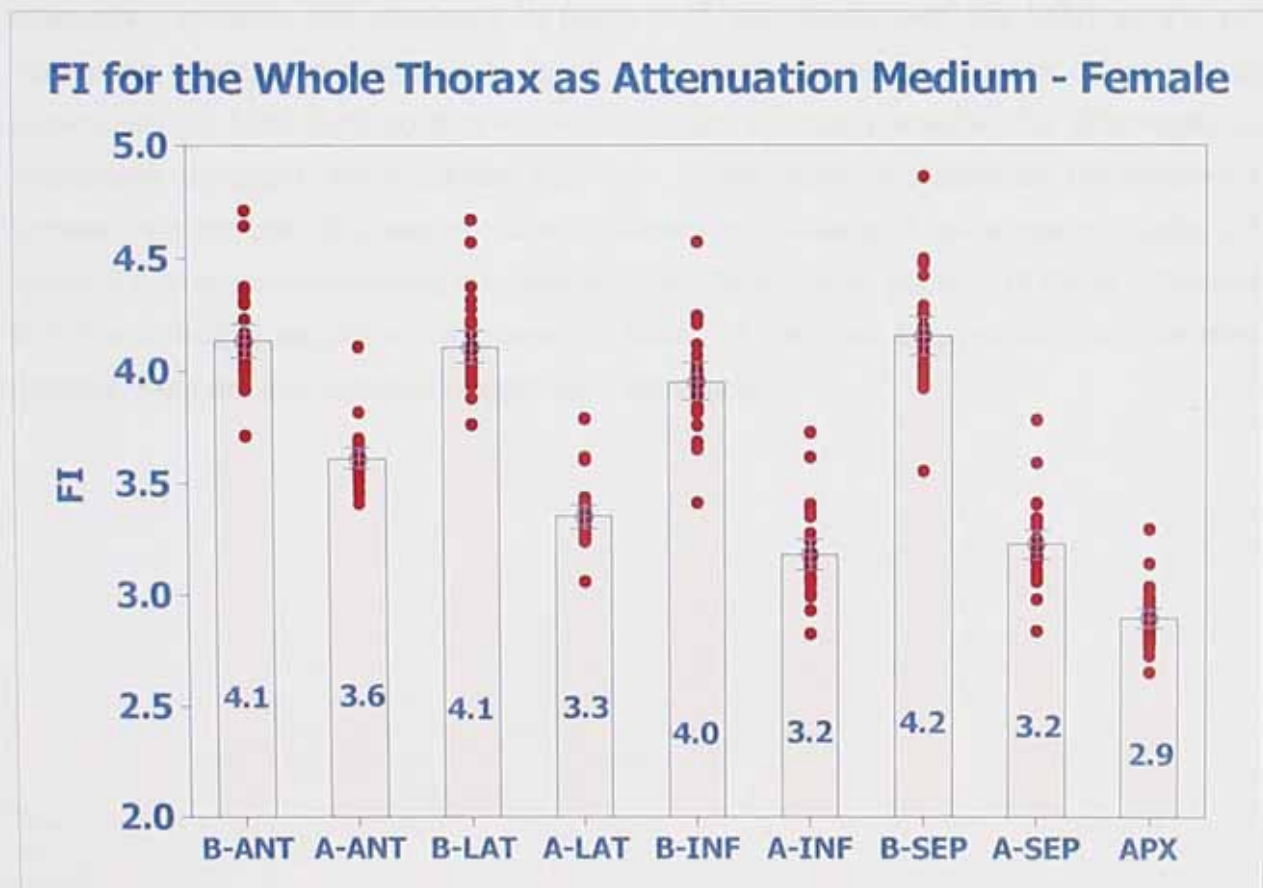
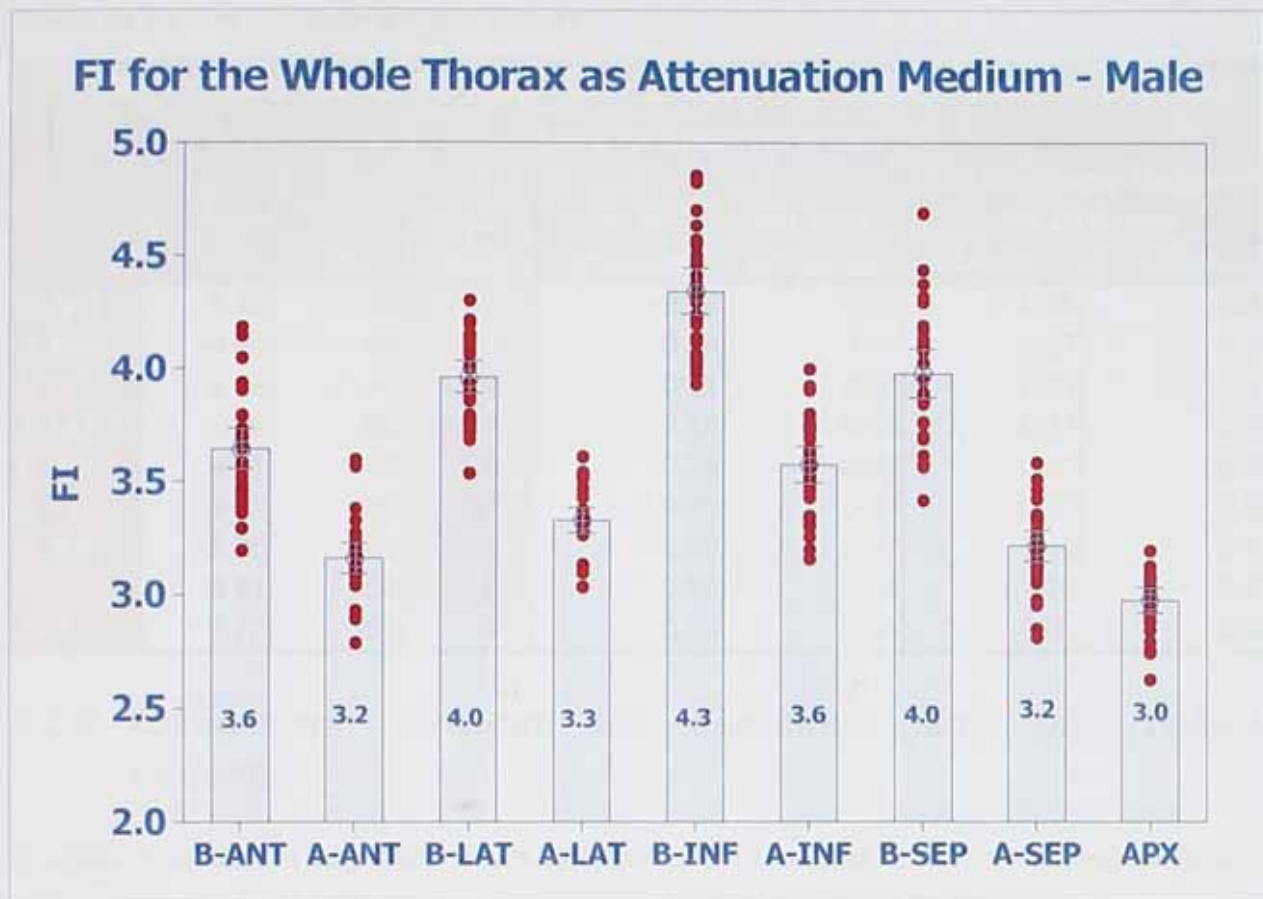


Figure 4-14: Fractional Index (FI) of the "Whole Thorax" as attenuation medium for the 9 segments.

Table 4-9: Results of the 2-tailed independent t-test to determine the equality of the means of the fraction indexes for the male and female simulated patients

Independent Samples Test - Comparing Fractions - Male vs Female								
	t-test for Equality of Means						95% Confidence Interval of the Difference	
	t	df	p (2-tailed)	Mean Difference	Std. Error Difference	95% Confidence Interval of the Difference		
						Lower	Upper	
B_ANT	-8.29	58	.000	-0.48	0.06	-0.60	-0.36	
A_ANT	-4.46	58	.000	-0.19	0.04	-0.27	-0.10	
B_LAT	2.16	58	.035	0.11	0.05	0.01	0.21	
A_LAT	4.95	58	.000	0.18	0.04	0.11	0.25	
B_INF	4.71	58	.000	0.30	0.06	0.17	0.42	
A_INF	9.13	58	.000	0.48	0.05	0.37	0.58	
B_SEP	-5.35	58	.000	-0.36	0.07	-0.49	-0.23	
A_SEP	8.81	58	.000	0.38	0.04	0.29	0.47	
APX	1.72	57	.091	0.06	0.04	-0.01	0.14	

4.3.8 Comparison Between the Simulated Male and Female Patients

In order to establish any differences between the male and female simulated patients a comparison was made of the differences in the PMUD, first when the whole thorax was used as attenuation medium and displayed in figure 4.15, then with only the body (remainder) as attenuation medium and displayed in figure 4.16 and finally with the heart as the only attenuation medium as displayed in figure 4.17. The t-test values of these differences are summarised in table 4.10 so that a conclusion can be made whether the differences are statistically important. An important emphasis in this study is placed on the differences between the amount of intensity losses between the basal and apical parts. Figure 4.18 displays a comparison between the male and female simulated patients of these differences and the statistical results are displayed in table 4.11 so that a conclusion can be made whether there are any statistically significant differences.

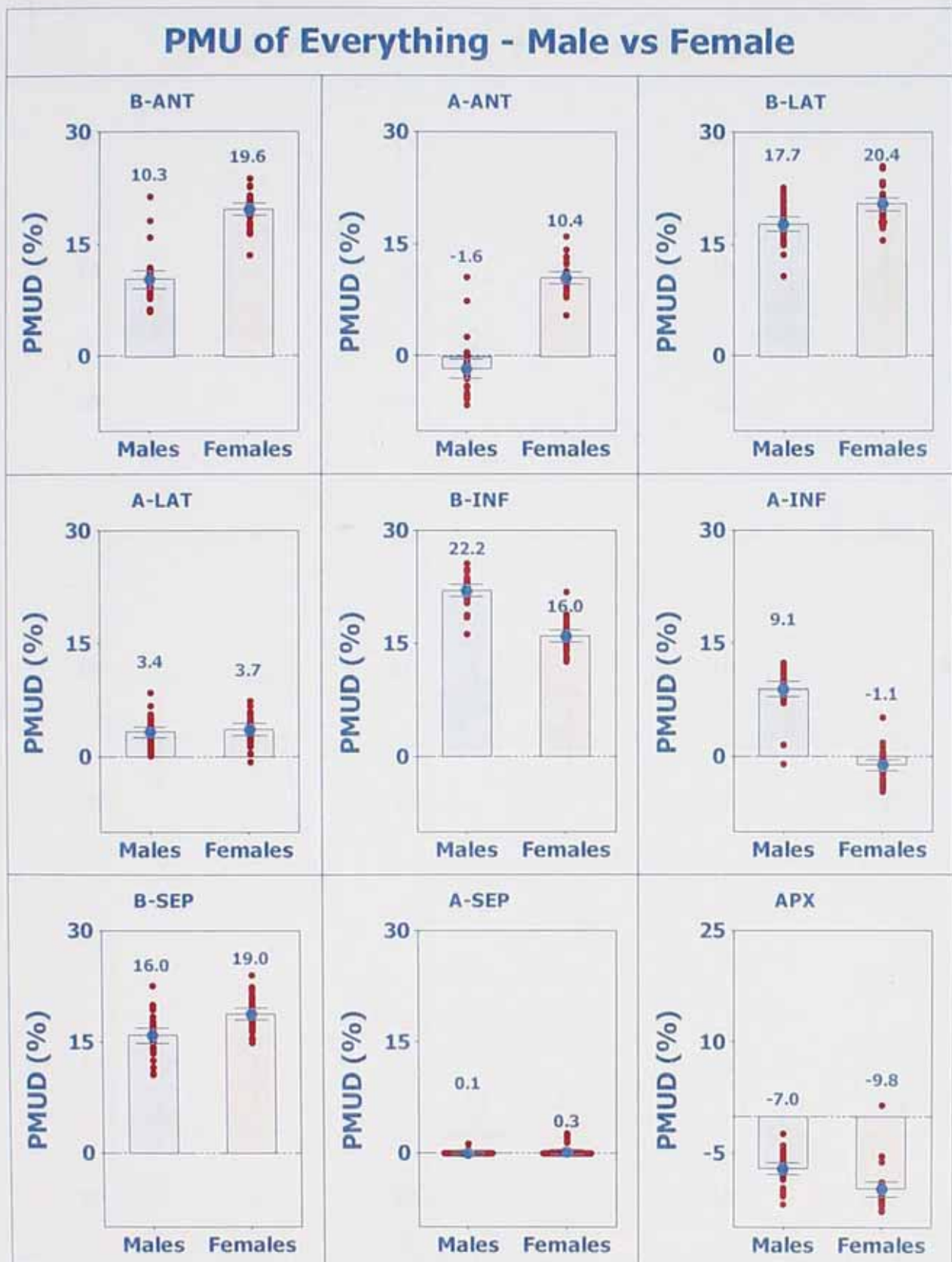


Figure 4-15: The means of the PMUD's of "Everything" for the Male and Female patient selection, presenting the differences between these two population groups (the y-axis represents the PMUD's).

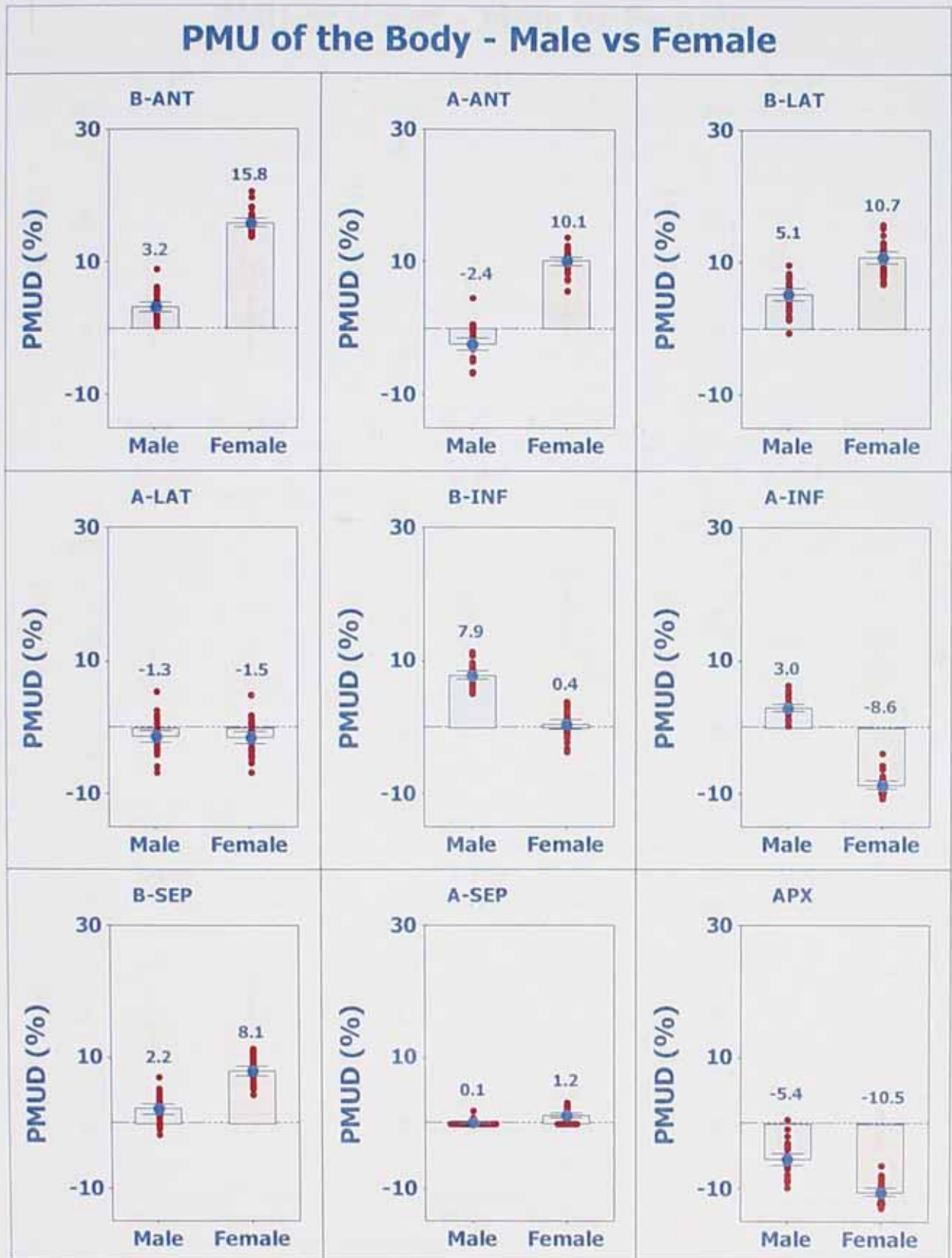


Figure 4-16: The means of the PMUD's of the Body for the Male and Female patient selection, presenting the differences between these two population groups (the y-axis represents the PMUD's).

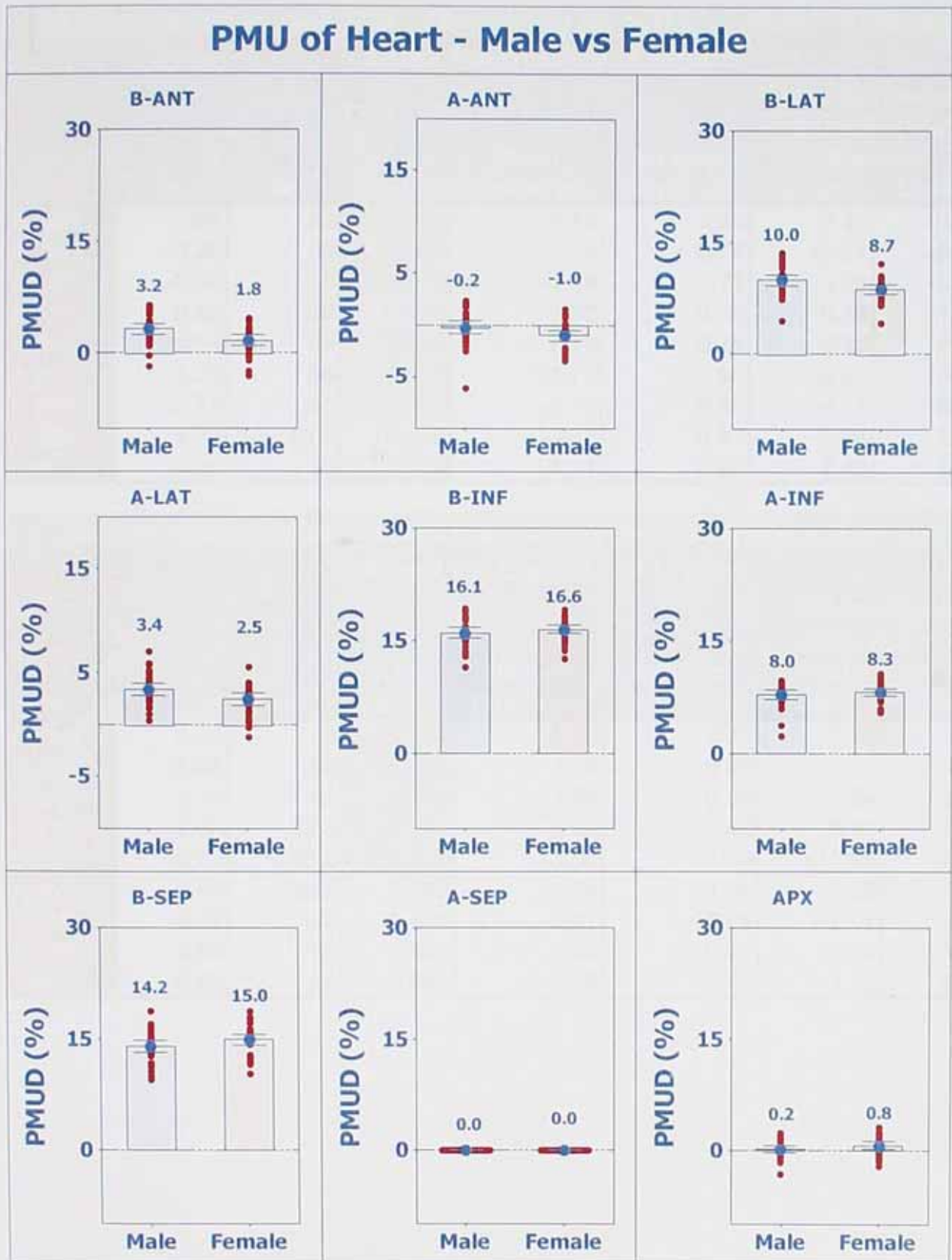


Figure 4-16: The means of the PMUD's of the Heart for the Male and Female patient selection, presenting the differences between these two population groups (the y-axis represents the PMUD's).

Table 4-10: Results of the 2-tailed independent t-test to determine the equality of the means of the PMUD's as a result of the Whole Thorax, Heart and Body between the two genders. The values in red indicate that there is a significant difference between the two genders for that segment

Independent Samples Test - Comparing Everything - Male vs Female							
	t-test for Equality of Means						
	t	df	p (2-tailed)	Mean Difference	Std. Error Difference	95% Confidence Interval of the Difference	
						Lower	Upper
B_ANT	10.64	58	0.000	9.12	0.86	7.41	10.84
A_ANT	-14.29	58	0.000	-11.15	0.78	-12.71	-9.59
B_LAT	-2.64	58	0.011	-1.88	0.71	-3.31	-0.45
A_LAT	0.80	58	0.428	0.56	0.70	-0.84	1.95
B_INF	9.84	58	0.000	7.79	0.79	6.20	9.38
A_INF	13.09	58	0.000	11.73	0.90	9.94	13.53
B_SEP	-2.73	58	0.008	-2.42	0.89	-4.19	-0.65
A_SEP	1.20	49.5	0.235	0.81	0.67	-0.54	2.16
APX	4.95	58	0.000	4.11	0.83	2.45	5.78

Independent Samples Test - Comparing Hearts - Male vs Female							
	t-test for Equality of Means						
	t	df	p (2-tailed)	Mean Difference	Std. Error Difference	95% Confidence Interval of the Difference	
						Lower	Upper
B_ANT	2.80	58	0.007	1.96	0.70	0.56	3.36
A_ANT	2.53	58	0.014	1.14	0.45	0.24	2.04
B_LAT	2.98	58	0.004	1.65	0.55	0.54	2.76
A_LAT	2.04	33.4	0.049	2.90	1.42	0.01	5.78
B_INF	-5.00	33.2	0.000	-8.50	1.70	-11.96	-5.04
A_INF	-0.89	32.2	0.380	-1.24	1.39	-4.08	1.60
B_SEP	-0.77	58	0.445	-0.57	0.75	-2.07	0.92
A_SEP	0.84	58	0.407	0.39	0.46	-0.54	1.31
APX	-0.62	58	0.540	-0.29	0.47	-1.23	0.65

Independent Samples Test - Comparing the Bodies - Male vs Female

	t-test for Equality of Means						
	t	df	p (2-tailed)	Mean Difference	Std. Error Difference	95% Confidence Interval of the Difference	
						Lower	Upper
B_ANT	-27.04	57	.000	-12.65	0.47	-13.58	-11.71
A_ANT	-22.10	53	.000	-12.54	0.57	-13.68	-11.40
B_LAT	-9.02	58	.000	-5.57	0.62	-6.80	-4.33
A_LAT	0.35	58	.725	0.22	0.63	-1.04	1.49
B_INF	15.08	58	.000	7.51	0.50	6.51	8.50
A_INF	30.30	57	.000	11.61	0.38	10.84	12.37
B_SEP	-11.62	58	.000	-5.89	0.51	-6.90	-4.88
A_SEP	-5.44	58	.000	-1.10	0.20	-1.50	-0.70
APX	9.77	53	.000	5.04	0.52	4.01	6.08

PMU Differences Between Basal and Apical - Male vs Female

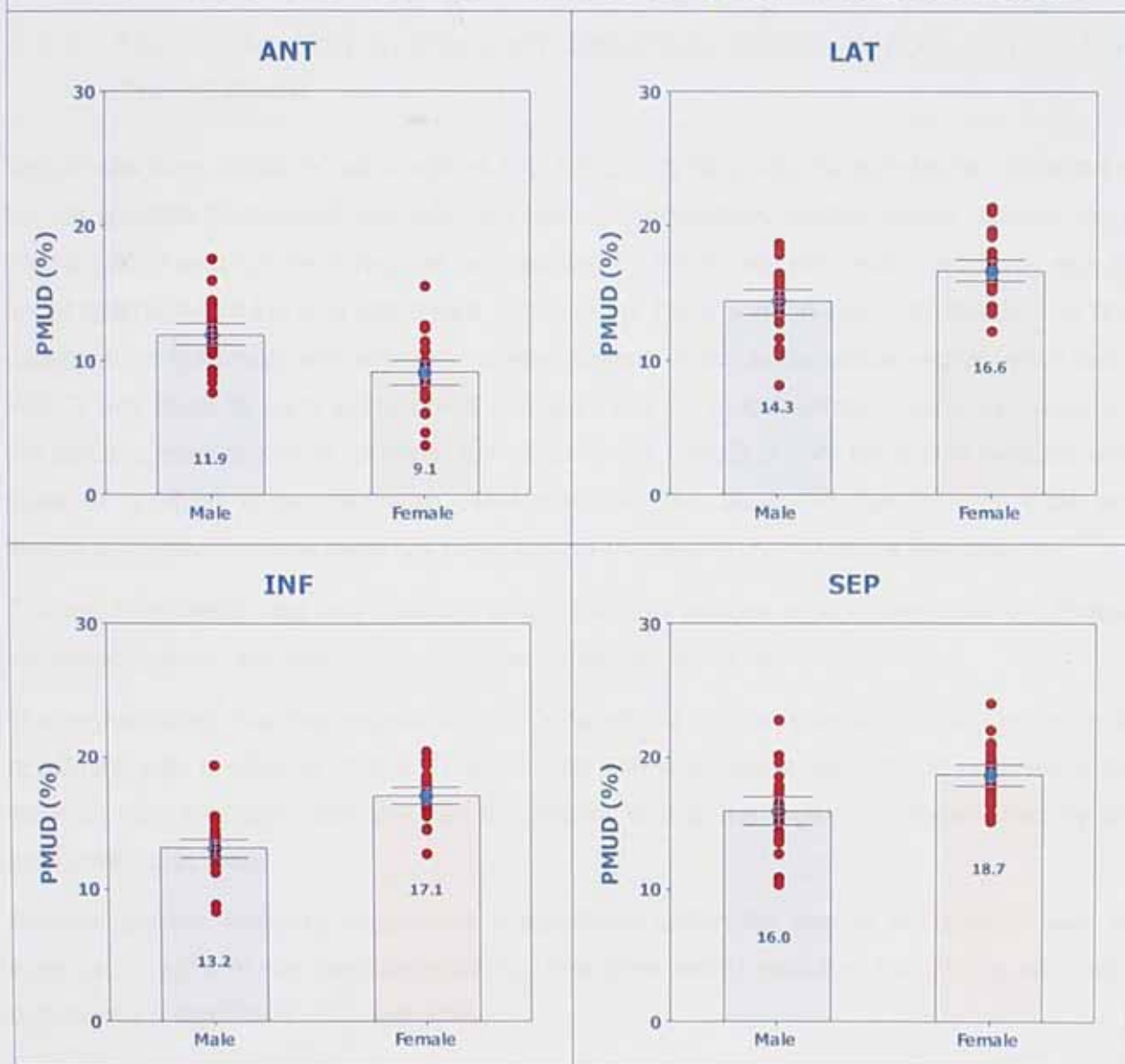


Figure 4-18: A comparison of the PMUD's when comparing the basal and apical regions in both male and female simulated patients for the anterior, lateral, inferior and septal walls (the y-axis represents the PMUD's).

Table 4-9: Results of the 2-tailed independent t-test to determine the equality of the means of the PMUD's when comparing the basal and apical regions of the anterior, lateral, inferior and septal walls for the male and female simulated patients

Independent Samples Test - Comparing Regions - Male vs Female							
	t-test for Equality of Means						
	t	df	p (2-tailed)	Mean Difference	Std. Error Difference	95% Confidence Interval of the Difference	
						Lower	Upper
ANT	3.55	58	0.001	2.02	0.57	0.88	3.16
LAT	-4.19	58	0.000	-2.43	0.58	-3.60	-1.27
INF	-6.42	58	0.000	-4.46	0.69	-5.85	-3.07
SEP	-4.75	58	0.000	-3.24	0.68	-4.61	-1.88

4.4 Discussion and Conclusion

4.4.1 The Distortion in the Left Ventricle When Not Applying Any Corrections

The results from figure 4.5 and table 4.1 to 4.3 clearly illustrate the substantial distortion of the left ventricle because of permutations such as attenuation, scatter, partial volume, etc. It shows that in most of the 9 regions represented by the 9 segment polar map there was an under estimation of the true intensities, but in some there was an over estimation. The only exception for both male and female simulated patients is the apical-septal region which has a PMUD very close to zero. Except for this region and the apical-anterior region in males and the apical-inferior region in females, the effect of the PMUD is very large with r-values very close to 1, which is the maximum value possible. This illustrates that for both male and female simulated patients there are distortions of the uniformity in 7 of the 9 segments.

The null hypothesis was only true in the apical-septal regions of both the male and female simulated patients and was rejected for the remainder of the regions.

The region which has the biggest loss of uniformity is the basal-inferior region in the male population with a value of 22.2%. This is in line with what was expected and reported in the literature and therefore confirms that the inferior wall is the region mostly affected by the permutations in men.

Female patients seem to experience a significant uniformity loss in the anterior wall as expected (19.6% in the basal-anterior) but the other walls, including the inferior wall, also experience a significant uniformity loss.

There is a substantial variation between patients, with some overlap with "normal". Therefore a correction method which just applied a mean value will result in (different) false positives

and negatives in some patients, and therefore only an individualised correction will cure all artefacts.

4.4.2 Comparison Between the Basal and Apical Regions of the Non-Uniformities Experienced

In this case the null hypothesis was rejected for all the segments, for both genders. This means that the non-uniformities experienced in the polar maps are substantially different between the apical and basal regions and the effect size of these differences was also very substantial (all close to 1, some even 1). It can be safely concluded from this simulation study that for both male and female patients, the non-uniformity found between the basal and apical regions is very substantial.

4.4.3 The Relative Non-Uniformities in the Basal and Apical Parts

From figure 4.7 and table 4.6 it can be seen that in male patients the apical and apical-anterior regions are over estimated. For the female patients the over estimation was found in the apical and apical-inferior regions.

Large under estimations, which were statistically significant, were experienced in the basal-anterior, basal-lateral, basal-inferior, apical-inferior and basal-septal regions for the male patients. For the female patients the severe under estimations were detected in the basal-anterior, apical-anterior, basal-lateral, basal-inferior and basal-septal regions.

It can be seen that all the basal segments for both genders experienced a severe under estimation and also one apical region for each gender. Both genders experience an over estimation in the apical region but the second segment experiencing this is different.

4.4.4 The Contribution to This Distortion by Each Anatomical Part

By analysing the PMUDs values as a result of the heart as attenuation medium and comparing them to the values obtained for the body from figures 4.8 and 4.9 it can be seen that the heart contributed more to the loss in the basal-inferior segment than the body for the male population. The contribution to the uniformity loss in the basal-inferior wall (also the region which experienced the most substantial uniformity loss) is $1/3$ for the body and $2/3$ s for the heart making the heart responsible for the most substantial uniformity loss in males. The same is true for the basal-lateral and basal-septal regions.

In females it seems that uniformity loss in the basal-inferior wall is almost entirely due to the heart. From figure 4.10 it is clear that the heart is the main contributor to the loss in uniformity for both male and female patients in all the regions except for the anterior wall in female patients.

4.4.5 The Effect of Scatter on the Intensity Distribution in the Left Ventricle

The effect of scatter in the female population can be seen from figure 4.13. The scatter contribution to the final images is between 24.5 and 28.6%. It can also be seen from table 4.8 that for all the segments the scatter contribution is more substantial for the apical parts of the regions than the basal parts. This was also true for the primary photons. It can therefore be concluded that scatter does contribute to the over estimation in the apical regions but so does the primary photons. The conclusion from this is that although scatter contributes to the over estimation, it is not the only cause and the over estimation is a result of other factors as well.

4.4.6 Fractional Intensity Losses in the Final Ventricular Images

The fractional indexes for both gender indicates a substantial loss of counts as a result of the attenuation and scatter. The average fraction for the male population was 3.5 and for the female population it was also 3.4. This means that for both male and female the original intensities were 3 and a ½ times the intensities in the final images.

This substantial loss in intensities is a result of these permutations and can be used as a reference to review the performance of any clinical correction method under investigation.

4.4.7 Investigating the Differences in Intensity Losses Experienced Between Males and Females

The simulations predicted that male patients will experience the most substantial intensity losses in the B-INF region and females in the B-ANT regions. It also suggests that females will experience substantial intensity losses in the other basal regions, including the B-INF segment. Both genders will experience an intensity gain in the apical regions. It also suggests that both genders experience a substantial loss of intensity in the B-INF segment as a result of the heart. Both genders also experience a substantial difference in the uniformity of the basal regions as compared to the apical regions. The fraction indexes suggest that both experience substantial intensity losses and the MFI values are actually the same.

4.4.8 Summary

This study illustrates that the inferior wall is the part mostly affected by scatter and attenuation with a PMUD of 22.2% in males and 16% in females. This study also demonstrates that inferior wall attenuation is just as prominent in females as in males. The main contributor to Inferior uniformity losses is the heart for both genders and it is a factor

that cannot be predicted by the gender of the patient only and stresses the need for an accurate attenuation correction technique. Attenuation leads to an under estimation in the basal areas which could compromise volume calculations. Un-corrected images also lead to an over estimation of the apical regions which could mask patients with apical thinning. Although there are still debates about the clinical significance of apical thinning, the general consensus is that it has no clinical significance and therefore the clinical impact of the apical over estimation should be negligible. The reasons for this over estimation are still unclear and more work needs to be done to determine the reason for it. This study also confirms the substantial loss of intensities as a result of the mentioned problems which makes absolute quantification very difficult when not applying the appropriate corrections.

In this study effects such as apical over estimation, shortening of the basal parts of the left ventricle, substantial inferior wall intensity losses in females and the fact that up to 90% of the original intensities in the LV are lost in uncorrected images were highlighted. The fact that self-absorption in the heart is a very important factor leading to substantial intensity losses in the inferior wall have also been established in this study and this is the first time that this has been determined to the best knowledge of the author. Some of the findings in this chapter can be found in some references but emphasising them again here and combining them in one systematic study should make a substantial contribution to the field. Further the work provides a framework to test any correction. Another important contribution of this study is that it quantifies these effects, which has not always been the case in previous reports of the effects which have been studied. In particular, this study illustrates that the use of gender to decide whether intensity loss defects are real defects or not is not a reliable method, because of overlap of the range of results for male and female. This study also confirmed that scattered photons contribute to about 30% of the intensities in the energy window and confirms the need for scatter corrections.

The position and orientation of the heart within the thorax can vary substantially from person to person and this can make the intensity loss artefacts discussed in this chapter even more unpredictable. The influence of these variations on the intensity loss artefacts will be the subject of the next chapter.

Chapter 5 - Attenuation

Variations as a Result of

Different Orientations and

Positions of the Myocardium in

the Thorax

5.1 Introduction

In the previous chapter many little known effects as a result of the problems in image reconstruction in MPI were highlighted and quantified. The quantified values were established for the fixed configuration of the heart within the thorax in the Visible Human. The study recorded in this chapter attempts to extend these results by investigating the effect that different positions and orientation of the heart within the thorax have on the amount of intensity losses experienced in the LV. There are substantial variations in the orientations and positions of the heart within the thorax in the general population.

The position and orientation of the myocardium within the thorax are defined by three rotational parameters and three translation parameters, i.e. xy-rotation (ψ)(horizontal), zy-rotation (β), xz-rotation (ϕ)(vertical), x-translation, y-translation and z-translation relative to the origin of a Cartesian coordinate system. Altering any of these parameters could potentially influence the extent and position of the attenuation of emitted photons from the radionuclide in the left ventricle. The exact values of these parameters, which define the orientation and position of the myocardium in the thorax, vary substantially from person to person. It is postulated that this can alter the extent and position of potential attenuation artefacts in the left ventricle. It has also been shown that females have a smaller rib cage size and a shorter diaphragm than males having the same height¹⁹³. This results in a higher diaphragm dome in males. This position of the diaphragm dome results in a more horizontal orientation of the heart in males as compared to the orientation in females.

In the current routine use of MPI studies, probably the most important parameter of these six parameters describing the orientation of the myocardium within the thorax, is the xz- rotation (ϕ), as the image has to be rotated in this direction to ensure the correct alignment for the accurate presentation of the patient's images in clinical examinations. Incorrect alignment results in lower reported sensitivity and specificity for the detection of perfusion defects¹⁹⁴. There can be substantial differences between patients; it has been reported¹⁹⁵ that a difference up to 57° between the minimum and maximum determined angles in a patient population of 167 patients. Both these observations indicate that this is a very important parameter to study.

5.2 Methods

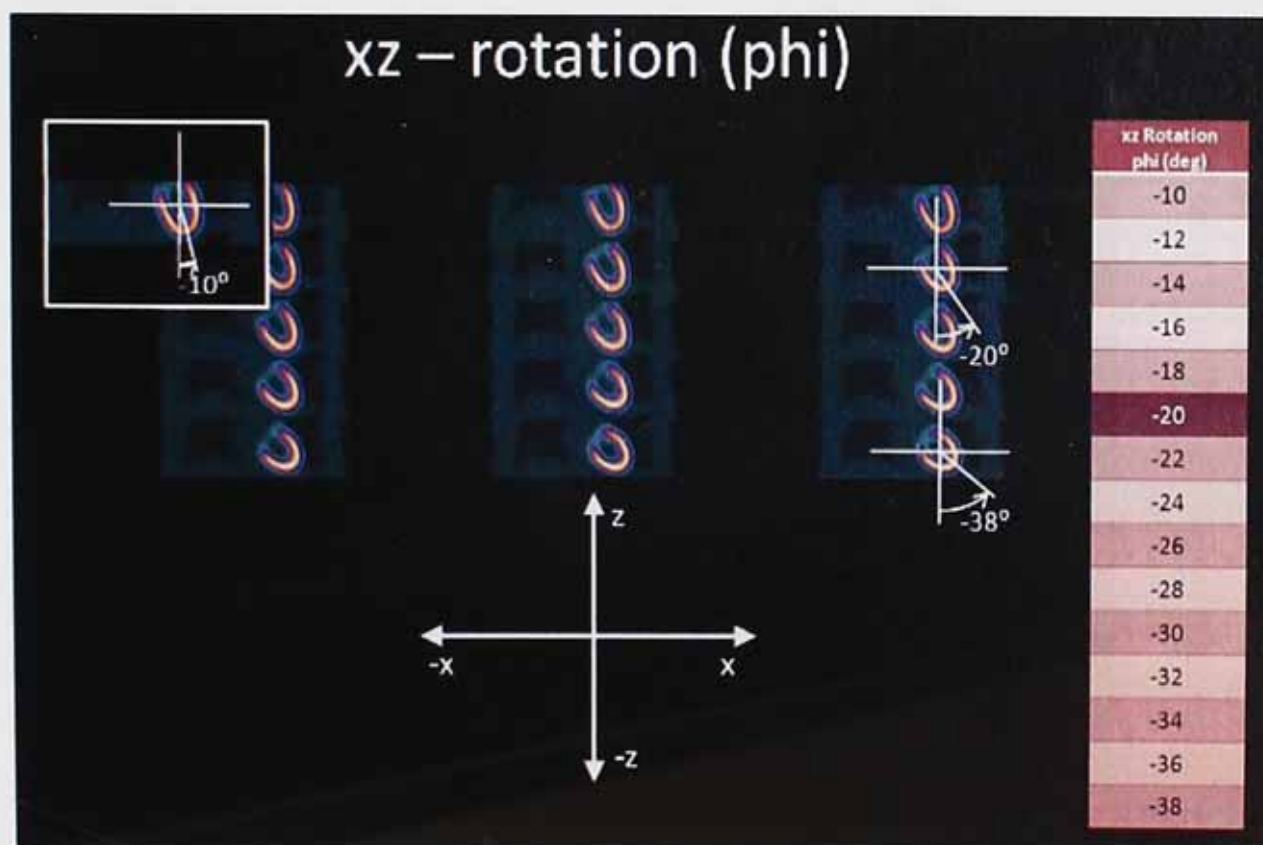
To investigate the effect of the different potential orientations (rotations) and positions of the heart within the thorax, six variation studies were performed. These included variations in the three different rotation parameters and variations in the three positional parameters. In each study, only one set of parameters was varied (by dividing it into 15 different values or variations, i.e. dividing the xz-orientation (ϕ) into 15 different angles) while the other five were kept constant, i.e. varying only the xz-orientation (ϕ) while keeping the xy- orientation (ψ), zy-orientation (β), x-position, y- position and z- position constant. The range in this study for each parameter is chosen to cover the normal patient range^{195, 145}. The reference values are the ones based on the Visible Human^{196,197} and are the dark cells in table 5.1

These potential variations were investigated by using 30 male patients who were selected as described in the previous chapter (section 4.8), and span the variation across the normal male patient range. For each of these male 'patients' the spatial parameters were divided in 15 subsets as displayed in table 5.1 and illustrated in figure 5.1 (a)-(f).

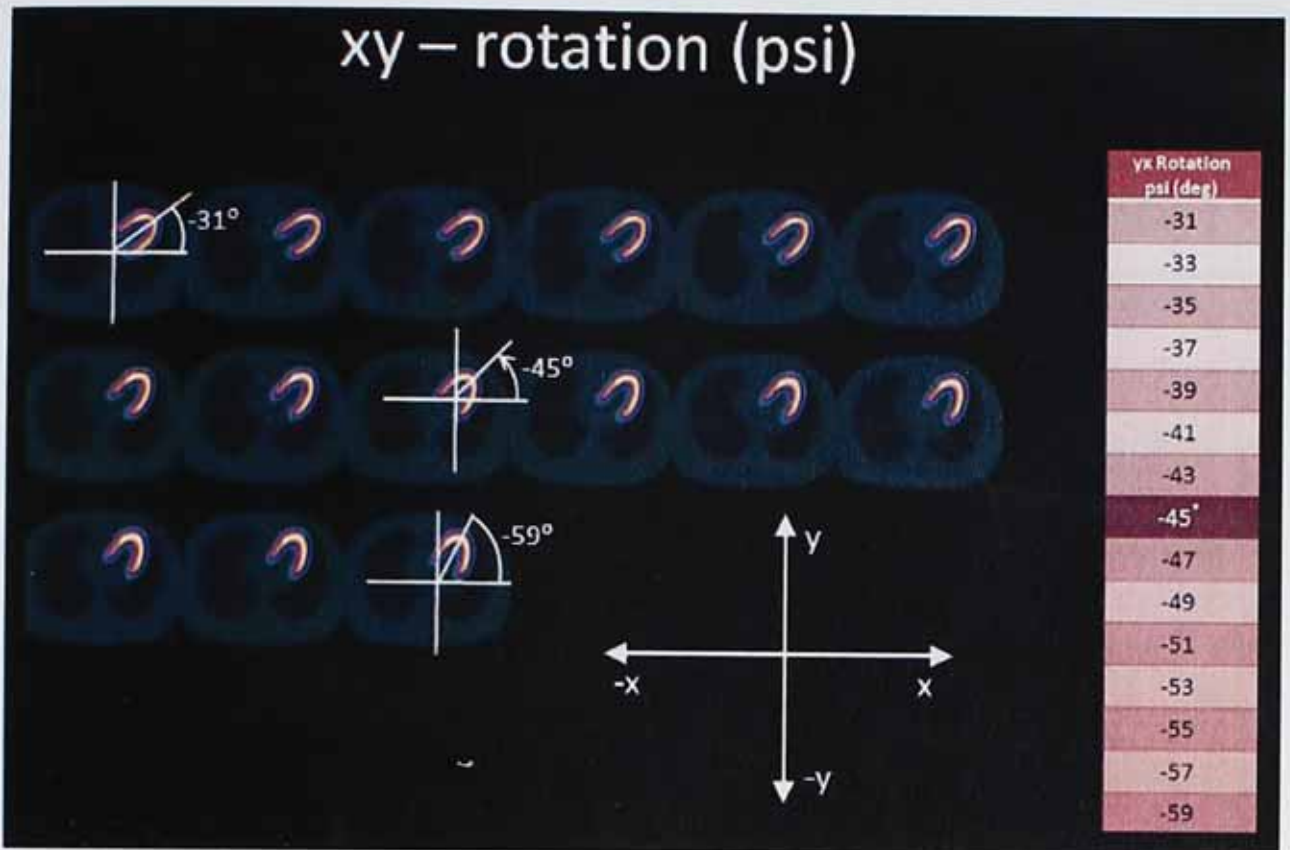
Table 5-1: The 15 variations for the 6 variation studies

xz Rotation phi (deg)	yx Rotation psi (deg)	zy Rotation beta (deg)	x Translation (mm)	y Translation (mm)	z Translation (mm)
-10	-31	-111	-14	-14	6
-12	-33	-108	-12	-12	8
-14	-35	-105	-10	-10	10
-16	-37	-102	-8	-8	12
-18	-39	-99	-6	-6	14
-20	-41	-96	-4	-4	16
-22	-43	-93	-2	-2	18
-24	-45	-90	0	0	20
-26	-47	-87	2	2	22
-28	-49	-84	4	4	24
-30	-51	-81	6	6	26
-32	-53	-78	8	8	28
-34	-55	-75	10	10	30
-36	-57	-72	12	12	32
-38	-59	-69	14	14	34

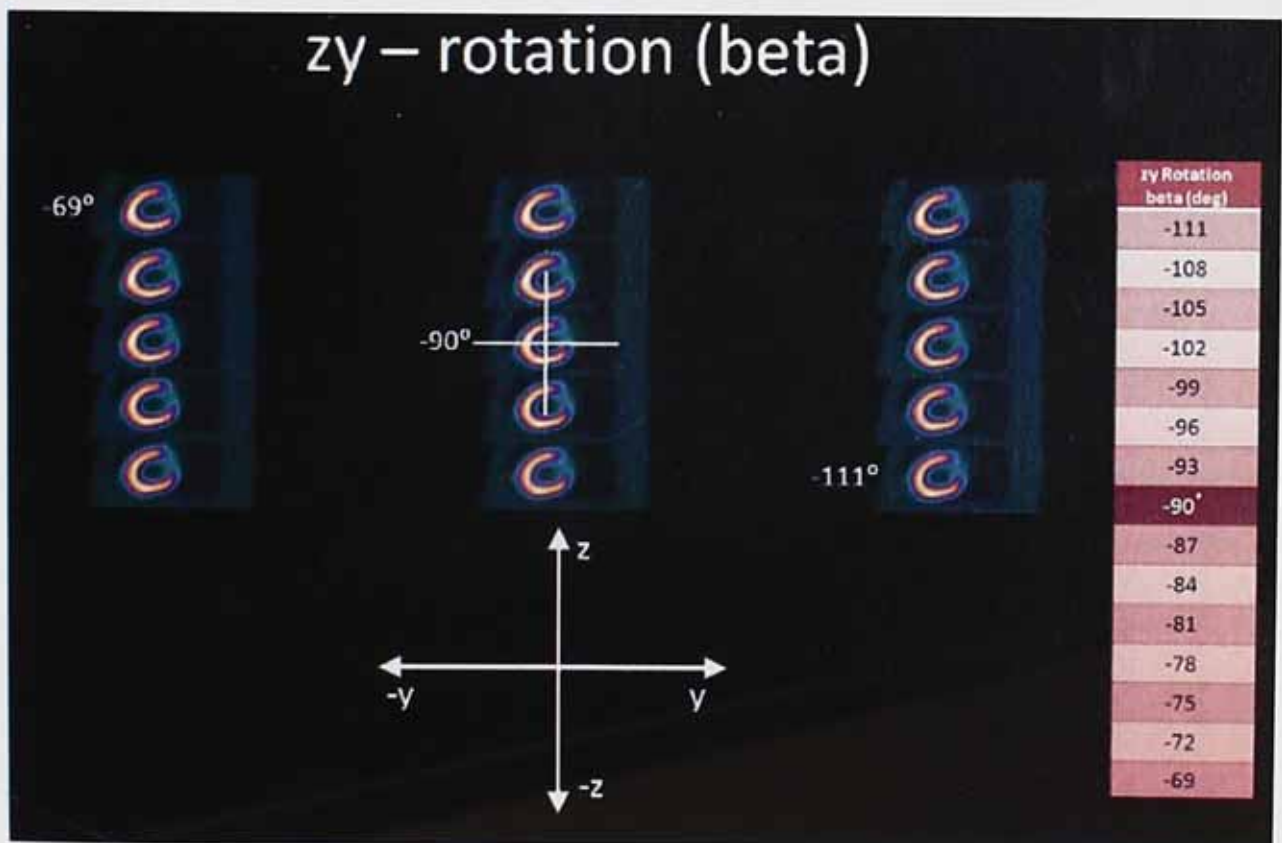
The following six images will illustrate the 3 translations and 3 translation which defines the 6 variation studies.



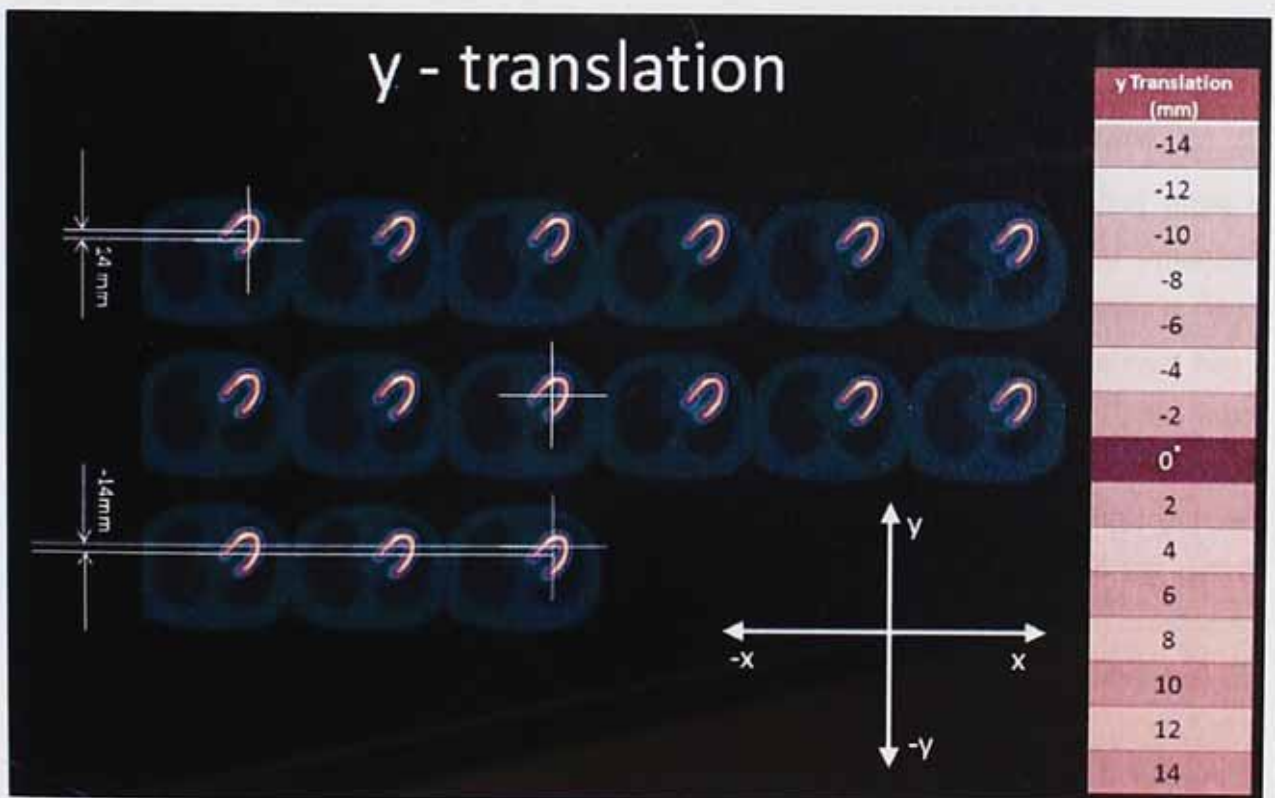
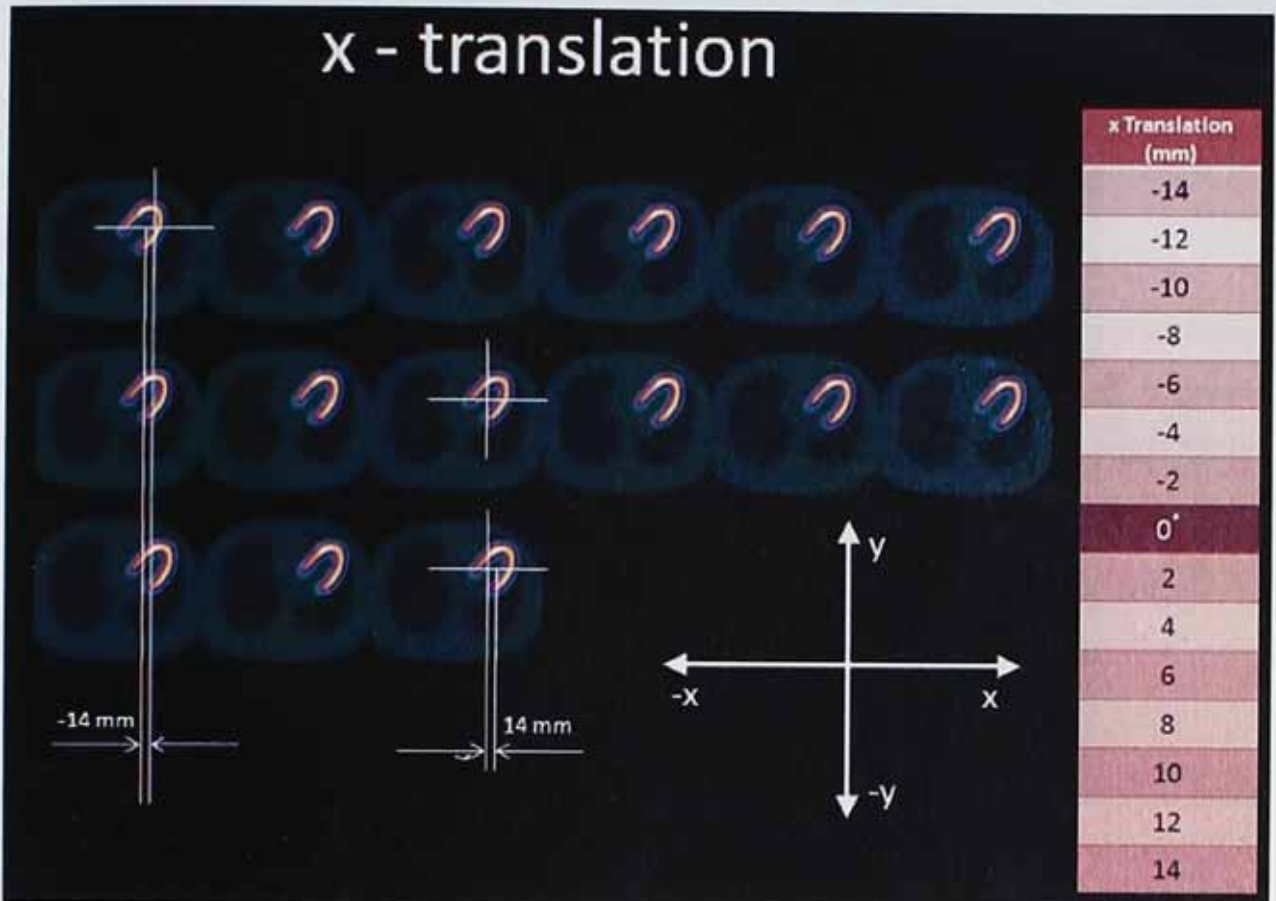
(a)

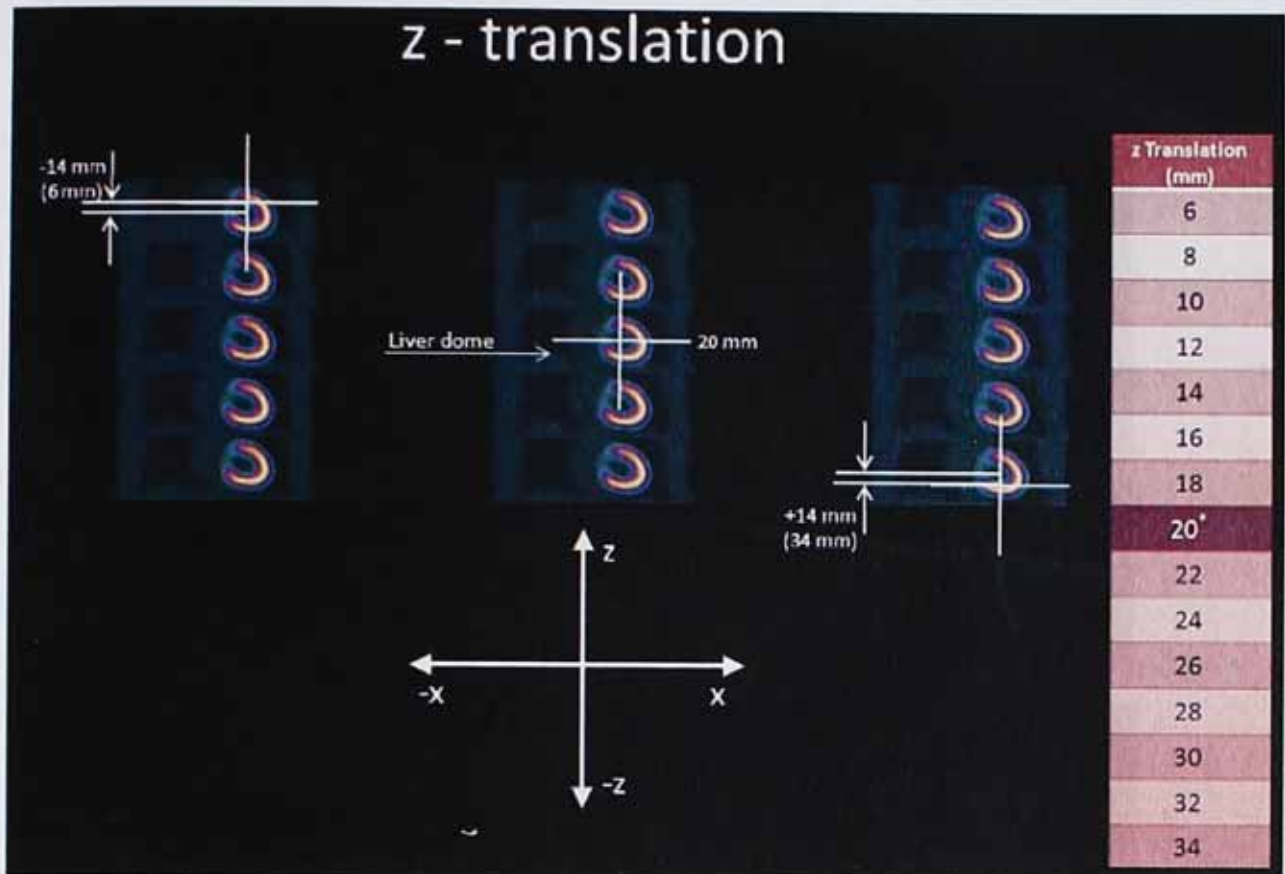


(b)



(c)



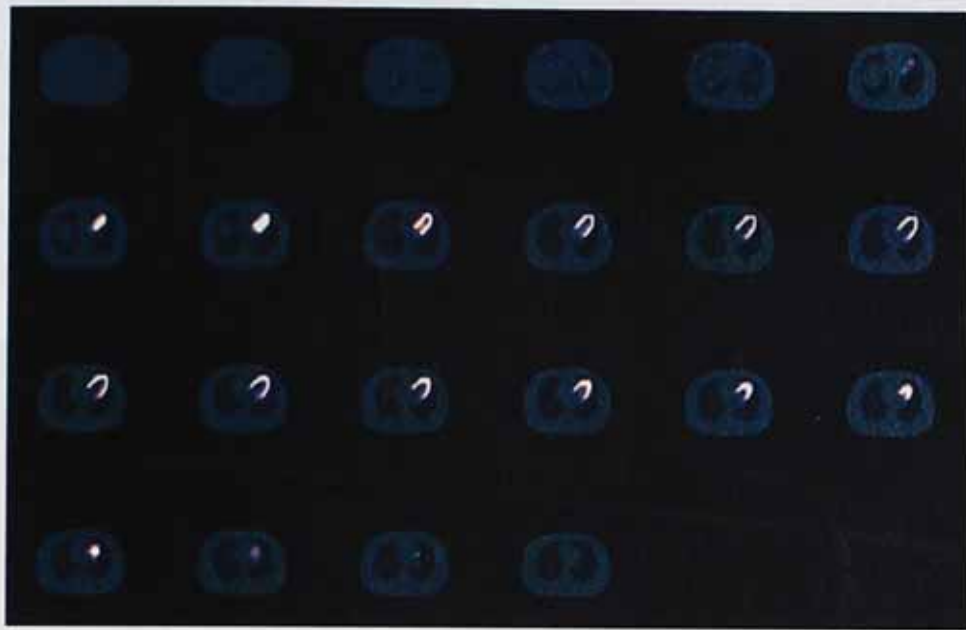


(f)

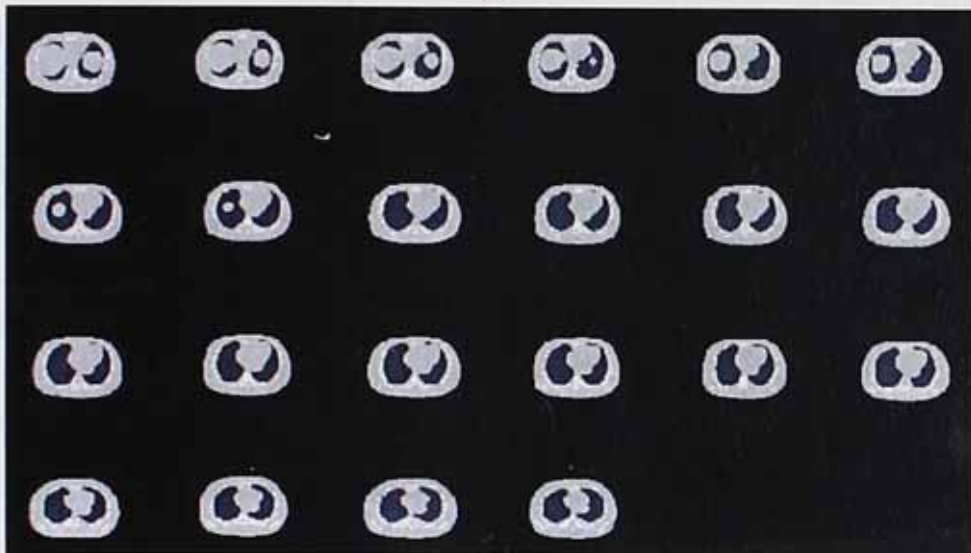
Figure 5-1: The 15 variations in each of the 6 variation studies (a) xz-rotation (ϕ), (b) xy-rotation (ψ), (c) zy-rotation (β), (d) x-translation, (e) y-translation and (f) z-translation.

5.2.1 Images Required for the Monte Carlo Simulations

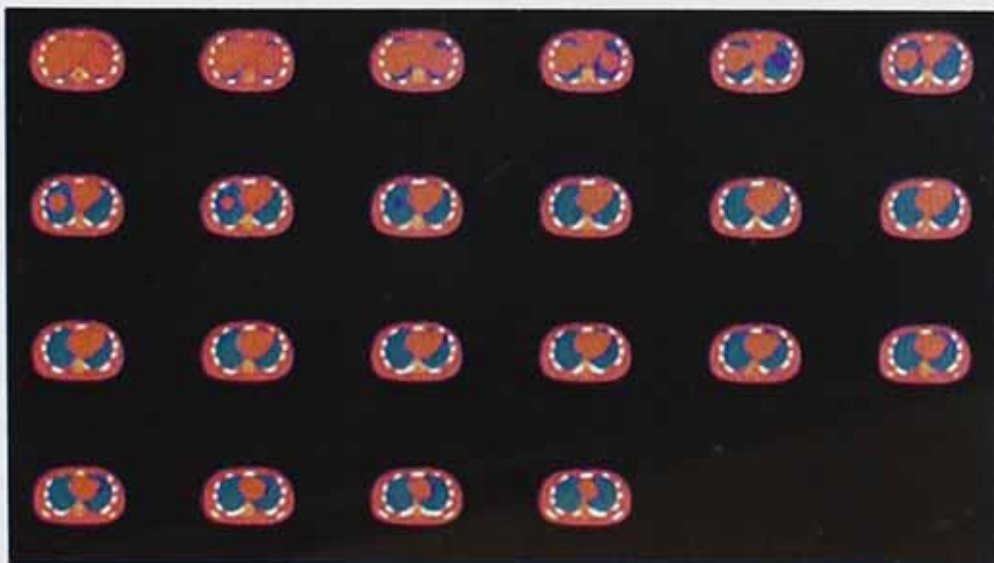
Each of the patient studies was simulated as a ^{99m}Tc SPECT study with the use of Monte Carlo simulations. The Monte Carlo simulation package used in this study (SIMSET) required an attenuation and activity index file that served as indexes into a translation table of attenuation coefficients and activity values for each of the patient studies being simulated. The NCAT program produced the activity and attenuation distributions as illustrated in figure 5.2 (a) and (b). Because the SIMSET program required index files (each tissue type has a specific index value rather than an attenuation coefficient assigned to them. These index values are then used in a look-up table to obtain the required attenuation coefficients), rather than distribution files, an index file has been created from the tissue density values in figure 5.2(b) as displayed in figure 5.2(c). An activity index file was also needed and the activity distribution shown in figure 5.2(a) also served as the index file. These files were created for each of the simulated patients. Each of the orientation variations (15) for every set (6), required a set of input files, i.e. a total of 90 for every simulated patient.



(a)



(b)



(c)

Figure 5-2: The simulation input files generated with the NCAT program. The activity distribution and index file (a), the attenuation distribution (b) and the attenuation index file (c).

For each spatial variation two simulations were performed as described in chapter 3, paragraph 3.4. First the NCAT activity distribution was created and then an attenuation distribution of the thorax. After converting these distributions to index files they were used as input for the simulation. This was the first simulation or real life simulation. The simulation with no attenuation medium was repeated, as if the photons propagated in air (air simulation), illustrated in figure 5.3 (a) and (b).

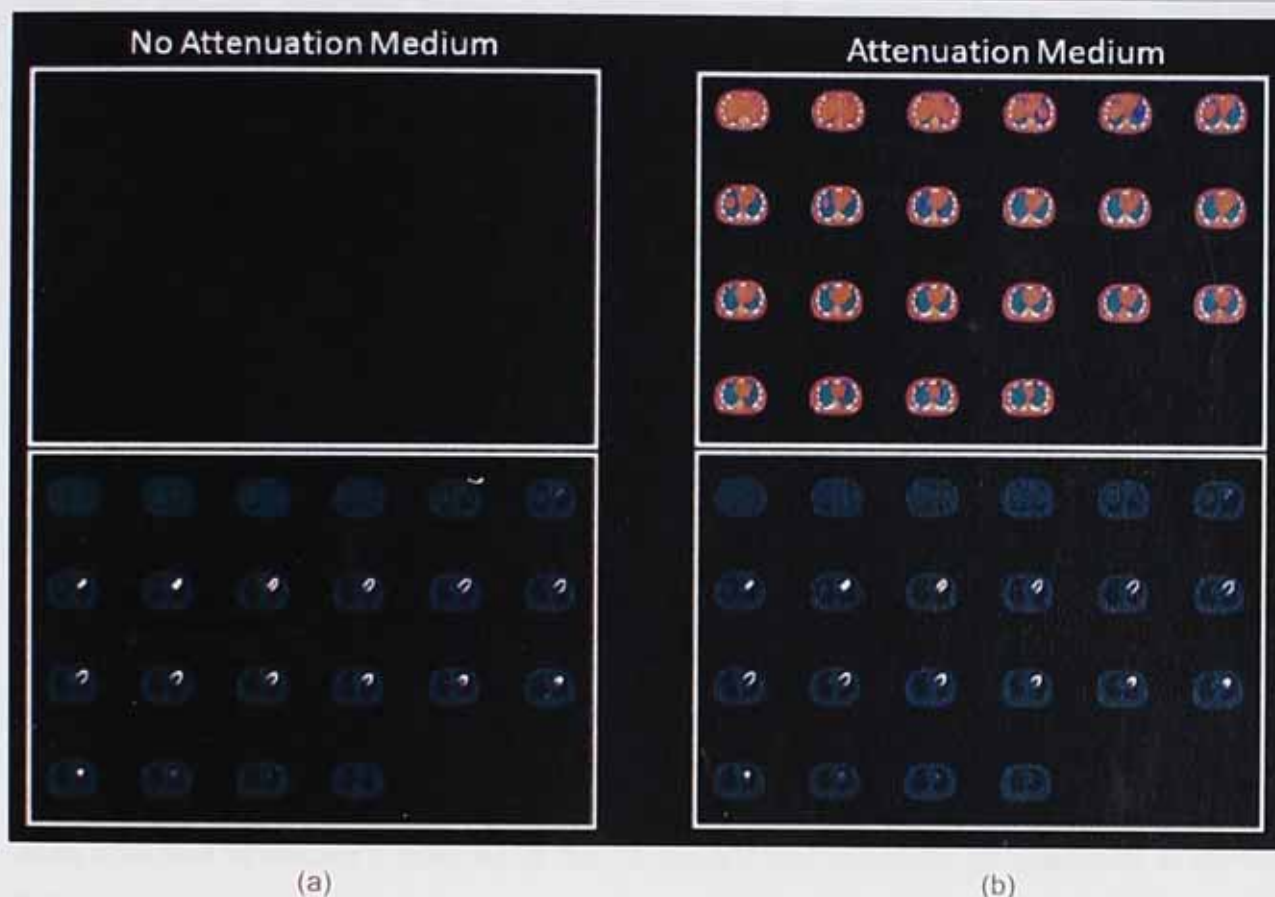


Figure 5-3: The simulation index input files generated with the NCAT program. The air simulation with the empty attenuation index file and the activity index file (a) and the real life simulation with the attenuation index file and the activity index file (b).

The output of the SIMSET simulation program provided a sinogram, therefore each set of simulations produced 2 sinograms. These sinograms were reconstructed as described in the section about reconstruction in the previous chapter (section 3.5) and analysed with the 4DMSPECT program by using a 5-segment model.

This process was repeated for all six variation studies. This gave a total of 90 variations in each patient simulation. To ensure that the above mentioned statistical analysis could be applied to these studies, the whole process was repeated for all 30 patients, giving a total of 2700 simulation sets, that is, 5400 individual simulations.

The hypothesis was that the intensity losses will change in either a linear or polynomial fashion. Therefore the intended statistical model to be used to determine the average

intensity losses for the six variation studies was polynomial regression (which includes linear regression).

5.2.2 Statistical Analysis

To be able to apply the statistical models on the data the output of the 4DMSPECT program had to be manually transferred to a spreadsheet. This involves a substantial amount of manually entered data and therefore appropriate data validation checks were conducted using a box-plot method and z-scores.

The z-scores of the skewness and kurtosis, together with the Shapiro-Wilk test were performed to ensure that the data follow normal distributions and they were visually inspected to confirm independence and interval data. Levene's test was used to test for homogeneity of variance.

After ensuring that the data is suitable for the application of a parametric test, regression analysis was performed and tested by using an independent t-test to see whether it is a valid statistical model. When regression was found to be a valid model, it was used to predict the outcome for unit changes in the variation under investigation. In the cases where it was not a valid statistical model, the mean was used and the assumption made that the outcome does not change for any changes in the predictor, i.e. the variation under investigation.

5.3 Results

After ensuring the integrity of the data by using the box-plot method and z-scores the data were analysed to ensure it adhered to the necessary four principles as described in section 3.7.

After the completion of the above mentioned tests polynomial regression was done for all five segments and the total on every polar map obtained for every value of the independent variable, as described in section 3.6. There were six variation studies and each of these studies was a study with its own independent variable but the dependent variable was the calculated PMUDs in each of these studies. The independent variables were the xz-orientation (ϕ), xy-orientation (ψ), zy-orientation (β), x-position, y-position and z-position and they were varied as depicted in table 5.1.

It was very clear from plotting the obtained PMUDs against each of the independent variables that a quadratic regression will not be a valid model and therefore only linear and cubic regressions were tested to see whether they are valid models. The outcome of the regression analysis are summarised in the tables and figures below.

5.3.1 Results of the Linear Regression

In table 5.2 the calculated PMUDs for each segment were used as the dependent variables and the xz-orientation (ϕ), xy-orientation (ψ), zy-orientation (β), x-position, y-position and z-position each as the independent variables for linear regression as the proposed model. Table 5.3 summarises the segments for each of these six cases where the linear model is a valid model and the cases where the mean would be the correct model. The calculated coefficients of the linear regression model (again for all 6 the variation studies) are shown in table 5.4. In the cases where the mean is an acceptable model the slope reduces to zero as expected. Figure 5.4 displays the plots of the dependent variable against the independent variables.

Table 5-2: Model summary for the linear regression model

Phi					Psi				
Model Summary					Model Summary				
	R	RSquare	Adjusted R Square	Std. Error of the Estimate		R	RSquare	Adjusted R Square	Std. Error of the Estimate
ANT	0.798	0.637	0.636	2.215	ANT	0.520	0.271	0.269	2.025
LAT	0.798	0.637	0.636	2.215	LAT	0.719	0.517	0.516	1.873
INF	0.620	0.384	0.383	1.917	INF	0.489	0.239	0.238	1.652
SEP	0.120	0.015	0.012	1.867	SEP	0.331	0.110	0.108	1.940
APX	0.233	0.054	0.052	2.816	APX	0.525	0.276	0.274	2.091
TOT	0.544	0.296	0.294	1.895	TOT	0.564	0.319	0.317	1.757
Beta					x-translation				
Model Summary					Model Summary				
	R	RSquare	Adjusted R Square	Std. Error of the Estimate		R	RSquare	Adjusted R Square	Std. Error of the Estimate
ANT	0.531	0.282	0.280	2.259	ANT	0.571	0.326	0.324	2.312
LAT	0.851	0.725	0.724	2.242	LAT	0.699	0.489	0.488	2.276
INF	0.716	0.513	0.512	2.031	INF	0.462	0.214	0.212	1.770
SEP	0.757	0.573	0.572	2.048	SEP	0.023	0.001	-0.002	1.772
APX	0.834	0.696	0.695	3.147	APX	0.211	0.045	0.043	2.851
TOT	0.783	0.614	0.613	1.953	TOT	0.522	0.272	0.270	1.926
y-translation					z-translation				
Model Summary					Model Summary				
	R	RSquare	Adjusted R Square	Std. Error of the Estimate		R	RSquare	Adjusted R Square	Std. Error of the Estimate
ANT	0.692	0.479	0.478	2.183	ANT	0.732	0.536	0.535	2.093
LAT	0.788	0.621	0.620	1.935	LAT	0.645	0.415	0.414	1.855
INF	0.469	0.219	0.218	1.784	INF	0.128	0.016	0.014	1.951
SEP	0.035	0.001	-0.001	1.877	SEP	0.066	0.004	0.002	1.745
APX	0.157	0.025	0.022	2.852	APX	0.163	0.027	0.025	2.444
TOT	0.505	0.255	0.254	1.970	TOT	0.448	0.201	0.199	1.600

Table 5-3: ANOVA results for the linear regression model. For all non-significant values the p-value are shown in red

ANOVA							ANOVA						
		Sum of Squares	df	Mean Square	F	p			Sum of Squares	df	Mean Square	F	p
ANT	Regression	8828.12	1	8828.12	1471.71	< .0001	ANT	Regression	682.46	1	682.46	166.42	< .0001
	Residual	2687.35	448	6.00		Residual		1837.14	448	4.10			
	Total	11515.47	449			Total		2519.60	449				
LAT	Regression	3850.37	1	3850.37	784.70	< .0001	LAT	Regression	1682.96	1	1682.96	479.83	< .0001
	Residual	2198.25	448	4.91		Residual		1571.32	448	3.51			
	Total	6048.62	449			Total		3254.28	449				
INF	Regression	1028.37	1	1028.37	279.74	< .0001	INF	Regression	384.56	1	384.56	140.99	< .0001
	Residual	1646.93	448	3.68		Residual		1221.98	448	2.73			
	Total	2675.30	449			Total		1606.54	449				
SEP	Regression	22.98	1	22.98	6.59	.011	SEP	Regression	207.59	1	207.59	55.16	< .0001
	Residual	1561.80	448	3.49		Residual		1685.87	448	3.76			
	Total	1584.78	449			Total		1893.46	449				
APX	Regression	204.02	1	204.02	25.74	< .0001	APX	Regression	746.97	1	746.97	170.83	< .0001
	Residual	3551.40	448	7.93		Residual		1958.88	448	4.37			
	Total	3755.42	449			Total		2705.85	449				
TOT	Regression	675.64	1	675.64	188.08	< .0001	TOT	Regression	646.74	1	646.74	209.43	< .0001
	Residual	1609.33	448	3.59		Residual		1383.47	448	3.09			
	Total	2284.97	449			Total		2030.21	449				

Beta ANOVA							x-translation ANOVA						
		Sum of Squares	df	Mean Square	F	p			Sum of Squares	df	Mean Square	F	p
ANT	Regression	896.83	1	896.83	175.74	< .0001	ANT	Regression	1158.19	1	1158.19	216.64	< .0001
	Residual	2286.16	448	5.10		Residual		2395.03	448	5.35			
	Total	3183.00	449			Total		3553.22	449				
LAT	Regression	5932.42	1	5932.42	1180.49	< .0001	LAT	Regression	2220.58	1	2220.58	428.67	< .0001
	Residual	2251.37	448	5.03		Residual		2320.70	448	5.18			
	Total	8183.79	449			Total		4541.28	449				
INF	Regression	1946.70	1	1946.70	471.77	< .0001	INF	Regression	381.44	1	381.44	121.78	< .0001
	Residual	1848.62	448	4.13		Residual		1403.18	448	3.13			
	Total	3795.33	449			Total		1784.62	449				
SEP	Regression	2525.08	1	2525.08	602.10	< .0001	SEP	Regression	0.72	1	0.72	0.23	.633
	Residual	1878.81	448	4.19		Residual		1406.74	448	3.14			
	Total	4403.88	449			Total		1407.45	449				
APX	Regression	10138.72	1	10138.72	1023.94	< .0001	APX	Regression	170.26	1	170.26	20.95	< .0001
	Residual	4435.97	448	9.90		Residual		3641.41	448	8.13			
	Total	14574.68	449			Total		3811.67	449				
TOT	Regression	2714.36	1	2714.36	711.36	< .0001	TOT	Regression	621.30	1	621.30	167.42	< .0001
	Residual	1709.45	448	3.82		Residual		1662.50	448	3.71			
	Total	4423.81	449			Total		2283.80	449				

y-translation ANOVA							z-translation ANOVA						
		Sum of Squares	df	Mean Square	F	p			Sum of Squares	df	Mean Square	F	p
ANT	Regression	1964.36	1	1964.36	412.22	< .0001	ANT	Regression	2268.14	1	2268.14	517.52	< .0001
	Residual	2134.86	448	4.77		Residual		1963.44	448	4.38			
	Total	4099.23	449			Total		4231.58	449				
LAT	Regression	1964.36	1	1964.36	412.22	< .0001	LAT	Regression	1095.85	1	1095.85	318.46	< .0001
	Residual	2134.86	448	4.77		Residual		1541.64	448	3.44			
	Total	4099.23	449			Total		2637.49	449				
INF	Regression	401.17	1	401.17	125.99	< .0001	INF	Regression	28.60	1	28.60	7.51	.006
	Residual	1426.49	448	3.18		Residual		1705.63	448	3.81			
	Total	1827.66	449			Total		1734.23	449				
SEP	Regression	1.94	1	1.94	0.55	.459	SEP	Regression	5.96	1	5.96	1.96	.163
	Residual	1578.68	448	3.52		Residual		1364.05	448	3.04			
	Total	1580.62	449			Total		1370.01	449				
APX	Regression	91.83	1	91.83	11.29	.001	APX	Regression	73.43	1	73.43	12.29	.001
	Residual	3643.66	448	8.13		Residual		2676.33	448	5.97			
	Total	3735.49	449			Total		2749.76	449				
TOT	Regression	596.59	1	596.59	153.73	< .0001	TOT	Regression	288.38	1	288.38	112.67	< .0001
	Residual	1738.61	448	3.88		Residual		1146.67	448	2.56			
	Total	2335.19	449			Total		1435.04	449				

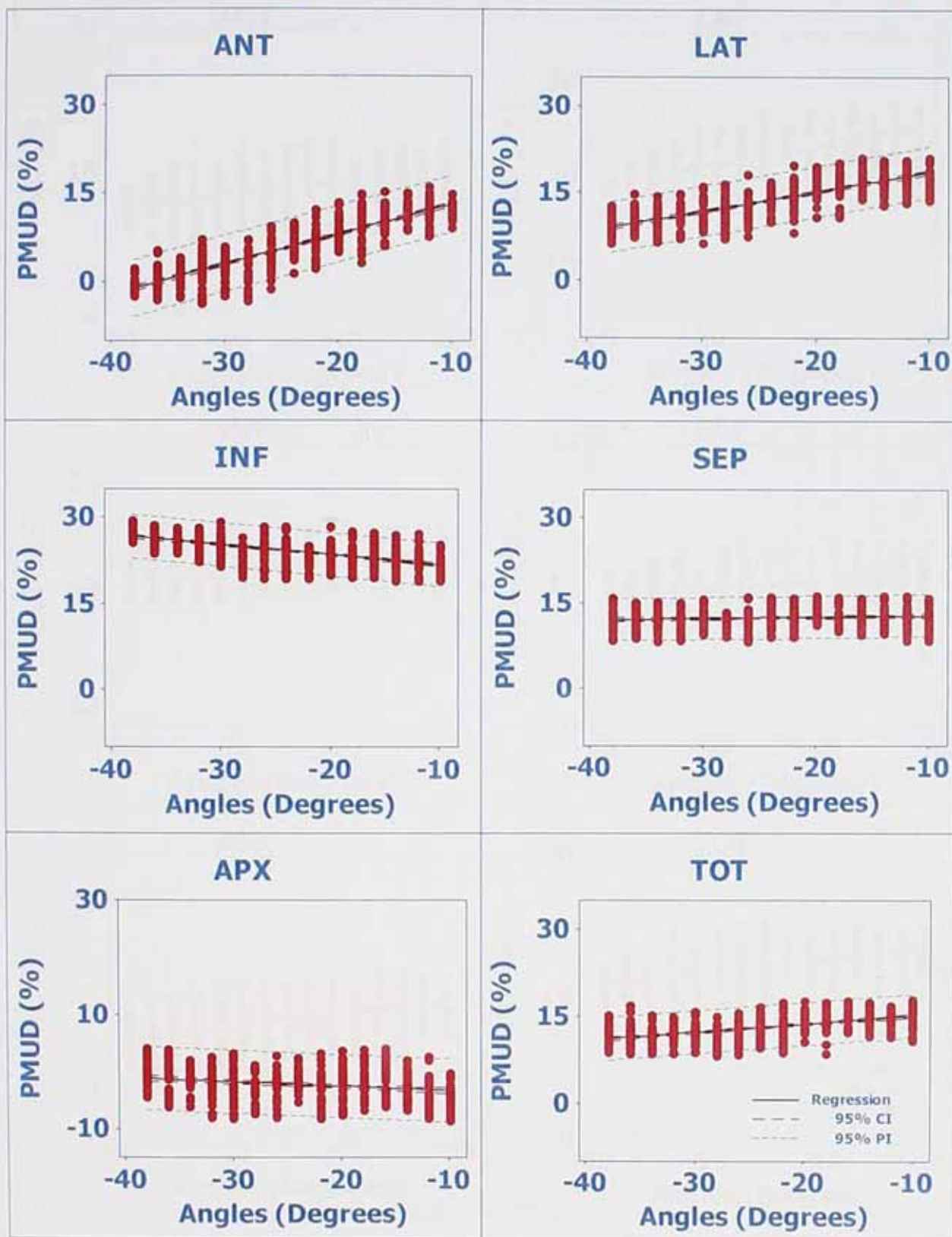
Table 5-4: Coefficients for the linear regression model. For all non-significant values the p-value are shown in red

Phi							Psi							
Coefficients							Coefficients							
		Unstandardized Coefficients		Standardized Coefficients	t	p			Unstandardized Coefficients		Standardized Coefficients	t	p	
		B	Std. Error	Beta					B	Std. Error	Beta			
ANT	slope	0.51	0.01	0.88	38.36	< .0001			slope	0.14	0.01	0.52	12.90	< .0001
	intercept	18.23	0.34		53.48	< .0001			intercept	19.86	0.51		39.23	< .0001
LAT	slope	0.34	0.01	0.60	28.01	< .0001			slope	0.22	0.01	0.72	21.90	< .0001
	intercept	21.95	0.31		71.21	< .0001			intercept	32.08	0.47		68.53	< .0001
INF	slope	-0.17	0.01	-0.62	-16.73	< .0001			slope	0.11	0.01	0.49	11.87	< .0001
	intercept	19.92	0.27		74.68	< .0001			intercept	31.86	0.41		77.17	< .0001
SEP	slope	0.03	0.01	0.12	2.57	.011			slope	0.08	0.01	0.33	7.43	< .0001
	intercept	13.07	0.26		50.31	< .0001			intercept	18.61	0.48		38.37	< .0001
APX	slope	-0.08	0.02	-0.23	-5.07	< .0001			slope	0.15	0.01	0.53	13.07	< .0001
	intercept	-4.06	0.39		-10.36	< .0001			intercept	8.79	0.52		16.81	< .0001
TOT	slope	0.14	0.01	0.54	13.71	< .0001			slope	0.14	0.01	0.56	14.47	< .0001
	intercept	16.47	0.26		62.45	< .0001			intercept	24.56	0.44		55.91	< .0001

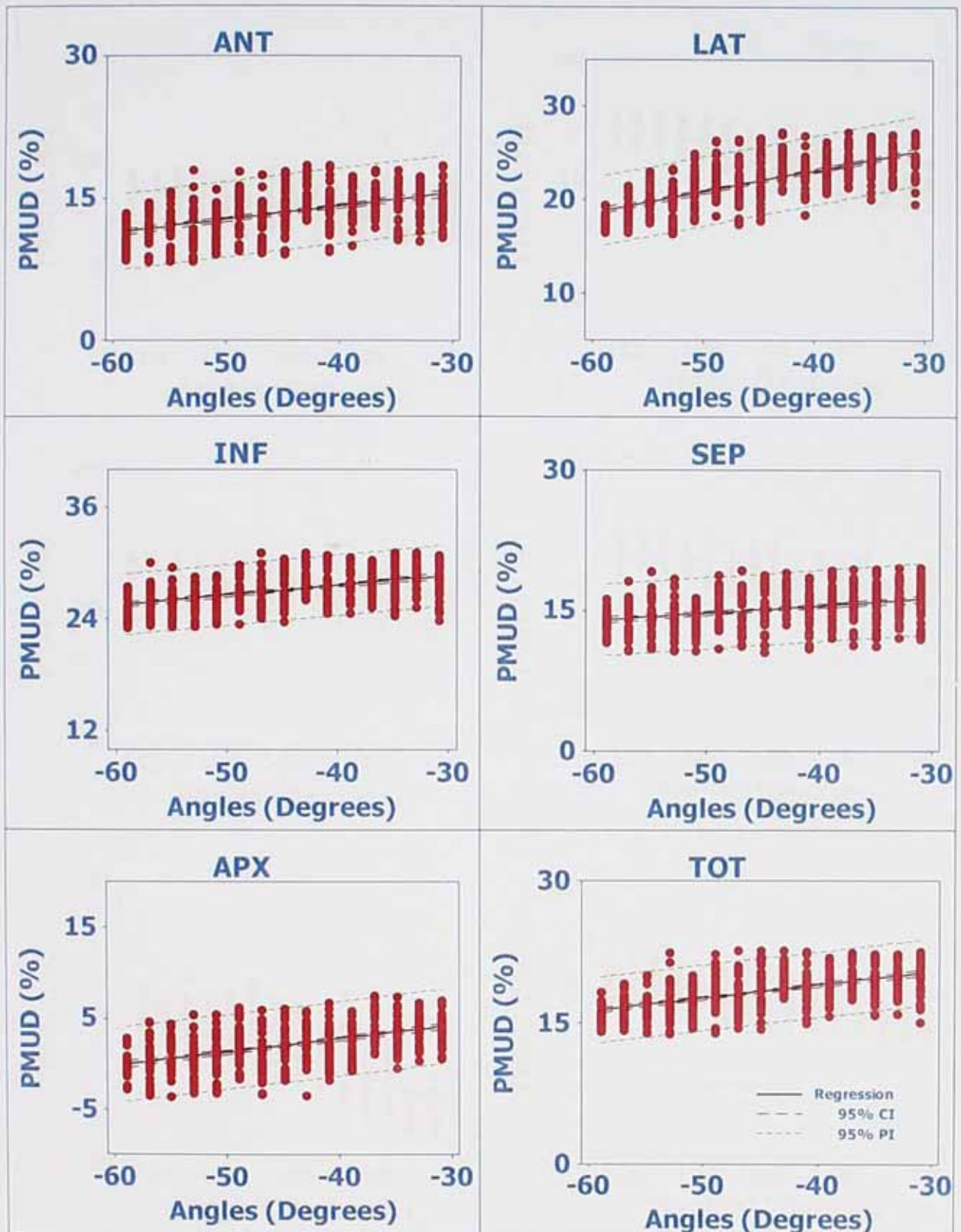
Beta							x-translation							
Coefficients							Coefficients							
		Unstandardized Coefficients		Standardized Coefficients	t	p			Unstandardized Coefficients		Standardized Coefficients	t	p	
		B	Std. Error	Beta					B	Std. Error	Beta			
ANT	slope	-0.11	0.01	-0.53	-13.26	< .0001			slope	0.19	0.01	0.57	14.72	< .0001
	intercept	-1.22	0.75		-1.64	.102			intercept	7.09	0.11		65.07	< .0001
LAT	slope	-0.28	0.01	-0.85	-34.36	< .0001			slope	0.26	0.01	0.70	20.70	< .0001
	intercept	-11.62	0.74		-15.67	< .0001			intercept	16.26	0.11		151.58	< .0001
INF	slope	-0.16	0.01	-0.72	-21.72	< .0001			slope	0.11	0.01	0.46	11.04	< .0001
	intercept	7.95	0.67		11.83	< .0001			intercept	24.54	0.08		294.10	< .0001
SEP	slope	-0.18	0.01	-0.76	-24.54	< .0001			slope	0.01	0.01	0.02	0.48	.633
	intercept	-3.92	0.68		-5.79	< .0001			intercept	12.65	0.08		151.37	< .0001
APX	slope	-0.37	0.01	-0.83	-32.00	< .0001			slope	0.07	0.02	0.21	4.58	< .0001
	intercept	-37.81	1.04		-36.33	< .0001			intercept	-2.00	0.13		-14.87	< .0001
TOT	slope	-0.19	0.01	-0.78	-26.67	< .0001			slope	0.14	0.01	0.52	12.94	< .0001
	intercept	-3.95	0.65		-6.12	< .0001			intercept	14.07	0.09		154.95	< .0001

y-translation							z-translation							
Coefficients							Coefficients							
		Unstandardized Coefficients		Standardized Coefficients	t	p			Unstandardized Coefficients		Standardized Coefficients	t	p	
		B	Std. Error	Beta					B	Std. Error	Beta			
ANT	slope	0.24	0.01	0.69	20.30	< .0001			slope	0.26	0.01	0.73	22.75	< .0001
	intercept	6.99	0.10		67.90	< .0001			intercept	7.51	0.10		76.12	< .0001
LAT	slope	0.29	0.01	0.79	27.09	< .0001			slope	0.18	0.01	0.64	17.85	< .0001
	intercept	15.97	0.09		175.06	< .0001			intercept	15.29	0.09		174.83	< .0001
INF	slope	0.11	0.01	0.47	11.22	< .0001			slope	-0.03	0.01	-0.13	-2.74	.006
	intercept	24.48	0.08		291.07	< .0001			intercept	23.21	0.09		252.37	< .0001
SEP	slope	0.01	0.01	0.04	0.74	.459			slope	0.01	0.01	0.07	1.40	.163
	intercept	12.77	0.09		144.32	< .0001			intercept	11.90	0.08		144.66	< .0001
APX	slope	0.05	0.02	0.16	3.36	.001			slope	0.05	0.01	0.16	3.51	.001
	intercept	-2.12	0.13		-15.80	< .0001			intercept	-2.77	0.12		-24.04	< .0001
TOT	slope	0.13	0.01	0.51	12.40	< .0001			slope	0.09	0.01	0.45	10.61	< .0001
	intercept	14.08	0.09		151.60	< .0001			intercept	13.39	0.08		177.53	< .0001

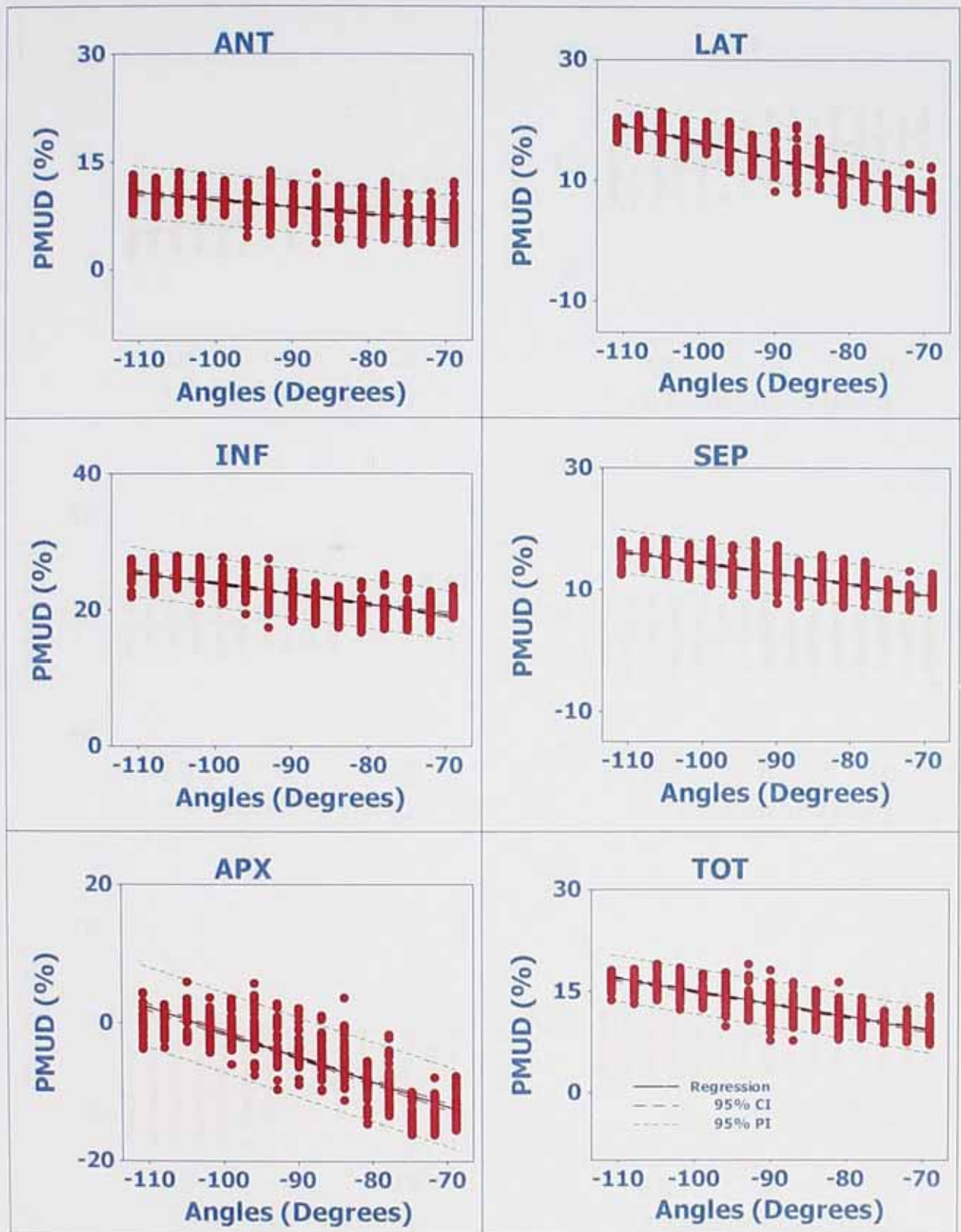
Linear Regression - Phi (XZ Rotation)



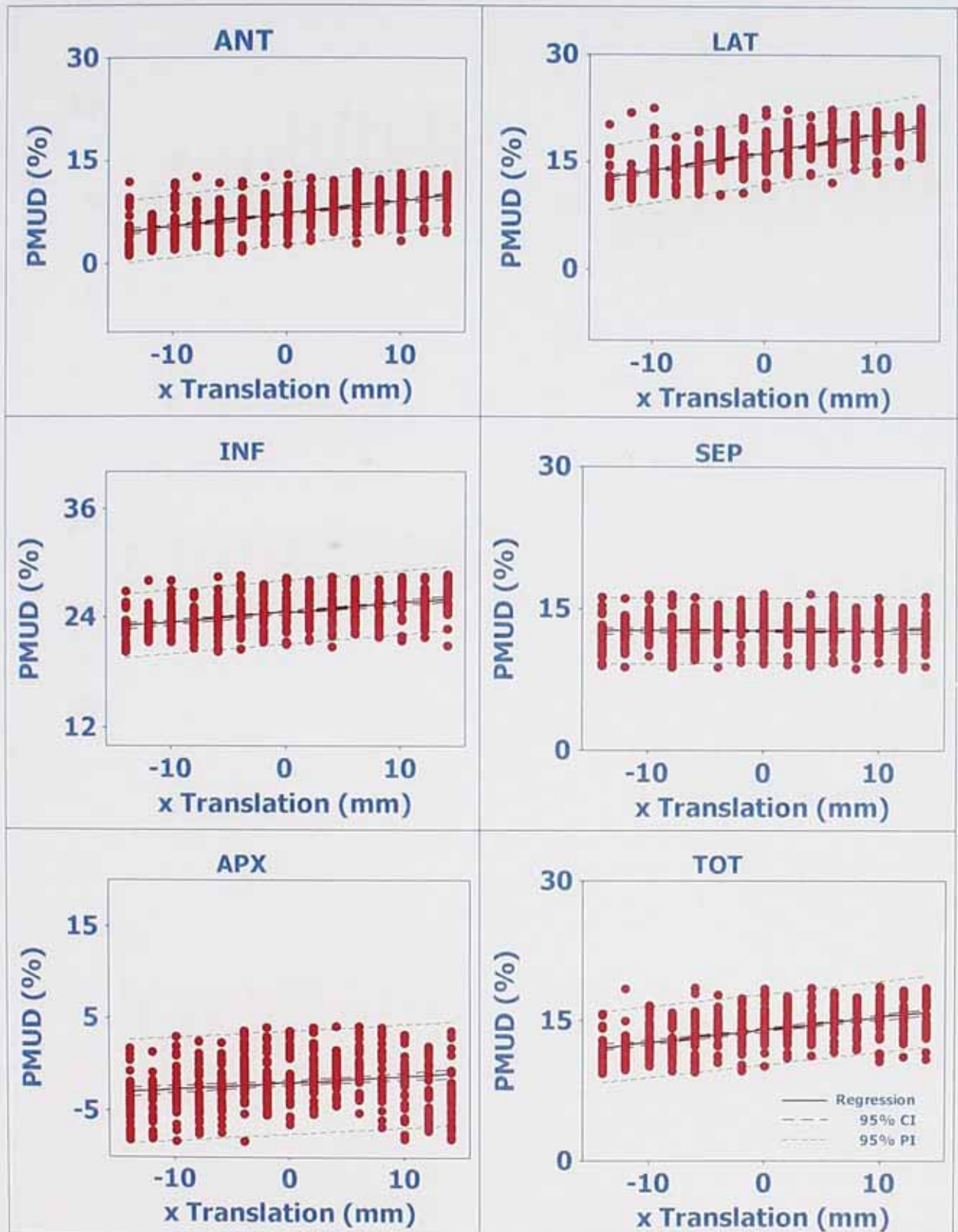
Linear Regression - Psi (XY Rotation)



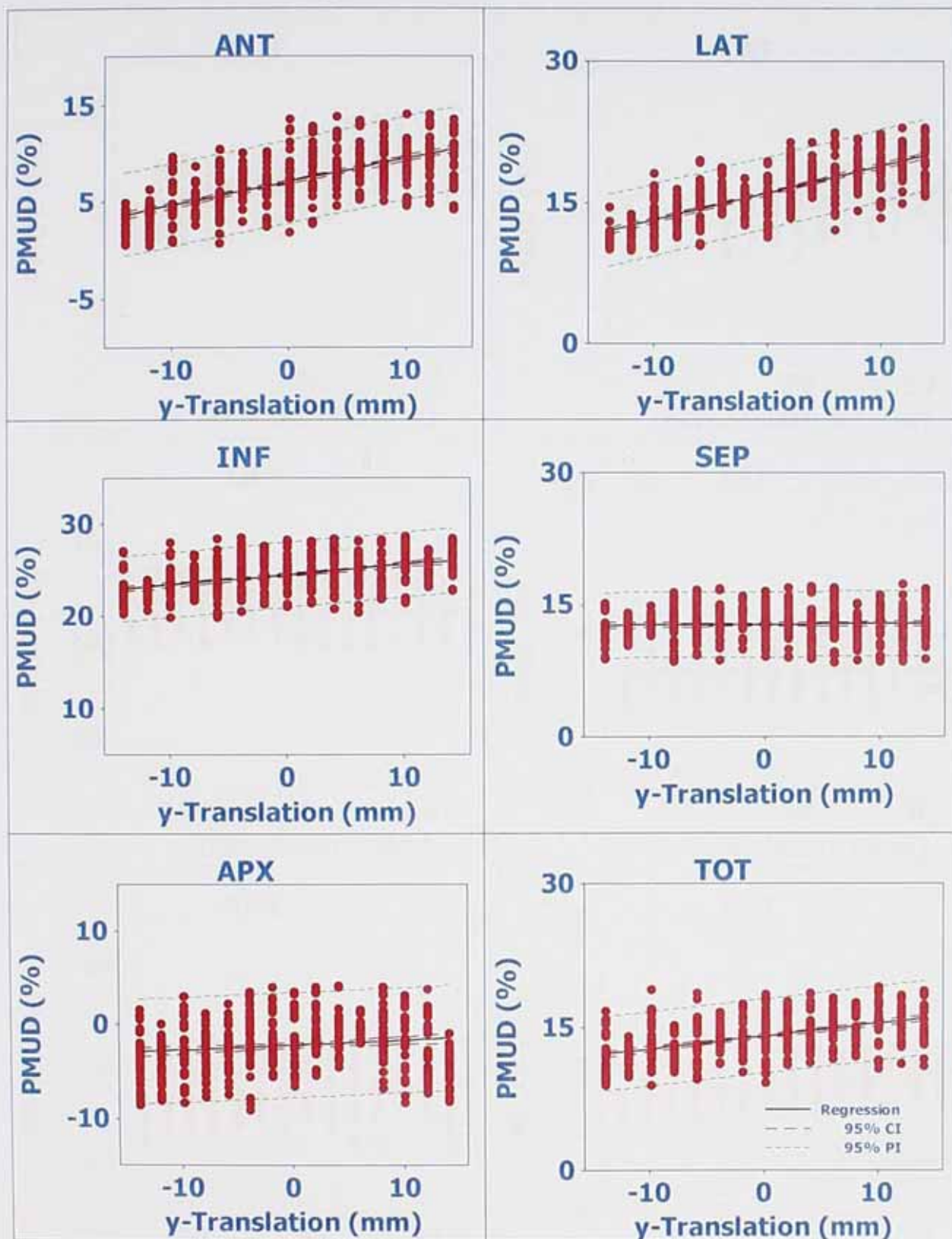
Linear Regression - Beta (ZY Rotation)



Linear Regression - X-Translation



Linear Regression - Y-Translation



Linear Regression - Z-Translation

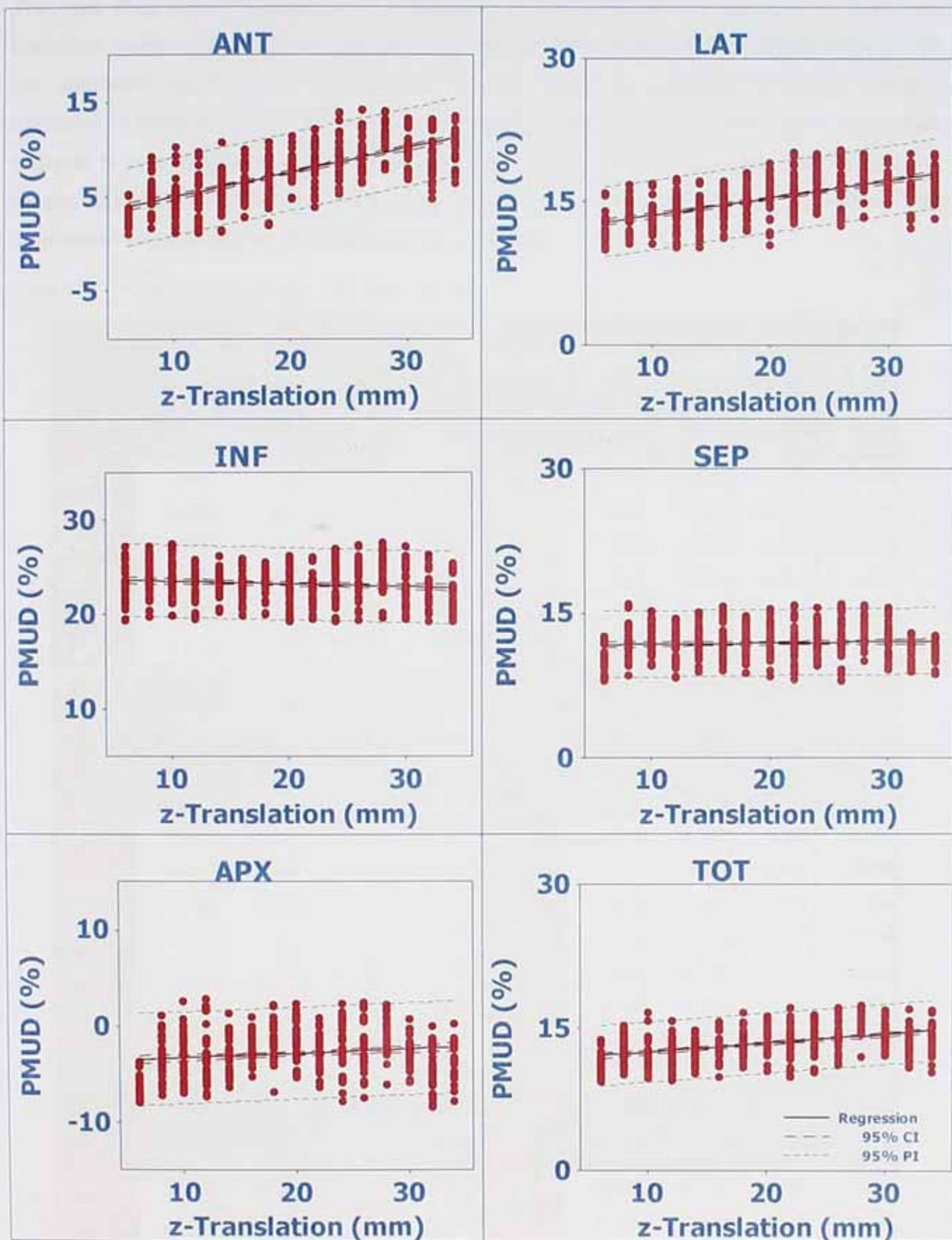


Figure 5-4: Linear regression results showing the percentage intensity losses on the y-axis and indicating the 95% confidence and prediction intervals.

5.3.2 Results of the Cubic Regression

The next step was to perform cubic regression to see whether this leads to an improved statistical model over the linear regression to describe the data. This was again done on the five segments together with the total of the polar maps, as described in section 3.6 and repeated to complete it for all six variation studies. The outcome of the cubic regression analysis is summarised in the table 5.5 gives the model summaries, table 5.6 the ANOVA results and table 5.1 gives the polynomial coefficients. Figure 5.5 displays the plots of the dependent variable against the independent variables.

Table 5-5: Model summary for the cubic regression model

Phi					Psi				
Model Summary					Model Summary				
	R	RSquare	Adjusted RSquare	Std. Error of the Estimate		R	RSquare	Adjusted RSquare	Std. Error of the Estimate
ANT	0.886	0.784	0.783	2.360	ANT	0.886	0.784	0.783	2.360
LAT	0.816	0.666	0.664	2.127	LAT	0.816	0.666	0.664	2.127
INF	0.666	0.444	0.440	1.826	INF	0.666	0.444	0.440	1.826
SEP	0.266	0.071	0.064	1.817	SEP	0.266	0.071	0.064	1.817
APX	0.392	0.154	0.148	2.669	APX	0.392	0.154	0.148	2.669
TOT	0.586	0.344	0.340	1.833	TOT	0.586	0.344	0.340	1.833

Beta					x-translation				
Model Summary					Model Summary				
	R	RSquare	Adjusted RSquare	Std. Error of the Estimate		R	RSquare	Adjusted RSquare	Std. Error of the Estimate
ANT	0.886	0.784	0.783	2.360	ANT	0.576	0.332	0.328	2.306
LAT	0.816	0.666	0.664	2.127	LAT	0.708	0.501	0.497	2.255
INF	0.666	0.444	0.440	1.826	INF	0.472	0.223	0.217	1.764
SEP	0.266	0.071	0.064	1.817	SEP	0.117	0.014	0.007	1.764
APX	0.392	0.154	0.148	2.669	APX	0.443	0.196	0.191	2.621
TOT	0.586	0.344	0.340	1.833	TOT	0.538	0.290	0.285	1.907

y-translation					z-translation				
Model Summary					Model Summary				
	R	RSquare	Adjusted RSquare	Std. Error of the Estimate		R	RSquare	Adjusted RSquare	Std. Error of the Estimate
ANT	0.754	0.569	0.566	2.022	ANT	0.712	0.508	0.504	2.127
LAT	0.671	0.450	0.447	1.803	LAT	0.799	0.638	0.635	1.896
INF	0.188	0.035	0.029	1.937	INF	0.479	0.230	0.225	1.777
SEP	0.306	0.094	0.087	1.669	SEP	0.172	0.030	0.023	1.854
APX	0.466	0.217	0.212	2.197	APX	0.469	0.220	0.215	2.556
TOT	0.503	0.253	0.248	1.551	TOT	0.516	0.266	0.261	1.961

Table 5-6: ANOVA results for the cubic regression model. The non-significant p-value is shown in red and therefore the significant p-values are those not marked in red.

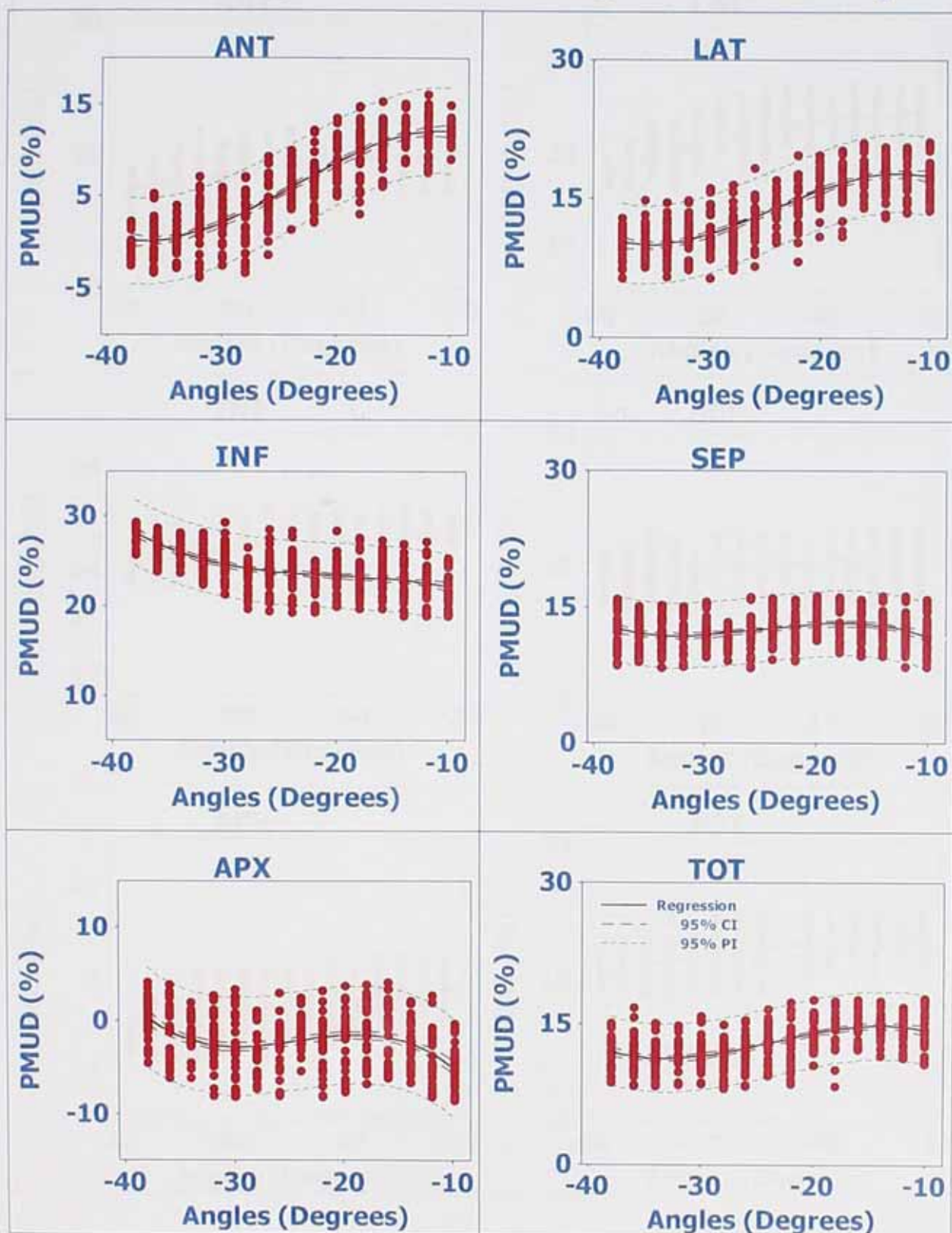
Phi							Psi						
ANOVA							ANOVA						
		Sum of Squares	df	Mean Square	F	p		Sum of Squares	df	Mean Square	F	p	
ANT	Regression	9030.68	3	3010.23	540.31	< .0001	ANT	Regression	9030.68	3	3010.23	540.31	< .0001
	Residual	2484.79	446	5.57		Residual		2484.79	446	5.57			
	Total	11515.47	449			Total		11515.47	449				
LAT	Regression	4031.12	3	1343.71	297.05	< .0001	LAT	Regression	4031.12	3	1343.71	297.05	< .0001
	Residual	2017.50	446	4.52		Residual		2017.50	446	4.52			
	Total	6048.62	449			Total		6048.62	449				
INF	Regression	1187.74	3	395.91	118.70	< .0001	INF	Regression	1187.74	3	395.91	118.70	< .0001
	Residual	1487.56	446	3.34		Residual		1487.56	446	3.34			
	Total	2675.30	449			Total		2675.30	449				
SEP	Regression	111.79	3	37.26	11.28	< .0001	SEP	Regression	111.79	3	37.26	11.28	< .0001
	Residual	1472.99	446	3.30		Residual		1472.99	446	3.30			
	Total	1584.78	449			Total		1584.78	449				
APX	Regression	578.26	3	192.75	27.06	< .0001	APX	Regression	578.26	3	192.75	27.06	< .0001
	Residual	3177.16	446	7.12		Residual		3177.16	446	7.12			
	Total	3755.42	449			Total		3755.42	449				
TOT	Regression	785.95	3	261.98	77.95	< .0001	TOT	Regression	785.95	3	261.98	77.95	< .0001
	Residual	1499.02	446	3.36		Residual		1499.02	446	3.36			
	Total	2284.97	449			Total		2284.97	449				
Beta							x-translation						
ANOVA							ANOVA						
		Sum of Squares	df	Mean Square	F	p		Sum of Squares	df	Mean Square	F	p	
ANT	Regression	9030.68	3	3010.23	540.31	< .0001	ANT	Regression	1180.54	3	393.51	73.97	< .0001
	Residual	2484.79	446	5.57		Residual		2372.68	446	5.32			
	Total	11515.47	449			Total		3553.22	449				
LAT	Regression	4031.12	3	1343.71	297.05	< .0001	LAT	Regression	2273.39	3	757.80	149.03	< .0001
	Residual	2017.50	446	4.52		Residual		2267.89	446	5.08			
	Total	6048.62	449			Total		4541.28	449				
INF	Regression	1187.74	3	395.91	118.70	< .0001	INF	Regression	397.10	3	132.37	42.55	< .0001
	Residual	1487.56	446	3.34		Residual		1387.52	446	3.11			
	Total	2675.30	449			Total		1784.62	449				
SEP	Regression	111.79	3	37.26	11.28	< .0001	SEP	Regression	19.22	3	6.41	2.06	.105
	Residual	1472.99	446	3.30		Residual		1388.23	446	3.11			
	Total	1584.78	449			Total		1407.45	449				
APX	Regression	578.26	3	192.75	27.06	< .0001	APX	Regression	748.55	3	249.52	36.33	< .0001
	Residual	3177.16	446	7.12		Residual		3063.12	446	6.87			
	Total	3755.42	449			Total		3811.67	449				
TOT	Regression	785.95	3	261.98	77.95	< .0001	TOT	Regression	661.21	3	220.40	60.58	< .0001
	Residual	1499.02	446	3.36		Residual		1622.59	446	3.64			
	Total	2284.97	449			Total		2283.80	449				
y-translation							z-translation						
ANOVA							ANOVA						
		Sum of Squares	df	Mean Square	F	p		Sum of Squares	df	Mean Square	F	p	
ANT	Regression	2407.31	3	802.44	196.18	< .0001	ANT	Regression	2080.63	3	693.54	153.23	< .0001
	Residual	1824.26	446	4.09		Residual		2018.60	446	4.53			
	Total	4231.58	449			Total		4099.23	449				
LAT	Regression	1187.83	3	395.94	121.82	.000	LAT	Regression	2823.00	3	941.00	261.86	< .0001
	Residual	1449.65	446	3.25		Residual		1602.70	446	3.59			
	Total	2637.49	449			Total		4425.70	449				
INF	Regression	61.07	3	20.36	5.43	.001	INF	Regression	420.00	3	140.00	44.36	< .0001
	Residual	1673.15	446	3.75		Residual		1407.66	446	3.16			
	Total	1734.23	449			Total		1827.66	449				
SEP	Regression	128.16	3	42.72	15.34	< .0001	SEP	Regression	46.80	3	15.60	4.54	.004
	Residual	1241.85	446	2.78		Residual		1533.82	446	3.44			
	Total	1370.01	449			Total		1580.62	449				
APX	Regression	597.49	3	199.16	41.27	< .0001	APX	Regression	822.42	3	274.14	41.97	< .0001
	Residual	2152.27	446	4.83		Residual		2913.07	446	6.53			
	Total	2749.76	449			Total		3735.49	449				
TOT	Regression	362.69	3	120.90	50.28	< .0001	TOT	Regression	620.78	3	206.93	53.83	< .0001
	Residual	1072.35	446	2.40		Residual		1714.41	446	3.84			
	Total	1435.04	449			Total		2335.19	449				

Table 5-7: Coefficients for the cubic regression model. The non-significant p-value is shown in red and therefore the significant p-values are those not marked in red.

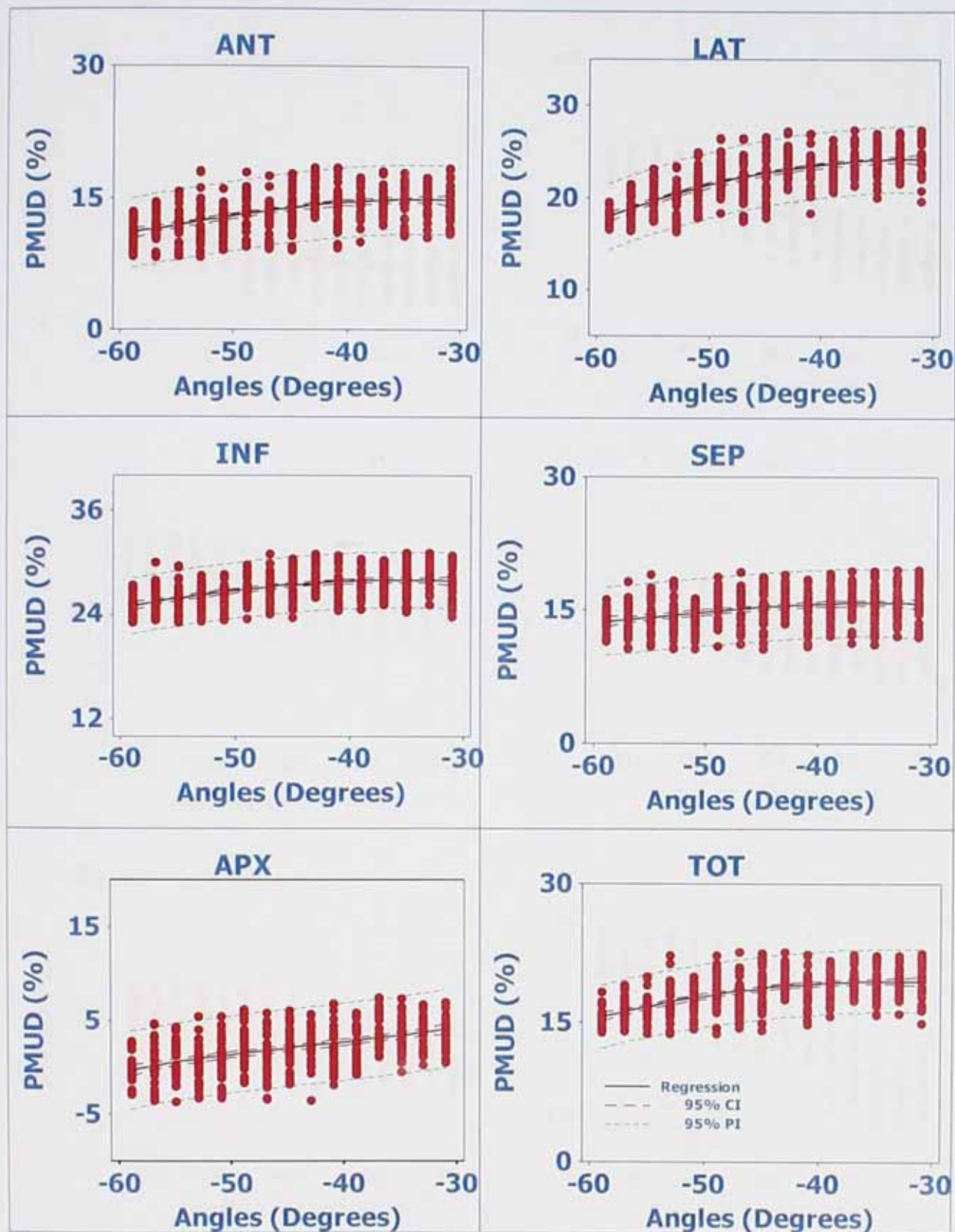
Phi							Psi						
Coefficients							Coefficients						
		Unstandardized Coefficients		Standardized Coefficients	t	p			Unstandardized Coefficients		Standardized Coefficients	t	p
		B	Std. Error	Beta					B	Std. Error	Beta		
ANT	b3	-1.567	0.368	-2.676	-4.258	< .0001		b3	-1.567	0.368	-2.676	-4.258	< .0001
	b2	-0.095	0.016	-7.928	-5.861	< .0001		b2	-0.095	0.016	-7.928	-5.861	< .0001
	b1	-0.001	0.000	-4.463	-5.976	< .0001		b1	-0.001	0.000	-4.463	-5.976	< .0001
	bo	4.624	2.555		1.810	.071		bo	4.624	2.555		1.810	.071
LAT	b3	-1.731	0.332	-4.080	-5.221	< .0001		b3	-1.731	0.332	-4.080	-5.221	< .0001
	b2	-0.093	0.015	-10.624	-6.317	< .0001		b2	-0.093	0.015	-10.624	-6.317	< .0001
	b1	-0.001	0.000	-5.857	-6.308	< .0001		b1	-0.001	0.000	-5.857	-6.308	< .0001
	bo	8.053	2.302		3.499	.001		bo	8.053	2.302		3.499	.001
INF	b3	-0.817	0.285	-2.894	-2.868	.004		b3	-0.817	0.285	-2.894	-2.868	.004
	b2	-0.038	0.013	-6.527	-3.006	.003		b2	-0.038	0.013	-6.527	-3.006	.003
	b1	-0.001	0.000	-4.353	-3.631	< .0001		b1	-0.001	0.000	-4.353	-3.631	< .0001
	bo	17.039	1.977		8.621	< .0001		bo	17.039	1.977		8.621	< .0001
SEP	b3	-1.426	0.283	-6.568	-5.034	< .0001		b3	-1.426	0.283	-6.568	-5.034	< .0001
	b2	-0.063	0.013	-14.052	-5.005	< .0001		b2	-0.063	0.013	-14.052	-5.005	< .0001
	b1	-0.001	0.000	-7.501	-4.839	< .0001		b1	-0.001	0.000	-7.501	-4.839	< .0001
	bo	2.961	1.967		1.505	.133		bo	2.961	1.967		1.505	.133
APX	b3	-3.064	0.416	-9.165	-7.364	< .0001		b3	-3.064	0.416	-9.165	-7.364	< .0001
	b2	-0.133	0.018	-19.411	-7.247	< .0001		b2	-0.133	0.018	-19.411	-7.247	< .0001
	b1	-0.002	0.000	-10.681	-7.222	< .0001		b1	-0.002	0.000	-10.681	-7.222	< .0001
	bo	-24.155	2.889		-8.362	< .0001		bo	-24.155	2.889		-8.362	< .0001
TOT	b3	-1.351	0.286	-5.181	-4.727	< .0001		b3	-1.351	0.286	-5.181	-4.727	< .0001
	b2	-0.069	0.013	-12.892	-5.466	< .0001		b2	-0.069	0.013	-12.892	-5.466	< .0001
	b1	-0.001	0.000	-7.310	-5.613	< .0001		b1	-0.001	0.000	-7.310	-5.613	< .0001
	bo	6.800	1.984		3.427	.001		bo	6.800	1.984		3.427	.001
Beta							x-translation						
Coefficients							Coefficients						
		Unstandardized Coefficients		Standardized Coefficients	t	p			Unstandardized Coefficients		Standardized Coefficients	t	p
		B	Std. Error	Beta					B	Std. Error	Beta		
ANT	b3	-1.567	0.368	-2.676	-4.258	< .0001		b3	0.206	0.032	0.633	6.438	< .0001
	b2	-0.095	0.016	-7.928	-5.861	< .0001		b2	-0.003	0.002	-0.075	-1.932	.054
	b1	-0.001	0.000	-4.463	-5.976	< .0001		b1	0.000	0.000	-0.067	-0.684	.494
	bo	4.624	2.555		1.810	.071		bo	7.329	0.164		44.767	< .0001
LAT	b3	-1.731	0.332	-4.080	-5.221	< .0001		b3	0.288	0.031	0.782	9.203	< .0001
	b2	-0.093	0.015	-10.624	-6.317	< .0001		b2	-0.005	0.002	-0.102	-3.042	.002
	b1	-0.001	0.000	-5.857	-6.308	< .0001		b1	0.000	0.000	-0.090	-1.063	.289
	bo	8.053	2.302		3.499	.001		bo	16.628	0.160		103.889	< .0001
INF	b3	-0.817	0.285	-2.894	-2.868	.004		b3	0.064	0.024	0.278	2.617	.009
	b2	-0.038	0.013	-6.527	-3.006	.003		b2	-0.002	0.001	-0.050	-1.202	.230
	b1	-0.001	0.000	-4.353	-3.631	< .0001		b1	0.000	0.000	0.201	1.895	.059
	bo	17.039	1.977		8.621	< .0001		bo	24.649	0.125		196.893	< .0001
SEP	b3	-1.426	0.283	-6.568	-5.034	< .0001		b3	-0.045	0.024	-0.221	-1.852	.065
	b2	-0.063	0.013	-14.052	-5.005	< .0001		b2	-0.001	0.001	-0.048	-1.010	.313
	b1	-0.001	0.000	-7.501	-4.839	< .0001		b1	0.000	0.000	0.265	2.219	.027
	bo	2.961	1.967		1.505	.133		bo	12.739	0.125		101.734	< .0001
APX	b3	-3.064	0.416	-9.165	-7.364	< .0001		b3	0.172	0.036	0.509	4.723	< .0001
	b2	-0.133	0.018	-19.411	-7.247	< .0001		b2	-0.016	0.002	-0.368	-8.670	< .0001
	b1	-0.002	0.000	-10.681	-7.222	< .0001		b1	-0.001	0.000	-0.324	-3.006	.003
	bo	-24.155	2.889		-8.362	< .0001		bo	-0.793	0.186		-4.265	< .0001
TOT	b3	-1.351	0.286	-5.181	-4.727	< .0001		b3	0.126	0.026	0.482	4.752	< .0001
	b2	-0.069	0.013	-12.892	-5.466	< .0001		b2	-0.004	0.001	-0.131	-3.284	.001
	b1	-0.001	0.000	-7.310	-5.613	< .0001		b1	0.000	0.000	0.043	0.427	.669
	bo	6.800	1.984		3.427	.001		bo	14.404	0.135		106.393	< .0001

y-translation						z-translation							
Coefficients						Coefficients							
		Unstandardized Coefficients		Standardized Coefficients	t	p			Unstandardized Coefficients		Standardized Coefficients	t	p
		B	Std. Error	Beta					B	Std. Error	Beta		
ANT	b3	0.346	0.028	0.974	12.333	< .0001	ANT	b3	0.234	0.029	0.671	7.948	< .0001
	b2	-0.007	0.001	-0.149	-4.788	< .0001		b2	-0.008	0.002	-0.168	-5.061	< .0001
	b1	-0.001	0.000	-0.263	-3.332	.001		b1	0.000	0.000	0.023	0.275	.783
	bo	8.026	0.144		55.911	< .0001		bo	7.558	0.151		50.056	< .0001
LAT	b3	0.267	0.025	0.951	10.668	< .0001	LAT	b3	0.262	0.026	0.722	9.971	< .0001
	b2	-0.005	0.001	-0.133	-3.781	< .0001		b2	-0.006	0.001	-0.127	-4.462	< .0001
	b1	-0.001	0.000	-0.334	-3.742	< .0001		b1	0.000	0.000	0.072	0.995	.320
	bo	15.650	0.128		122.302	< .0001		bo	16.419	0.135		122.033	< .0001
INF	b3	0.034	0.027	0.148	1.250	.212	INF	b3	0.058	0.025	0.247	2.339	.020
	b2	-0.002	0.001	-0.069	-1.482	.139		b2	-0.001	0.001	-0.036	-0.868	.386
	b1	0.000	0.000	-0.300	-2.542	.011		b1	0.000	0.000	0.241	2.283	.023
	bo	23.366	0.137		169.967	< .0001		bo	24.566	0.126		194.822	< .0001
SEP	b3	0.047	0.023	0.234	2.042	0.042	SEP	b3	-0.062	0.026	-0.286	-2.412	0.016
	b2	-0.008	0.001	-0.290	-6.430	< .0001		b2	-0.003	0.001	-0.097	-2.090	0.037
	b1	0.000	0.000	-0.183	-1.595	0.111		b1	0.001	0.000	0.349	2.946	0.003
	bo	12.468	0.118		105.274	< .0001		bo	12.977	0.132		98.591	< .0001
APX	b3	0.060	0.030	0.211	1.980	.048	APX	b3	0.200	0.035	0.599	5.638	< .0001
	b2	-0.016	0.002	-0.436	-10.410	< .0001		b2	-0.017	0.002	-0.400	-9.558	< .0001
	b1	0.000	0.000	-0.051	-0.483	.629		b1	-0.001	0.000	-0.481	-4.527	< .0001
	bo	-1.557	0.156		-9.985	< .0001		bo	-0.828	0.181		-4.566	< .0001
TOT	b3	0.151	0.021	0.731	7.028	< .0001	TOT	b3	.113	.027	.430	4.170	< .0001
	b2	-0.005	0.001	-0.193	-4.709	< .0001		b2	-.003	.001	-.096	-2.378	.018
	b1	0.000	0.000	-0.307	-2.955	.003		b1	.000	.000	.082	.799	.425
	bo	13.776	0.110		125.174	< .0001		bo	14.325	.139		102.944	< .0001

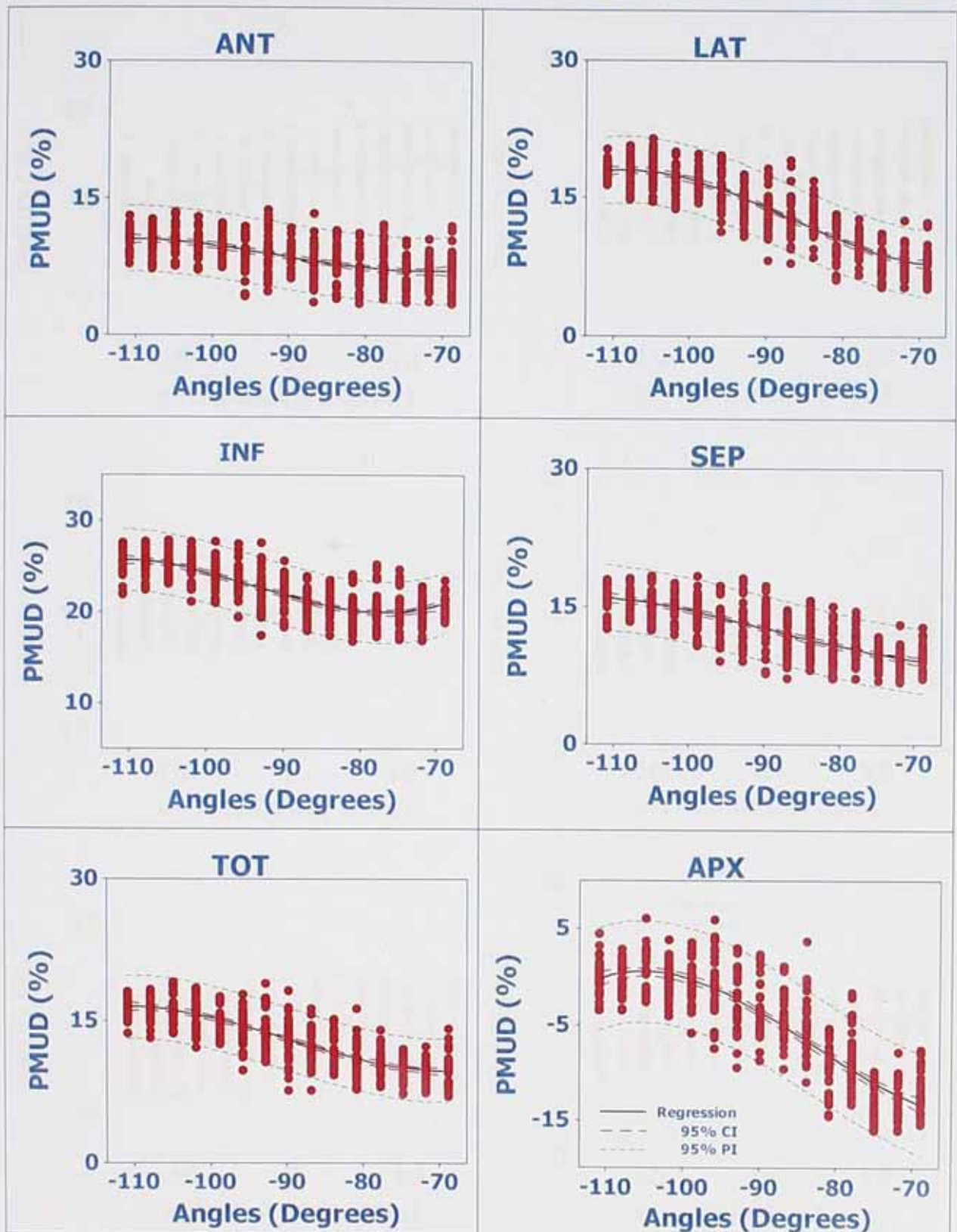
Cubic Regression - Phi (XZ Rotation)



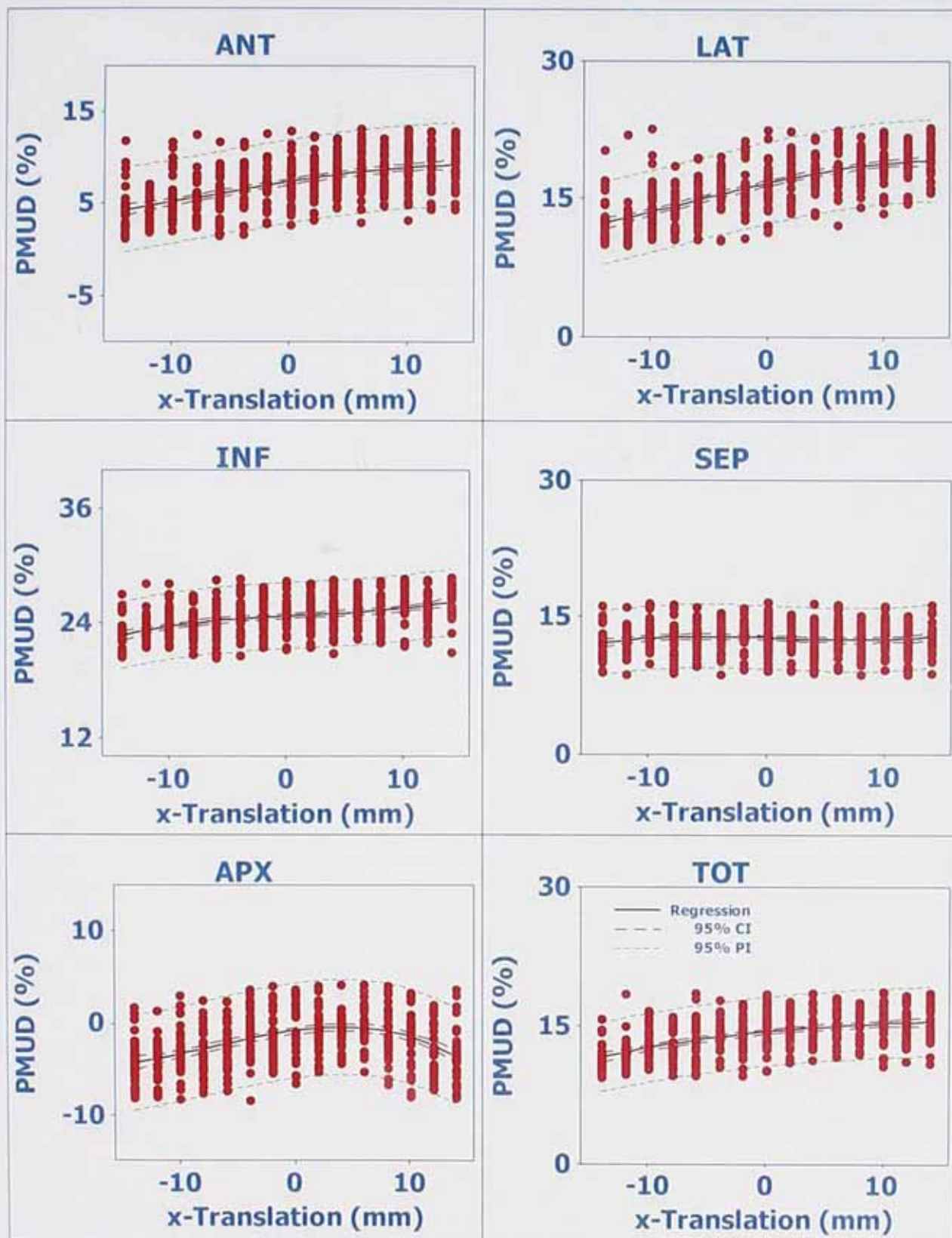
Cubic Regression - Psi (XY Rotation)



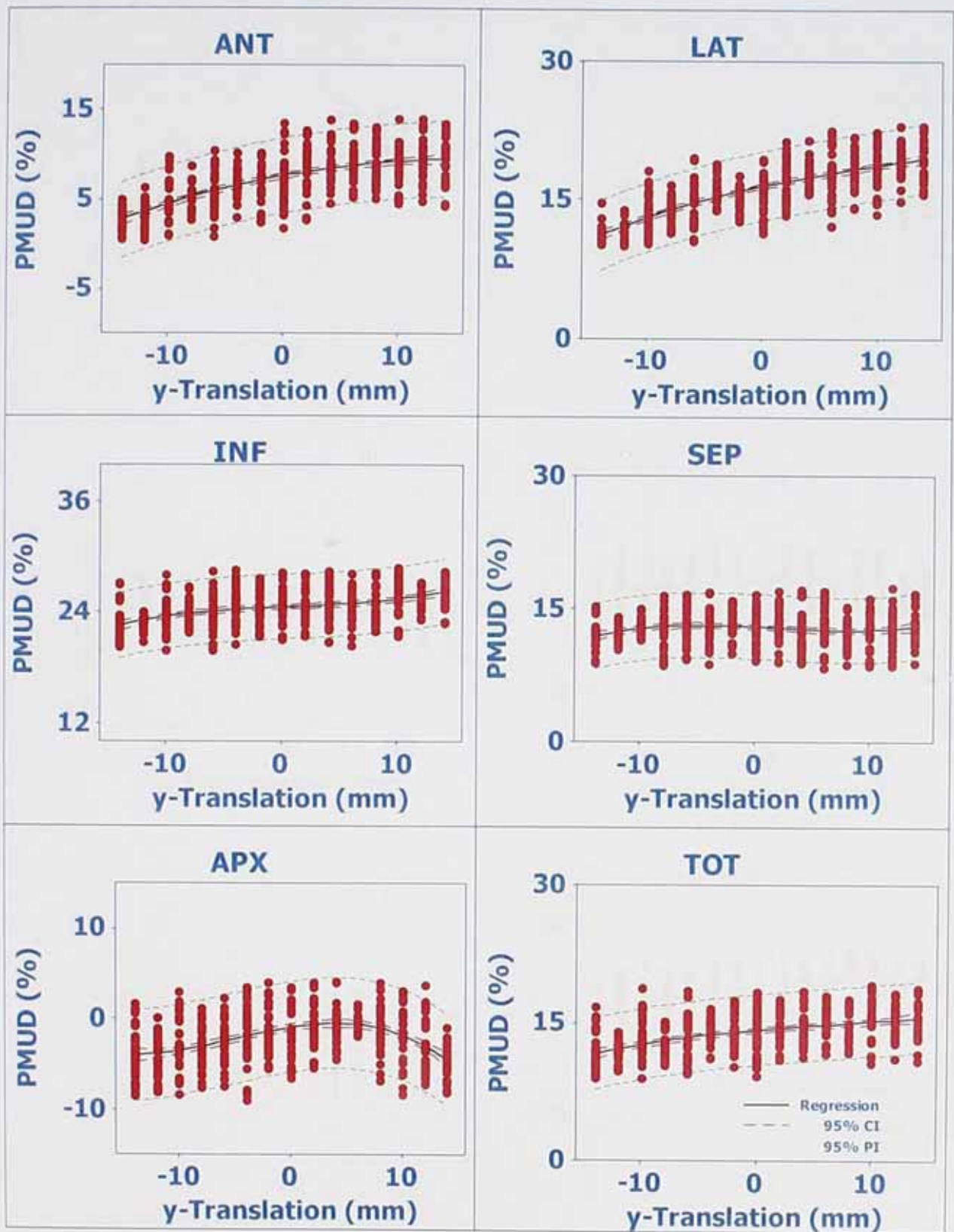
Cubic Regression - Beta (ZY Rotations)



Cubic Regression - X-Translation



Cubic regression - Y-Translation



Cubic Regression - Z-Translation

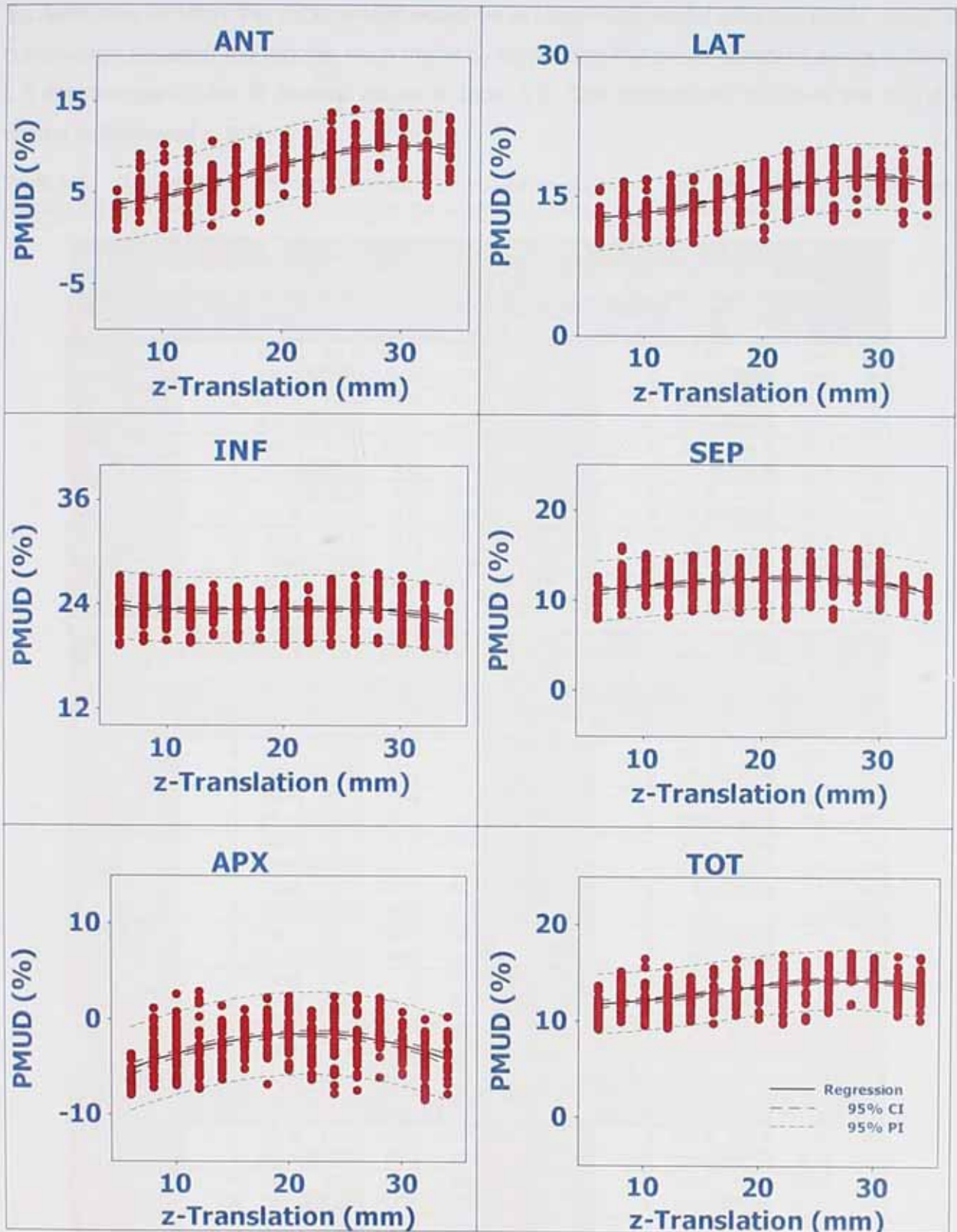


Figure 5-5: Cubic regression results showing the percentage intensity losses on the y-axis and indicating the 95% confidence and prediction intervals.

5.3.3 Comparison Between the Linear and Cubic Regression

To determine whether the cubic model would be an improved model over the linear model a comparison between the models were made by comparing the mean standard errors in table 5.8 and comparing the R Square values in table 5.9. The comparison between the F and t values is displayed in table 5.10.

Table 5-8: Comparison of the mean standard error between the linear and cubic regressions. The non-significant p-value is shown in red and therefore the significant p-values are those not marked in red.

Phi							Psi						
Comparing Mean Square Errors							Comparing Mean Square Errors						
Part	Source	df	Sum of Squares	Mean Square	F	p	Part	Source	df	Sum of Squares	Mean Square	F	p
ANT	Linear	1	8828.12	8828.12	1471.71	<.0001	ANT	Linear	1	682.46	682.46	166.42	<.0001
	Cubic	3	9030.68	3010.23	540.31	<.0001		Cubic	3	730.39	243.46	60.82	<.0001
LAT	Linear	1	3850.37	3850.37	784.70	<.0001	LAT	Linear	1	1682.96	1682.96	479.83	<.0001
	Cubic	3	4031.12	1343.71	297.05	<.0001		Cubic	3	1813.24	604.41	186.64	<.0001
INF	Linear	1	1028.37	1028.37	279.74	<.0001	INF	Linear	1	384.56	384.56	140.99	<.0001
	Cubic	3	1187.74	395.91	118.70	<.0001		Cubic	3	435.91	145.30	55.26	<.0001
SEP	Linear	1	22.98	22.98	6.59	0.011	SEP	Linear	1	207.59	207.59	55.16	<.0001
	Cubic	3	111.79	37.26	11.28	<.0001		Cubic	3	226.00	75.33	20.13	<.0001
APX	Linear	1	204.02	204.02	25.74	<.0001	APX	Linear	1	746.97	746.97	170.83	<.0001
	Cubic	3	578.26	192.75	27.06	<.0001		Cubic	3	748.42	249.47	56.83	<.0001
TOT	Linear	1	675.64	675.64	188.08	<.0001	TOT	Linear	1	646.74	646.74	209.43	<.0001
	Cubic	3	785.95	261.98	77.95	<.0001		Cubic	3	712.23	237.41	80.70	<.0001

Beta							x translation						
Comparing Mean Square Errors							Comparing Mean Square Errors						
Part	Source	df	Sum of Squares	Mean Square	F	p	Part	Source	df	Sum of Squares	Mean Square	F	p
ANT	Linear	1	896.83	896.83	175.74	<.0001	ANT	Linear	1	1158.19	1158.19	216.64	<.0001
	Cubic	3	746.94	248.98	75.11	<.0001		Cubic	3	1180.54	393.51	73.97	<.0001
LAT	Linear	1	5932.42	5932.42	1180.49	<.0001	LAT	Linear	1	2220.58	2220.58	428.67	<.0001
	Cubic	3	5973.46	1991.15	590.17	<.0001		Cubic	3	2273.39	757.80	149.03	<.0001
INF	Linear	1	1946.70	1946.70	471.77	<.0001	INF	Linear	1	381.44	381.44	121.78	<.0001
	Cubic	3	1991.74	663.91	229.72	<.0001		Cubic	3	397.10	132.37	42.55	<.0001
SEP	Linear	1	2525.08	2525.08	602.10	<.0001	SEP	Linear	1	0.72	0.72	0.23	0.633
	Cubic	3	2360.98	783.66	245.69	<.0001		Cubic	3	19.22	6.41	2.06	0.105
APX	Linear	1	10138.72	10138.72	1023.94	<.0001	APX	Linear	1	170.26	170.26	20.95	<.0001
	Cubic	3	10511.60	3503.88	485.80	<.0001		Cubic	3	748.55	249.52	36.33	<.0001
TOT	Linear	1	2714.36	2714.36	711.36	<.0001	TOT	Linear	1	621.30	621.30	0.23	0.633
	Cubic	3	2707.38	902.46	317.19	<.0001		Cubic	3	661.21	6.41	2.06	0.105

y translation							z translation						
Comparing Mean Square Errors							Comparing Mean Square Errors						
Part	Source	df	Sum of Squares	Mean Square	F	p	Part	Source	df	Sum of Squares	Mean Square	F	p
ANT	Linear	1	1964.36	1964.36	412.22	<.0001	ANT	Linear	1	2268.14	2268.14	517.52	<.0001
	Cubic	3	2407.31	802.44	196.18	<.0001		Cubic	3	2080.63	693.54	153.23	<.0001
LAT	Linear	1	1964.36	1964.36	412.22	<.0001	LAT	Linear	1	1095.85	1095.85	318.46	<.0001
	Cubic	3	1187.83	395.94	121.82	0.000		Cubic	3	2823.00	941.00	261.86	<.0001
INF	Linear	1	401.17	401.17	125.99	<.0001	INF	Linear	1	28.60	28.60	7.51	0.006
	Cubic	3	61.07	20.36	5.43	0.001		Cubic	3	420.00	140.00	44.36	<.0001
SEP	Linear	1	1.94	1.94	0.55	0.459	SEP	Linear	1	5.96	5.96	1.96	0.163
	Cubic	3	128.16	42.72	15.34	<.0001		Cubic	3	46.80	15.60	4.54	0.004
APX	Linear	1	91.83	91.83	11.29	0.001	APX	Linear	1	73.43	73.43	12.29	0.001
	Cubic	3	597.49	199.16	41.27	<.0001		Cubic	3	822.42	274.14	41.97	<.0001
TOT	Linear	1	596.59	596.59	153.73	<.0001	TOT	Linear	1	288.38	288.38	112.67	<.0001
	Cubic	3	362.69	120.90	50.28	<.0001		Cubic	3	620.78	206.93	53.83	<.0001

Table 5-9: Comparison of models of the linear regression against that of the cubic regressions. When the R Squares are compared, the best (highest) values are shown in green

Phi						Beta					
Comparing Models						Comparing Models					
Part	Source	R	RSquare	Adjusted R Square	Std. Error of the Estimate	Part	Source	R	RSquare	Adjusted R Square	Std. Error of the Estimate
ANT	Linear	0.798	0.637	0.636	2.215	ANT	Linear	0.520	0.271	0.269	2.025
	Cubic	0.886	0.784	0.783	2.360		Cubic	0.538	0.289	0.286	2.002
LAT	Linear	0.798	0.637	0.636	2.215	LAT	Linear	0.719	0.517	0.516	1.873
	Cubic	0.816	0.666	0.664	2.127		Cubic	0.000	0.000	0.000	0.000
INF	Linear	0.620	0.384	0.383	1.917	INF	Linear	0.489	0.239	0.238	1.652
	Cubic	0.666	0.444	0.440	1.826		Cubic	0.000	0.000	0.000	0.000
SEP	Linear	0.120	0.015	0.012	1.867	SEP	Linear	0.331	0.110	0.108	1.940
	Cubic	0.266	0.071	0.064	1.817		Cubic	0.000	0.000	0.000	0.000
APX	Linear	0.233	0.054	0.052	2.816	APX	Linear	0.525	0.276	0.274	2.091
	Cubic	0.392	0.154	0.148	2.669		Cubic	0.000	0.000	0.000	0.000
TOT	Linear	0.544	0.296	0.294	1.895	TOT	Linear	0.564	0.319	0.317	1.757
	Cubic	0.586	0.344	0.340	1.833		Cubic	0.000	0.000	0.000	0.000

Psi						x-translation					
Comparing Models						Comparing Models					
Part	Source	R	RSquare	Adjusted R Square	Std. Error of the Estimate	Part	Source	R	RSquare	Adjusted R Square	Std. Error of the Estimate
ANT	Linear	0.531	0.282	0.280	2.259	ANT	Linear	0.571	0.326	0.324	2.312
	Cubic	0.000	0.000	0.000	0.000		Cubic	0.576	0.332	0.328	2.306
LAT	Linear	0.851	0.725	0.724	2.242	LAT	Linear	0.699	0.489	0.488	2.276
	Cubic	0.000	0.000	0.000	0.000		Cubic	0.708	0.501	0.497	2.255
INF	Linear	0.716	0.513	0.512	2.031	INF	Linear	0.462	0.214	0.212	1.770
	Cubic	0.000	0.000	0.000	0.000		Cubic	0.472	0.223	0.217	1.764
SEP	Linear	0.757	0.573	0.572	2.048	SEP	Linear	0.023	0.001	-0.002	1.772
	Cubic	0.000	0.000	0.000	0.000		Cubic	0.117	0.014	0.007	1.764
APX	Linear	0.834	0.696	0.695	3.147	APX	Linear	0.211	0.045	0.043	2.851
	Cubic	0.000	0.000	0.000	0.000		Cubic	0.443	0.196	0.191	2.621
TOT	Linear	0.783	0.614	0.613	1.953	TOT	Linear	0.522	0.272	0.270	1.926
	Cubic	0.000	0.000	0.000	0.000		Cubic	0.538	0.290	0.285	1.907

y-translation						z-translation					
Comparing Models						Comparing Models					
Part	Source	R	RSquare	Adjusted R Square	Std. Error of the Estimate	Part	Source	R	RSquare	Adjusted R Square	Std. Error of the Estimate
ANT	Linear	0.692	0.479	0.478	2.183	ANT	Linear	0.732	0.536	0.535	2.093
	Cubic	0.754	0.569	0.566	2.022		Cubic	0.712	0.508	0.504	2.127
LAT	Linear	0.788	0.621	0.620	1.935	LAT	Linear	0.645	0.415	0.414	1.855
	Cubic	0.671	0.450	0.447	1.803		Cubic	0.799	0.638	0.635	1.896
INF	Linear	0.469	0.219	0.218	1.784	INF	Linear	0.128	0.016	0.014	1.951
	Cubic	0.188	0.035	0.029	1.937		Cubic	0.479	0.230	0.225	1.777
SEP	Linear	0.035	0.001	-0.001	1.877	SEP	Linear	0.066	0.004	0.002	1.745
	Cubic	0.306	0.094	0.087	1.669		Cubic	0.172	0.030	0.023	1.854
APX	Linear	0.157	0.025	0.022	2.852	APX	Linear	0.163	0.027	0.025	2.444
	Cubic	0.466	0.217	0.212	2.197		Cubic	0.469	0.220	0.215	2.556
TOT	Linear	0.505	0.255	0.254	1.970	TOT	Linear	0.448	0.201	0.199	1.600
	Cubic	0.503	0.253	0.248	1.551		Cubic	0.516	0.266	0.261	1.961

Table 5-10: F and t values and their significance

Statistics and their significance - Linear Regression													
	test	ANT		LAT		INF		SEP		APX		TOT	
		statistic	p										
Phi	F	358.23	<.0001	215.81	<.0001	45.42	<.0001	1.94	0.187	3.52	0.083	35.28	<.0001
	t (slope)	18.93	<.0001	14.69	<.0001	-6.74	<.0001	1.39	0.187	-1.88	0.083	5.94	<.0001
Psi	F	166.4234	<.0001	479.8287	<.0001	140.986	<.0001	55.16	<.0001	170.8328	<.0001	209.43	<.0001
	t (slope)	12.90	<.0001	21.90	<.0001	11.87	<.0001	7.43	<.0001	13.07	<.0001	14.47	<.0001
Beta	F	175.7442	<.0001	1180.491	<.0001	471.77	<.0001	602.1024	<.0001	1023.935	<.0001	711.3595	<.0001
	t (slope)	-13.26	<.0001	-34.36	<.0001	-21.72	<.0001	-24.54	<.0001	-32.00	<.0001	-26.67	<.0001
x-trans	F	216.6435	<.0001	428.673	<.0001	121.784	<.0001	0.228	0.633	20.947	<.0001	167.424	<.0001
	t (slope)	14.72	<.0001	20.70	<.0001	11.04	0.633	0.48	<.0001	4.58	<.0001	12.94	<.0001
y-trans	F	412.2211	<.0001	412.2211	<.0001	125.9891	<.0001	0.550054	0.459	11.29138	0.001	153.7272	<.0001
	t (slope)	20.30	<.0001	27.09	<.0001	11.22	<.0001	0.74	0.459	3.36	0.001	12.40	<.0001
z-trans	F	517.5236	<.0001	318.455	<.0001	7.51074	0.006	1.95659	0.163	12.29254	0.001	112.669	<.0001
	t (slope)	22.75	<.0001	17.85	<.0001	-2.74	0.006	1.40	0.163	3.51	0.001	10.61	<.0001

Statistics and their significance - Cubic Regression													
	test	ANT		LAT		INF		SEP		APX		TOT	
		statistic	p										
Phi	F	540.31	<.0001	297.05	<.0001	118.70	<.0001	11.28	<.0001	27.06	<.0001	77.95	<.0001
Psi	F	60.82	<.0001	186.64	<.0001	55.26	<.0001	20.13	<.0001	56.83	<.0001	80.7	<.0001
Beta	F	75.11	<.0001	590.17	<.0001	229.72	<.0001	245.69	<.0001	485.8	<.0001	317.19	<.0001
x-trans	F	73.97	<.0001	149.03	<.0001	42.55	<.0001	2.06	0.105	36.33	<.0001	60.58	<.0001
y-trans	F	196.18	<.0001	121.82	0.000	5.43	0.001	15.34	<.0001	41.27	<.0001	50.28	<.0001
z-trans	F	153.23	<.0001	261.86	<.0001	44.36	<.0001	4.54	0.004	41.97	<.0001	53.83	<.0001

5.3.4 Final Outcome of the Analysis

After deciding that the linear model is a valid model and sections 5.4.1 and 5.4.2 suggested that this will be the most suitable model to use, the difference in the percentage intensity loss to be expected as a result of a unit change in the independent value was calculated and are displayed in table 5.11 and the minimum and maximum values in the percentage intensity losses for the ranges used in the studies, are displayed in table 5.12.

Table 5-11: Percentage intensity losses at the reference orientation of the Visible Human and the percentage unit intensity losses when deviating from it when using the linear regression model

Percentage Count Loss							
	Part:	ANT	LAT	INF	SEP	APX	TOT
Phi	Ref*	9.1	16.5	23.5	13.8	-1.7	14.6
	%UCL	0.51	0.34	-0.17	0.03	-0.08	0.14
Psi	Ref*	13.9	22.6	27.7	15.3	2.4	18.8
	%UCL	0.14	0.22	0.11	0.08	0.15	0.14
Beta	Ref*	9.0	13.7	22.0	13.2	-3.5	13.3
	%UCL	-0.11	-0.28	-0.16	-0.18	-0.37	-0.19
x-trans	Ref*	7.2	16.5	25.0	12.9	-1.0	14.5
	%UCL	0.19	0.26	0.11	0.01	0.07	0.14
y-trans	Ref*	7.1	15.7	24.6	12.8	-1.3	13.9
	%UCL	0.24	0.29	0.11	0.01	0.05	0.13
z-trans	Ref*	8.1	15.3	22.9	12.1	-1.2	13.7
	%UCL	0.26	0.18	-0.03	0.01	0.05	0.09

* Values for the orientation of the 'Visible Human'

%UCL - Percentage Unit Count Loss

Table 5-12: The maximum intensity losses found for the variation ranges used in this study

Minimum and Maximum values*			ANT	LAT	INF	SEP	APX	TOT
Phi	bot	-38	-0.5	9.6	27.9	12.4	0.2	11.7
	top	-10	11.9	17.3	21.8	11.9	-4.8	14.3
	range		12.4	7.6	6.1	0.5	5.0	2.5
Psi	bot	-59	10.9	17.9	24.8	13.6	-0.6	15.4
	top	-31	14.8	24.1	27.9	15.7	4.0	19.5
	range		3.9	6.3	3.0	2.1	4.6	4.1
Beta	bot	-111	10.5	18.1	25.6	15.9	0.3	16.6
	top	-69	7.2	8.3	20.6	9.4	-12.1	10.1
	range		3.3	9.7	4.9	6.5	12.4	6.5
x-trans	bot	14	9.3	19.3	26.4	12.8	-3.2	15.7
	top	-14	4.3	12.5	22.5	11.9	-4.2	11.6
	range		4.9	6.8	3.9	0.9	0.9	4.0
y-trans	bot	14	9.5	19.3	26.3	13.0	-4.5	15.7
	top	-14	2.6	11.3	22.7	11.8	-3.9	11.9
	range		6.9	8.0	3.6	1.2	0.6	3.7
z-trans	bot	34	10.0	17.0	22.1	10.9	-3.9	13.7
	top	6	2.6	12.2	23.1	10.1	-6.3	11.1
	range		7.4	4.8	1.0	0.7	2.3	2.6

*Values for the range of angles used in this study.

5.4 Discussion and Conclusion

5.4.1 Deciding Which Model to Use

For all six of the variation studies linear and cubic regressions have been done. These results are summarised in tables 5.2 to 5.4 for the linear regression analysis and tables 5.5 to 5.7 for the cubic regression analysis providing the goodness of fit statistics. Figures 5.4 and 5.5 contain the graphical presentation of these analysis including 95% prediction and confidence intervals as graphical presentations.

These graphical presentations together with the numerical results of tables 5.8 to 5.10 should be analysed to determine the appropriate statistical model to use in the six variation studies. Section 3.7.1 discussed the different techniques to be used in deciding the choice of an appropriate model and an important aspect of that discussion is the fact that the model should be simple and easy to interpret. The simplicity of the model will be improved if the same model, either linear or cubic, are used for all the segments in a specific variation study. Using the same model for all the segments of all six variation studies will maximise the simplicity but this can only be done if a single model is suitable for all of them. Taking these

arguments into consideration a model can be used even if it is less appropriate than another model according to the results but the results also show that it is still a valid model.

5.4.2 Variation Studies

Both the graphical analysis and the numerical analysis confirm that both the linear and cubic regression models are valid statistical models for all the segments in all the variation except for those marked in red in table 5.10. For these segments the mean will be the most appropriate statistical model, indicating that the amount of intensity losses is not influenced by variations in the specific variation parameter.

Based on the graphical analysis and the numerical analysis in table 5.9 the cubic regression is the best presentation of most of the data but in all the cases, except those exceptions marked in red in table 5.10, the linear model is also a valid model. To make the outcome of the analysis as simple as possible to implement and for it to be useful the choice of the linear regression as a statistical model will be the most appropriate for the six variation studies.

By applying these models one can see that changes in most parameters will lead to a comparable change in non-uniformity. Changes in the phi angle have the biggest effect on the anterior wall but none on the septal and very little on the septum. Therefore there can be potentially substantial differences in the anterior segment between patients which may result in "defects" being reported in the final study. It is already known that this is an area affected mostly by breast attenuation in females (reflected in the changes in the body size) but this study shows the orientation of the heart can influence this phenomenon substantially. In addition the anterior wall is also one of the most visible parameters in the display on the final reconstructed images. Changes in other parameters also have an effect in most segments but it seems that none of the translation variations have much effect on the uniformity in the apex and septum. The z-translations also have little effect on changes in the inferior wall which is a very interesting observation. It is widely accepted that the inferior wall is affected substantially by the tissue underneath the diaphragm pushing upwards. The z-translation is the parameter influencing the relative position of these tissues the most. Table 5.11 gives the values of the Visible Human and the studies' estimate of changes due to patient variability.

5.4.3 Summary

Table 5.11 summarises the percentage intensity loss for each segment for the orientations and positions of the heart of the Visible Human as well as the percentage intensity loss to be expected for a unit change in the variation (1 degree or 1 mm), assuming a linear regression model. Although these unit changes can be used to predict the amount of intensity loss in a specific segment when a specific variation between a patient study and that of the Visible Human is known. The table at present will be of limited use because only one variation is

modelled and the 5 other variations must be those of the Visible Human. For example, if the phi angle difference between the patient and the Visible Human is 10° , meaning the patient's phi orientation is -30° , as opposed to -20° for the Visible Human, one can expect a percentage intensity loss of 4.1% (9.1% - 5%) for the patient in the anterior segment. This will only be a valid argument if the psi angle, beta angle, x-trans, y-trans and z-trans of the patient is the same as that of the Visible Human. The statistical models in this study do not make provision for situations where two or more of the orientation differs from the Visible Human but a number of parameters show only limited variation. Therefore it could be possible that changes in several parameters might result in a linear combination of the effects of each parameter change. The main benefit from this study is that it provides an insight into the level of variation one can expect in a specific segment when a specific parameter changes. These models also demonstrate the complexity of intensity losses caused in different segments of the left ventricle when analysing the intensity distribution in it and the absolute necessity of techniques to compensate for these permutations. Further study with the model used here would evaluate the effect of variation of groups of the parameters, but, as the study has demonstrated the need for correction techniques at this stage, the further study is of only academic value.

To emphasise this it will be worthwhile to remember what was mentioned earlier, changes of up to 57° have been reported between patients for the vertical orientation (phi), which, from this analysis, indicates a difference of up to 28.5% (0.51% difference in intensities for every 1° change) in the percentage intensity loss in the anterior segment. This difference in intensity loss will exist even if the patients under comparisons are of the same gender, the same weight, height, chest size, etc., meaning exactly the same anatomy with the only difference the vertical orientation of the heart in the thorax. This means that two patients with exactly the same anatomy with the only difference between them the orientation of the heart, can present two completely different final image sets, one could potentially be classified as normal and the other as abnormal, if no corrections are applied.

Table 5.12 gives the range of intensity losses for the minimum and maximum values of the different values used in this study for the angles and translations. However, precise ranges of all of the anatomical variations in the general population are not known, except for the phi angle as mentioned previously. A best estimate for the other 5 parameters has been used but further work to establish the normal range in humans is required to confirm this, and therefore further refinement of the minimum and maximum values of intensity losses is worthwhile.

The previous chapter investigated the changes in the segments of the left ventricle because of differences between genders and studied which part of the thorax is mostly responsible for the loss of uniformities in the polar maps and it was clear that the heart itself is a very

important factor in the loss on polar map uniformities, as was illustrated in section 4.3.5. In this chapter the changes in intensity losses because of different orientations and positions of the heart were investigated. Such intensity losses will manifest themselves as polar map uniformity losses. This again emphasises the complexity of intensity losses caused in the final reconstructed images of the left ventricle, without detailed knowledge of the anatomy of the individual patient. The range of the intensity losses in different individuals indicates that an individual, rather than a population average correction, is essential. Currently transmission based attenuation correction methods are commercially available as well as corrections for the other permutations leading to these intensity losses, i.e. partial volume, scatter, etc. but it was demonstrated in chapter 2 that they suffer from important drawbacks and lack universal acceptance. This chapter, together with the previous one, highlighted the range of intensity losses and their impact on the final reconstructed images of the left ventricle. Armed with this knowledge one can investigate the effectiveness of the mentioned commercially available systems. The next chapter will investigate how a specific commercially available system is actually performing in correcting for these intensity losses.

Chapter 6 - Determination of the Extent of Attenuation Correction in Patients by Using a Commercially Available Correction Solution

6.1 Introduction

As described in detail in chapter 2 the full clinical potential of Myocardial Perfusion Imaging (MPI) has not been realised because of numerous factors producing artefacts that degrade image quality and result in misinterpretation of the results¹⁹⁸. Photon attenuation, scatter radiation, partial-volume errors, and other perturbations compromise the accuracy obtainable with MPI⁴⁹.

The application of depth-dependent resolution recovery, attenuation correction using external source devices, and scatter correction has been developed for Nuclear Medicine Imaging in general, and it has been suggested that these techniques will also improve the specificity for MPI and an improvement in its specificity and substantial advances had been made in implementing these solutions.

Attenuation correction, and transmission based methods in particular, still lack wide spread implementation and some of the reasons for this lack of acceptance are that it seems to introduce additional artefacts, and add cost and complexity. The results of the studies in Chapters 3 to 5 illustrate the importance of attenuation correction and the risk of not implementing it. Although transmission based attenuation correction is viewed with a great deal of scepticism, it is currently commercially available on most gamma camera systems. It is often combined with correction methods for both depth-dependent collimator blurring and scatter. In this chapter a study to evaluate such a commercially available solution which uses transmission scanning, scatter correction and depth-dependent resolution recovery is described. The study attempted to determine the level of Improvement achieved with such a

method compared to the total intensity losses estimated in the phantom studies in chapter 4 despite the reservation about using transmission scanning¹³¹. This will be important because the implementation of these available systems could be used to substantially improve the outcome of MPI. However, this needs to be carefully evaluated, as such systems could introduce alternative artefacts. The closeness of the correction of this commercial system to the ideal will determine whether the system should be implemented despite its other drawbacks, or whether the lengthy development of alternative emission-based methods is worthwhile.

The clinical attenuation compensation techniques currently available commercially^{199,200,201,202,203}, use attenuation maps reconstructed from data obtained in transmission scans. Siemens introduced a 3D OSEM reconstruction algorithm utilising Transmission Attenuation Correction, Scatter Compensation as well as 3D Resolution Recovery and 3D Collimator and Detector Response Correction²⁰². Because Transmission based attenuation corrections are not universally accepted, it was decided to determine the improvement achieved by this specific implementation of a Transmission Based Attenuation correction technique together with a Resolution Recovery Implementation (TBAR) and to compare the intensity gains achieved by the commercial system to the losses predicted by the Monte Carlo simulations in Chapter 4.

The questions which this study will attempt to answer are:

1. What is the intensity gain in each of the 9 segment model when using TBAR?
2. What is the difference in the intensity gain between male and female patients?
3. How does the amount of intensity gain obtained by using TBAR in male and female patients compare to the losses predicted by the Monte Carlo simulations?
4. Is there a intensity reduction in the apical parts of the left ventricle in the attenuation correction images as compared to the non-attenuation images?
5. What is the total intensity gain experienced in the different segment of the final left ventricular images?
6. Did the basal parts of the left ventricle experience a bigger intensity gain than the apical regions?
7. Did the inferior wall experience the most gain and if so, is that true for both male and female patients?
8. Did the anterior wall in female patients experience a significant intensity gain?
9. How does the overall amount of intensities gained by using TBAR compare to the losses predicted by the Monte Carlo simulations?

This study will investigate these questions by studying the specific implementation using scanning line sources of Gd-153 with parallel-hole collimators which is available on the Siemens c.cam system known as c.clear and the images reconstructed with Flash 3D, the resolution recovery implementation discussed in paragraph 2.3.5. The effectiveness of this

implementation was evaluated using the same analysis as described in chapters 4 and 5 using Monte Carlo simulations, and compared to the results of those simulations.

6.2 Methods

6.2.1 Patient Selection and Analysis

The purpose of this study was to estimate the level of the effectiveness of the above mentioned commercial system in correcting for the intensity losses in MPI quantified in the previous analyses in this project. This was done by comparing intensity gains in patient studies against the intensity losses predicted by the Monte Carlo simulations in chapter 4. There were some limitations in the current study relating to the availability and interpretation of patient data. Only patients who were judged to have normal MPI scans by standard clinical reporting were included. The study also included patients x and y where the clinician had identified defects which he decided had no clinical relevance, and were artefacts of the imaging process. This analysis therefore represents a preliminary study which should be extended in future using more data and abnormal scans, where the confirmation of defects can be established as artefacts, or otherwise, in a research study which includes a "gold standard" test such as angiography.

Twenty-one male patients (mean age \pm SD was 66.6 ± 8.3) and nineteen female patients (mean age \pm SD was 59.4 ± 12.6) were analysed. These patients were imaged on a c-cam system in the incline position with the arms placed above their heads. The gamma camera system uses a dual head configuration with the two heads at a 90° angle. Data were acquired in a 128×128 matrix with a pixel size of 0.48×0.48 cm.

Simultaneous transmission/emission scanning was performed. Emission data was acquired with a 15% energy window centred at 140 keV. These patients had been referred for standard clinical studies with ethical approval that the resulting data could be used in this study. Further acquisition parameters were 2.813° per step, 90° each head and 15 seconds per projection starting at the LAO and ending in the RPO position. Transaxial images of 128×128 pixels were reconstructed using 8 iterations with 4 subsets of OSEM which included resolution recovery. The Convolution Kernel used was: 3DOSEM, 8i, 4s\Btw, 0.40, 5, which indicates a 3D implementation of OSEM, 8 iterations with 4 subsets and the reconstruction filter was a Butterworth filter with order 5 and cut-off of 0.4.

The choice of the 20 % energy window for the Monte Carlo simulations was based upon the examples provided by the authors of the simulation package and was also the window used in the verification simulations, and subsequently all the Monte Carlo simulations. However, modern gamma cameras now use a 15% energy window and the nature of the project was such that patient settings could not be altered.

From reangulated tomographic images, polar maps of regional myocardial tracer uptake were generated using the commercial package (4DMSPECT developed at the University of Michigan). From non-corrected and attenuation-corrected images, average tracer uptake was measured in 9 polar map segments (B-ANT: Basal anterior, A-ANT: Apical anterior, B-LAT: Basal lateral, A-LAT: Apical lateral, B-INF: Basal inferior, A-INF: Apical inferior, B-SEP: Basal septal, A-SEP: Apical septal, APX: Apical) and the percentage gain in each segment calculated.

6.2.2 Analysing the "Distortion" on the Left Ventricle

For both the male and female patients, the PMUD, PMUDI and the FI were calculated as described in chapter 5. These results were used to establish the effects on each of the 9 polar map regions as described in chapter 5.

6.2.3 Comparing the Basal and Apical Portions for Both Genders

To investigate and quantify the "distortion" of the uniformity of the intensity distribution in the reconstructed left ventricle the PMUD for all the 9 segments was calculated and compared.

If the null hypothesis, that the whole thorax as attenuation medium does not correct for the position and intensity distribution in the patient, is true the PMUD of each segment will be equal to zero.

The experimental hypothesis was that effects such as attenuation, scatter and the partial volume effect do alter the position and intensity distribution in the final image, which lead to the original "distortion" existing in the final images, and that correcting for these effects leads to a significant difference between the means of the segments when they were compared and the values of the PMUD's will not be equal to zero.

In this case the manipulations were done on the same patient images and therefore the dependent means t-test was used to test the null hypothesis and it was a two-tailed test. It was found that the null hypothesis does not hold true, i.e. the experimental hypothesis is valid, the effect size was calculated and expressed as r-values to calculate the extent of "distortion" in the final images of the left ventricle.

6.2.4 Comparing the Results of the Male Patients Against Those of the Female Patients

Using the PMUD and FI a comparison was done between the male and female studies to see which region are the most influenced by these permutations, described in chapter 2, for the two genders and how they differ, especially the inferior wall for both and the anterior wall

for females. The difference between the basal and apical regions was also determined. The amount of intensity gained was also compared by using the FI.

6.2.5 Comparing the Results of the Patients Against Those Predicted by the Monte Carlo Simulations

The means of the PMUD and FI for the male and female patients were compared against the PMUD and FI of the Monte Carlo simulated male and female patients by using the independent samples t-test. A comparison has also been made between the MFI's, i.e. the mean of the values of the 9 segments, to establish the intensities gained by implementing TBAR.

6.3 Results

6.3.1 Tests to Ensure that a Parametric Model Will be Valid for the Attenuation Corrected Patient Studies on the Commercial System

Box-plot methods and z-scores assured the integrity of the data. Levene's tests confirmed the homogeneity of variance (homoscedasticity) and inspection also confirmed that they adhere to the principles of independence and interval data. Using the z-scores for skewness and kurtosis, as well as the Shapiro-Wilk test confirmed the normal distribution of the data.

6.3.2 The "Distortion" in the Left Ventricle in the Attenuation Corrected Patient Studies

Figure 6.1 illustrates the PMUD values obtained for the 9 segment model for both the male and female patients when using transmission attenuation correction and table 6.1 displays the mean and 95% confidence intervals for these PMUDs.

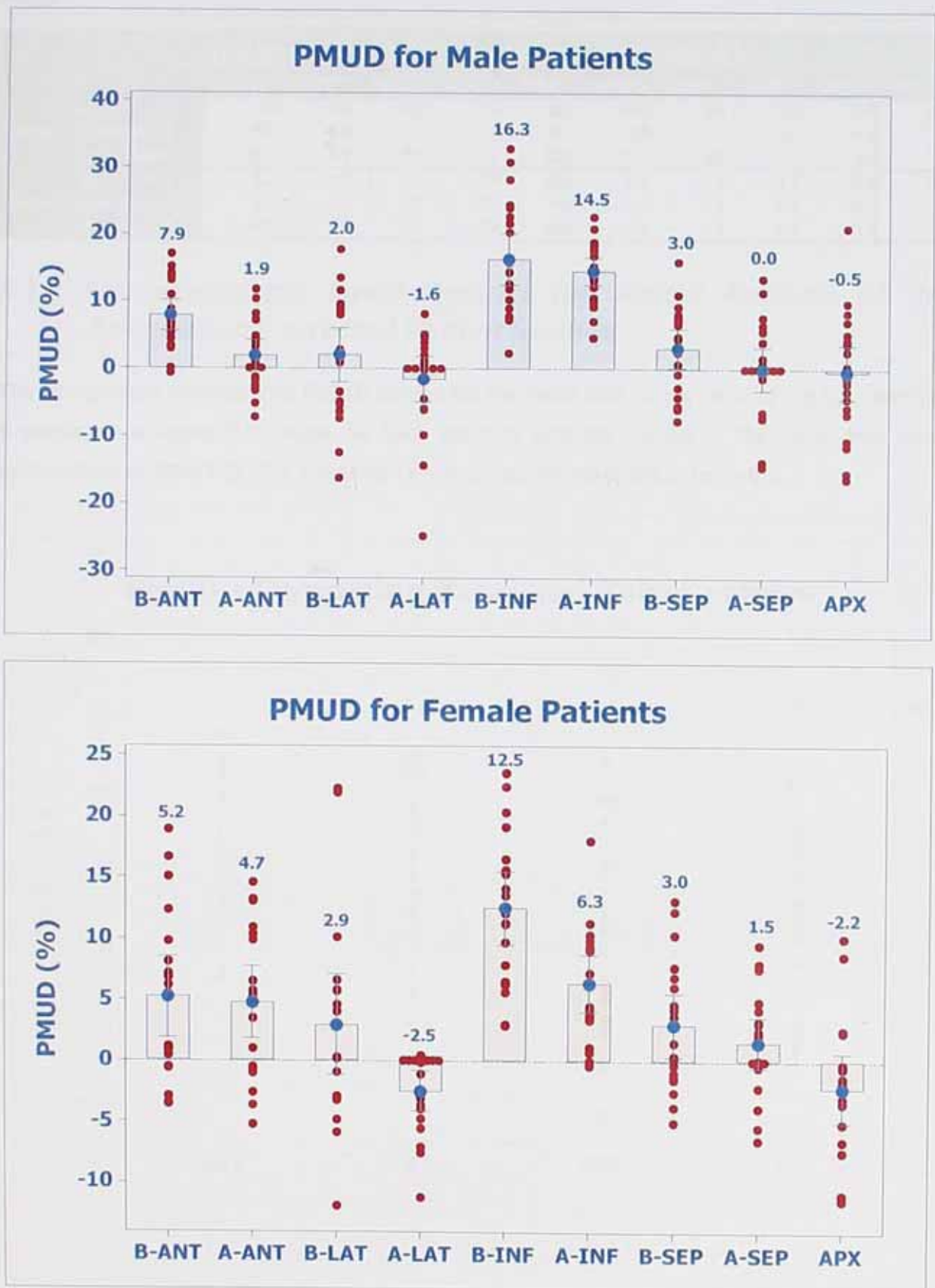


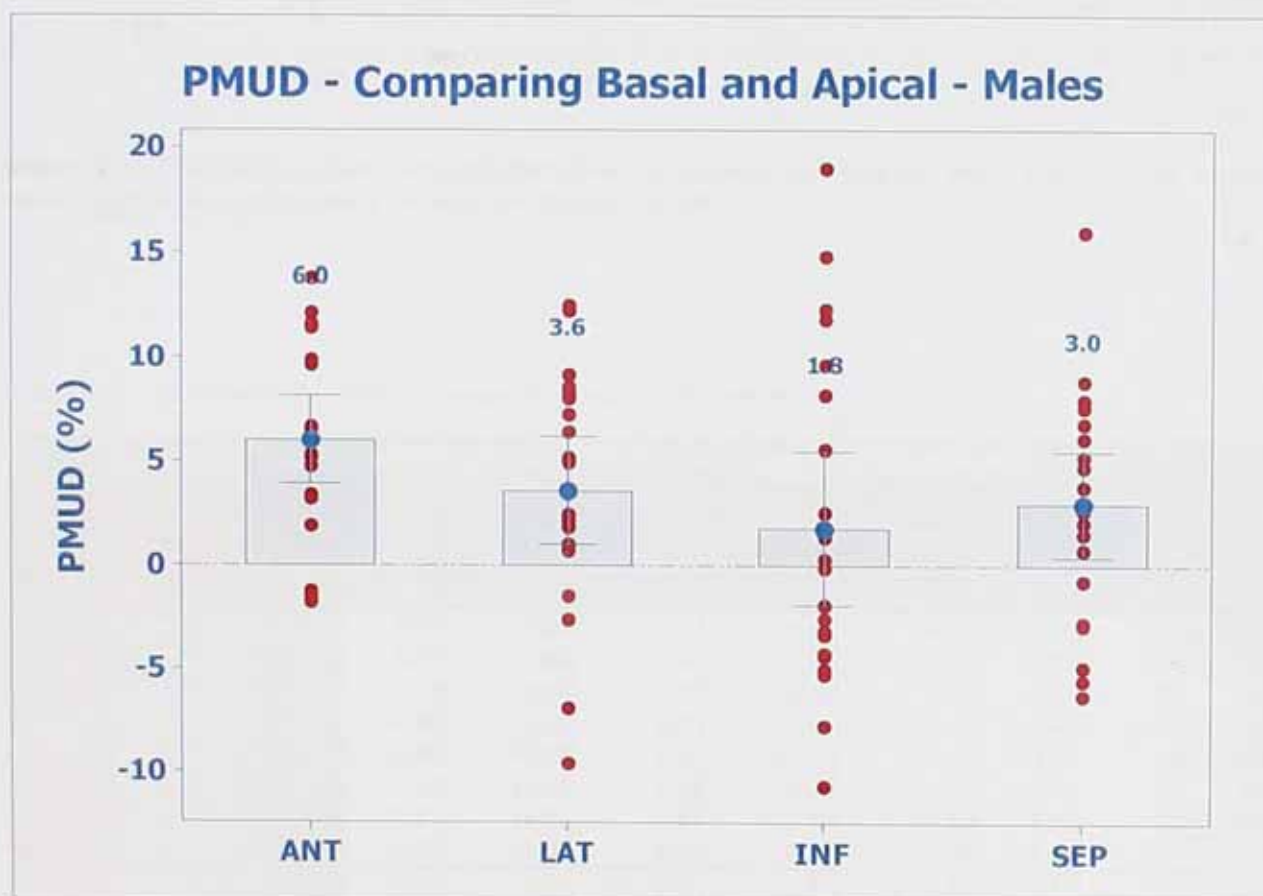
Figure 6-1: PMUD of the 9 segments of male and female patients as a result of transmission attenuation corrections using Gd-153 line sources.

Table 6-1: Summary of the means of the PMUD values for both male and female patients as well as the PMUDI

The Mean and 95% CI for Means of the PMUD											
		B-ANT	A-ANT	B-LAT	A-LAT	B-INF	A-INF	B-SEP	A-SEP	APX	PMUDI
Male	Mean	7.9	1.9	2.0	-1.6	16.3	14.5	3.0	0.0	-0.5	4.8
	Lower Bound	5.6	-0.5	-2.0	-5.0	12.5	12.5	0.1	-3.3	-4.6	
	Upper Bound	10.2	4.2	6.0	1.8	20.2	16.6	5.9	3.3	3.6	
Female	Mean	5.2	4.8	2.9	-2.5	12.5	6.3	2.9	1.5	-2.2	3.5
	Lower Bound	1.9	1.8	-1.2	-4.1	9.5	4.0	0.4	-0.5	-5.0	
	Upper Bound	8.6	7.7	7.1	-0.8	15.5	8.6	5.5	3.6	0.6	

6.3.3 Comparing the Basal Against the Apical Regions of the Attenuation Corrected Patient Studies

The comparison between the PMUD values for the basal and apical parts of the left ventricle is displayed in figure 6.2 below, for both genders and the results of the dependent t-test summarised in table 6.2. The calculated r-values are represented in table 6.3.



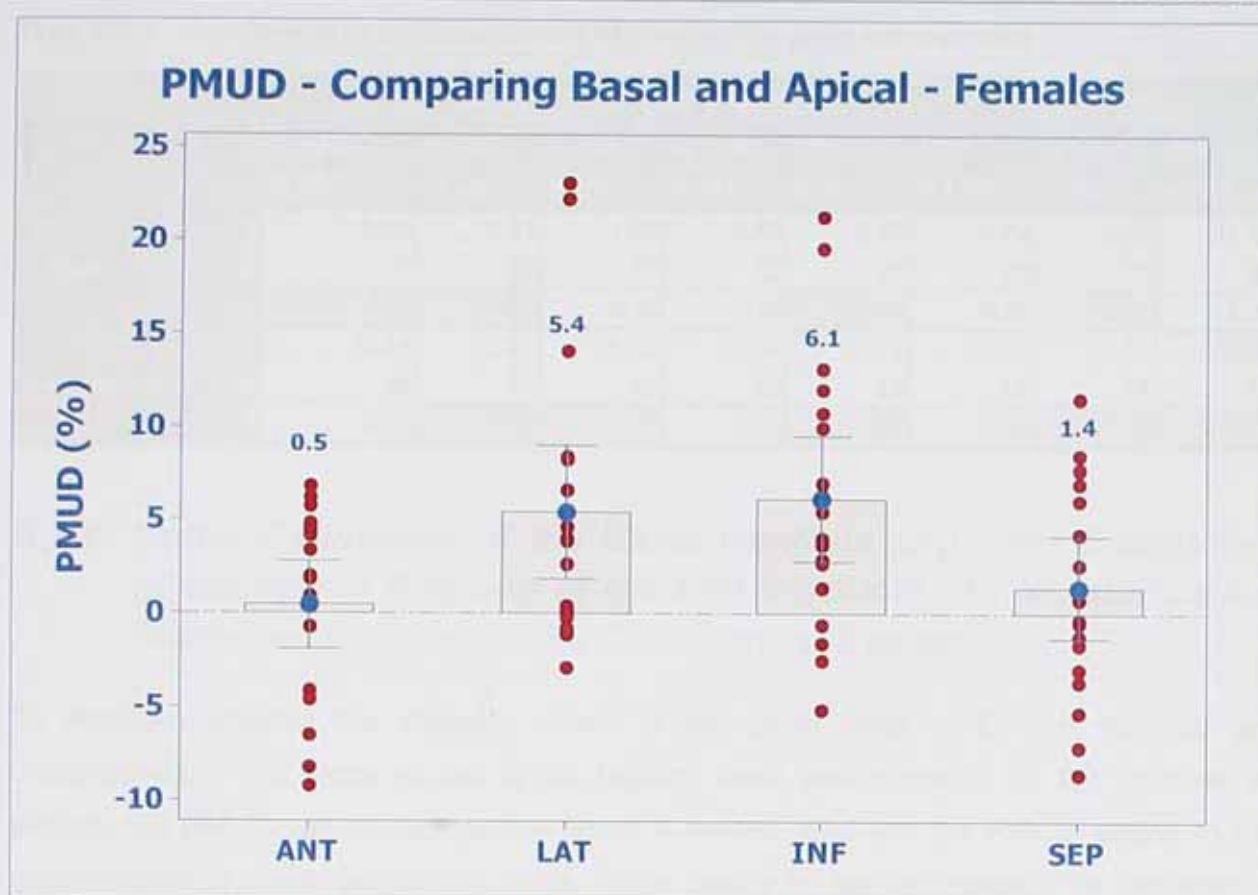


Figure 6-2: The PMUD's when comparing the difference between the basal and apical regions of the anterior, lateral, inferior and septal walls in the male and female patients.

Table 6-2: Comparing the PMUD's between the apical and basal parts

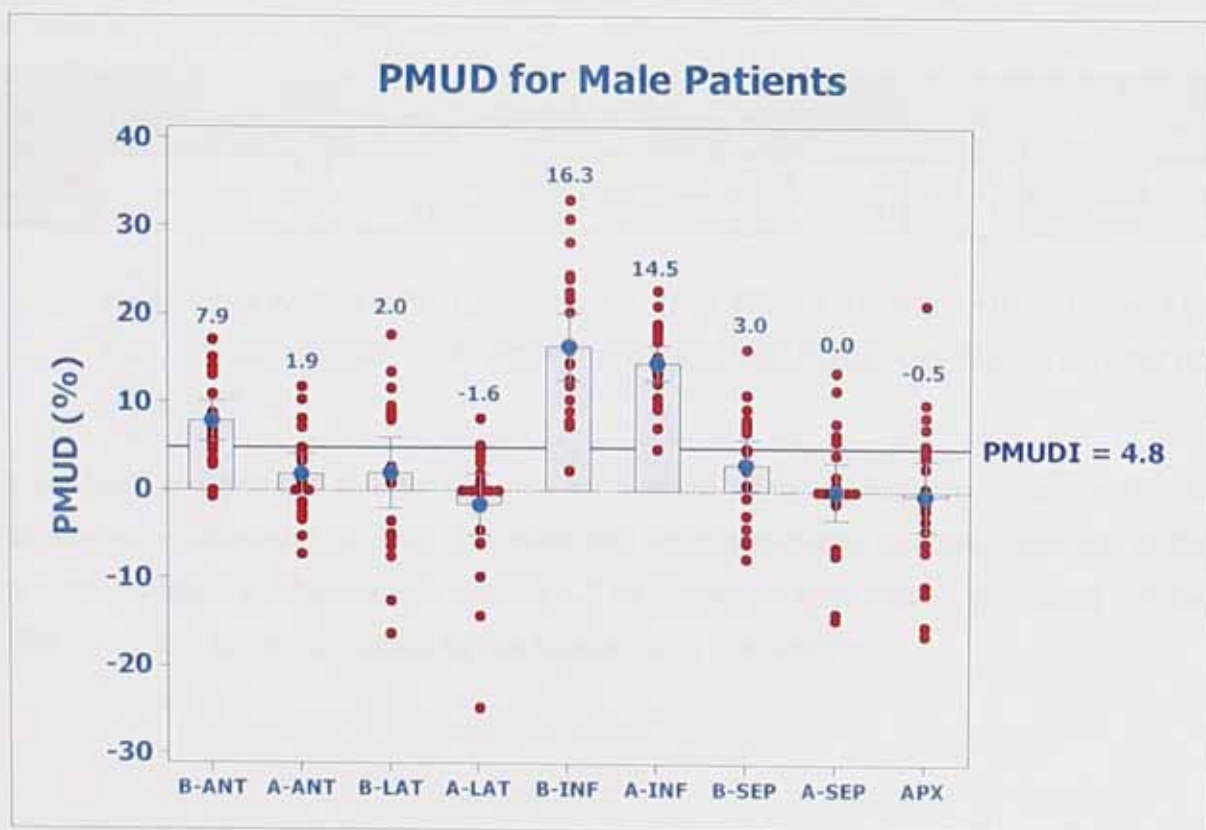
Paired Samples Test - PMUD - Comparing Basal vs Apical									
		Paired Differences					t	df	p (2-tailed)
		PMUD	Std. Deviation	Std. Error PMUD	95% Confidence Interval of the PMUD				
					Lower	Upper			
Male	A_ANT - B_ANT	-6.04	4.63	1.01	-8.15	-3.93	-5.98	20	.000
	A_LAT - B_LAT	-3.61	5.69	1.24	-6.20	-1.02	-2.91	20	.009
	A_INF - B_INF	-1.79	8.07	1.76	-5.46	1.88	-1.02	20	.322
	A_SEP - B_SEP	-2.98	5.55	1.21	-5.50	-0.45	-2.46	20	.023
	APX - B_ANT	-8.40	10.78	2.35	-13.31	-3.49	-3.57	20	.002
	APX - B_LAT	-2.47	14.36	3.13	-9.00	4.07	-0.79	20	.440
	APX - B_INF	-16.81	14.02	3.06	-23.19	-10.43	-5.50	20	.000
	APX - B_SEP	-3.47	10.66	2.33	-8.32	1.39	-1.49	20	.152
Female	A_ANT - B_ANT	-0.46	4.88	1.12	-2.81	1.89	-0.41	18	.687
	A_LAT - B_LAT	-5.43	7.35	1.69	-8.97	-1.89	-3.22	18	.005
	A_INF - B_INF	-6.15	7.02	1.61	-9.54	-2.77	-3.82	18	.001
	A_SEP - B_SEP	-1.41	5.66	1.30	-4.14	1.32	-1.09	18	.292
	APX - B_ANT	-7.40	10.19	2.34	-12.31	-2.49	-3.17	18	.005
	APX - B_LAT	-5.14	12.64	2.90	-11.23	0.96	-1.77	18	.093
	APX - B_INF	-14.67	9.64	2.21	-19.32	-10.02	-6.63	18	.000
	APX - B_SEP	-5.14	9.01	2.07	-9.48	-0.80	-2.49	18	.023

Table 6-3: The r-values when comparing the PMUD's between the apical and basal parts

		r-values of the PMUD's							
		A_ANT- B_ANT	A_LAT- B_LAT	A_INF- B_INF	A_SEP- B_SEP	APX- B_ANT	APX- B_LAT	APX- B_INF	APX- B_SEP
Male	t	-5.98	-2.91	-1.02	-2.46	-3.57	-0.79	-5.50	-1.49
	df	20	20	20	20	20	20	20	20
	r	0.80	0.55	0.22	0.48	0.62	0.17	0.78	0.32
Female	t	-0.41	-3.22	-3.82	-1.09	-3.17	-1.77	-6.63	-2.49
	df	18	18	18	18	18	18	18	18
	r	0.10	0.60	0.67	0.25	0.60	0.39	0.84	0.51

6.3.4 Under Estimation of the Basal Regions and Over Estimation of the Apical Regions of the Left Ventricle of the Attenuation Corrected Images on the Commercial System

To establish whether the intensity values in the basal parts of the left ventricle are underestimated and those in the apical regions been overestimated by the commercial system, the PMUD values displayed in figure 6.1 were used and the PMUDI added to the graphs so that a conclusion can be made. These results for the two genders are displayed in figure 6.3 and summarised in table 6.4.



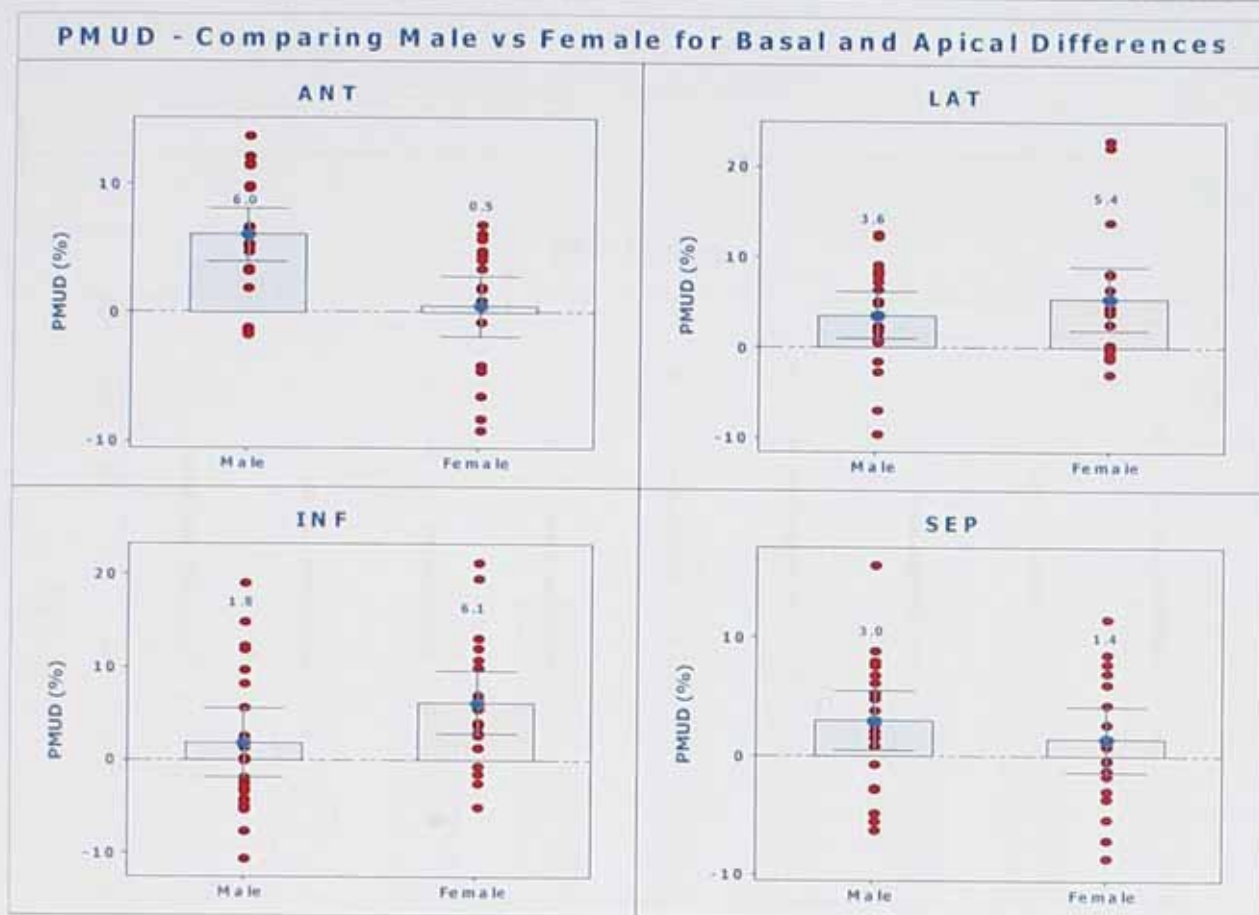


Figure 6-3: Showing the PMUDI values to determine the amount of under estimation in the basal regions.

Table 6-4: PMUD and PMUDI values to determine the amount of under estimation in the basal regions and over estimation in the apical regions

PMUD and PMUDI Values										
	B-ANT	A-ANT	B-LAT	A-LAT	B-INF	A-INF	B-SEP	A-SEP	APX	PMUDI
Male	7.9	1.9	2.0	-1.6	16.3	14.5	3.0	0.0	-0.5	4.8
Female	5.2	4.7	2.9	-2.5	12.5	6.3	3.0	1.5	-2.2	3.5

6.3.5 Fraction Intensity Losses in the Final Ventricular Images of the Attenuation Corrected Patient Studies on the Commercial System

To establish the amount of intensity gain as a result of the corrections done the fractional indexes were calculated for both the male and female patients and are displayed in figure 6.4. These results will be used in section 6.3 to determine how these corrections compared to the amount of losses predicted by the Monte Carlo simulations.

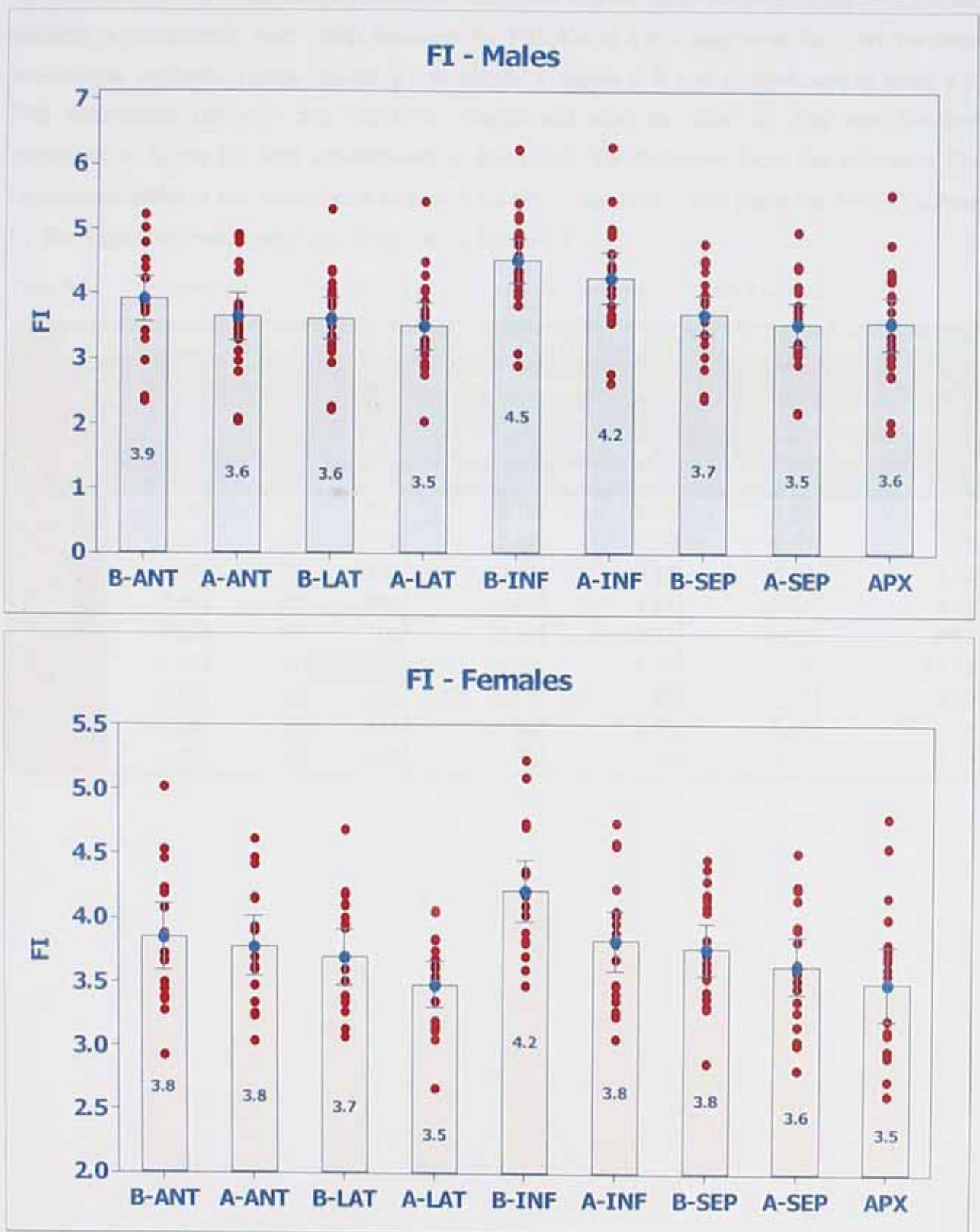


Figure 6-4: The fraction indexes in the 9 segments to indicate the intensity gain in each segment.

6.3.6 Comparing Attenuation Corrected Male Against Female Patients on the Commercial System

To assess how the commercial correction method's results differ between male and female patients a comparison was made between the PMUDs of the 9 segments for both the male and female patients. These results are displayed in figure 6.5 and summarised in table 6.5. The differences between the fractional images will also be used for this analysis and displayed in figure 6.6 and summarised in table 6.6. To determine how the effects of the corrections differ in the corrections obtained for the basal and apical parts the PMUD values for the 2 genders calculated are displayed in figure 6.7.

Table 6-5: Comparing the uniformity gains (PMUD) between the two genders in the 9 segments

Independent Samples Test - Comparing PMUD - Male vs Female								
	t-test for Equality of Means						95% Confidence Interval of the Difference	
	t	df	p (2-tailed)	Mean Difference	Std. Error Difference	Lower	Upper	
B_ANT	1.39	33	.173	2.70	1.94	-1.25	6.65	
A_ANT	-1.61	35	.116	-2.88	1.79	-6.51	0.75	
B_LAT	-0.35	38	.726	-0.97	2.75	-6.53	4.59	
A_LAT	0.47	29	.642	0.85	1.81	-2.85	4.55	
B_INF	1.65	37	.108	3.84	2.33	-0.88	8.57	
A_INF	5.57	37	.000	8.21	1.47	5.22	11.19	
B_SEP	0.02	38	.988	0.03	1.86	-3.75	3.80	
A_SEP	-0.83	33	.411	-1.54	1.85	-5.29	2.22	
APX	0.71	35	.480	1.70	2.38	-3.13	6.53	

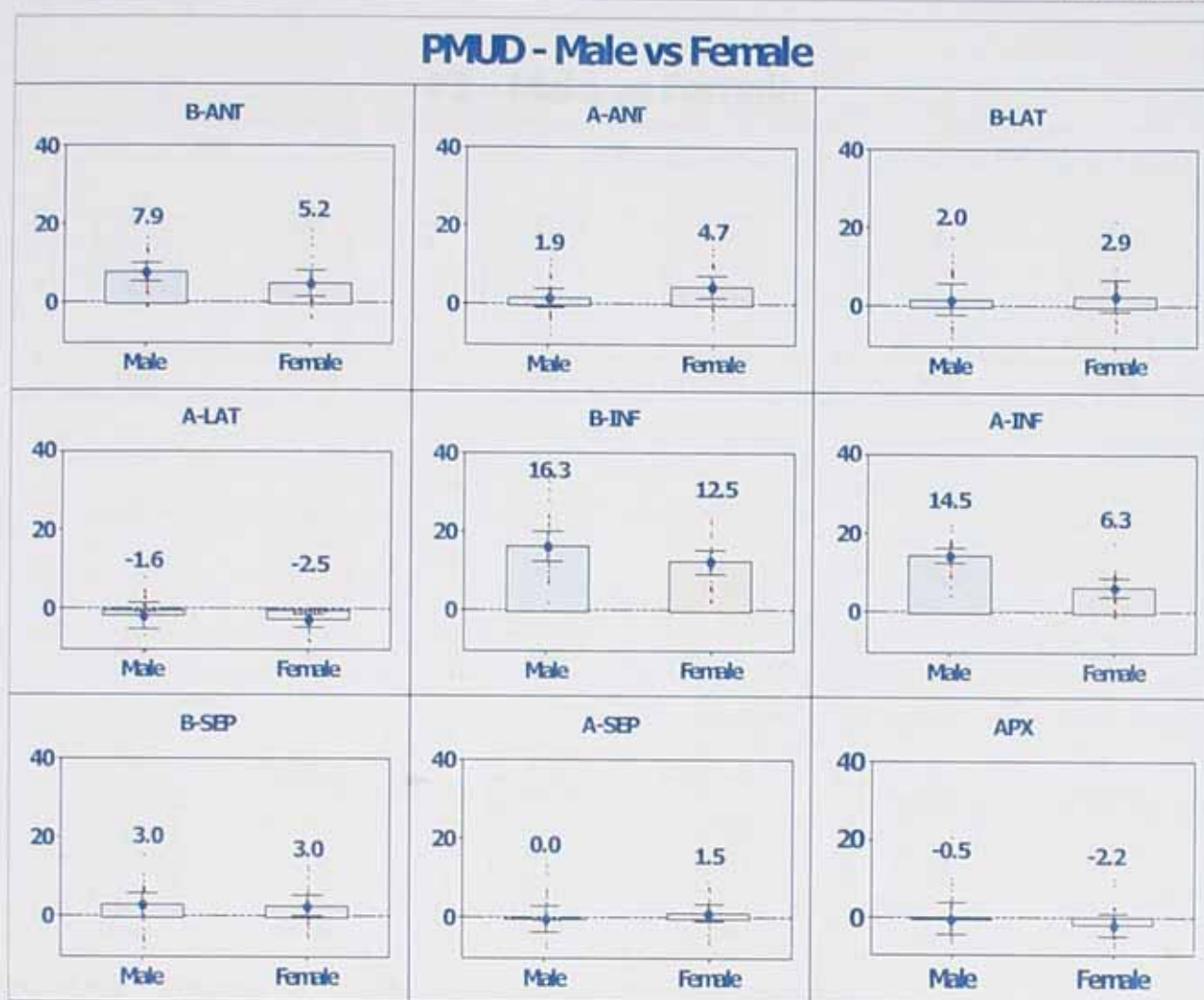


Figure 6-5: Comparison of percentage intensity gain in the 9 segments between male and female patients as a result of transmission attenuation corrections using Gd-153 line sources (in each graph the y-axis represents the % intensities gained from the attenuation correction).

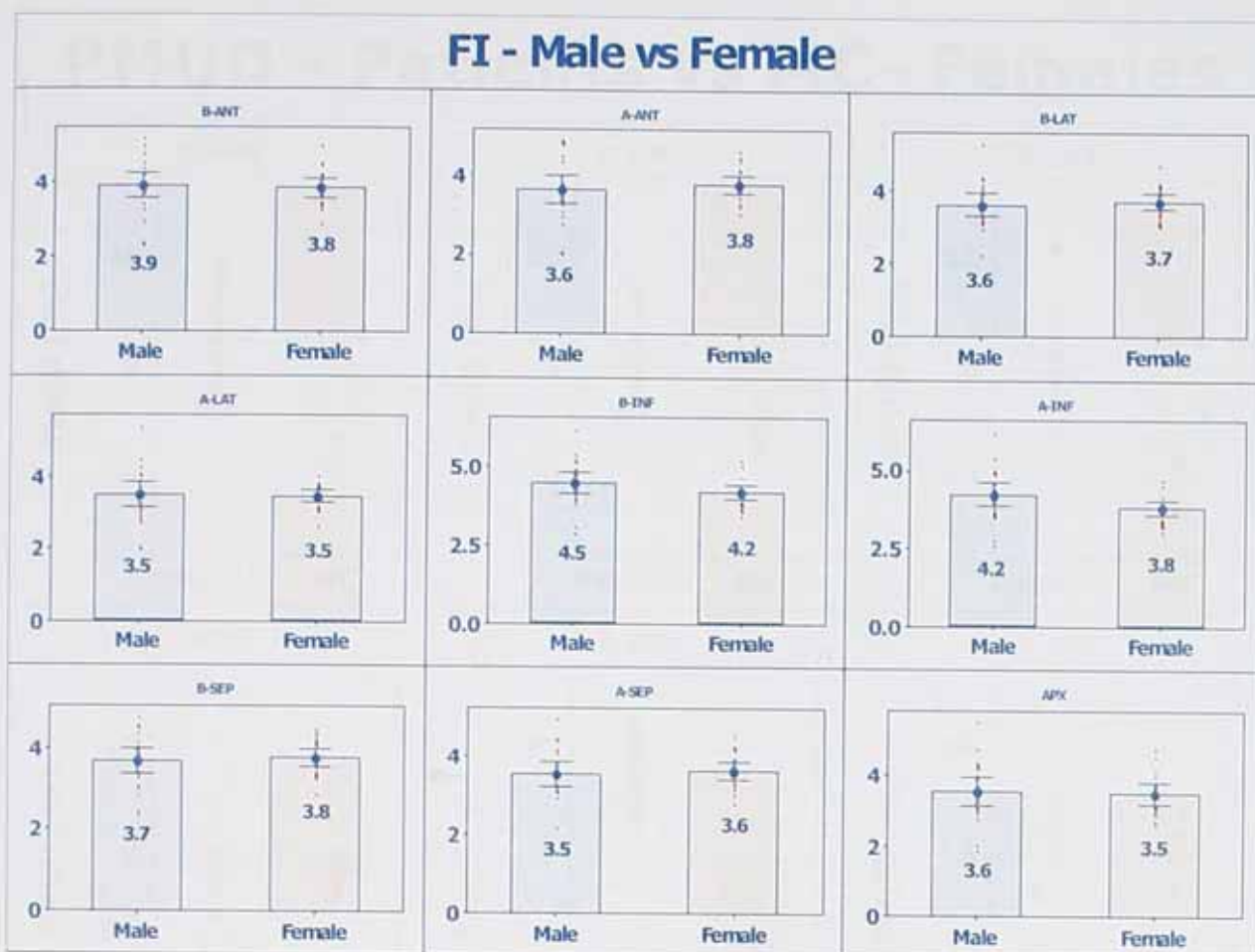


Figure 6-6: Comparing the FI's of the male population to the female population.

Table 6-6: Comparing the FI's of the male population to the female population

Independent Samples Test - Comparing FI - Male vs Female								
	t-test for Equality of Means							
	t	df	p (2-tailed)	Mean Difference	Std. Error Difference	95% Confidence Interval of the Difference		
						Lower	Upper	
B_ANT	0.28	36	.781	0.06	0.20	-0.35	0.47	
A_ANT	-0.63	33	.535	-0.13	0.21	-0.56	0.29	
B_LAT	-0.43	34	.669	-0.08	0.19	-0.46	0.30	
A_LAT	0.13	38	.896	0.03	0.20	-0.38	0.43	
B_INF	1.51	35	.140	0.30	0.20	-0.10	0.70	
A_INF	1.88	38	.068	0.42	0.22	-0.03	0.87	
B_SEP	-0.43	34	.667	-0.08	0.18	-0.44	0.28	
A_SEP	-0.40	38	.688	-0.08	0.20	-0.48	0.32	
APX	0.26	36	.796	0.06	0.24	-0.42	0.54	

PMUD - Patients vs MC- Females

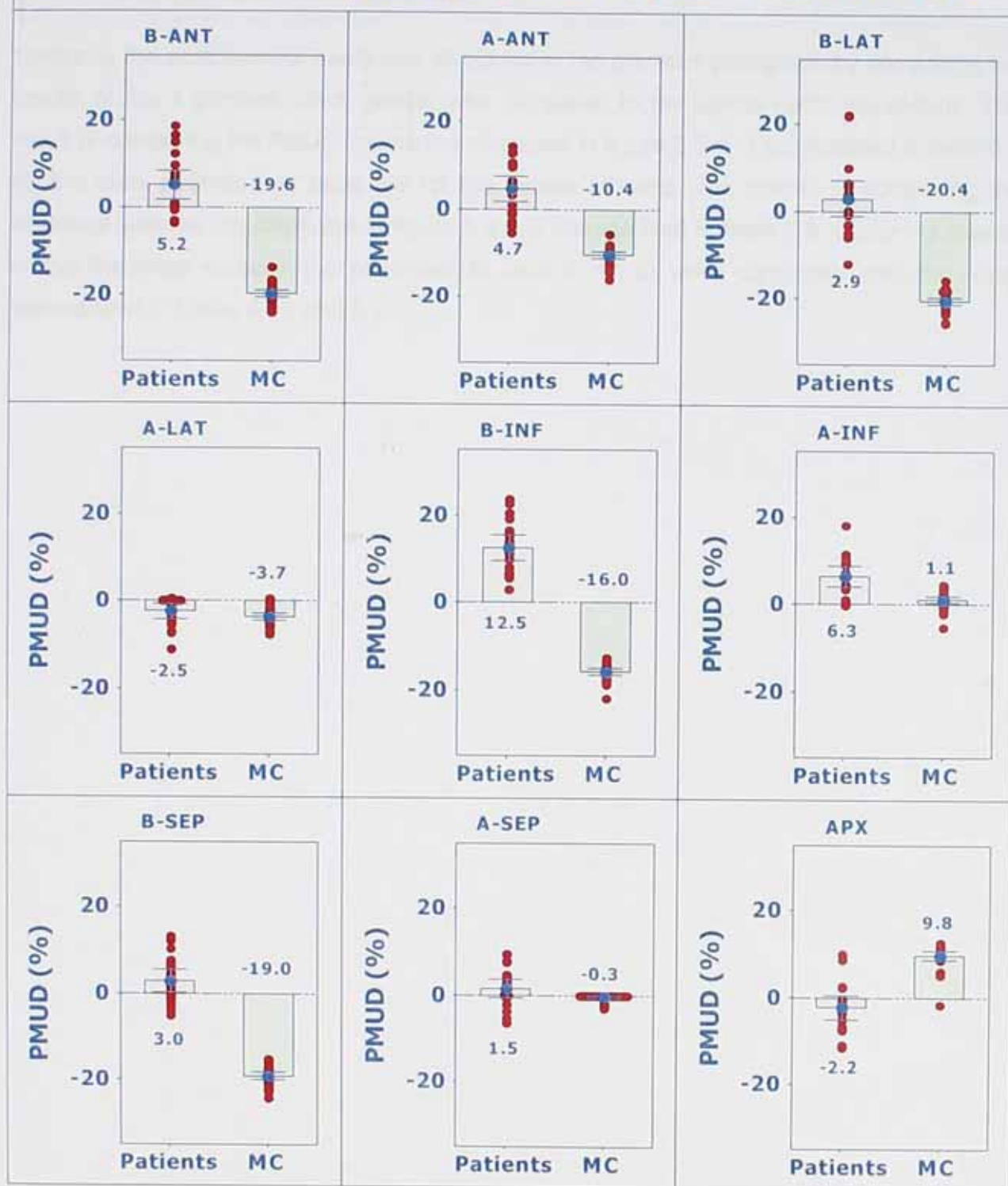


Figure 6-7: Comparing the PMUD's when comparing the difference obtained after attenuation correction for the basal and apical regions of the male population against that of the female population.

6.3.7 Comparing the Results of the Attenuation Corrected Patients on the Commercial System Against Those Predicted by the Monte Carlo Simulations

Similar to the comparisons made and displayed in the previous paragraph by comparing the results of the 2 genders, each gender was compared to the Monte Carlo simulations. The result of comparing the PMUD values are displayed in figure 6.8 and summarised in table 6.7 for the male patients and table 6.8 for the female patients. The results of comparing the fractional indexes are displayed in figure 6.9 and summarised in table 6.9. Lastly the means of the fractional indexes (as described in section 4.2.2) were compared and the result summarised in tables 6.10 and 6.11.

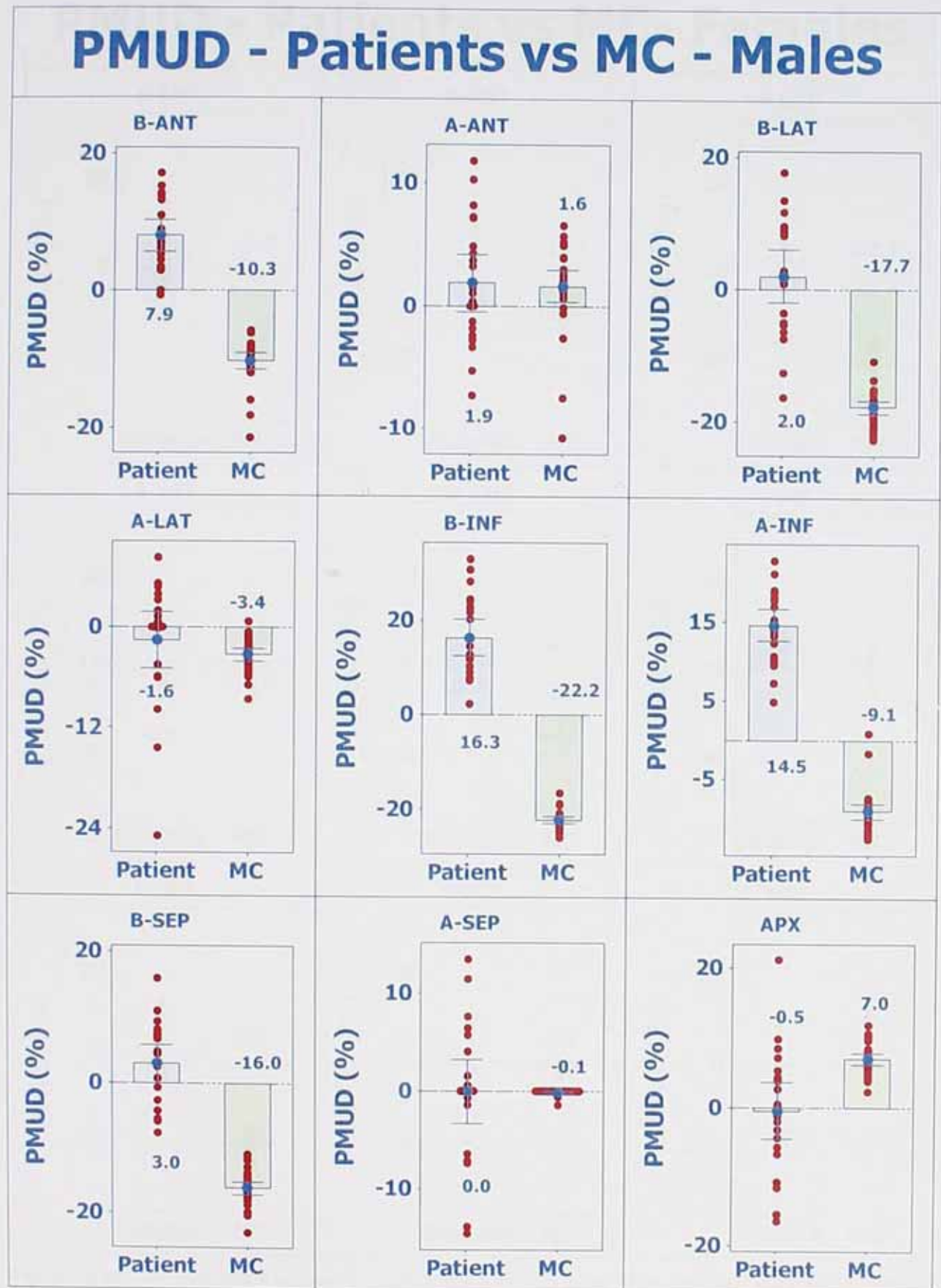


Figure 6-8 a: A comparison between the uniformities gained by using TBAR to the uniformity losses predicted by the Monte Carlo simulations – Male patients.

PMUD - Patients vs MC- Females

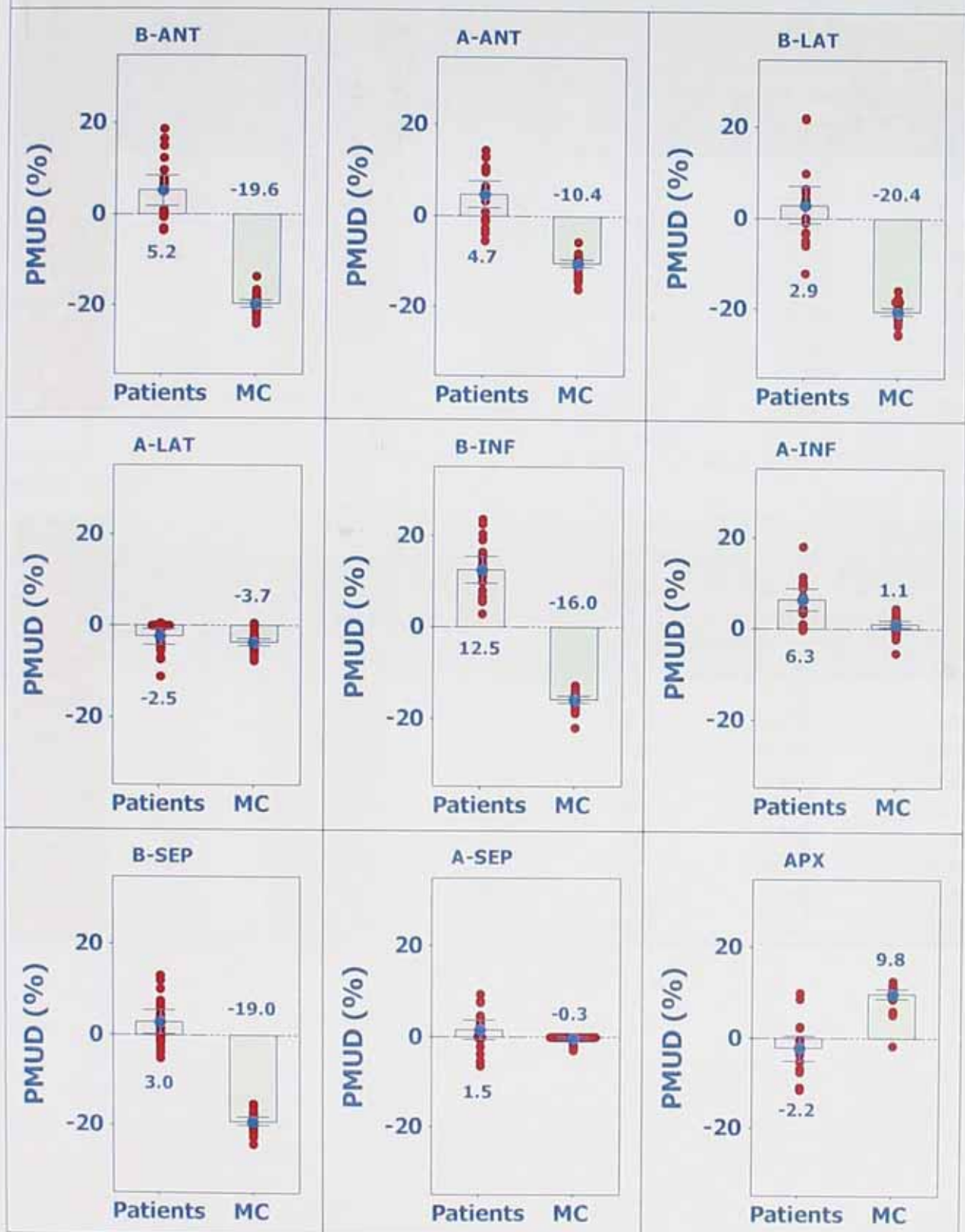


Figure 6-9 b: A comparison between the uniformities gained by using TBAR to the uniformity losses predicted by the Monte Carlo simulations – Female patients.

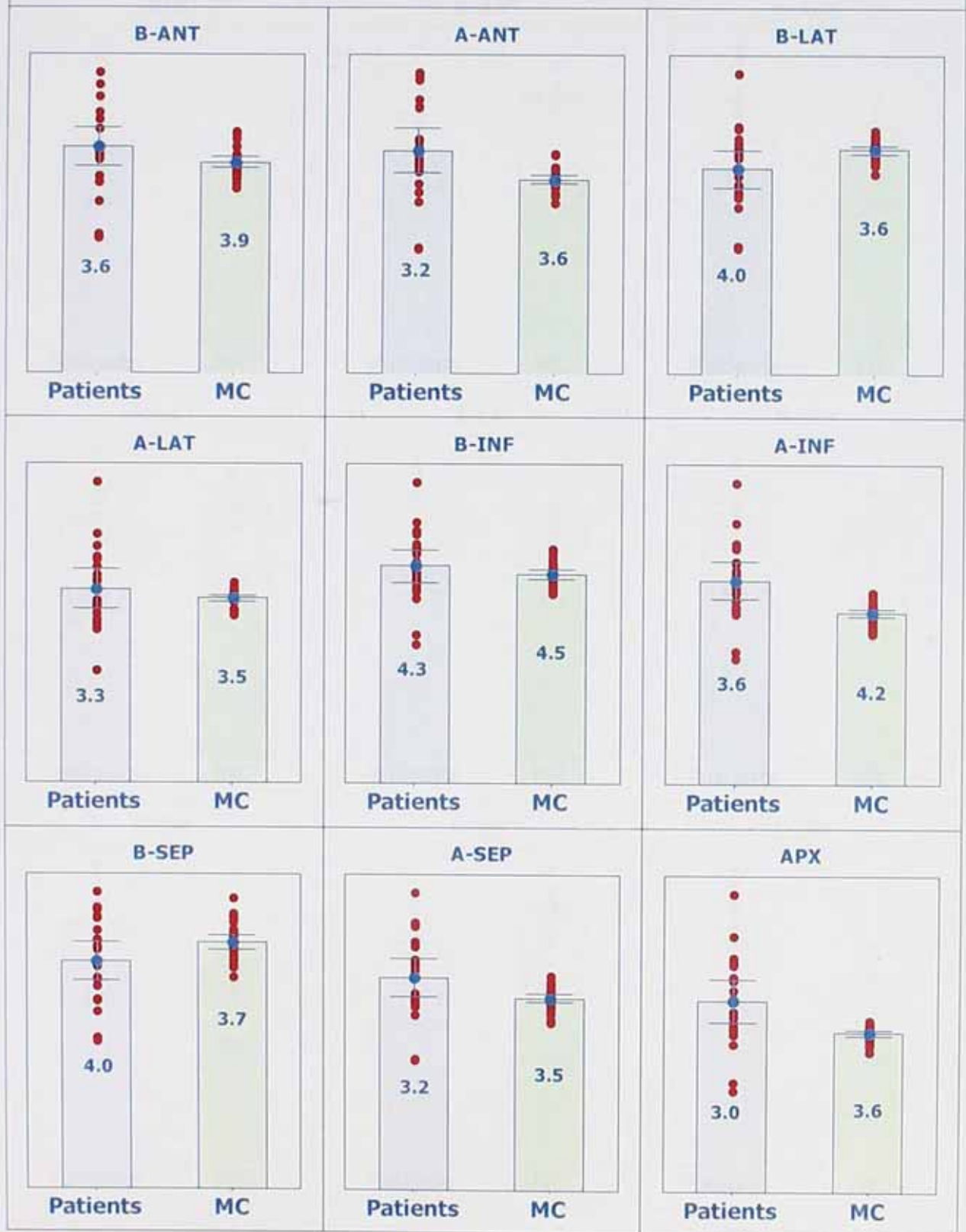
Table 6-7: The mean and 95% confidence intervals for the percentage intensity gain in the 9 segments for the male patients

Independent Samples Test - Comparing PMUD - Female vs MC								
	t-test for Equality of Means							
	t	df	p (2-tailed)	Mean Difference	Std. Error Difference	95% Confidence Interval of the Difference		
						Lower	Upper	
B_ANT	10.59	47	.000	14.35	1.35	11.62	17.07	
A_ANT	4.72	47	.000	5.69	1.20	3.26	8.11	
B_LAT	10.57	47	.000	17.42	1.65	14.11	20.74	
A_LAT	7.91	47	.000	6.22	0.79	4.64	7.81	
B_INF	2.90	47	.006	3.57	1.23	1.09	6.04	
A_INF	-7.61	47	.000	-7.44	0.98	-9.41	-5.47	
B_SEP	14.56	47	.000	16.03	1.10	13.82	18.24	
A_SEP	-1.56	47	.124	-1.25	0.80	-2.87	0.36	
APX	-6.15	47	.000	-7.60	1.24	-10.09	-5.12	

Table 6-8: 2-tailed paired t-tests to compare the means of the attenuation gain in each of the 9 segments against each other in the male population

Independent Samples Test - Comparing PMUD - Male vs MC								
	t-test for Equality of Means							
	t	df	p (2-tailed)	Mean Difference	Std. Error Difference	95% Confidence Interval of the Difference		
						Lower	Upper	
B_ANT	2.05	49	.046	2.39	1.16	0.05	4.73	
A_ANT	-2.91	49	.005	-3.50	1.20	-5.92	-1.09	
B_LAT	9.25	49	.000	15.71	1.70	12.30	19.12	
A_LAT	3.47	49	.001	4.98	1.44	2.09	7.87	
B_INF	3.67	49	.001	5.89	1.60	2.67	9.11	
A_INF	-5.38	49	.000	-5.47	1.02	-7.51	-3.43	
B_SEP	10.01	49	.000	13.07	1.31	10.44	15.69	
A_SEP	0.05	49	.961	0.06	1.30	-2.55	2.68	
APX	-3.82	49	.000	-6.50	1.70	-9.92	-3.08	

FI - Male vs MC



FI - Female vs MC

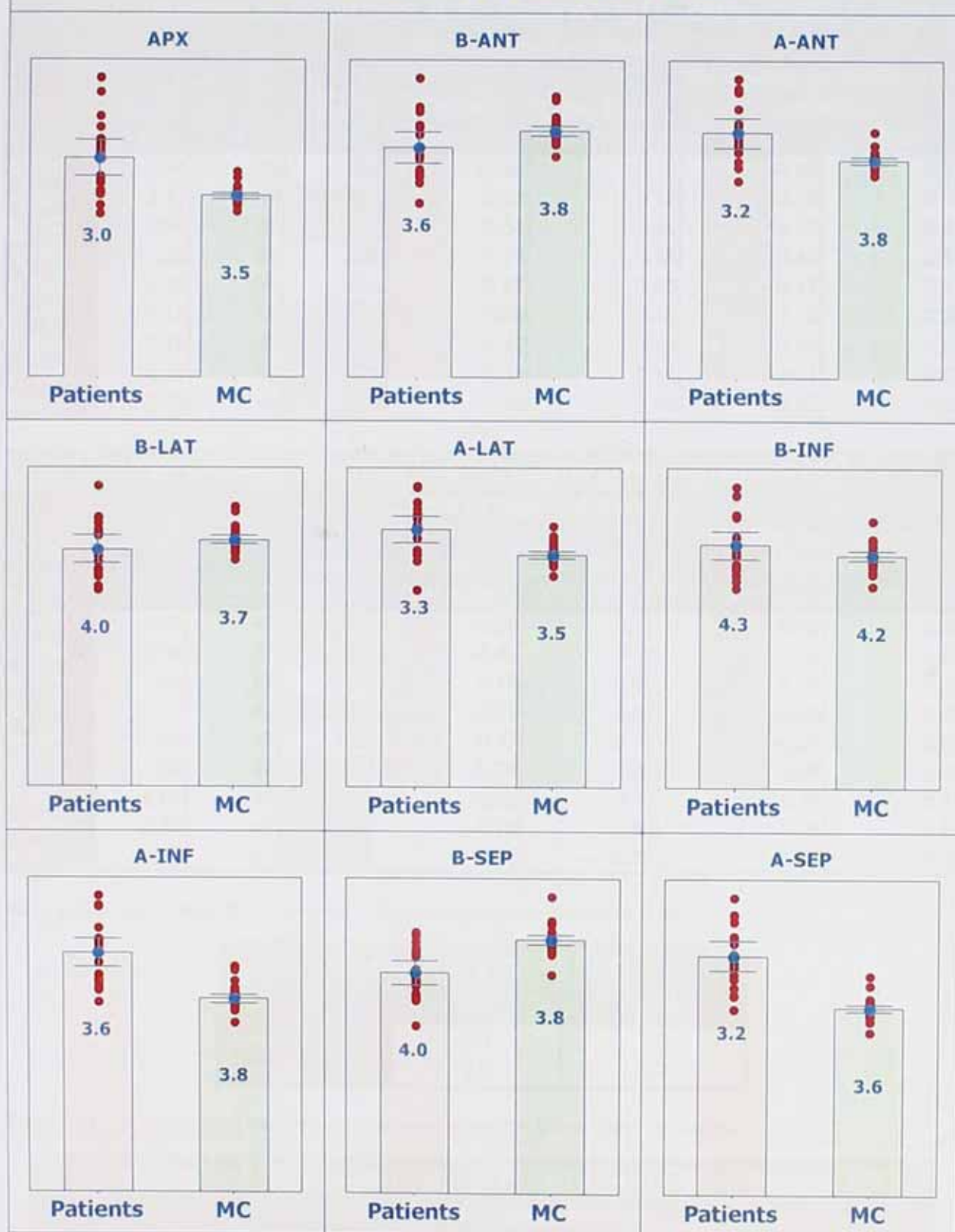


Figure 6-10: A comparison between the intensity gained by using TBAR to the intensity losses predicted by the Monte Carlo simulations.

Table 6-9: A comparison between the intensity gained by using TBAR to the intensity losses predicted by the Monte Carlo simulations

Independent Samples Test - Comparing FI - Male vs MC								
	t-test for Equality of Means						95% Confidence Interval of the Difference	
	t	df	p (2-tailed)	Mean Difference	Std. Error Difference	Difference		
						Lower	Upper	
B_ANT	-1.78	49	.082	-0.26	0.15	-0.55	0.03	
A_ANT	-3.17	49	.003	-0.48	0.15	-0.79	-0.18	
B_LAT	2.50	49	.016	0.34	0.14	0.07	0.61	
A_LAT	-1.24	49	.220	-0.18	0.15	-0.48	0.11	
B_INF	-1.15	49	.254	-0.17	0.15	-0.47	0.13	
A_INF	-4.17	49	.000	-0.69	0.16	-1.02	-0.36	
B_SEP	2.16	49	.036	0.30	0.14	0.02	0.57	
A_SEP	-2.41	49	.020	-0.33	0.14	-0.61	-0.06	
APX	-3.63	49	.001	-0.59	0.16	-0.92	-0.26	

Independent Samples Test - Comparing FI - Female vs MC								
	t-test for Equality of Means						95% Confidence Interval of the Difference	
	t	df	p (2-tailed)	Mean Difference	Std. Error Difference	Difference		
						Lower	Upper	
B_ANT	2.62	47	.012	0.28	0.11	0.06	0.49	
A_ANT	-4.54	47	.000	-0.43	0.09	-0.62	-0.24	
B_LAT	1.62	47	.111	0.15	0.09	-0.04	0.34	
A_LAT	-4.53	47	.000	-0.34	0.07	-0.49	-0.19	
B_INF	-1.67	47	.102	-0.17	0.10	-0.37	0.03	
A_INF	-7.69	47	.000	-0.74	0.10	-0.94	-0.55	
B_SEP	6.07	47	.000	0.58	0.10	0.39	0.77	
A_SEP	-8.58	47	.000	-0.79	0.09	-0.98	-0.61	
APX	-5.13	47	.000	-0.59	0.12	-0.83	-0.36	

Table 6-10: Summary of the MFI values of the patients and the Monte Carlo simulations

Summary of MFI's		
	MC	TBAR
Male	3.5	3.8
Female	3.5	3.7

Table 6-11: Comparing the MFI between the genders and the Monte Carlo simulations

Independent Samples Test - MFI Between Patients and MC								
	t-test for Equality of Means						95% Confidence Interval of the Difference	
	t	df	p (2-tailed)	Mean Difference	Std. Error Difference	Difference		
						Lower	Upper	
MF_M	-1.60	49	0.117	-0.22	0.14	-0.50	0.06	
MF_F	-2.73	47	0.009	-0.23	0.08	-0.40	-0.06	
MF_MC	1.35	56	0.182	0.06	0.04	-0.03	0.15	
MF_P	0.28	32	0.781	0.05	0.19	-0.33	0.43	

6.4 Discussion and Conclusion

6.4.1 Attenuation Correction in Attenuation Corrected Male Patients on the Commercial System

For the male patients using the commercial system the most significant attenuation gains were in the basal-anterior, basal-inferior and the apical-inferior regions. Of these, the most significant segment was the basal-inferior, the difference of the mean of this attenuation in this segment is significantly greater than that obtained in other segments as indicated in table 6.3. This is in line with other published results¹⁸².

The mean of the attenuation gain in many of the apical segments is very small and in some segments even negative (apical and apical-lateral and in the apical-septal segment it is 0.5%). The results for the average of the patients has a range that encompasses 0, but some individual patients (for the 21 male patients, 11 in the apex and 9 in the apical-septal and apical-anterior and 8 in the apical-lateral segments were negative) clearly have a negative value but none of them experienced a negative attenuation gain in the basal-inferior region.

6.4.2 Attenuation Correction in Female Patients on the Commercial System

For the female patients the mean of the basal-inferior wall attenuation correction is substantially higher for the basal-anterior and the apical-anterior sections as well as the apical-anterior wall attenuation compensation, making this segment the one to benefit the most from the attenuation correction and it illustrates the benefits of applying transmission based attenuation correction, scatter correction and resolution recovery.

The mean of the attenuation gain in some of the apical segments is also very small and in some segments also even negative (apical and apical-lateral). In all these segments the 95% intervals do include 0 and therefore one cannot conclude that the gain in these segments will also be negative but in a substantial number of the patients it is actually negative (for the 19 female patients, 9 in the apex and 11 in the apical-lateral segments were negative). Again none of them experienced a negative attenuation gain in the basal-inferior region.

6.4.3 Comparing the Correction in Male to That in Female Patients on the Commercial System

In both the male and female patients studies the segment which gained the most by the attenuation correction was the basal-inferior region. From table 6.5 it can be concluded that the means of the basal-inferior and apical-inferior regions differ substantially between the

male and female patients but in the remainder of the segments there are no significant differences between the means of the two genders.

The conclusion is that both genders experienced the most attenuation gain in the basal-inferior region which is greater in the male population than the female population and this difference can be most likely be attributed to anatomical differences. In the remainder of the regions the two genders experienced the same amount of gain (or loss), even in the two anterior regions. This again illustrates the benefits of these correction techniques.

6.4.4 Comparing the Attenuation Correction Obtained in Patients on the Commercial System Against the Attenuation Losses Predicted by the Monte Carlo Simulations

A. Significant Inferior Wall Attenuation

The most prominent attenuation correction is in the basal-inferior region for both males and females (a mean of 22.1 for males and 16.7 for females as a percentage). The second most significant correction in males is the apical-inferior wall. For the female patients the second most significant is both the apical-inferior and basal-anterior regions. These results are in line with the predictions from the Monte Carlo Simulations made in chapter 4 that the inferior wall is the most significant affected by attenuation and that the second most significant regions is the anterior regions in females.

B. The Effect of the Heart Itself as Attenuation Medium

The Monte Carlo simulations in chapter 4 predict that the heart is a very important contributor to the attenuation experienced in the inferior wall. The female heart is generally smaller²⁰⁴ than that of males and this could be the reason for the difference in the female patients in the inferior regions being lower than in males.

C. Under Estimation of the Basal Regions of the Left Ventricle

As shown in Chapter 4 these regions are subject to the greatest intensity losses in the uncorrected images. It is appropriate, therefore, that the TBAR system makes the greatest corrections here and as illustrated by the FI values figure 6.9 (values of 3.6 for the male patients and 4.0 for the TBAR method in the B-LAT segment, etc.) the TBAR method makes a complete correction for the intensity losses experience by the simulated scans.

D. The Overestimation and “Correction” of the Apical Region

Monte Carlo simulations made in chapter 4 predict that non-attenuated Myocardial Perfusion images experienced an overestimation of the intensity in the apical regions and this observation was also reported in the literature¹⁸² where the uncorrected intensities were compared against those determined in a PET study which served as the reference.

In the patient studies many of the patients experience a negative gain in many of the apical regions when attenuation correction was applied to these regions. This is a well-known fact and the subject of many studies^{205,206,207} and is often described as "an apparent apical defect caused by attenuation correction". Traditionally, it has been assumed that attenuation correction will always either keep the observed intensity in a region constant or increase the observed intensity. Hence, the reduction of the intensity in the apical region when such corrections were made was assumed to be an error of the method, introducing an artefact. As a result of the simulations in chapter 4 it is clear that the reduction in observed intensity is due to the loss of intensity as a result of the partial-volume effect, non-uniform attenuation, depth-dependent detector response, scatter and statistical noise as described in chapter 4 and therefore the reduction in intensities is appropriate and has a valid cause. This is not well known and the general acceptance of this can be difficult to achieve, but this is the third study where this has been established. However it is the first study to demonstrate that the amount of intensities over estimated by the non-corrected images is equal to the intensity reduction achieved by the correction method.

E. The Intensities Gained by Implementation of TBAR

As shown in chapter 2 the intensity losses in the uncorrected image can be as high as 90% and this will result in substantial intensity losses in the final images displayed. The Mean Fractional Index (MFI), defined in section 4.2.2., is a measurement of the intensities gained when using a correction method or the intensity losses as a result of the shortcoming of imaging methodology. The MFI's has been calculated for both the male and female simulated patients in chapter 4 and this provide a quantitative measurement for the intensity losses as a result of the simulated Myocardial Perfusion Scans. These values are displayed in table 6.10 together with the values calculated for the patient studies using the TBAR method illustrating that this method restores all the intensity losses experience by the simulated scans. These findings illustrates that the commercial system with transmission based attenuation correction, together with scatter and attenuation correction, corrects for all the intensity losses experienced.

F. Summary

The Monte Carlo simulations used in this study are the gold standard against which the TBAR method has been evaluated. These simulations provide the values in the areas where intensity losses would be anticipated in patient studies. The patient studies experienced most of the predictions from the Monte Carlo simulations, one of the most obvious ones is the fact that the inferior wall experiences the most attenuation during a patient acquisition and also that the inferior wall's attenuation in females is often more severe than that of the anterior wall. The patient studies also confirm that the basal parts of the left ventricle experience

more attenuation which leads to a smaller left ventricular cavity observed. It seems that attenuation correction corrects for the over estimation of the apical parts, meaning that not only an increase in areas where losses are experienced, but also a decrease in areas where there are an over estimation. These results illustrate the importance of attenuation correction and that it is hugely beneficial and should be used routinely in clinical studies. The results of this study also suggest that by implementing attenuation correction in combination with resolution recovery and scatter correction leads to substantial improvements in the intensity losses experienced with Myocardial Perfusion Scans, bringing us much closer to the original goal of absolute quantification. Unfortunately there are still drawbacks as a result of the use of hardware such as line sources or an added CT scanner which has the disadvantage of added, patient dose, scan time and cost. Therefore, the approach used in the TBAR method provides a substantial advance to correct for all the permutations in MPI (attenuation, scatter and depth dependent resolution problems). Unfortunately the technique still has the substantial disadvantages of additional patient dose, additional scanning time and increased cost, added to that of the resistance to the general acceptance of transmission attenuation correction.

The results of this chapter seem to verify that a substantial advance has been made with the introduction of the commercially available solutions, even with the use of transmission scanning. The introduction of an acceptable emission based attenuation correction, which can be combined with the correction for the collimator depth-dependent blurring and correction for scatter, will be another substantial step, especially if it can break down the resistance of using attenuation correction on a routine basis. The next chapter discusses the introduction of two such emission based attenuation correction techniques which were also discussed in paragraph 2.4.5.

It is also recommended that this study be extended to overcome the limitations of the patient selection discussed in paragraph 6.2.1. Although this can lead to a slightly different outcome of the results obtained here, one can expected it not to differ enough to alter most of the conclusion that has been made in this chapter.

Chapter 7 - The Proposed Methods of Inferred & Derived Anatomy for Attenuation Correction in the Thorax

7.1 Introduction

The need for an accurate attenuation correction technique has been established in the previous studies in chapters 4 and 5 but chapter 2 confirmed the problems and lack of universal acceptance of current methods that rely on transmission based correction. Chapter 6 investigated a commercially available method for correcting for attenuation, scatter and depth-dependent collimator blurring by using transmission based correction and therefore also demonstrated the advantages of using these correction techniques. In this study it was established that the commercially available TBAR method corrects for all the intensity losses experienced by the simulated patient studies and that it also corrected the distortion experience by the LV, i.e. under estimation of the basal areas and over estimation of the apical areas. The advantages of this method are clear but it still suffers some serious shortcomings, as discussed, and also lack universal acceptance, therefore this study will introduce two new emission based correction techniques which could be suitable for accurate individual attenuation correction without the drawbacks it poses, i.e. additional radiation dose, increased cost and time, of transmission based methods.

As suggested in chapter 2 although the thorax is far less homogeneous than the brain it may be feasible to extend the method of inferred anatomy to provide non-uniform attenuation correction in the thorax to make emission based attenuation correction a reality.

To achieve this image registration must be used to devise the patient specific attenuation map. This involves the creation of a source and target object. The target object, relating to the patient, contains the size, shape and orientation required and the source object must be changed to conform to that of the target image.

The source object in this instance is an attenuation map created from the NCAT phantom. Figure 7.1(a) shows a typical slice created from the NCAT phantom with the different

attenuation coefficients, but it is not suited to be registered to the image data as it shows all the structures seen in a CT image which are not seen in an MPI image. The critical feature of the source object is the image of the left ventricle, which can be extracted from the structural source object, along with the body outline, to give a "functional" source object. Therefore a functional image of the NCAT phantom needs to be created, i.e. the creation of an activity object by simulating the injection of a radioactive tracer into the attenuation object. This is an image set with a uniform background value and a higher uniform activity in the left ventricle, Figure 7.1(b) shows the same slice as in Figure 7.1(a) with only this activity instead of attenuation coefficients. The target object is the activity object created out of the patient data from the MPI image consisting of a uniform body outline and the left ventricle as shown in Figure 7.1(c).

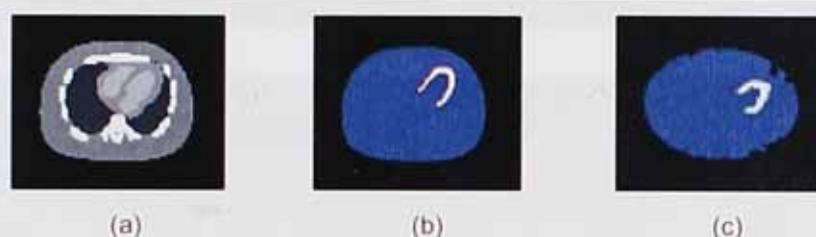


Figure 7-1: A typical slice from the attenuation object created out of the NCAT phantom (a), the functional image of this slice (b) and a slice from the target object created from the patient data (c).

The source object is a pre-defined set of images which can be used in every patient study. These were originally created from the NCAT phantom. The target image must be created from the patient data in each individual study. The body outline and left ventricle needs to be determined for the specific patient and both are then given a constant activity value to create the functional images which will serve as the target images. The creation of the objects shown above will be discussed in more detail in section 7.2 and 7.3.

In a normal image registration process two sets of objects are used, the source object and the target object. In this study three sets of objects are used. The first is the functional target object, a typical slice as shown in Figure 7.1(c), that will be created out of the patient data. The rest are two source objects, i.e. the attenuation source object (Figure 7.1(a) shows a typical slice) and functional source object (Figure 7.1(b) shows again a typical slice), both created from the NCAT phantom. A corrected version of the attenuation source object, which matches both the patient's outline and their heart shape, Figure 7.1(a), is the desired outcome, but the functional source object, Figure 7.1(b) will be used to determine the registration parameters that describe the difference between the attenuation source object and the patient data. The registration parameters will be determined from the corrected "functional" source object and then used to alter the attenuation source object to produce the desired outcome.

7.2 Creation of the Source Object

The source objects are pre-defined sets of attenuation maps and "functional" images created from the NCAT phantom as displayed in figure 7.2.

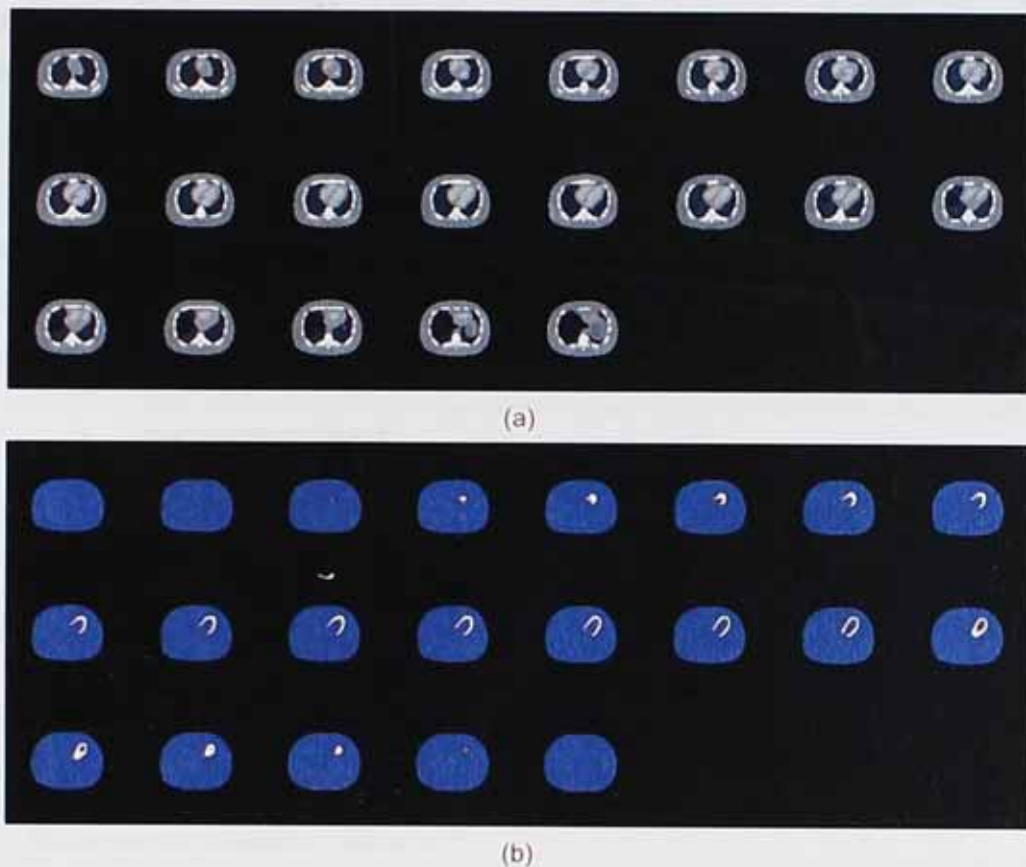


Figure 7-2: The provided NCAT attenuation map (a) and functional map (b) which need to be modified to adhere to the spatial representation of the patient under investigation.

These data sets consist of a fixed number of slices that must be reduced (or increased) to coincide with the same number of slices in the patient study that will be used in the final reconstruction. Therefore the number of relevant slices in the patient data needs to be determined as described below in "Determination of the patient data slices". The x and y dimensions of the source objects and the target object will match but the z dimension, that represents the number of slices, must be changed in the attenuation source object and the functional source object by the use of polynomial warping to add or subtract slices. This provides the final attenuation source object and functional source object.

7.3 Creation of the Target Object

A well-defined outline of the body is necessary for the registration of the source object to the target object and the steps outlined below are applied to every slice in the patient data set. This technique is known as segmentation which refers to the process of partitioning a digital image into multiple segments (sets of pixels). The goal of segmentation is to simplify and/or change the representation of an image into something that is more meaningful and easier to

analyse²⁰⁸. Image segmentation is typically used to locate objects and boundaries (lines, curves, etc.) in images. More precisely, image segmentation is the process of assigning a label to every pixel in an image such that pixels with the same label share certain visual characteristics.

The target object consists of the body outline and the segmentation of the left ventricle derived from the acquired patient data.

To obtain the body and the left ventricle outlines, an initial reconstruction of the patient data must be done. To minimize the background data (see Figure 7.3), an iterative reconstruction using the Maximum Likelihood Expectation Maximisation reconstruction algorithm²⁰⁹ is used instead of filtered backprojection (fbp). This provides the input data for the segmentation steps described below.



Figure 7-3: The same patient data set reconstructed by using filtered backprojection (fbp) (a) and the Maximum Likelihood Expectation Maximisation (MLEM) reconstruction method (b) showing the reduced background produced by the iterative reconstruction method in (b).

7.3.1 Segmentation of the Body Outline

Segmentation of the body outline is achieved by first using clustering, followed by thresholding, erosion and the application of an automatic masking algorithm. This method has been presented at a scientific meeting by the author^{210,211}, having been developed in the early stages of this project, and the software necessary to implement it has been developed by the author by using the Interactive Data Language (IDL)²¹² and the algorithm will be described below.

Binary images of the original images are created with the use of clustering so that the body outline could be established. Clustering^{213,214} is the classification of objects into different groups, or more precisely, the partitioning of a data set into subsets (clusters), so that the data in each subset (ideally) shares some common trait. These results are shown as a single slice in Figure 7.4(a). These images contain a substantial amount of background noise that lead to a poorly defined outline of the body.

Thresholding²¹³ (also called masking) is used to isolate features within an image, which are above, below, or equal to a specified pixel value. The value (known as the threshold level) determines how masking occurs. By experimentally choosing an appropriate threshold level,

setting all the image values below this threshold to zero and creating another binary image, the amount of background can be substantially reduced from the original image, leaving the body outline with still some background clusters. Using an empirically determined threshold value will achieve this. Although this leads to an improvement of the body outline, unfortunately this body outline is still not well defined as shown in Figure 7.4(b).

The remaining background values that do not contribute to the body outline can be further reduced by the use of erosion²¹³. Erosion reduces the size of objects in relation to their background by using a structuring element. This operation is commonly known as "shrink" or "reduce". It can be used to remove islands smaller than the structuring element. Over each pixel of the image, the origin of the structuring element is overlaid. If each nonzero element of the structuring element is contained in the image, the output pixel is set to one. Letting $A \otimes B$ represent the erosion of an image A by structuring element B , erosion can be defined as:

$$C = A \otimes B = \bigcap_{b \in B} (A)_b$$

where $(A)_b$ represents the translation of A by b . The structuring element B can be visualized as a probe that slides across image A , testing the spatial nature of A at each point. If B translated by i,j can be contained in A (by placing the origin of B at i,j), then i,j belongs to the erosion of A by B . The basic erosion morphological operation is then applied to get rid of most of the background clusters as shown in Figure 7.4(c).

The remaining clusters can be removed by applying an elliptical mask²¹⁵ to the image. It uses a "mass density" method, in which each pixel has a "weight" that can be used to determine the centre of mass and mass distribution of a region of interest (ROI). Although the masking algorithm can be applied straight away without the thresholding and erosion steps, it can be seen from figure 7.4 that the application of these steps will lead to a more accurate determination of the centre of mass and therefore a more accurate elliptical fit by removing the "noise" around the image. The ellipse is fitted to this mass distribution. Next the mass distribution tensor is calculated for these pixels and the tensor is used to calculate the eigenvalues and eigenvectors. The eigenvalues give the semi-major and semi-minor axes of the ellipse we are trying to find. The major and minor axes give the ellipse. The orientation of the ellipse is found from the first eigenvector. The orientation is calculated in degrees counter-clockwise from the x-axis. The points that make up the ellipse itself are now calculated. These points are now used to define a ROI that describes the outline of the patient. All points outside of this ROI are set equal to zero. This gives a well-defined body outline that can be used in the registration algorithm by removing the "spikes" from the body outline as shown in Figure 7.4(d).

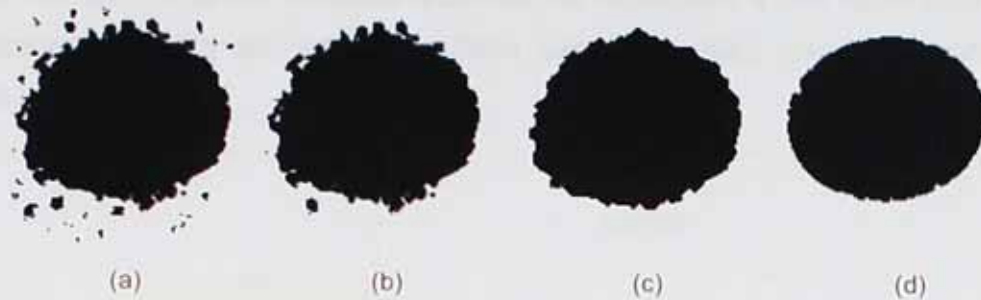


Figure 7-4: The originally binary image (a), the binary image of the body outline after applying thresholding (b), the body outline after erosion (c) and the outline after masking (d).

Applying these steps to all the relevant slices of the patient data provides the body outline, shown in Figure 7.5(b), of the functional target object and together with the left ventricle clusters determined in the part described below, provides the functional target object for the registration.

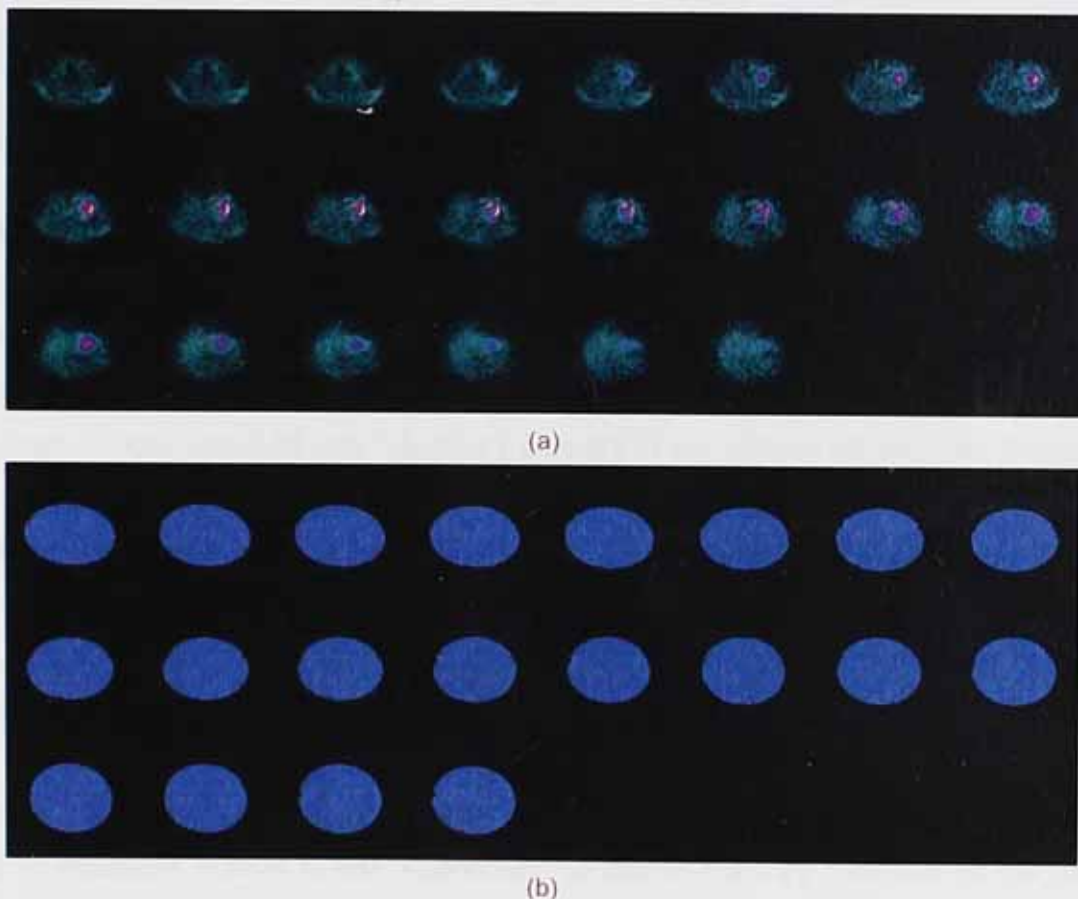


Figure 7-5: Segmentation of the body outline. The images after the initial reconstruction of a patient dataset (a) and the body outline of the same data set after application of the body outline segmentation steps (b).

7.3.2 Segmentation of the Left Ventricle

The second part of the registration requires a well defined outline of the left ventricle only. It is therefore necessary to create a binary image of the patient slices that contains only the left ventricle. A variable threshold together with cluster size and position discrimination and quadranting is used to achieve this. The method described in this section is similar to a

published method¹⁹⁴ and the software necessary to implement it has again been developed by the author by using the Interactive Data Language (IDL) and the algorithm will be described below.

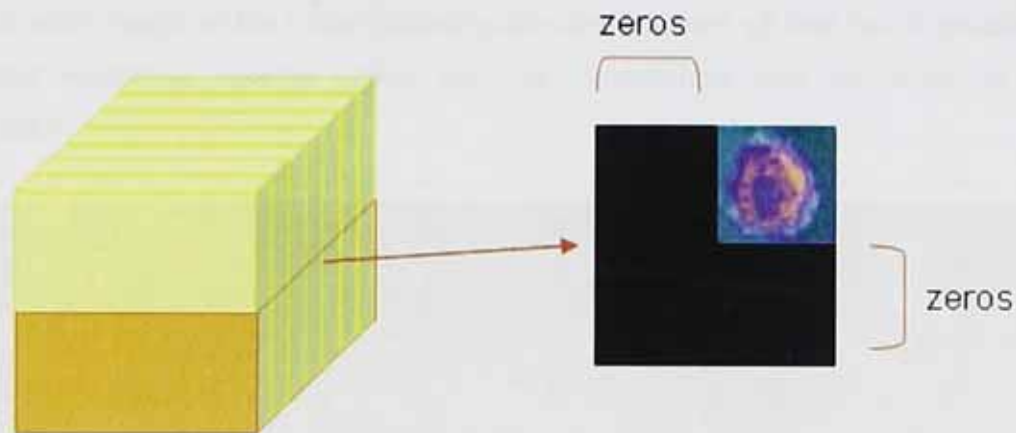
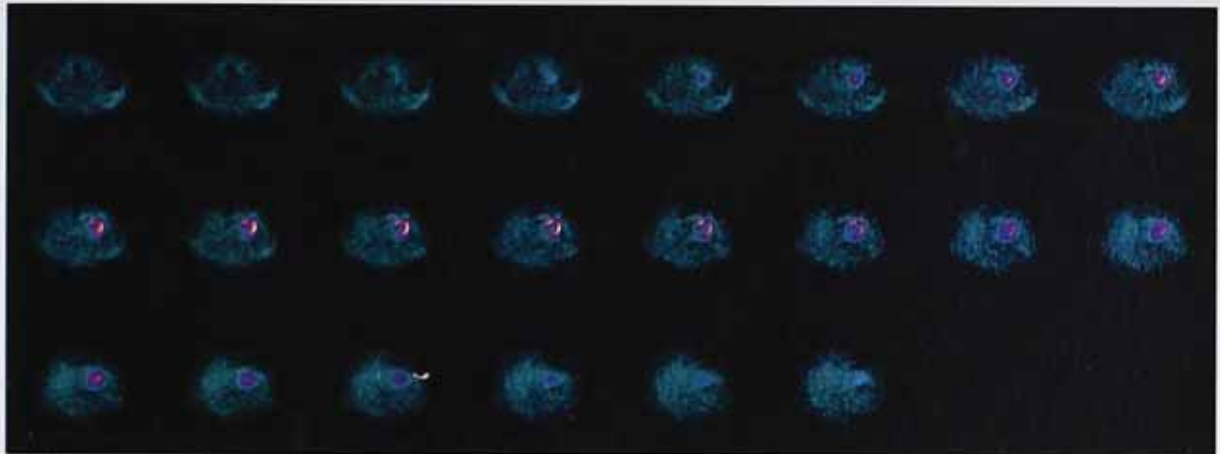


Figure 7-6: Automatic segmentation of left ventricular myocardium. The initial threshold used in the clusterification process is based on the maximal intensity activity in the upper half of the transaxial image volume, i.e., the area that should contain at least part of the heart if the study has been correctly reconstructed and reoriented. When present, hepatic activity is generally confined to the lower left quadrant of the short-axis image volume, while splenic or intestinal activity is likely to appear in the lower right quadrant.

The maximal voxel intensity value C_{max} in the upper right quadrant of the images set ($128 \times 128 \times L$ ($L < 128$)) transaxial image volume is calculated; if the study has been correctly acquired and reconstructed, that regional maximum is likely to correspond to the myocardium as illustrated in figure 7.6. The entire transaxial volume is then thresholded to 50% of C_{max} . The volume is now binarised and the binary clusters in the volume determined. Each cluster, or set of connected voxels, is identified. When all clusters have been determined, those physiologically too small (< 50 ml) to represent the LV myocardium are eliminated. If only one cluster remains and its volume is smaller than 250 ml, the cluster is assumed to correctly identify the LV myocardium. If two or more clusters remain (suggesting that thresholding was successful in separating the LV from other "hot" structures), the one closest to the center of the upper right quadrant of the transaxial image volume is chosen. In either case, if the candidate LV cluster's volume is greater than 250 ml (suggesting that spurious hepatic, splenic or intestinal activity is still "connected" to that in the LV), "erosion" of the cluster is performed by raising the threshold in 5% steps from the original value of $C_{max}/2$, until the cluster is broken into two or more pieces. The two larger subclusters are selected and assigned to the liver and the LV myocardium (again, based on likely location considerations) and this will eliminate splenic and/or intestinal activity by setting those clusters to zero. Then, dilation of the clusters containing the liver and LV is performed by iteratively adding 1-voxel wide layers of voxels, therefore increasing the number of voxels, checking every voxel in each layer to ensure that its addition will not reconnect the clusters. This dilation is continued until the original $C_{max}/2$ threshold is reached and this results in producing a cluster

containing the correct size of the LV. The binary cluster representing the LV is used as a mask in the subsequent phases of the algorithm.

Figure 7.7(a) shows all the reconstructed slices of a typical patient data set and Figure 7.7(b) is the final segmentation of the left ventricle from the patient data. This data will be used to determine which slices of the initial reconstruction are relevant so that the attenuation source object and functional source object can be determined and be used in the final reconstruction.



(a)



(b)

Figure 7-7: Segmentation of the left ventricle. The images after the initial reconstruction of a patient dataset (a) and the left ventricle of the same data set after application of the left ventricle segmentation steps (b).

This whole process has been developed step by step to ensure proper working by testing the steps manually. It was then automated but the final implementation does provide image sets for quality assurance which could be adjusted manually, if necessary, as illustrated by figure 7.8.

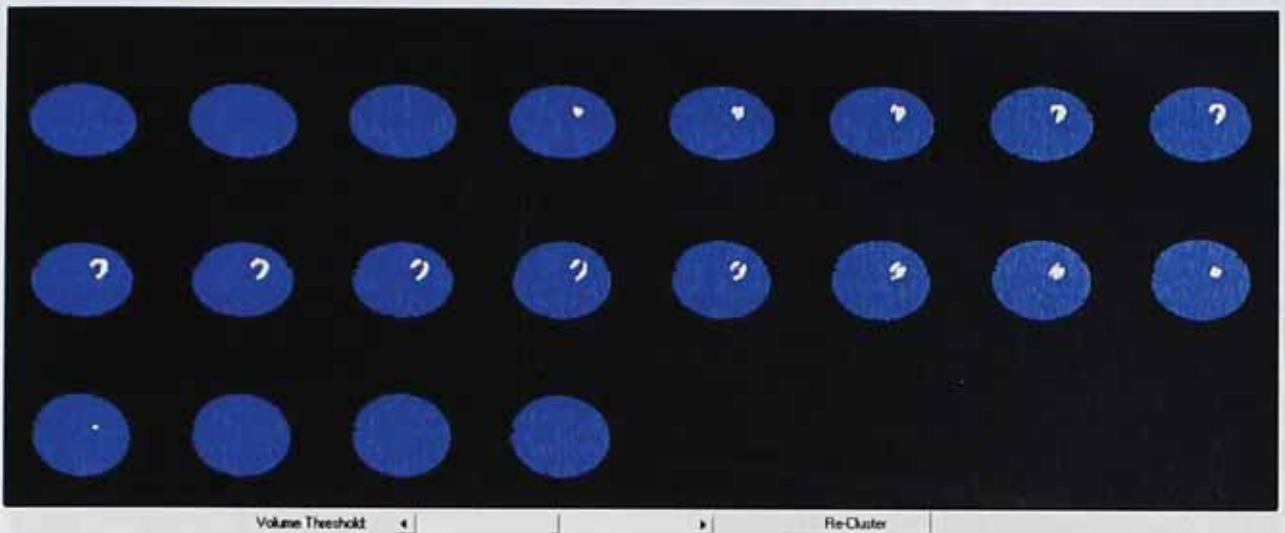


Figure 7-8: Quality control of the segmentation process. LV cluster's volume of 250 ml can be adjusted should the segmentation not be satisfactory and the clustering process repeated.

7.3.3 Determination of the Patient Data Slices

The predefined NCAT attenuation map and functional images consist of a fixed number of slices but the actual number of slices required varies for each individual patient and therefore this number needs to be adjusted for each individual patient. Therefore the actual number of slices needs to be determined so that the predefined NCAT attenuation map and functional images could be adjusted to provide the correct number of slices. The number of slices of the original NCAT data required for each patient is determined from the segmented LV images together with the body outline.

In a patient study the data is acquired over the whole field of view, i.e. the full 128x128 or 64x64 matrix. Reconstruction is done by the selection of only the relevant part of the acquired data and these required slices are often manually chosen and therefore can include unnecessary slices. It is therefore necessary to determine which of these slices used in the reconstruction are relevant. This relevant number of slices is then used to adjust the number of slices of the supplied NCAT data.

After the segmentation of both the body outline and the left ventricle they are combined into a single data set as shown in Figure 7.9(a) to decide which of these slices to use. The first step is to determine the first non-zero LV slice as displayed in Figure 7.9(a). The first relevant slice is the slice one lower than this first non-zero LV slice as displayed in Figure 7.9(b). The next step is to determine the last non-zero LV slice as displayed in Figure 7.9(a) and the last relevant slice will be the next slice after this non-zero LV slice as displayed in Figure 7.9(b). This then establishes the relevant slices which are used to determine the slices for the attenuation correction reconstruction of the patient data. The original NCAT data are now

also resampled so that the number of slices is the same as those of the patient data set in the attenuation source object and the functional source object.

This step has to be introduced to ensure the correct function of the algorithm and the software necessary to implement this method. It has again been developed by the author by using the Interactive Data Language (IDL).

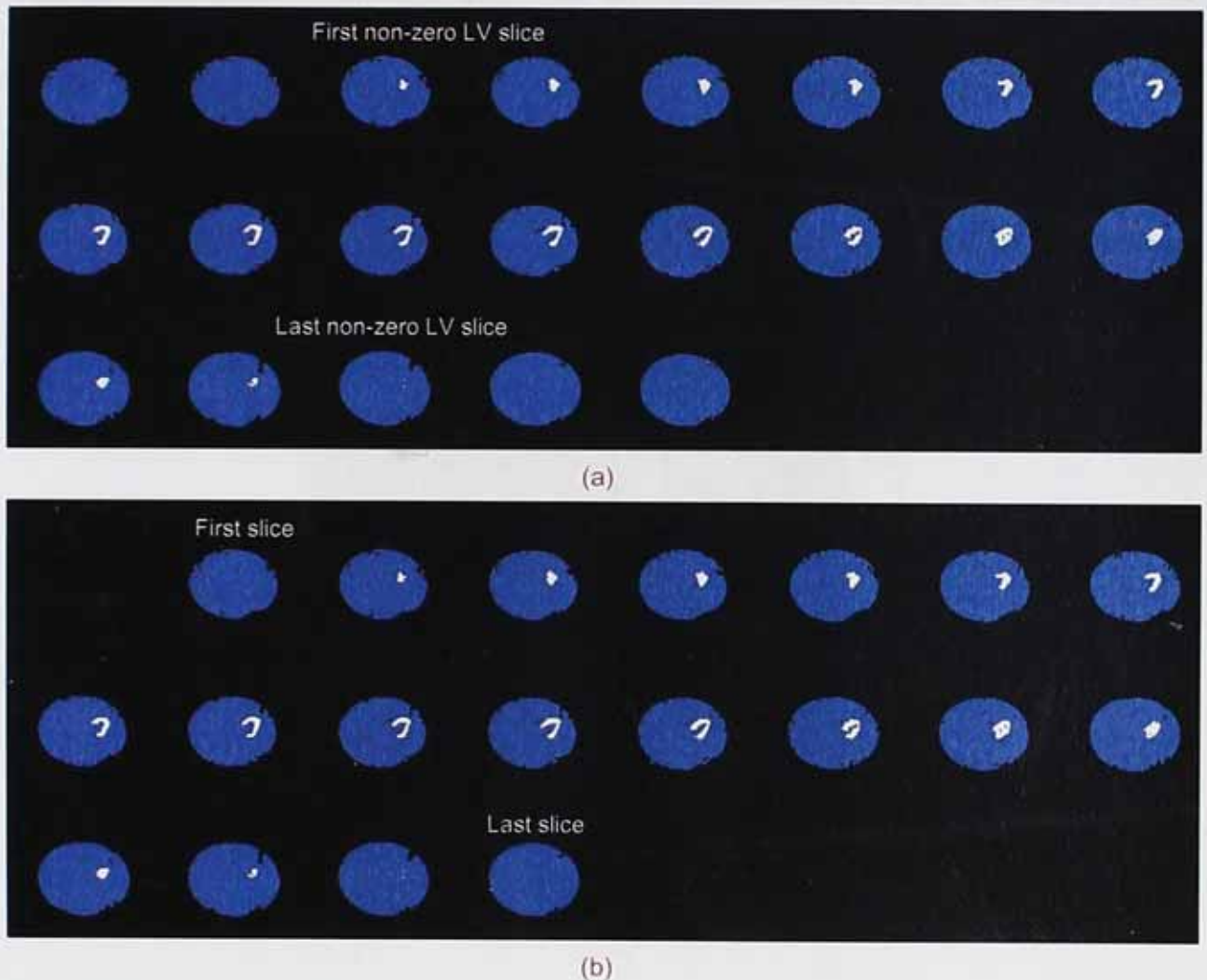


Figure 7-9: Segmentation of the complete patient data set. The body outline segmentation together with the left ventricle segmentation indicating the first and last non-zero LV slices (a) and the same data set after the selection of the relevant slices (b).

7.4 Registration of the Source Object to the Relevant Target Object

Registration returns an image array with a specified geometric correction applied. In this study images are warped using control (tie) points such that locations (x_i, y_i) on the source object which are shifted to locations (x_o, y_o) on the target object. The registration algorithm used in this section has not previously been introduced to the best knowledge of the author and this is the first implementation of this algorithm and once again the software necessary to implement it has again been developed by the author by using the Interactive Data Language (IDL). This method was easy and straight forward to implement and provided the registration results without any lengthy delays. Commercially available registration programs,

i.e. AIR²¹⁶, were used originally but it proved too cumbersome and ensuring that the whole attenuation correction process will be an automated process, required the incorporation of this program into the existing attenuation source code, something that would be both time consuming and difficult to achieve.

The registration process in this study was implemented as a two step process which is fully automated. The whole process starts with the automated selection of the slices of the patient data, as is done in any routine processing of MPI studies and shown in figure 7.10, to do the initial iterative reconstruction as described in the beginning of paragraph 7.3. The functional objects containing the correct number of slices are then obtained automatically as described above. The functional source object is then registered to the functional target object and the results displayed in a quality control image set which allows manual adjustment and repeated registration should that be deemed necessary.

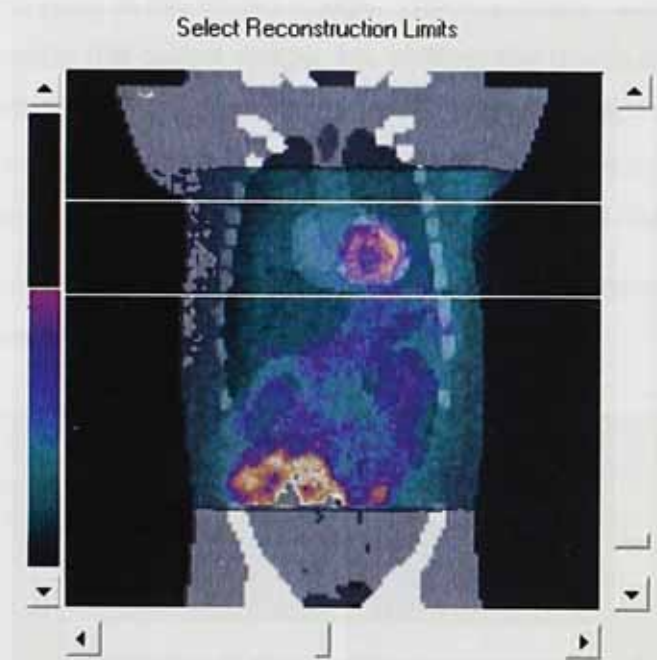


Figure 7-10: Selection (between the 2 white lines) of the slices for the initial reconstruction.

The first stage of the registration process is the main part in which the body outlines of the functional source object are matched to the body outlines of the functional target object. This result is used to provide an attenuation map consisting of the lung, bone and remainder of the body as attenuation objects as well as an initial position for the heart object. The same spatial transformations are applied to the segmented LV which forms part of the original functional image (source image). This LV functional source object is then matched to the LV functional target object to produce the final heart attenuation object. Only the LV is used to determine the registration parameters of the whole heart because the LV is the only part which can be segmented in a patient study as it is the only part of the heart taking up the radio-pharmaceutical in the vast majority of cases. The position of the LV in the functional

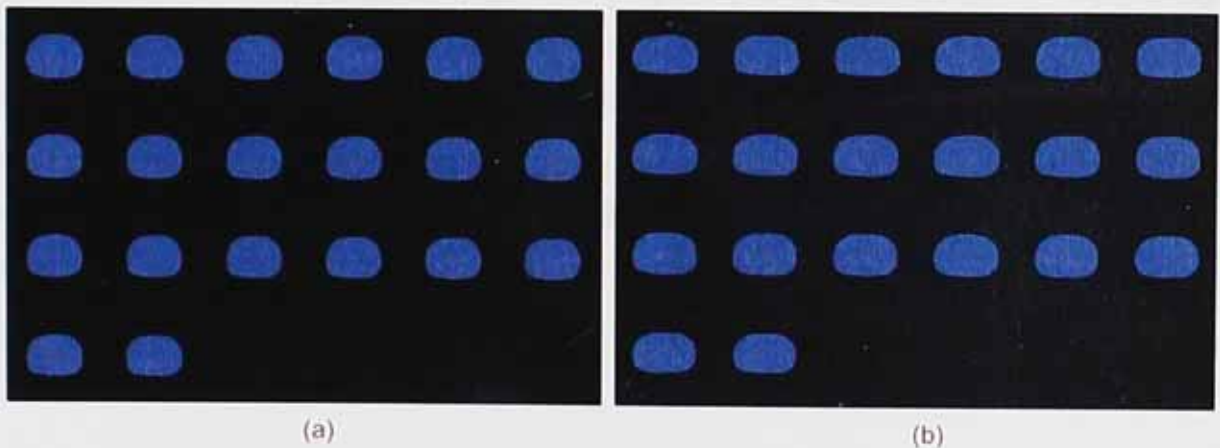
image is used to adjust the position of the heart in the structural image to produce the final attenuation map. This could potentially lead to the formation of small "gaps" in the attenuation map which are filled by the lungs as explained in the remainder of this section.

The registration is done for every slice separately and is therefore a 2-D registration process. The tie points of the first part in both the source and target objects are determined by fitting an ellipse to the source object (body outline of the NCAT phantom) providing (x_i, y_i) and to the target object (body outline of the patient) providing (x_o, y_o) . Performing a fit of the ellipse as described earlier does this.

The data locations (x_o, y_o) define an irregular grid, which is then triangulated by using a Delaunay triangulation²¹⁷ of this planar set of points. Delaunay triangulations are very useful for the interpolation, analysis, and visual display of irregularly gridded data.

The surfaces defined by (x_o, y_o, x_i) and (x_o, y_o, y_i) are interpolated to obtain the locations in the input image of each pixel in the output image. These surface values are then interpolated to a regular grid to provide the output image, i.e. shifting the points at locations (x_i, y_i) to (x_o, y_o) . Since Delaunay triangulations have the property that the circumcircle of any triangle in the triangulation contains no other vertices in its interior, interpolated values are only computed from nearby points. Linear or smooth quintic polynomial interpolation can be used.

This registration process is performed on the functional source object and the result is used to create an initial attenuation map as explained above.



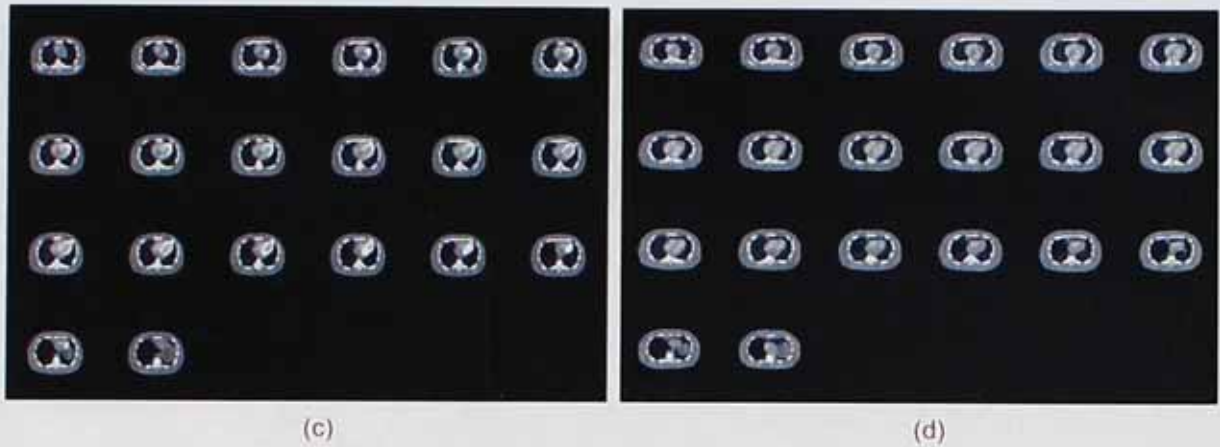


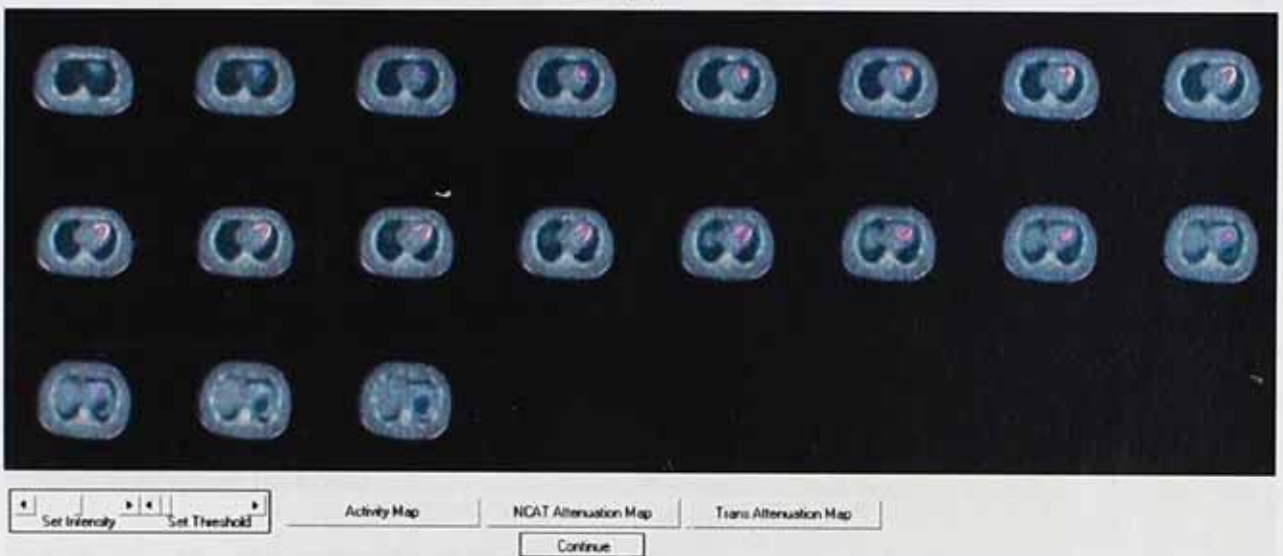
Figure 7-6: The original and final source objects of the first part of the registration. The body outline before (a) and after (b) registration. The attenuation map before (c) and after (d) registration.

The second part of the registration uses the initial LV functional source object and the segmented LV of the patient data as the target object. The differences in the position between these two sets of objects are then used to determine the left ventricle registration parameters. These registration parameters are then used to “fine tune” the heart attenuation object to produce the final heart attenuation object. The size, shape and initial orientation of the source heart object have been determined in the first part of the registration process and only the orientation of the heart is now adjusted by “fine tuning” it. The “fine tuning” of the heart consists of the determination of the top and right side of the left ventricle segmentation. The heart attenuation object is then moved up/down and/or left/right to coincide with the segmented left ventricle. The attenuation map’s final construction consists of first determining the body outline of the map; this is then filled with the attenuation coefficient correlating to that of the lungs. The skeleton, muscle, soft tissue and other organs are then added to make up the complete thorax before the final heart object is added.

This heart object together with the lung, bone and remainder of the body attenuation objects provide the final attenuation maps. These maps will act as input into an iterative MLEM reconstruction algorithm to get the attenuation corrected images.



(a)



(b)

Figure 7-7: Quality control of the registration process. Adjusting the Intensity and Contrast allow the verification of the registration of the left ventricle (a) as well as the body (b).

7.5 Testing of the segmentation and Registration

The testing of the algorithm was done in a step by step fashion. First each segmentation step was tested manually on images without any extra-cardiac activity and defects (referred to as normal uptake images) to ensure that it is working properly. The steps were then combined in an automated algorithm and again tested on normal uptake images without any extra-cardiac activity. Only after ensuring its proper working on these images, was it tried out on normal patient studies (no apparent defects) but will contain extra-cardiac activity. Different scenarios were identified, i.e. studies with very hot gall bladders, liver, spleen and gut uptake. These tested studies include those where it was very difficult to distinguish between LV and extra-cardiac activity. The final step was to include abnormal studies with enlarged LV's and severe perfusion defects which included extra-cardiac activity.

To date, the segmentation and registration algorithm has been tested on 60 patients as detailed in table 7.1 and a number of images from some of the more difficult cases are displayed below in figures 7.13 to 7.16.

Table 7-1: Results of the segmentation and registration

Segmentation and Registration		
Total Nr Patients:	60	
Status of Images		
Normal Uptake:	7	
Gallbladder Uptake:	40	
Liver Uptake:	19	
Gut Uptake:	11	
Liver/ Gut Uptake:	6	
Significant Defects:	30	
Dilated:	10	
	Failed	Success Rate
Segmentation:	0	100%
~ registration:	2	97%

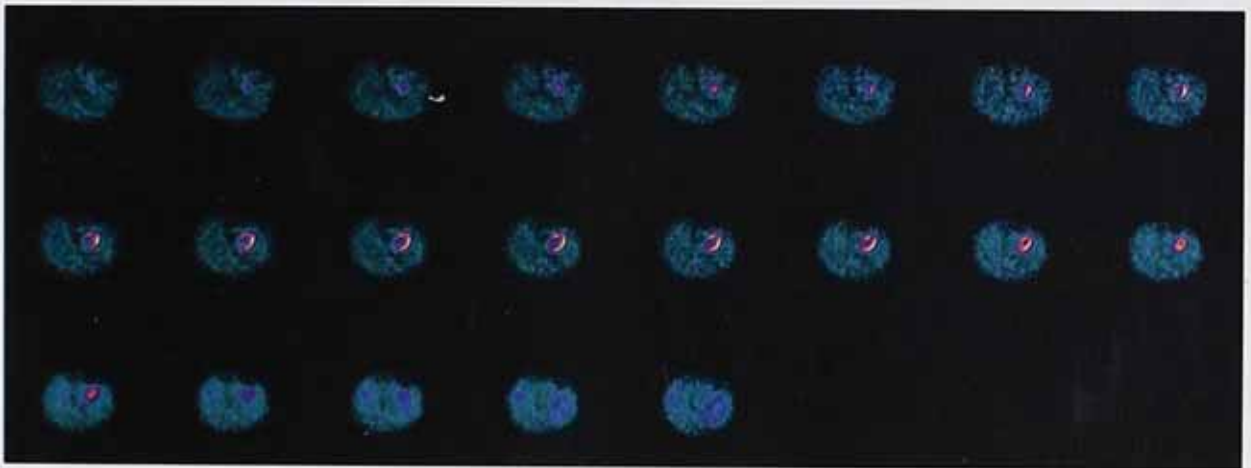
The registration process was verified with the use of a fusion display. The original reconstructed images were overlaid over the determined attenuation map. The contrast and intensity of the original reconstructed images can be adjusted to aid in the verification as displayed in figure 7.11. This process forms part of the final algorithm to ensure quality control during the process.

7.5.1 Patient with a Hot Gall Bladder

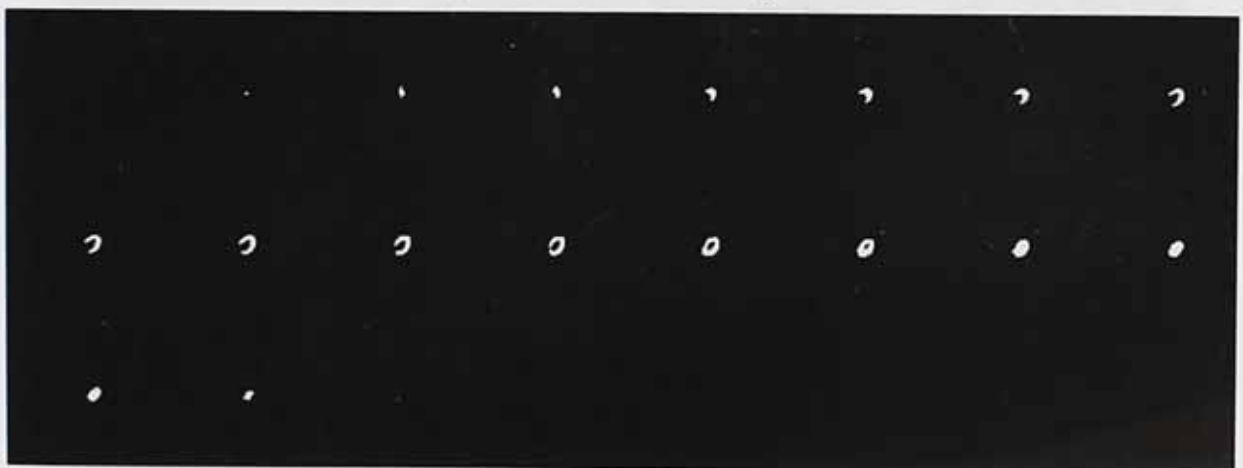
Hot gall bladders can cause serious problems during segmentation and therefore it is important that the algorithm can handle these cases effectively. Figure 7.13 illustrates such a case and illustrates that the algorithm successfully segmented the images that has lead to a successful image registration.



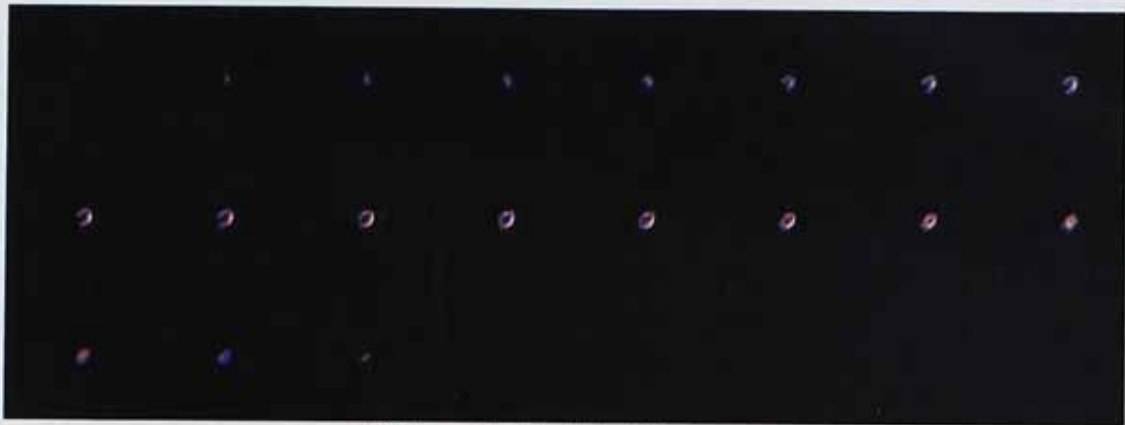
(a) Raw Images



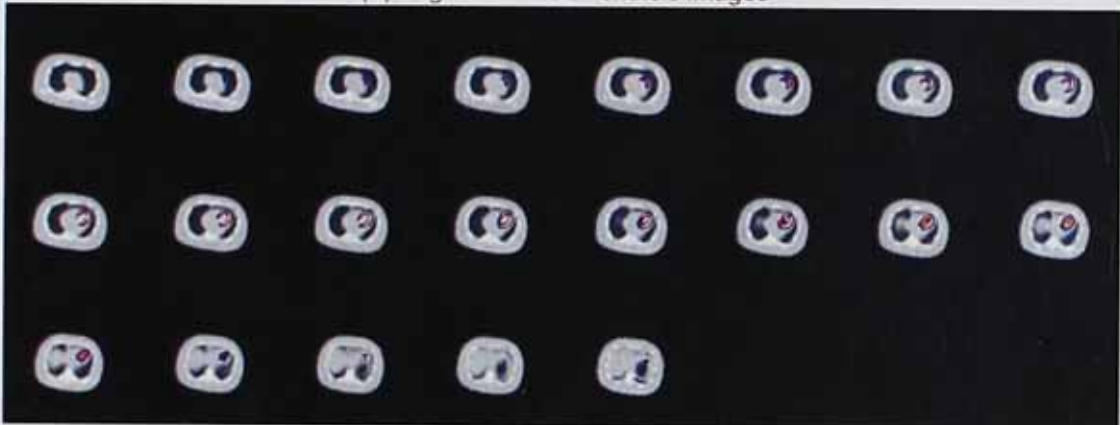
(b) Initial Reconstructed Images



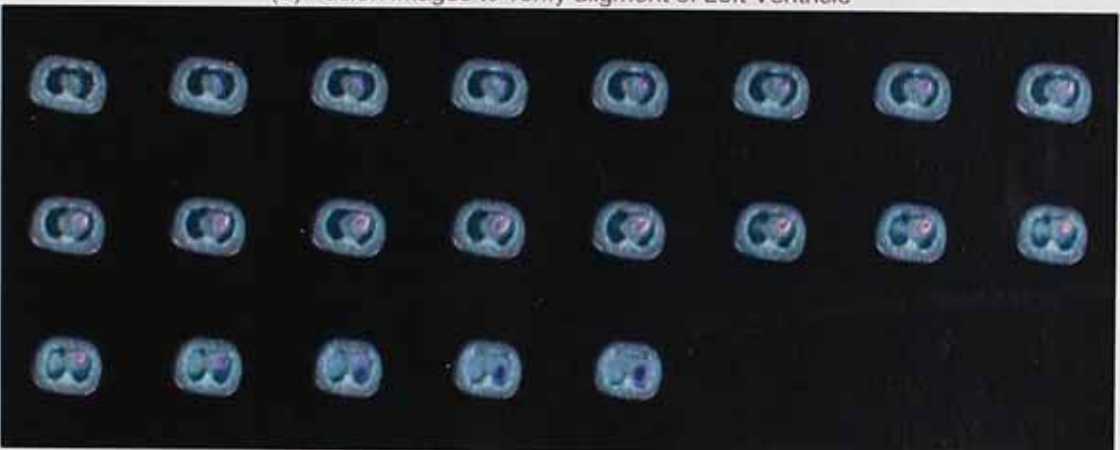
(c) Clustering of the Left Ventricle



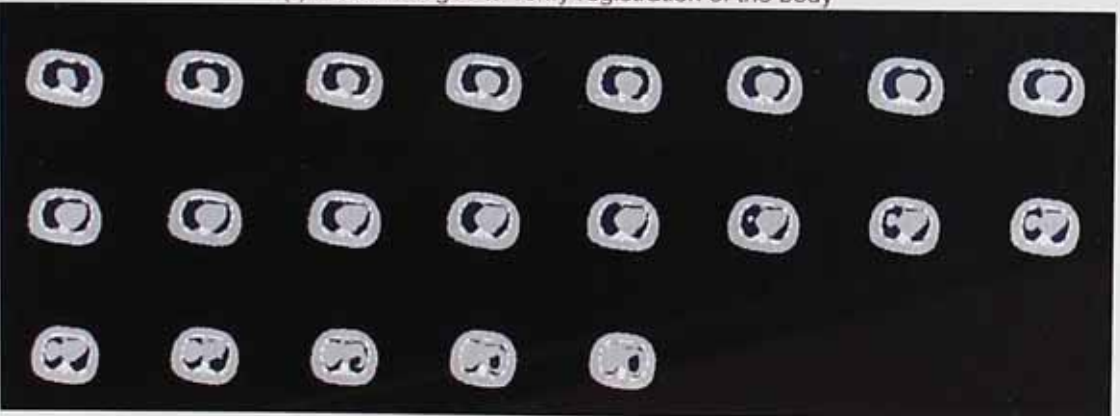
(d) Segmented Left Ventricle images



(e) Fusion images to verify alignment of Left Ventricle



(f) Fusion images to verify registration of the body

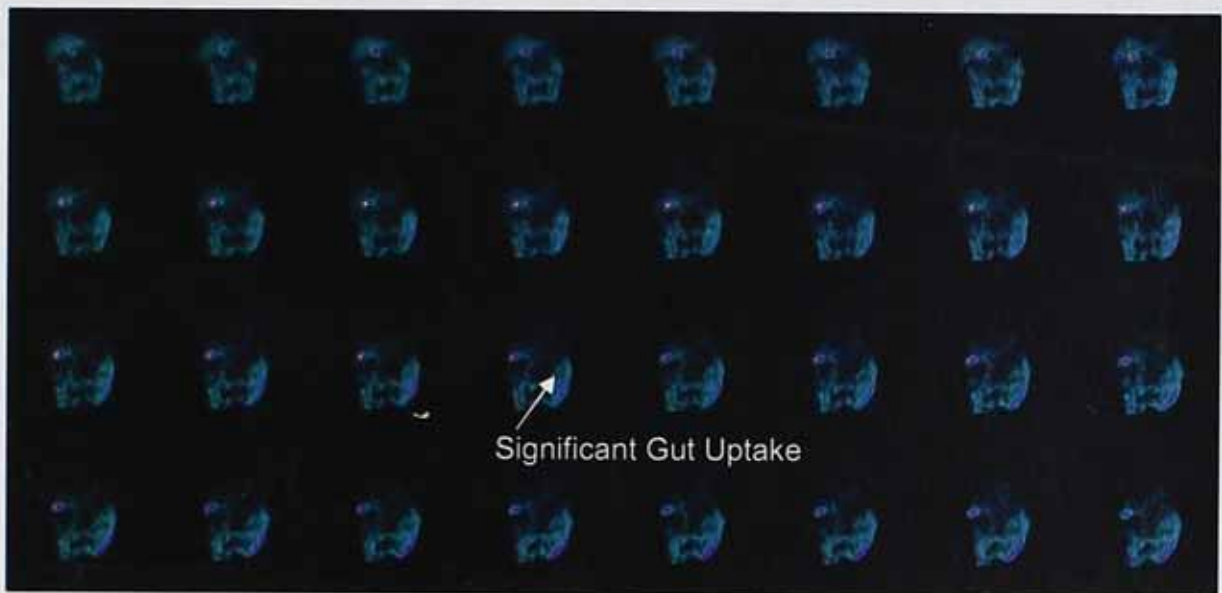


(g) Final attenuation map

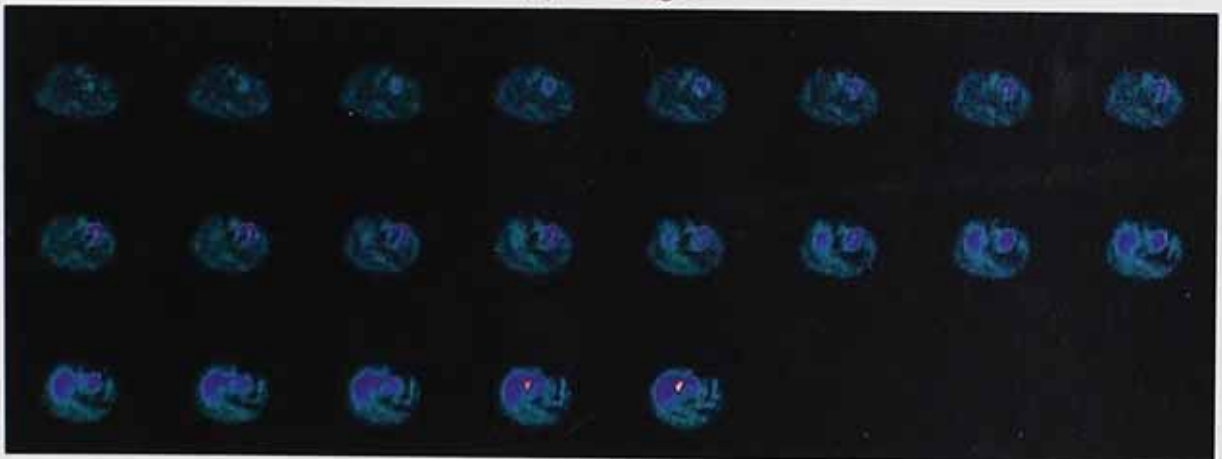
Figure 7-8: The images obtained for a patient with an extremely hot gall bladder. (a) Raw images illustrating the "masking" effect of this situation. (b) The original reconstructed images (c) The body and LV segmented images (d) Images illustrating the removal of all the non-LV pixels (e) Overlay of this images over the final attenuation map illustrating the successful outcome of the registration parts and (f) The final attenuation map.

7.5.2 Patient with Substantial Gut Uptake

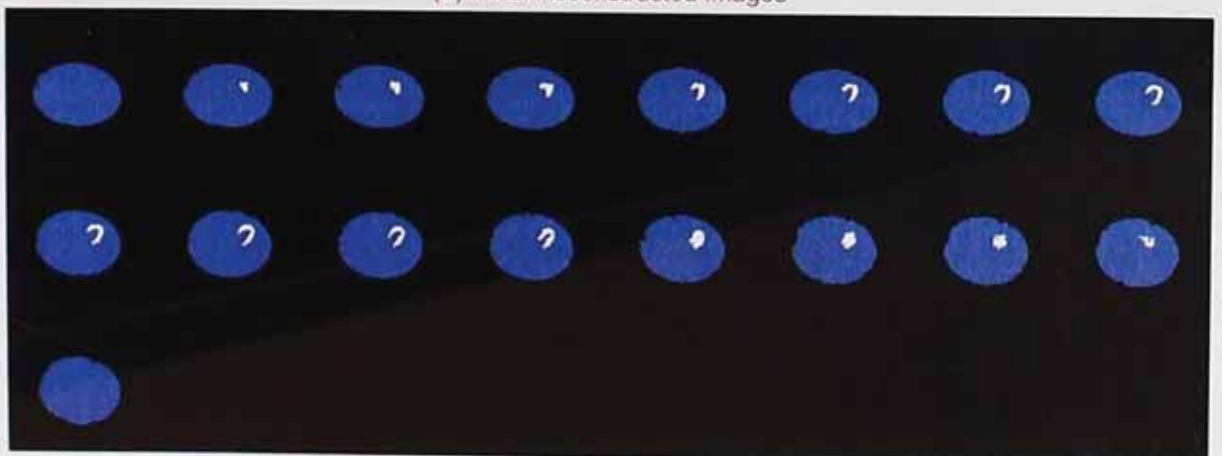
Gut uptake is one of the most important obstacles in the successful segmentation of the images and considerable effort has been taken when writing the algorithm to ensure that it can handle these cases successfully. Figure 7.14 illustrates such a case and illustrates once again that the algorithm successfully segmented the images that has lead to a successful image registration.



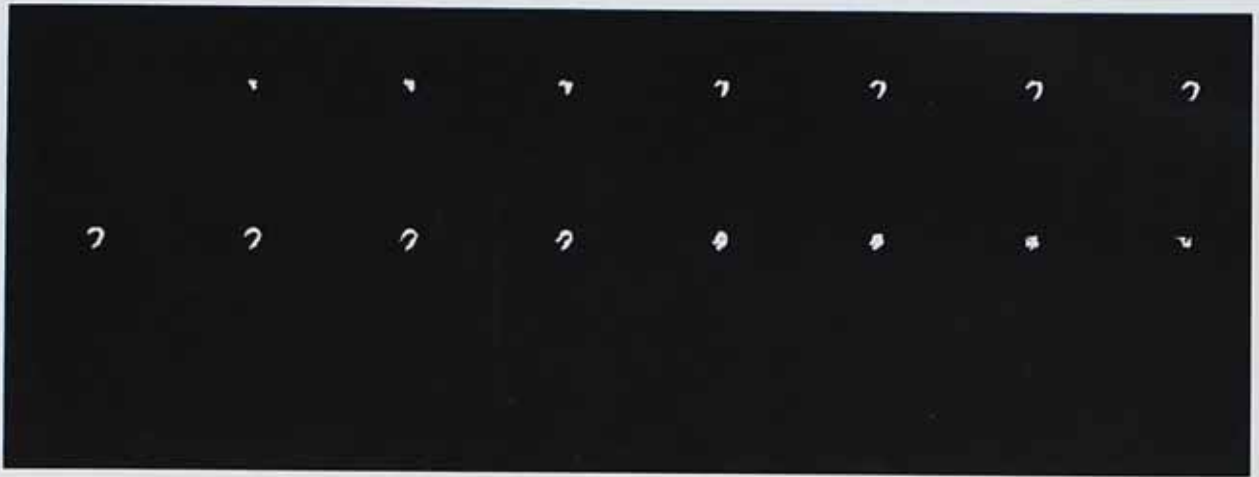
(a) Raw Images



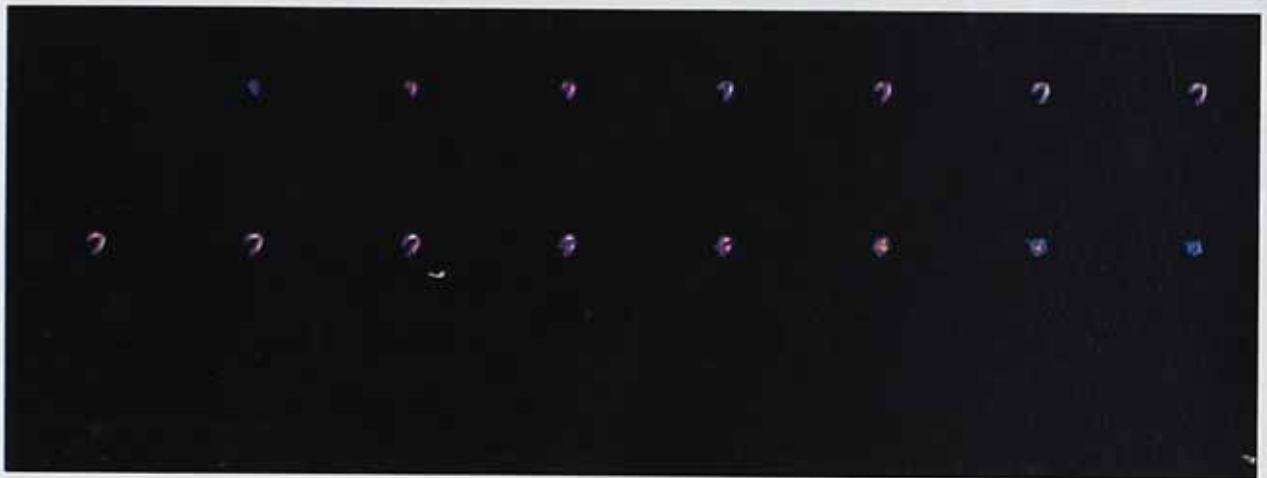
(b) Initial Reconstructed Images



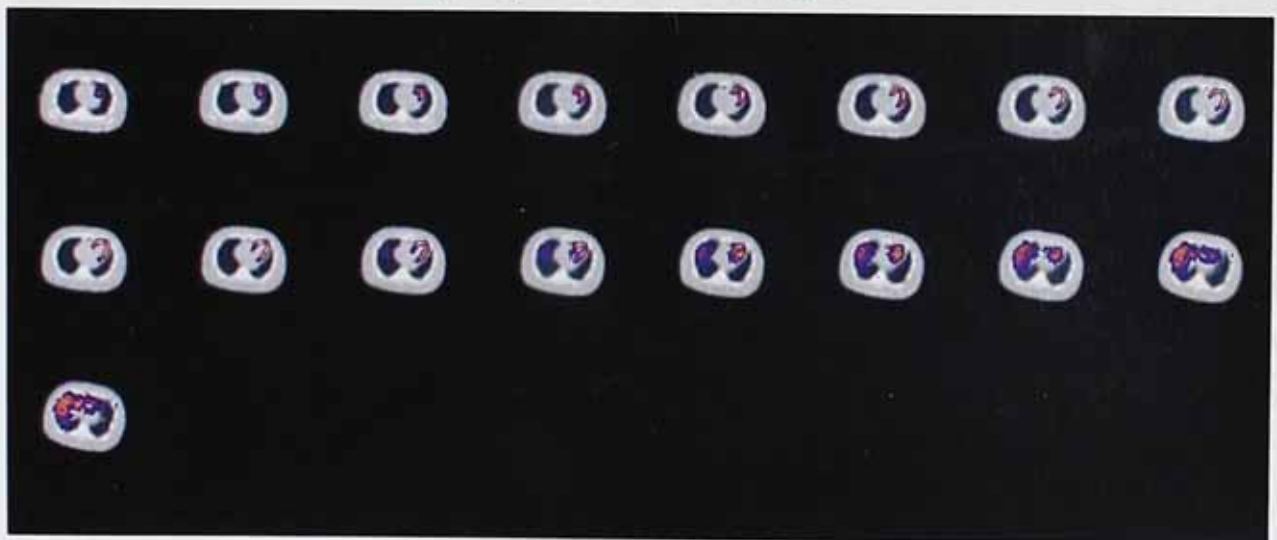
(c) Functional Images



(d) Clustering of the Left Ventricle



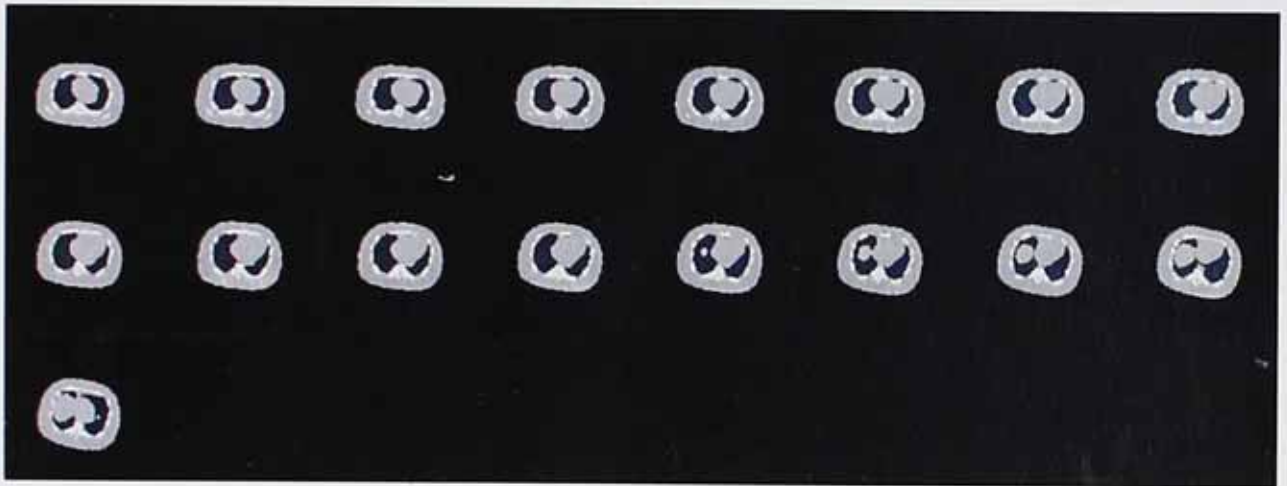
(e) Segmented Left Ventricle images



(f) Fusion images to verify alignment of Left Ventricle



(g) Fusion images to verify registration of the body

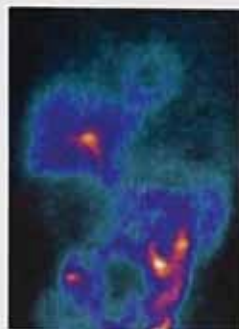


(h) Final attenuation map

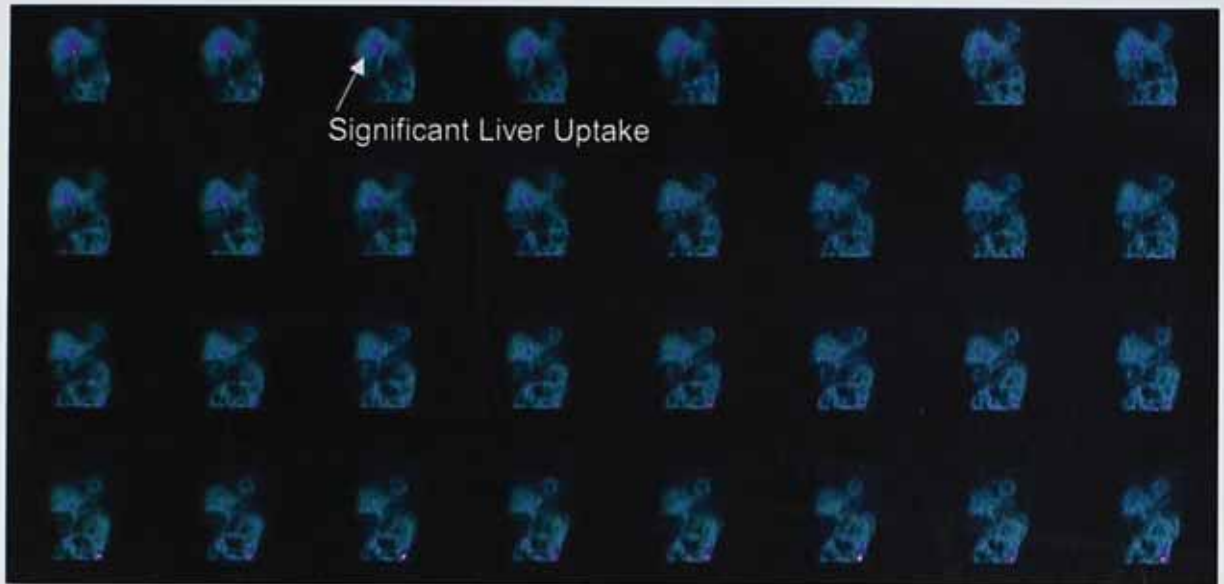
Figure 7-9: Set of images from a patient with substantial gut uptake.

7.5.3 Patient with Substantial Liver Uptake

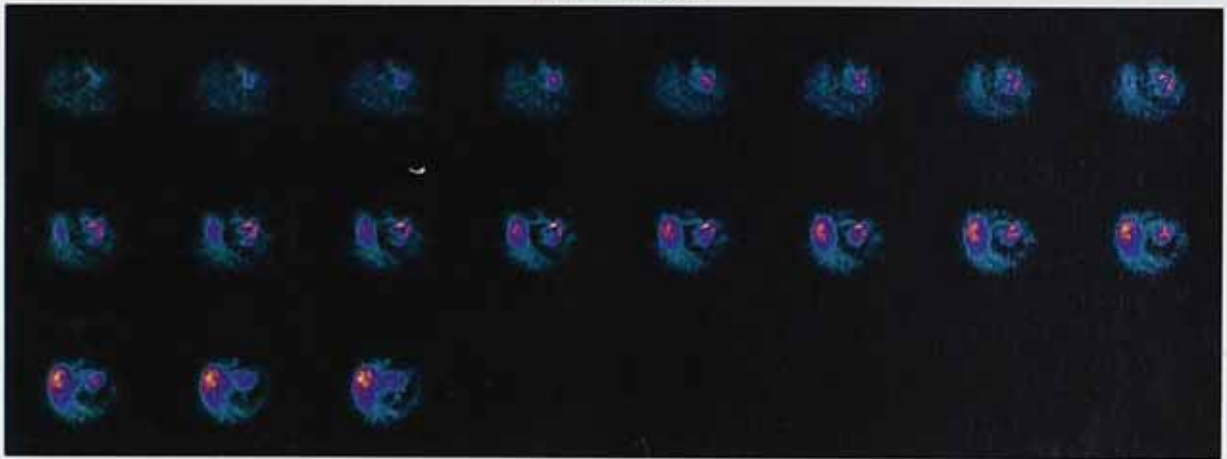
Another important obstacle to obtain successful segmentation is liver uptake and therefore the algorithm should be able to handle these cases as well to once again ensure successful segmentation. Figure 7.15 illustrates a case with severe liver uptake and illustrates that the algorithm successfully segmented these images once again that has lead to a successful image registration.



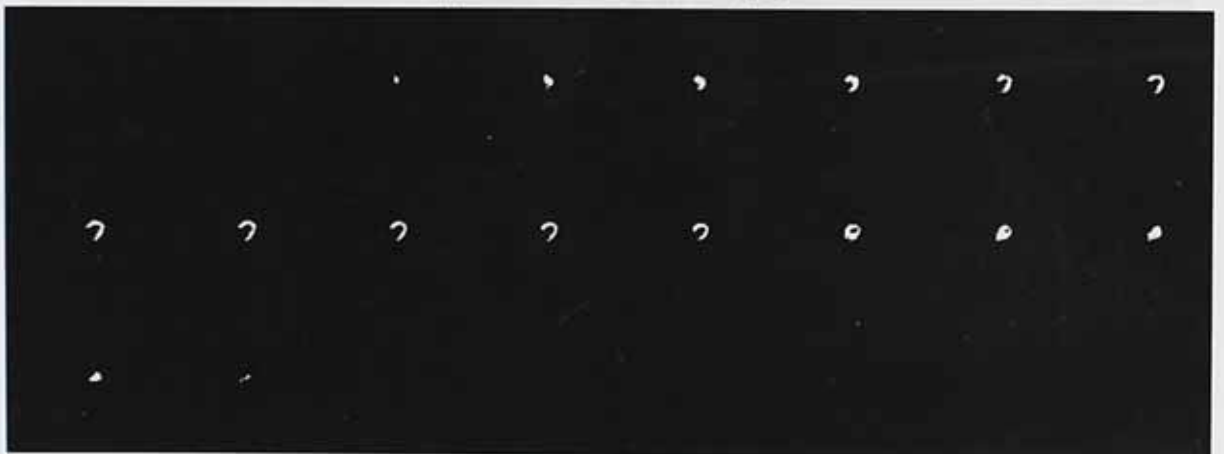
(a) Substantial Liver Uptake



(b) Raw Images



(c) Initial Reconstructed Images



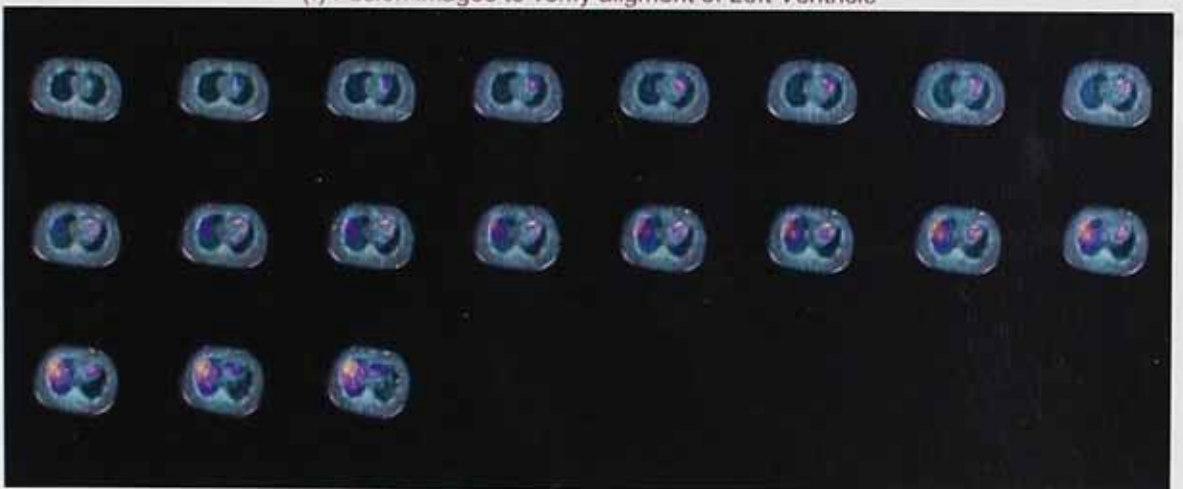
(d) Clustering of the Left Ventricle



(e) Segmented Left Ventricle images



(f) Fusion images to verify alignment of Left Ventricle



(g) Fusion images to verify registration of the body

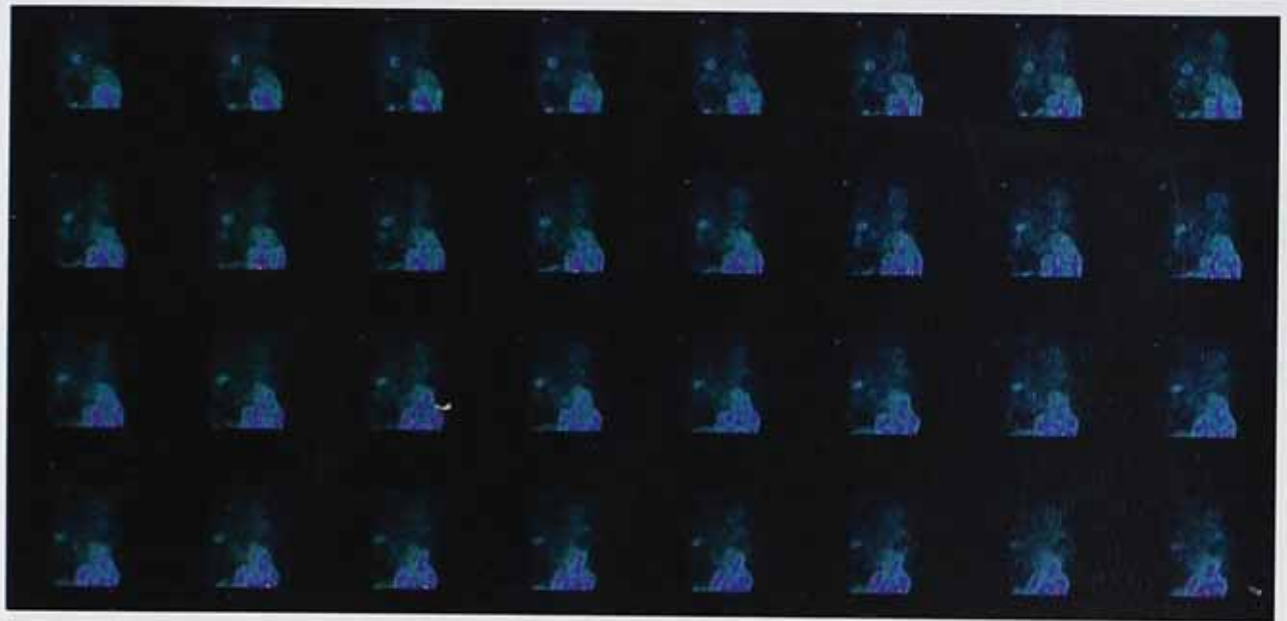


(h) Final attenuation map

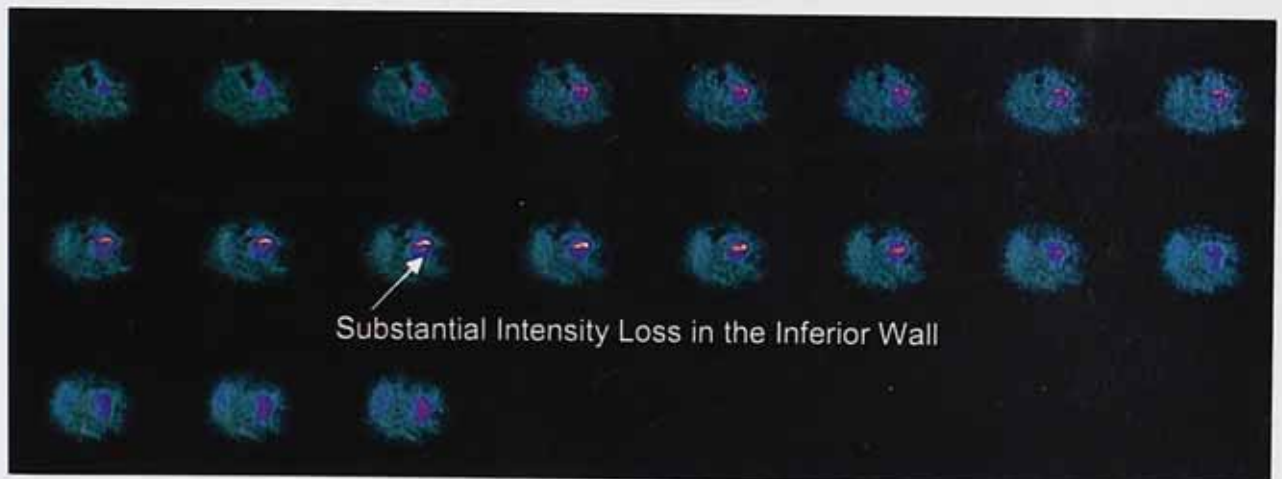
Figure 7-10: Set of images from a patient with substantial liver uptake.

7.5.4 Patient with Substantial Intensity Loss in the Inferior Wall

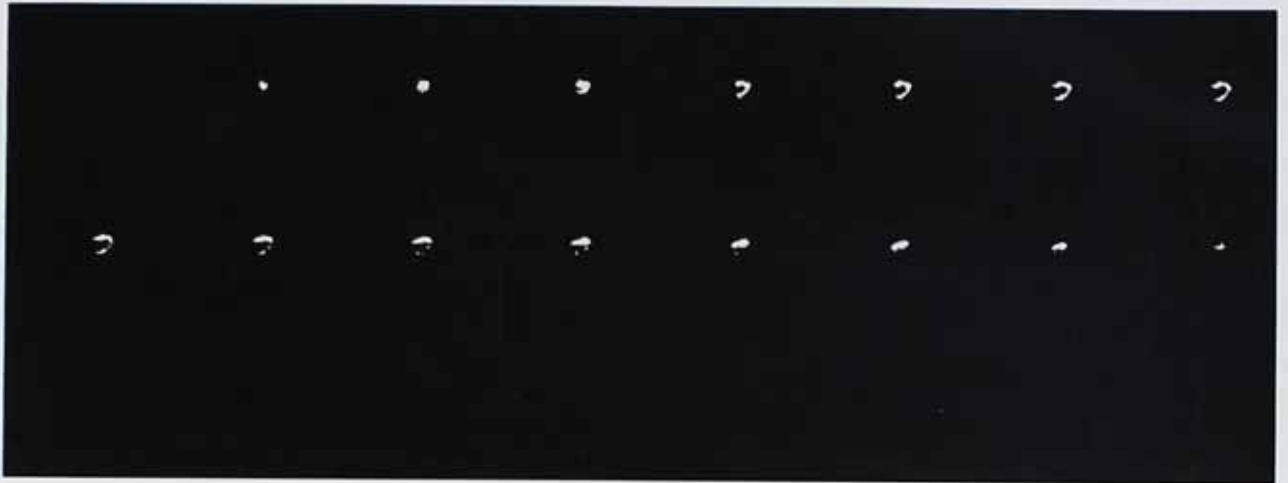
The algorithm must be able to detect the whole left ventricle and this can be complicated when there is a substantial (or even absence) of intensity values in a part on the left ventricle. Figure 7.16 illustrates a case where there is a substantial loss of intensity values in the inferior wall but the algorithm also passed this obstacle to obtain a successful image registration.



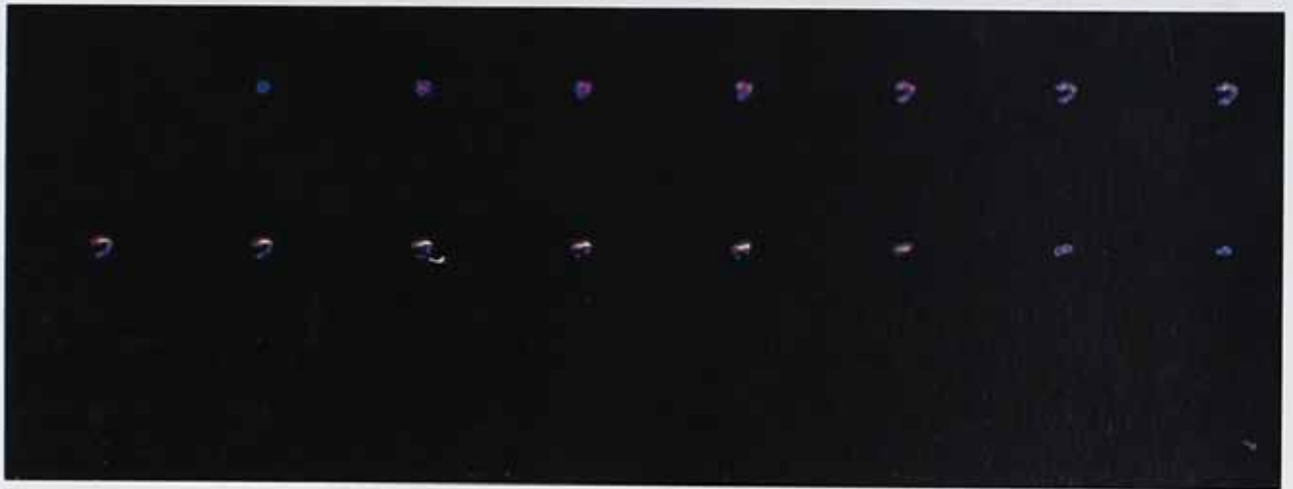
(a) Raw Images



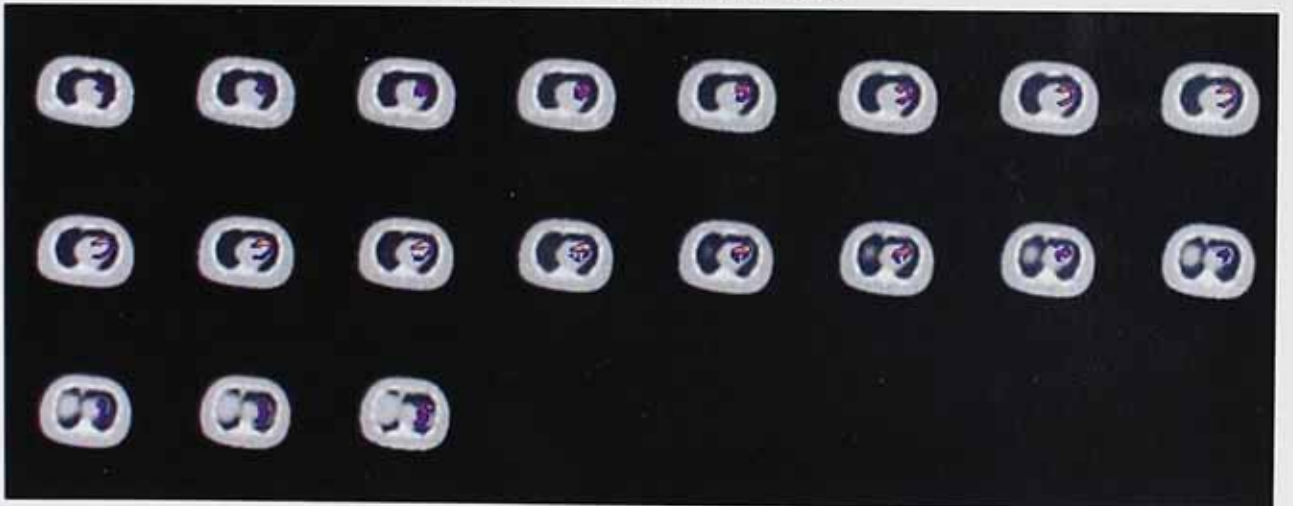
(b) Initial Reconstructed Images



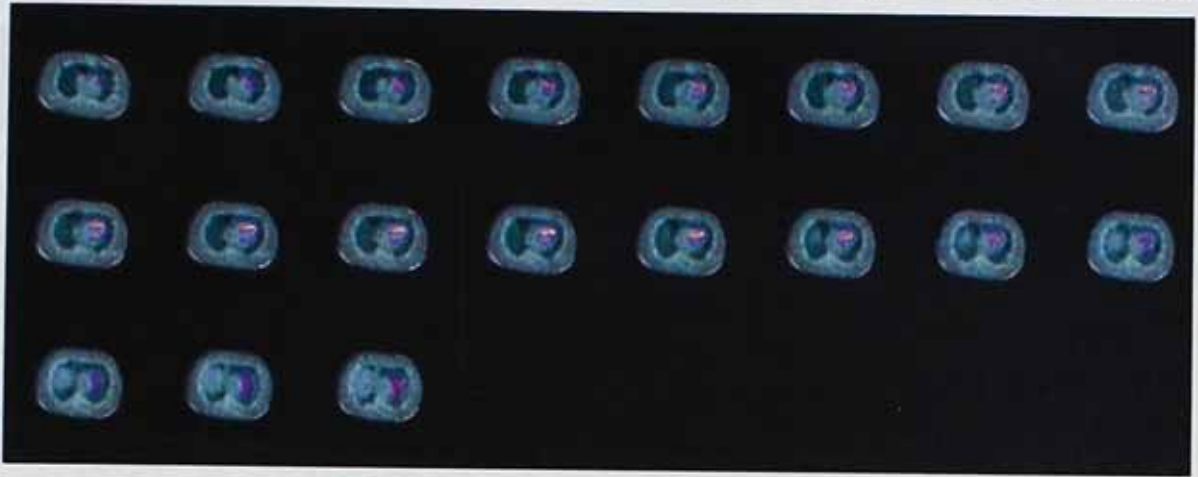
(c) Clustering of the Left Ventricle



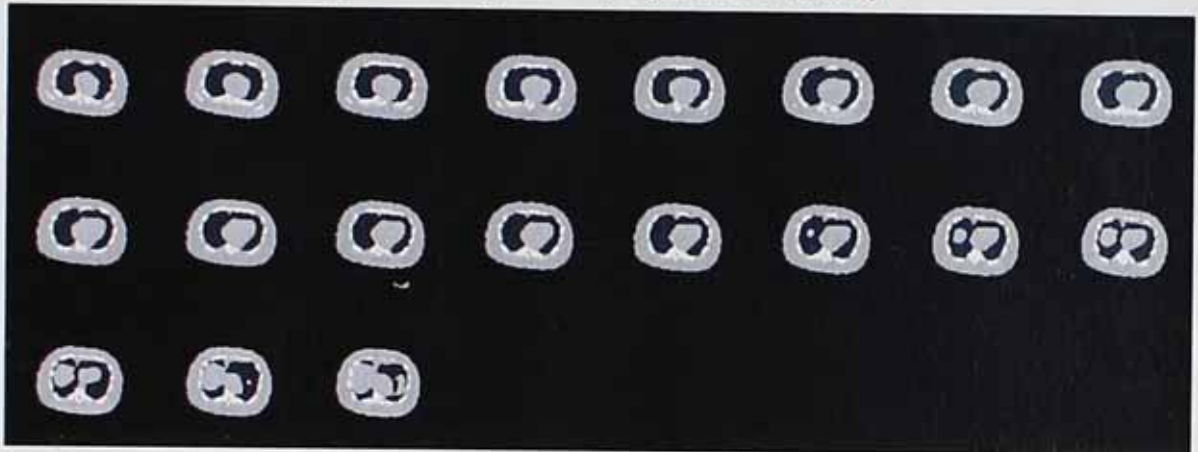
(d) Segmented Left Ventricle images



(e) Fusion images to verify alignment of Left Ventricle



(f) Fusion images to verify registration of the body

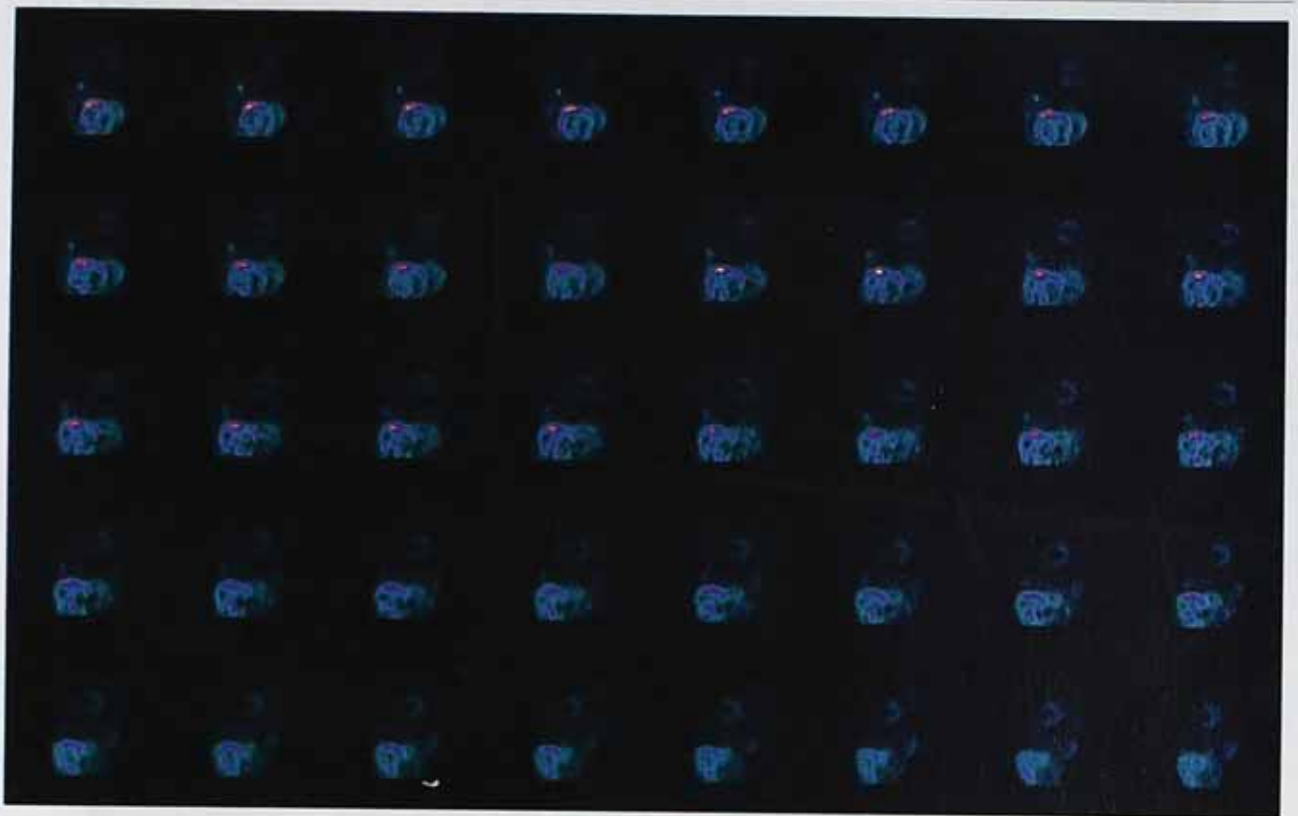


(g) Final attenuation map

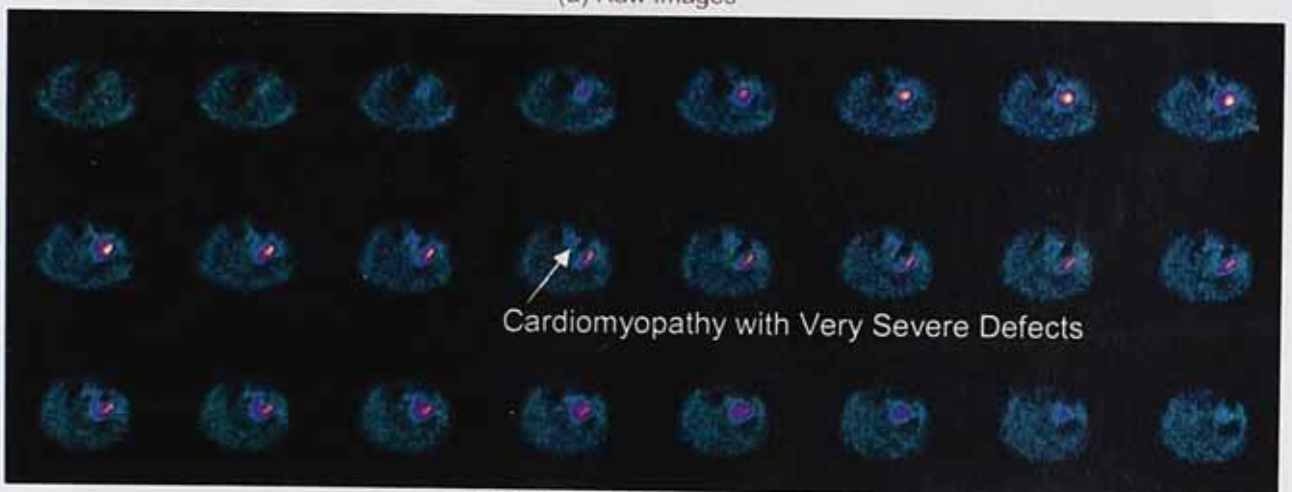
Figure 7-11: Set of images from a patient with substantial intensity loss in the inferior wall.

7.5.5 *Cardiomyopathy with Very Severe Defects*

The above mentioned intensity losses can be further complicated in cases with cardiomyopathy and in these cases there is often a part which has no intensity values. Figure 7.17 illustrates the successful segmentation and consequently image registration.



(a) Raw Images



(b) Initial Reconstructed Images



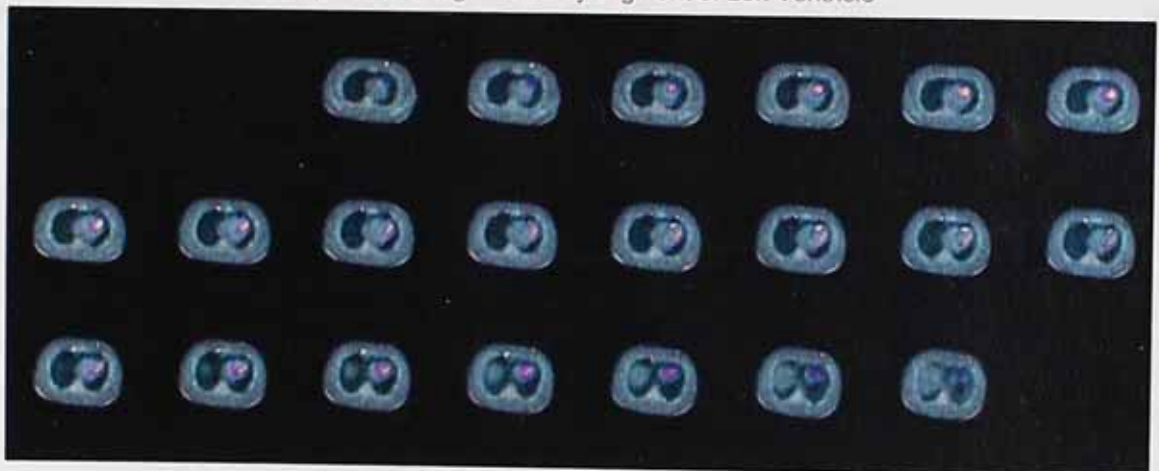
(c) Clustering of the Left Ventricle



(d) Segmented Left Ventricle images



(e) Fusion images to verify alignment of Left Ventricle



(f) Fusion images to verify registration of the body



(g) Final attenuation map

Figure 7-12: Set of images from a patient with a dilated heart with very severe defects.

7.6 The method of derived anatomy

Another attractive method of emission based attenuation correction is to use a derived NCAT attenuation map. This differs from the previous method, which starts with an existing attenuation map which was spatially altered to relate to a specific patient, by a method which does not make use of an existing attenuation map and the map is created from first principles for each patient. The NCAT phantom software uses a parameter file as input which defines the parameters of the "patient" to be created by the software. Should it be feasible to derive the required parameters from the patient data a patient specific attenuation map can be created from the parameter file alone which can be used in the reconstruction process.

The automated segmentation used in the method of inferred anatomy can be extended to derive the required parameters and it includes both the segmentation of the LV and body outline used in the method of inferred anatomy. In this method an additional step is required, which is extracting of the mid-myocardial surface (this is similar to a published method^{194,218} but there are some small differences in the method discussed here, especially the fitting of the ellipsoid) and included in the automated algorithm. In this algorithm no use will be made of image registration and the initial reconstruction will again be used to obtain the images to be used in the segmentation and mid-myocardial surface extraction to determine the values necessary for the NCAT input parameter file. The determination of the mid-myocardial surface closely resembles the method as described in the literature but its output has never been used before to determine the values of the input NCAT parameter file.

7.6.1 Mid-Myocardial Surface Extraction and Fit

The center of mass (COM) of the three-dimensional binary mask segmenting the LV myocardium is chosen as the origin of the sampling coordinate system. If segmentation of the LV was successful, the COM will be located within the LV cavity, even in the presence of large perfusion defects. Radial count profiles originating from the COM are generated to achieve three-dimensional, spherical sampling of the product of the binary mask and the transaxial image volume. The locus of the profiles first maxima identifies the maximal count myocardial surface, which is an acceptable proxy for the mid-myocardial surface. Sampling is every 10° longitudinally (18 total) and every 10° latitudinally (36 total), resulting in 684 count profiles. It should be noted that a variable, potentially large number of these profiles are uniformly zero. In fact, both the basal portion of the myocardium at the valve plane and all perfusion defects will correspond to "holes" in the mask, for which no maxima are returned.

A fit of the mid-myocardial surface to a quadratic surface is performed by using the moments and the quadratic form of the ellipsoid equation²¹⁹ and the long axis of the quadratic surface is considered an initial estimate of the long axis of the LV.

The surface extraction process is then repeated using a new origin for the sampling coordinate system, determined as the projection of the original COM onto the estimate of the long axis. This approach seeks to obviate errors in mid-myocardial surface extraction, especially in cases where the original COM is close to the wall due to extensive perfusion defects. The process is iterated until the long-axis angular variation is less than 0.5° , which generally requires two to three iterations.

We now have an estimate of the mid-myocardial surface, plus the ellipsoid that best fits it. This image of the myocardial surface may contain some "perfusion holes" ie defects caused by disease, artefact, the basal part, etc. These "perfusion holes" needs to be filled by an automated method to get the best fitted estimate of the shape, size and orientation of the LV. To incorporate perfusion data from under perfused areas into the fit (fill the holes), a set of myocardial "likelihood profiles" (24 latitudinally, 32 longitudinally) is generated by extracting count profiles normal of the ellipsoid from the unmasked and non thresholded image and convolving them with a feature detector consisting of the double derivative of a Gaussian with a s.d. $\sigma = 10$ mm. The s.d. value of 10mm was chosen based on expected feature size and camera resolution and observed LV myocardial count profiles, which are seen to approximate Gaussians with standard deviations of approximately 10 mm. The number of samples was chosen so that a sampling frequency of approximately 5 mm from count profile to count profile at the myocardium would result for a typical LV geometry (75mm from apex to base, 50mm from superior to inferior wall). The local maxima of these profiles are extracted (there is generally at least one local maximum per profile). The final mid myocardial surface is then defined as that set of surface points, one per profile. An ellipsoid is finally fitted to this myocardial surface and the resulting long axis returned as that of the LV.

The method of Mid-Myocardial Surface Extraction and Fit described here, as well as the segmentation of the LV, form part of commercially available packages such as the quantitative gated SPECT (QGS)/quantitative perfusion SPECT (QPS) program^{220,221}, which is routinely used in nuclear cardiology examinations. Therefore no source code or programs are available and the desired part of the commercially available programs cannot be used on its own to do the segmentation and fitting and therefore the method was developed for this project by using the Interactive Data Language (IDL)²¹².

7.6.2 Testing the Mid-Myocardial Surface Extraction and Fit

The segmentation of the LV has been extensively tested for the method of inferred anatomy and it has been founded to be very robust in dealing with even difficult cases, see section 7.5. This segmentation forms the first stage of the method of derived anatomy, and will perform in a similar manner. The method of derived anatomy then uses the mid-Myocardial Surface Extraction and Fit. This part was successfully tested on ideal images (simulated

image set with no attenuation medium) as illustrated in figure 7.18 and 7.19 but further testing is necessary on normal and abnormal patient data.

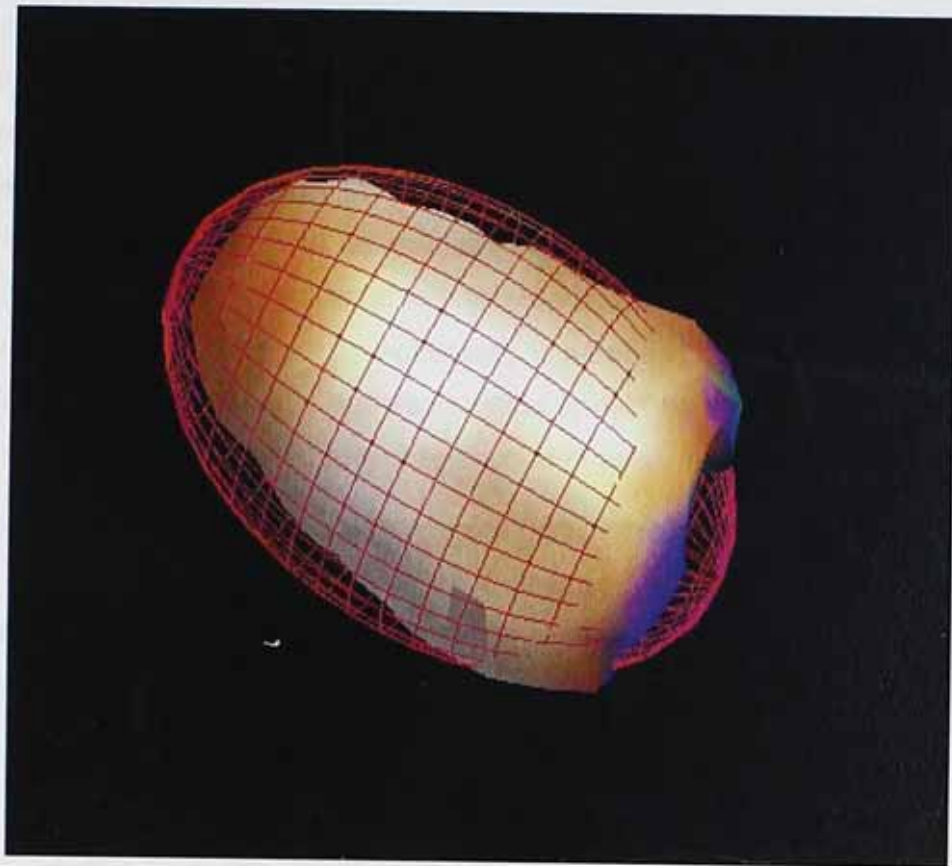


Figure 7-13: The fit (mesh) fitted to the extracted data points of the mid-myocardial surface.

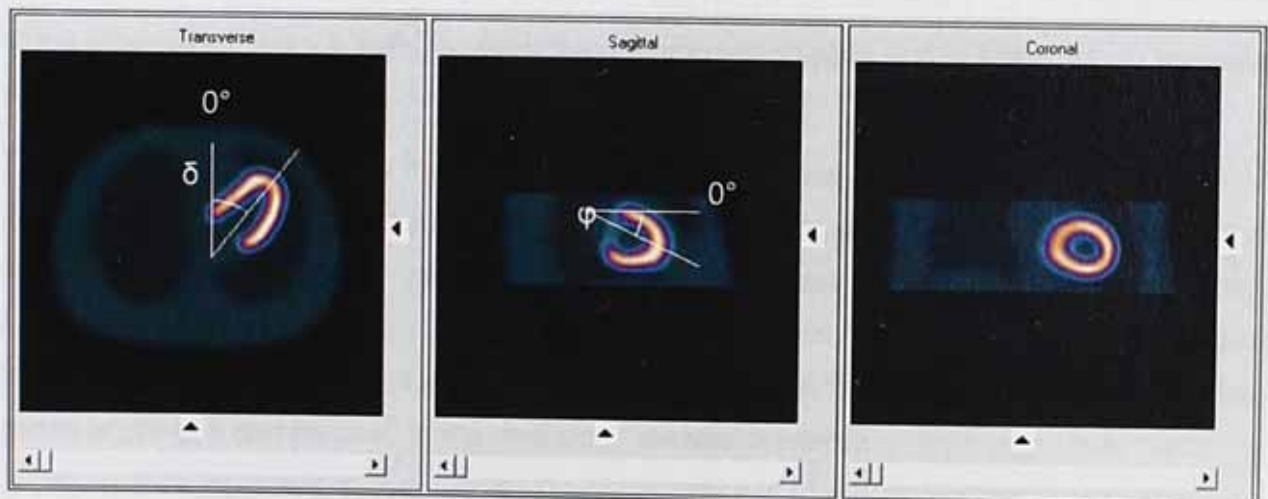


Figure 7-14: Determination of the angles required by the NCAT parameter file.

7.7 Conclusion

This study demonstrates the successful creation of an inferred attenuation map of the thorax. It illustrates that it is possible to segment the thorax to obtain the body and only the left ventricle so that the input images for the registration process can be obtained. It also illustrates the successful registration so that the final attenuation map can be obtained. It

handled difficult cases such as hot gall bladders, spurious hepatic, splenic or intestinal activity, even those where it is difficult to distinguish between extra-cardiac and LV activity as well as studies which contained perfusion "holes". The segmentation was successful in all the tested cases and the registration was successful in all but 2 of the 60 cases, giving a success rate of 97% which compared favourably with the success rate of commercially available programs such as the quantitative gated SPECT (QGS)/quantitative perfusion SPECT (QPS) which had a segmentation success rate of 98.7%²²⁰ when tested. It is worthwhile noting that the patient studies which failed the registration in this study were patients with severely dilated myocardia with very severe defects, cases in which the benefits of attenuation correction would not be necessary to establish the clinical interpretation of the scan. Therefore the segmentation and registration should be suitable for use in the clinical environment as part of the inferred anatomy method of attenuation correction.

It is also worthwhile to note that the only manual part of the attenuation correction process is the loading of the patient study which is then displayed as depicted in figure 7.10 for the manual selection of the slices. The remainder of the process, i.e. initial reconstruction, segmentation, image registration, determination of the final attenuation map and the attenuation corrected reconstruction are executed automatically to produce the attenuation corrected images.

Another worthwhile point is the fact that the initial reconstruction serves a dual purpose. It is always good practice to display both corrected and uncorrected images when interpreting the reconstructed images. Although the initial reconstruction is necessary for the determination of the attenuation map, it also provides the uncorrected images and is therefore an essential but not an additional step.

The successful extraction of the mid-myocardial surface has also been demonstrated in an ideal situation. The successful extraction of the surface, together with the LV segmentation, makes the determination of values for the NCAT parameter file possible so that a patient specific attenuation map can be obtained. The extraction method does need additional testing and development, if necessary, to ensure it will be suitable to handle more difficult cases and that it can be used in the method of derived anatomy.

7.8 Future Work

The method of inferred anatomy has been tested successfully on a wide range of patient data illustrating that it could be useful as an attenuation correction method to improve the outcome of patient studies but the method needs to be verified against a standard, either transmission attenuation maps or coronary angiography as a gold standard, to verify its suitability in a clinical environment. The method of derived anatomy needs some more development and testing before it will also have to be tested against a gold standard to verify

its suitability in a clinical environment. This testing can be performed by using the previous Monte Carlo simulated data with the associated attenuation maps that has been used to generate the required attenuation in the simulations and to compare the attenuation correction results to the simulations without the attenuation medium. The next step will be to use patient data that has been acquired with attenuation maps and where these maps have been used to correct for attenuation. By replacing these attenuation maps with the inferred and/or derived maps, the reconstruction can be repeated and the two sets of reconstruction data compared. This testing will be part of follow-up studies and not be part of the thesis.

The segmentation part as well as the registration could be further improved. Note that the segmentation forms part of both of the two proposed methods. The areas where it could be improved are:-

1. the detection of lung areas in both male and females and
2. the breasts in females.

Currently the body outline of females does include the breast areas but it is more an "averaging" than the exact detection of the size and shape as a result of the detection of the body outline and using the breast as part of the body instead of explicitly deriving the parameters of the breasts, i.e. angles, tilt, etc. to define these parameters in the NCAT parameter file.

The lungs areas cannot be established from the current reconstruction of the emission data. The lung/body ratio does vary between patients and the exact outline of the lungs could be used to determine the size of the rib long and short axis. The importance of using the exact rib cage dimensions together with the body dimensions instead of an approximation (as is currently the case) when the body outline is known is not clear at the moment. This could be established with a Monte Carlo simulation study.

The possibility of improved segmentation should be investigated with the use of MAP-EM reconstruction methods. MAP stands for maximum a posteriori by incorporating a priori knowledge into the reconstruction algorithm. This means that one uses existing knowledge to guide the reconstruction process for a more robust and reliable solution. This prior or existing knowledge are often referred to as priors. Examples of such prior knowledge are knowledge about the range of the attenuation coefficients, the anatomical outline of the patient, etc. The reconstruction problem can be formulated as a Bayesian model²²². In a Bayesian model the posterior distribution is obtained from the likelihood and prior distribution. The prior representing the knowledge of the spatial distribution of the source can be modelled as a Gibbs distribution and the likelihood can be modelled as a Poisson distribution²²³.

Such an implementation has been proposed¹³⁹ where the a priori knowledge about absolute attenuation values was implemented as a bi- or trimodal probability distribution. The

attenuation map can be expected to be locally smooth and the local smoothing prior is implemented using a 2-D Gibbs distribution.

The initial reconstruction can then be performed by using the MAP algorithm with priors containing the range of attenuation coefficients and a Gibbs distribution to obtain images which will make improved segmentation possible so that segmentation of the lungs and breasts could be a possibility.

The image registration algorithm can also be extended to a fully 3-D algorithm to take into consideration the spatial relationship between slices. This will have an impact only on the method of inferred anatomy.

Chapter 8 - Conclusions and Further Work

8.1 Conclusions

The main purpose of this project was to investigate the current limitations of MPI so that the areas which will benefit most from improving could be identified. Identification of these areas led to investigations into the reason why they still pose problems. By doing so it has been possible to identify and investigate future improvements.

Chapter 2 illustrated in detail the extensive work that has been done to improve the usability and accuracy of Myocardial Perfusion Imaging (MPI) over the years. From this analysis the main factors that degrade the image quality and the quantitative accuracy of emission tomography reconstructions were identified as:

- ▶ Attenuation of the photons travelling toward the detector,
- ▶ The detection of scattered as well as primary photons,
- ▶ Depth-dependent collimator response correction (frequency-distance principle),
- ▶ The finite spatial resolution of the imaging systems or partial-volume effect.

There are other problems associated with the degrading of image quality in MPI such as patient movement, breathing, etc. but this project concentrated on the limitations introduced by the imaging and processing equipment itself.

These limitations are reflected in the measurement of the sensitivity and specificity of the imaging technique. Many solutions for these limitations have been suggested over the years but it seems that the implementation of generally accepted methods has been escalated recently, especially for MPI techniques. This is especially true with the recent introduction of depth-dependent resolution recovery and scatter techniques as well as new camera architecture designs. The potential improvement of the sensitivity and specificity of MPI with these improvements has not been widely reported yet but one can expect that it might be realised soon.

It seems that the one single issue still causing debates and discussions is attenuation correction. It is a very intensively studied topic but despite this fact it still lacks universal clinical implementation. The conclusion of the author for the reasons for this is three-fold.

The first is that some people involved in the use of MPI do not appreciate the complexity and often unpredictable nature of the defects caused by attenuation. This leads to an almost

cavalier approach that attenuation defects are always very simple to identify and that these defects are also always predictable and that can be allowed for by an experienced reporter of MPI studies. Although it is true that experienced reporters are able to distinguish between many defects caused by attenuation as compared to true defects, the uncertainty caused by doubt does exist and there are cases where it is not possible to distinguish between an artefact and an abnormality and some of these aspects have been highlighted in this study and are the subject of the next couple of paragraphs.

The real contributions of the individual anatomical parts in the thorax are not well known and especially the effect of the heart itself. The PMUD values in table 4.7 demonstrates clearly that the attenuation caused by self-absorption in males is actually greater than the attenuation caused by the soft tissue and skeleton combined, and in females the contribution of the heart is similar to the attenuation caused by the combination of the soft tissue and skeleton. The impact of this self-absorption of the heart has been demonstrated for the first time in this study and this was further extended in chapter 5 which illustrated that the position of the defect is more unpredictable as a result of their dependence on the position and orientation of the heart. It has been clearly shown that the attenuation caused by the self-absorption of the heart can be significant. As the orientation and position of the left ventricle in a specific patient is unknown to the interpreter of the study, it is impossible for any reporter, no matter how knowledgeable or experienced, to "mentally" correct for any defects caused by the self-absorption of the heart.

Section 4.3.4, especially figure 4.6 and table 4.6 illustrated that the attenuation not only causes defects, but also distorts the left ventricle by under estimating the basal parts and over estimating the apical parts. Although this effect has been reported previously in the literature, the extend of this effect is not that well known. This effect has been properly highlighted in this study and this is also something that "mental" correction will not succeed in correcting. This distortion will also have an effect on quantitative analysis such as ejection fraction calculations.

Another aspect that seems to attract little attention, although there is evidence for it in the literature, is the fact that inferior wall attenuation defects are also a wide spread problem in female patients, not just male patients, as illustrated in figure 4.9. The reason for this fact is the self-absorption on the heart, as discussed earlier. This study demonstrated clearly for the first time that the heart can cause significant inferior wall attenuation defects in female patients. The results in this study show its importance, and need to be highlighted to a wider audience in a published paper. Seeing that it is mainly caused by the heart, "mental" correction will again fail.

From this discussion it is very clear that even experienced reporters simply cannot correct "mentally" for a significant number of attenuation defects. It is not just a problem identifying

the relevant defects, because the consequences of anatomical variations can also lead to a significant number of patients been misdiagnosed by experienced reporters with such an approach. For less experienced reporters the pitfalls are even bigger and this project has illustrated that the effect of attenuation can be very subtle and seemingly unpredictable and thus could result in incorrect reporting, and therefore inappropriate patient treatment and management.

The second reason is that the introduction of transmission based methods can lead to artefacts which are difficult to identify and which can alter the outcome of the study. These include truncation of the transmission images, mis-registration, cross-talk between the emission and transmission data and the introduction of artefacts, especially in the apical region. This has led to many debates about the usefulness of the technique and also to the lack of its clinical implementation. This project, together with many other studies published in the literature, found that the implementation of transmission correction techniques, does improve the usefulness of MPI, despite its drawbacks. Careful analysis of the images will prevent or identify truncation problems and many of the commercial available transmission correction systems seem to have developed techniques to overcome, or at least, minimise cross-talk and mis-registration problems. A proper image quality assurance implementation as part of the routine analysis of the MPI data, will identify the existence of truncation and mis-registration cases and therefore will minimise or even eliminate these problems. Therefore the only real objective to the implementation of transmission base attenuation correction, where available, is the apparent introduction of additional apical "defects". It has been illustrated in the literature that in the non-attenuation corrected image, there is often an over estimation of the apical region, which make these images even less reliable for interpretation. These findings are not that well known and need to be brought to the attention of a much wider audience. The significance of this effect has also been confirmed in this study (in chapter 4) and should be highlighted to a wider audience in a published paper.

However, this study went even further and demonstrated in chapter 6 that the use of transmission attenuation correction (together with depth-dependent resolution recovery and scatter correction) corrects this effect and does not necessarily introduce any other defects. This is a very important result and the first time that it has been reported. The realisation that these "apical defects" actually exist in the patient study as real defects and are not a "creation" of attenuation correction, could be extremely helpful in breaking down some of the resistance towards transmission attenuation correction. Therefore the proper implementation of image quality assurance protocols and the knowledge that transmission attenuation correction is not introducing these "apparent" defects will counteract any arguments for not implementing it, now that it is available and possible to obtain the equipment to implement it.

The third reason is the cost, unavailability and the possibility that it cannot be implemented on all systems, as well as the complexity of the technique and the additional burden of longer scanning time and increased patient dose. Many institutions in the world can simply not afford to obtain transmission attenuation correction capability. Furthermore, the new breed of specialised cardiac cameras is making the implementation of transmission attenuation correction almost impossible on such systems. The benefits of implementing transmission attenuation have been clearly demonstrated in this study, especially in chapter 6. By using transmission attenuation correction together with depth dependent resolution recovery and scatter correction leads to the elimination of many of the inherent system problems in MPI. Therefore it is concluded that where it be possible to implement transmission attenuation correction, then this should be done as the patient benefits obtained far outweigh the additional burden of additional scanning time and dose. The aspect of cost, availability and implementability, however, do remain serious issues that will prevent the implementation of attenuation correction techniques in many institutions and systems. To overcome this, the novel approaches of chapter 7 can be developed further so that transmission attenuation can be replaced by emission attenuation correction. Additionally, figure 4.14 illustrated the effect caused by scatter in the distortion in the left ventricle and although these results are not new they confirm the existing knowledge about the contribution of scatter. Chapter 4 also reconfirmed the fact that almost 90% of the counts in the MPI studies are lost as the result of the different degrading factors, leaving only a small amount of counts left to use for interpretation and analysis. As only a very small amount of the injected tracer actually reaches the left ventricle (about 2%), the 90% loss of counts does have a significant impact on the final outcome of the study. This leads to increased patient doses and therefore every attempt should be made to minimise these count losses. If this is achieved then it should be possible to reduce the amount of injected tracer, and hence reduce patient dose. It has been illustrated in chapter 6 that the combination of transmission attenuation correction, scatter correction and depth dependent resolution recovery leads to the recovery of most of the counts in the left ventricle. This leads to the possibility of reducing the injected activity given to the patient. Although transmission scanning increases the radiation dose to the patient, the recovery of counts and subsequently reduction in injected activity, can go a long way to offset this. This is the subject of a number of studies in the literature and an active field of investigation. In addition the introduction of an emission-based attenuation correction method will achieve the reduction of injected activity without the increase dose of transmission scanning.

This study illustrated that the correct and individual implementation of attenuation correction can be potentially very beneficial and will overcome the problems associated with the technique. It furthermore illustrated that a generic patient-average system is not capable of providing the appropriate attenuation correction.

8.2 Future Work

The effect of the range of recent introductions, both software and camera developments, on the improvement of the sensitivity and specificity of MPI is something to anticipate and hopefully relevant studies will be forthcoming in the near future. The execution of such studies will rely on the availability of the recent introductions.

Another aspect which will need attention is the extension of the recent software developments to be applicable with the new camera configurations and designs. Although some of these camera developments will limit the need for some of the corrections reported here, it will not completely remove the need. The patient will always cause attenuation and scatter within the body with a significant impact on the acquired images.

The one conclusion which urgently needs to be reached is the introduction of method(s) for attenuation correction which will be universally accepted and which is also easy and relatively cheap to implement. Such techniques have been introduced in this project and it is work which will be continued by the author.

Although MPI has come a long way and significant advancements have been made, should the stage be reached where universally accepted attenuation correction methods are available together with the other techniques and improvements discussed, it will really lead to a significant advance in the usefulness of Myocardial Perfusion Imaging, and therefore improved patient diagnosis, treatment and subsequent improved health.

Appendix A – Source Code used for the Reconstruction of the Simulated Studies

```
+
; NAME:
;   Nikul_proj
;
; PURPOSE:
;   Compute projection or backprojection using coefficients pre-computed
;   by Nikul_coeff.
;
; CATEGORY:
;   Reconstruction
;
; CALLING SEQUENCE:
;   Nikul_proj, image, sinogram, projnum, prcf
;
; INPUTS:
;   IMAGE: the reconstruction image. When keyword BACKPROJECT is set, the
;   backprojection is ADDED to this image.
;
;   SINOGRAM: When keyword BACKPROJECT is zero or not set, the sinogram
;   receives the projection values.
;
;   PROJNUM: the number of the current projection (row number in the
;   sinogram).
;
;   PRCF:   pointer obtained from Nikul_coeff.
;
; KEYWORD PARAMETERS:
;   BACKPROJECT: when set, a backprojection from SINOGRAM into IMAGE is
;   computed. When not set or zero, a projection from IMAGE into
;   SINOGRAM is computed.
;
; OUTPUTS:
;   The output is IMAGE or SINOGRAM, depending on the keyword BACKPROJECT.
;
; COMMON BLOCKS:
;   NC_lib_common required finding the reconstruction library.
;
; PROCEDURE:
;   Calls a module from the reconstruction library.
;
; MODIFICATION HISTORY:
;   Written by:  Johan Nuyts, 10 april 1996
;
;*****
pro Nikul_proj, image, sinogram, projnum, prcf, backproject=backproject, $
      maxim=maxim
```

```

common NC_lib_common
projnum = fix(projnum)
if keyword_set(maxim) then $
    dummy = call_external(NC_recon, 'Nikul_projmaxim', image, sinogram,$
        projnum, prcf) $
else if keyword_set(backproject) $
then dummy = call_external(NC_recon, 'Nikul_bproj', image, sinogram,$
    projnum, prcf) $
else dummy = call_external(NC_recon, 'Nikul_proj', image, sinogram, projnum,
    prcf)

end
*****
;+
; NAME:
;   Nikul_free
;
; PURPOSE:
;   Deallocate memory allocated by Nikul_coeff.
;
; CATEGORY:
;   Reconstruction
;
; CALLING SEQUENCE:
;   Nikul_free, pcoeff
;
; INPUTS:
;   PCOEFF: the pointer to the memory allocated by the external c-code,
;           and returned by Nikul_coeff.
;           PCOEFF is set to zero.
;
; COMMON BLOCKS:
;   NC_lib_common: required to find the reconstruction library.
;
; RESTRICTIONS:
;   Calling the routine with an invalid pointer will cause a core dump.
;   Calling with a pointer equal to zero will cause an error message.
;
; PROCEDURE:
;   Calls the deallocation routine in the reconstruction c-library.
;
; MODIFICATION HISTORY:
;   Written by: Johan Nuyts, 10 apr 1996
;-
*****
pro Nikul_free, prcf

common NC_lib_common

if n_elements(prcf) eq 0 then begin
    print, 'Nikul_free: pointer does not exist'
    return
endif

if prcf eq 0 then begin
    print, "Nikul_free: pointer is already 0"
    return
endif

```

```

prcf = call_external(NC_recon, 'Nikul_free', prcf)

end
;*****
;+
; NAME:
;   Nikul_coeff
;
; PURPOSE:
;   Pre-computation of the linear interpolation coefficients required for
;   projection and backprojection.
;
; CATEGORY:
;   Reconstruction.
;
; CALLING SEQUENCE:
;   pcoeff = Nikul_coeff(nrdet, nrproj, startangle=S, deltaangle=D, $
;                       radius=R, coroffset=C, arc_radius = arc_radius)
;
; INPUTS:
;   NRDET: Number of detectors (or number of columns in the sinogram)
;
;   NRPROJ: Number of projections (or number of rows in the sinogram).
;
; KEYWORD PARAMETERS:
;
;   STARTANGLE: projection angle in radians of first sinogram row.
;               Zero means projection along y-axis (and upward).
;               Default: zero.
;
;   DELTAANGLE: offset in radians to next projection angle.
;               Positive is clockwise.
;               Default: NRPROJ / !pi
;
;   RADIUS:      Radius of the field of view in pixels.
;               If very large or set to -1, the (back)projection will be
;               computed for the entire reconstruction image. Otherwise,
;               the computation will be limited to pixels within the
;               circle.
;               Warning: in iterative reconstruction, artifacts will occur
;               when reconstructing a truncated field of view. RADIUS should
;               be larger than for the largest enclosed circle.
;               Default: -1
;
;   COROFFSET   Center of rotation offset. When not set, ignored.
;               When set to a single value, the same center of rotation
;               offset is used for all angles.
;               When set to an array of length NRPROJ, a different center of
;               rotation offset is used for every angle.
;
;   ARC_RADIUS  Radius of the PET-system in pixels (convert if known in
;               cm and sinogram pixels known). Ignored if set to zero or not
;               set. If specified, an arc-correction is included in the
;               computations of the interpolation coefficients.
;
; OUTPUTS:
;   PCOEFF: a long int, which contains a pointer that can be used by
;           Nikul_proj and Nikul_free.
;

```

```

: COMMON BLOCKS:
:   Uses NC_lib_common to find the reconstruction library.
:
: SIDE EFFECTS:
:   A structure of a few Mb will be allocated by the C-procedure. This
:   memory cannot be accessed by IDL, it is intended to be reused by other
:   C-modules. Keep the value of PCOEFF unchanged, otherwise that memory
:   gets lost.
:
: PROCEDURE:
:   Calls a routine from the C reconstruction library, which computes the
:   coefficients and stores them in newly allocated memory, which can be
:   accessed by other modules from the same library.
:   IDL cannot access that memory.
:   Use Nikul_free to deallocate the memory.
:
: MODIFICATION HISTORY:
:   Written by:  Johan Nuyts, 10 apr 1996
:   added: ProjCoeffArray
:
: *****
function Nikul_coeff, nrdet, nrproj, startangle = startangle, $
                    deltaangle = deltaangle, radius = radius, $
                    coroffset = coroffset, arc_radius= arc_radius

    common NC_lib_common

    if n_elements(startangle) eq 0 then startangle = 0.0
    if n_elements(deltaangle) eq 0 then deltaangle = !pi / nrproj
    if n_elements(radius)      eq 0 then radius      = -1.0
    if n_elements(arc_radius)  eq 0 then arc_radius = 0.0
    if n_elements(coroffset)  eq 0 $
        then cor = fltarr(nrproj) $
    else if n_elements(coroffset) eq 1 $
        then cor = fltarr(nrproj) + float(coroffset[0]) $
    else if n_elements(coroffset) eq nrproj $
        then cor = float(coroffset) $
    else begin
        print, "Nikul_coeff: size of coroffset incorrect!"
        return, 0
    endelse

    nrdet      = fix(nrdet)
    nrproj     = fix(nrproj)
    startangle = float(startangle)
    deltaangle = float(deltaangle)
    radius     = float(radius)
    arc_radius = float(arc_radius)

    prcf = call_external(NC_recon, 'Nikul_coeff3', nrdet, nrproj, startangle, $
                        deltaangle, radius, cor, arc_radius)

    return, prcf

end

```

```

;*****
;+
; NAME:
;   Nikul_spectproj
;
; PURPOSE:
;   Compute projection or backprojection using coefficients pre-computed
;   by Nikul_coeff.
;
; CATEGORY:
;   Reconstruction
;
; CALLING SEQUENCE:
;   Nikul_spectproj, image, sinogram, attenimg, projnum, prcf
;
; INPUTS:
;   IMAGE: the reconstruction image. When keyword BACKPROJECT is set, the
;         backprojection is ADDED to this image.
;
;   SINOGRAM: When keyword BACKPROJECT is zero or not set, the sinogram
;             receives the projection values.
;
;   ATTENIMG: Attenuation image. Pixel values contain linear attenuation
;             coefficient per pixel.
;
;   PROJNUM: the number of the current projection (row number in the
;           sinogram).
;
;   PRCF:   pointer obtained from Nikul_coeff.
;
; KEYWORD PARAMETERS:
;   BACKPROJECT: when set, a backprojection from SINOGRAM into IMAGE is
;               computed. When not set or zero, a projection from IMAGE into
;               SINOGRAM is computed.
;
; OUTPUTS:
;   The output is IMAGE or SINOGRAM, depending on the keyword BACKPROJECT.
;
; COMMON BLOCKS:
;   NC_lib_common, required finding the reconstruction library.
;
; PROCEDURE:
;   Calls a module from the reconstruction library.
;
; MODIFICATION HISTORY:
;   Written by:  Johan Nuyts, 10 april 1996
;
;*****
pro Nikul_spectproj, image, sinogram, attenimg, projnum, prcf, $
    backproject=backproject

    common NC_lib_common
    if n_elements(image) le 1 then image = attenimg * 0

    projnum = fix(projnum)

    if keyword_set(backproject) $
        then dummy = call_external(NC_recon, 'Nikul_abproj', image, sinogram, $

```

```

        attening, projnum, prcf) $
    else dummy = call_external(NC_recon, 'Nikul_ajroj', image, sinogram, $
        attening, projnum, prcf)
end
;*****
;+
; NAME:
;   NIsino_subset
;
; PURPOSE:
;   Generates an index, defining a subset of projections from a sinogram.
;   The ML-EM algorithm (or any other iterative algorithm) can then be
;   applied to the subset only, to decrease the processing time.
;   The algorithm generates consecutive subsets, in such a way that
;   1) after number_of_subset calls, all projections have been included
;      in exactly one subset
;   2) Each subset is a) as different (in projection angle) as possible from
;      the all previous subset and
;      b) as different as possible from the previous subset.
;
;   The idea of accelerating the reconstruction with subsets is due
;   to MH Hudson and RS Larkin, "Accelerated image reconstruction
;   using ordered subsets of projection data", IEEE Trans Med Imaging,
;   1994; 13: 601-609.
;
; CALLING SEQUENCE:
;   subset = NIsino_subset, nrsubsets, nrangles, subsetnum, subsetmask, previous
;
; INPUTS:
;   NRSUBSETS
;     The number of subsets to be generated. This number must not be larger
;     than the total number of projection. There is no other restriction.
;     If the remainder of nrangles divided by nrsubsets is nonzero, the
;     number of projections per subset will vary. As far as I know, this
;     has no noticeable effect on the convergence.
;
;   NRANGLES
;     The number of projections or projection angles.
;
;   SUBSETNUM
;     Supply a variable which is equal to zero in the first call.
;     NIsino_subset will then initialize the variables SUBSETMASK and PREVIOUS.
;     NIsino_subset will increment subsetnum after each subsequent call,
;     and reset it to zero when all projections are processed.
;
;   SUBSETMASK
;     Variable for internal use, used to remember which subsets have been
;     processed. Do not modify it between calls to NIsino_subset.
;     Passing internal variables to the caller is preferred to a common block,
;     so that, if ever required, two or more iterative schemes can be executed
;     in an interleaved way.
;
;   PREVIOUS
;     Internal variable, used to remember which subset was processed most
;     recently. Do not modify.
;
;

```

```

; KEYWORD PARAMETERS:
;   none
;
; OUTPUTS:
;   SUBSET:
;     An array of indices defining the subset. This array can be used by
;     NIpj to restrict the scope of its calculations.
;
; COMMON BLOCKS:
;   none
;
; SIDE EFFECTS:
;   none
;
; PROCEDURE:
;   See comments in the source.
;
; MODIFICATION HISTORY:
;   Written by:  Johan Nuyts, K.U.Leuven, Belgium
;               aug-1995
;
;*****
function NIsino_subset, nrsubsets, nrangles, subsetnum, subsetmask, previous

;-----
; Check whether parameters are meaningful
;-----

if nrsubsets gt nrangles then begin
  print, 'NIsino_subset: nrsubsets must not be larger than nrangles!' + $
    string(7b)
  return, -1
endif

;-----
;--- New start. First subset contains first projection.
;--- Initialize the mask.
;-----

if subsetnum eq 0 then begin
  subset = indgen(ceil(float(nrangles) / nrsubsets)) * nrsubsets
  subsetmask = indgen(nrsubsets) * 0
  subsetmask[0] = 1
  previous = 0

;-----
;--- subsetmask:
;--- - subsetmask index represent first projection of the subset.
;--- - For processed subsets, mask is set to 1, the others are zero.
;--- Algorithm:
;--- Extend the subsetmask with last element in front and first at the end
;--- to reflect cyclic nature of the projections.
;--- Scan from left to right and right to left, and calculate for every
;--- element in the mask the distance to the closest subset that was already
;--- processed.
;--- Find the subsetmask elements with maximum distance: one of these must be
;--- processed now.
;--- From these, select the one with maximum distance to the previously
;--- processed subset (stored in PREVIOUS).
;-----

```

```

endif else begin

nlen = n_elements(subsetmask)-1
subsetmask = [subsetmask[nlen], subsetmask, subsetmask[0]]
newlen = nlen + 2
leftdistar = intarr(newlen+1)
rightdistar = intarr(newlen+1)
leftdist = 1000
rightdist = 1000
for i = 0, newlen do begin
  if subsetmask[i] eq 1 $
    then leftdist = 0 $
    else leftdist = leftdist + 1
  leftdistar[i] = leftdist

  j = newlen - i
  if subsetmask[j] eq 1 $
    then rightdist = 0 $
    else rightdist = rightdist + 1
  rightdistar[j] = rightdist
endfor

distar = leftdistar < rightdistar
distar = distar[1:newlen-1]
subsetmask = subsetmask[1:newlen-1]

firstproj = where(distar eq max(distar))

compare = abs(firstproj - previous) < (nrsubsets - abs(firstproj - previous))

firstproj = firstproj(where(compare eq max(compare)))

firstproj = firstproj[0]
subsetmask[firstproj] = 1
subset = indgen(ceil(float(nrangles) / nrsubsets)) * nrsubsets + firstproj

previous = firstproj

endelse

;-----
;--- Make sure the subset is not too long. This step reduces the calculation
;--- of the subset to a call to indgen with sufficiently large parameter
;-----
subset = subset(where(subset le (nrangles-1)))
subsetnum = subsetnum + 1
if subsetnum ge nrsubsets then subsetnum = 0
return, subset

end
;*****
;+
; NAME:
;   Niproj
;
; PURPOSE:
;   Calculate a projection of a reconstruction image into a sinogram, or
;   calculate a backprojection from the sinogram into the reconstruction

```

```
image.  
The operation can be restricted to a subset of projections.  
  
CALLING SEQUENCE:  
Niproj, image, sinogram, firstangle, deltangle  
  
INPUTS:  
IMAGE  
The reconstruction image.  
Must be provided in the case of projection.  
In the case of backprojection, it is created if it does not exist.  
The image must be two or three dimensional. The third dimension is  
regarded as perpendicular to the reconstruction plane.  
  
SINOGRAM  
The sinogram image.  
Must be provided in the case of backprojection.  
In the case of projection, it is created if it does not exist.  
If both sinogram and image are provided, they must have the same number  
of dimensions.  
  
FIRSTANGLE  
Angle in radians corresponding to the first projection. Set it to  
zero if the first projection is vertical.  
Default: 0.  
Ignored when PCOEFF is non-zero.  
  
DELTAANGLE  
Angle between two consecutive projections in radians.  
Ignored when PCOEFF is non-zero.  
  
OPTIONAL INPUTS:  
NRANGLES  
Provide it if the sinogram to be calculated is not yet allocated.  
If it is calculated, the number of angles equals the number of rows  
(second coordinate) in the sinogram.  
Ignored when PCOEFF is non-zero.  
  
KEYWORD PARAMETERS:  
SUBSET  
Set it to an array containing the indices of the projections that must  
be involved in the calculations.  
Default: all projections.  
  
BILINEAR  
If set, bilinear interpolation is applied.  
Otherwise, nearest neighbor interpolation is applied.  
See RIEMANN.  
Ignored when PCOEFF is non-zero (uses always bilinear interpolation).  
  
CENTER  
Set this to the center of the projection image. Different from RIEMANN,  
the default is (number_of_projection_pixels - 1.0) / 2.0.  
(See RIEMANN).  
Ignored when PCOEFF is non-zero.  
  
COR
```

```

: Position of the center of rotation in the image.
: Default = [nr_columns - 1., nr_rows - 1] / 2. This is different from
: the default provided by RIEMANN.
: (See RIEMANN).
: Ignored when PCOEFF is non-zero.
:
: D
: Sampling distance. See RIEMANN
: Ignored when PCOEFF is non-zero.
:
: BACKPROJECT
: If set, a backprojection is applied.
: If not, a projection is applied.
: See RIEMANN
:
: NEW
: If set, the output image is cleared before storing the result of
: projection or backprojection. Otherwise, the result is added to the
: contents of the output image.
:
: PCOEFF
: If the keyword is not set or equal to zero, (back)projections are
: computed with the RIEMANN command.
: If the keyword is set to the result of a call to Nikul_coeff, the
: (back)projections are computed by calling a routine from the
: c-library.
:
: SPECTATTEN
: If this keyword is not set or equal to zero, no attenuation is
: assumed. (For PET-type attenuation, the non-attenuated projections can
: be multiplied with the attenuation along each projection line to
: produced attenuated projections.)
: For spect-type attenuation, the attenuation must be included in
: the projection calculations. For SPECT-type attenuation, set
: SPECTATTEN to an image containing the linear attenuation
: coefficients per pixel. In this case, the keyword PCOEFF must
: be set as well, since RIEMANN cannot compute attenuated
: projections.
:
: OUTPUTS:
: IMAGE or SINOGRAM is updated, depending on the value of the BACKPROJECTION
: keyword.
:
: COMMON BLOCKS:
: none
:
: SIDE EFFECTS:
: none
:
: PROCEDURE:
: Carries out a few initializations and calls RIEMANN to do the job.
:
: MODIFICATION HISTORY:
: Written by: Johan Nuyts, K.U.Leuven, Belgium
: aug-1995
:
: .....
```

```

pro Nlproj, image, sinogram, firstangle, deltaangle, nrangles, $
  bilinear = bilinear, center = center, cor = cor, d = d, $
  backproject = backproject, subset = subset, new=new, $
  pcoeff = pcoeff, spectatten=spectatten, maxim=maxim

common Nikul_common, nrriemann, nrkulproj

;-----
;--- Default values
;-----

if n_elements(firstangle) eq 0 then firstangle = 0
if not keyword_set(bilinear) then bilinear = 0
if n_elements(d) eq 0 then d = 1
if not keyword_set(backproject) then backproject = 0
if n_elements(pcoeff) eq 0 then begin
  if keyword_set(maxim) then begin
    print, 'Nlproj: maximum intensity projection requires pcoeff'
    return
  endif
endif
if n_elements(pcoeff) eq 0 and n_elements(spectatten) gt 1 then begin
  image = -1
  print, 'Nlproj: if SPECTATTEN is set, PCOEFF must be set as well!'
  return
endif
if n_elements(nrriemann) eq 0 then nrriemann = 0L
if n_elements(nrkulproj) eq 0 then nrkulproj = 0L

;-----
;--- Allocate a sinogram if it does not exist already
;--- The size is that of the largest projection in the image
;--- (See IDL-help for RIEMANN)
;-----

if n_elements(sinogram) le 1 then begin
  if backproject then begin
    image = 0
    print, 'Nlproj: no sinogram given' + string(7b)
    return
  endif
  imsize = size(image)
  nrdet = imsize[1] / d
  if imsize[0] lt 3 then sinogram = fltarr(nrdet, nrangles) $
    else sinogram = fltarr(nrdet, nrangles, imsize[3])
endif

;-----
;--- Allocate an image if it does not exist.
;--- The size is such that its largest projection will fit
;--- in the sinogram matrix.
;-----

if n_elements(image) le 1 then begin
  if not backproject then begin
    sinogram = 0
    print, 'Nlproj: no image given' + string(7b)
    return
  endif
  sinosize = size(sinogram)
  nrcols = sinosize[1] * d

```

```

    if sinosize[0] lt 3 then image = fltarr(ncols, ncols) $
        else image = fltarr(ncols, ncols, sinosize[3])
endif

;-----
;--- Clear the images if requested
;-----

if keyword_set(new) then $
    if backproject then image = image * 0.0 else sinogram = sinogram * 0.0
;-----

;--- Calculate the centers of the image.
;--- The defaults used by RIEMANN are not the ones we want to use:
;--- RIEMANN uses nrpixels/2, we want (nrpixels-1)/2.
;-----

sinosize = size(sinogram)
imgsize = size(image)

if sinosize[0] lt 3 then nplanes = 1 else nplanes = sinosize[3]

if n_elements(center) eq 0 then center = 0.5 * (sinosize[1] - 1.0)
if n_elements(cor) eq 0 then cor = 0.5 * (imgsize[1:2] - 1.0)

;-----
;--- Calculate nrangles. If the caller supplies both the sinogram and the
;--- number of angles, check whether this is ok.
;-----

sinosize = size(sinogram)
if n_elements(nrangles) eq 0 then nrangles = sinosize[2]
if nrangles ne sinosize[2] then begin
    if nrangles gt 1 and sinosize[0] gt 1 then begin
        print, 'Niproj: sinogram size and nrangles not identical' + string(7b)
        return
    endif
endif

if n_elements(subset) eq 0 then subset = indgen(nrangles)
if n_elements(deltaangle) eq 0 then deltaangle = !pi/float(nrangles)

for plane = 0, nplanes-1 do begin
;-----
;--- 3D projection: copy the sinogram, because riemann may wish to
;--- add to its contents, and cannot add directly to
;--- sinogram[*,*,plane].
;--- Copy also image, otherwise an implicit copy is forced for every
;--- subset. Afterwards, the tmpsino is put back in the original
;--- sinogram in the case of projection, and the tmpimg in the case of
;--- backprojection.
;--- In the case of backprojection, the newly calculated values are
;--- divided by the number of projections.
;-----

    tmpsino = sinogram[*,*,plane]
    tmpimg = image[*,*,plane]
    if n_elements(spectatten) gt 1 then tmpatten = spectatten[*,*,plane]

    tmpsize = size(tmpsino)
    if tmpsize[0] eq 1 then tmpsino = reform(tmpsino, tmpsize[1],1,
        /overwrite)

```

```

centerl = center[0]
if n_elements(pcoeff) eq 0 then begin
  for j = 0, n_elements(subset)-1 do begin
    i = subset[j]
    riemann, tmpsino, tmpimg, firstangle + i * deltaangle, $
    row = i, backproject = backproject, bilinear = bilinear,
    $
    d = d, cor = cor, center = center
    nrriemann = nrriemann + 1
  endfor
endif else begin
  for j = 0, n_elements(subset)-1 do begin
    i = subset[j]
    if n_elements(spectatten) le 1 $
      then NIkul_proj, tmpimg, tmpsino, i, pcoeff,
        backproject=backproject, maxim=maxim $
      else NIkul_spectproj, tmpimg, tmpsino, tmpatten, $
        i, pcoeff, backproject=backproject
    nrkulproj = nrkulproj + 1
  endfor
endelse
if backproject eq 0 then sinogram[*,*,plane] = tmpsino $
else image[*,*,plane] = tmpimg / n_elements(subset)
endifor

end
:*****
:+
: NAME:
:   Nimlosem
:
: PURPOSE:
:   Maximum Likelihood expectation maximisation (Shepp, Vardi, IEEE TMI 1982,
:   MI-1:113-122 and Lange, Carson, J Comput Assist Tomog, 1984, 8:306-316).
:   The procedure also implements Ordered Subsets (Hudson, Larkin, IEEE-TMI
:   1994;13:601-609).
:
: CALLING SEQUENCE:
:   recon = Nimlosem(sinogram)
:
: INPUTS:
:   SINOGRAM: the sinogram. First coordinate is the pixel in the projection,
:   second coordinate points to the projection angle.
:
: KEYWORD PARAMETERS:
:
:   RECON
:   The initial image. If not provided, a homogenous image is used.
:   Supply the previous reconstruction if you want to continue iterating
:   on the same image.
:
:   NRITER
:   Number of iterations. For multiple subsets, one iteration includes
:   one ML-EM-iteration per subset.
:
:   NRSUBSETS
:   The number of subsets. Any number is accepted, it does not have to
:   be divider of the number of projections. If it is not, the subsets

```

```

: will not have the same amount of projections.
: See Hudson and Larkin - paper.
: For multiple subsets, the calculation of the likelihood is approximate,
: and is always lower than the true value. See the LIKELIHOOD keyword.
: Default: 1.
:
: ONLYSUBSET
: If set, only the subset with the number ONLYSUBSET will be used in the
: ML-computation. When not set, the ML-computation is carried out for
: all subsets.
:
: SHOWSUB
: When set, shows the reconstruction after each sub-iteration in the
: current display window.
:
: SHOWFINAL
: When set, shows the reconstruction after each iteration in the current
: display window.
:
: LIKELIHOOD
: A value proportional the log-likelihood (See Shepp and Vardi-paper) is
: calculated for each iteration. In fact, the variable part of the
: log-likelihood is calculated, and divided by the maximum attainable
: value (reached when calculated projection is identical to the
: measurement). The log-likelihood should increase but never reach 1,
: except maybe for simulations.
: If the keyword is omitted, the likelihood is not calculated.
: If the keyword is set to a non-existing variable, that variable is
: set to an array with consecutive likelihoods.
: If the keyword is set to an array, the new array is appended.
: For multiple subsets, only an approximate value is calculated, using
: only the new reprojections of the current subset, together with the
: older (and actually obsolete) reprojections of the previously processed
: subsets. As a result, the approximate value is always lower than the
: true value.
: If multiple subsets are used in a second call to NIMLOSEM, it is
: recommended that you would provide the previously obtained CALCSINO.
: If you don't, the procedure cannot use the reprojections of the
: previous iteration, resulting in strong underestimations of the
: likelihood. This does not influence the final reconstruction image.
:
: CALCSINO
: Calculated sinogram. If keyword is set but the image does not exist,
: it is created. If it exists, it is reused. In subsequent calls to
: NIMLOSEM for the same image, the procedure needs the previously
: calculated sinogram for the calculation of the likelihood, if multiple
: subsets are used. The sinogram is calculated anyway, so no time is
: saved by not providing it.
:
: STARTANGLE
: Angle corresponding to the first projection (in radians). Default: 0.
:
: DELTAANGLE
: Angle between two consecutive projections (in radians).
: Default: pi / number of angles
:
: ATTENUATION
: An image of the same size as sino, containing the attenuation factors.

```

```

/ For the ECAT 931 PET, this the inverse (pixel by pixel) of the atn-file,
/ which contains the attenuation correction.
/
/ PCOEFF
/ If the keyword is not set or equal to zero, (back)projections are
/ computed with the RIEMANN command.
/ If the keyword is set to the result of a call to NIKul_coeff, the
/ (back)projections are computed by calling a routine from the
/ c-library.
/
/ BACKATTEN
/ In every iteration, the backprojected ratio of measurement and
/ prediction must be divided by the sum of detection probabilities.
/ This sum equals 1 if no PET- or SPECT-attenuation is specified.
/ If there is attenuation, the sum of detection probabilities is
/ computed by backprojecting the a sinogram with all pixels set to 1.
/ If backatten does not exist or is set to a single value, this
/ backprojection is computed. If backatten is set, it is reused.
/
/ NORM_PER_SUBSET
/ In theory, BACKATTEN should be recomputed for every subset.
/ However, a lot of time is saved by computing BACKATTEN once using all
/ projections, and using it also for individual subsets.
/ When NORM_PER_SUBSET is set, BACKATTEN is recomputed for every subset.
/ Otherwise, it is just computed once using all projections.
/
/ OUTPUTS:
/ RECON: the resulting reconstruction.
/
/ COMMON BLOCKS:
/ Calls NImage, which reads the lookup table block.
/
/ SIDE EFFECTS:
/ Displays an image in the current display window, if the keyword
/ SHOWSUB or SHOWFINAL is set.
/
/ RESTRICTIONS:
/ The projections are calculated using the RIEMANN function, which expects
/ that the projection array contains more pixels than the dimension of
/ the reconstruction image. This routine uses the same number of columns
/ for the projection as for the reconstruction image, apparently without
/ adverse effects.
/
/ PROCEDURE:
/ Calls NIsino_subset to define the sinogram subsets, and NIm1 for
/ the actual ML-EM calculations.
/
/ EXAMPLE:
/ See batchfile NIexample_ml.pro.
/
/ MODIFICATION HISTORY:
/ Written by: Johan Nuyts, K.U.Leuven, Belgium
/           aug-1995
/
/*****
function NImlosem, sinogram, nrsubsets = nrsubsets, recon = recon,      $
          nriter = nriter, showsub = showsub, showfinal = showfinal, $

```

```

likelihood = likelihood, calcsino = calcsino,          $
startangle = startangle, deltaangle = deltaangle,    $
attenuation = attenuation, spectatten = spectatten,  $
backatten = backatten, norm_per_subset=norm_per_subset, $
onlysubset = onlysubset, pcoeff = pcoeff, fwhm=fwhm

if n_elements(onlysubset) eq 0 then onlysubset = -1
if n_elements(startangle) eq 0 then startangle = 0

;-----
;--- Eliminate negative values
;--- Allocate recon-image if not provided
;-----

sino = sinogram > 0
if n_elements(nriter) eq 0 then nriter = 1
if n_elements(nrsubsets) eq 0 then nrsubsets = 1
sinosize = size(sino)
nrangles = sinosize[2]
if sinosize[0] lt 3 then nplanes = 1 else nplanes = sinosize[3]
if n_elements(recon) le 1 then recon = fltarr(sinosize[1], sinosize[1], $
nplanes) + 1
if n_elements(deltaangle) eq 0 then deltaangle = acos(-1) / nrangles

;-----
;--- Allocate memory for calculated sinogram
;-----

iter = 0
if n_elements(calcsino) le 1 then calcsino = sino * 0

;-----
;--- Calculate upper limit of likelihood
;-----

if n_elements(likelihood) eq 0 then likelihood = -1
lik = 1
dummy = sino
isnul = where(dummy le 1e-15)
if isnul[0] ne -1 then dummy[isnul] = 1e-15
maxlik = total(-dummy + dummy * alog(dummy))

;-----
;--- Precompute the backprojection of the weights if attenuation is
;--- specified.
;--- If not done, NIm1 will do it the first time, but then the computation
;--- is restricted to the subset if one is in use.
;-----
;--- If PET-attenuation is required, compute the sum of all weights in
;--- every reconstruction pixel
;-----

if n_elements(attenuation) gt 1 and n_elements(backatten) le 1 and not
keyword_set(norm_per_subset) then begin
backatten = recon * 0
NImproj, backatten, attenuation, startangle, deltaangle, nrangles,$
/bil, /back, pcoeff=pcoeff
endif

;-----
;--- If SPECT-attenuation is required, compute the sum of all weights in
;--- every reconstruction pixel

```

```

-----
if n_elements(spectatten) gt 1 and n_elements(backatten) le 1 and not
  keyword_set(norm_per_subset) then begin
  backatten = recon * 0
  allones = sino * 0 + 1
  Niproj, backatten, allones, startangle, deltaangle, nrangles, /bil,$
  /back, spectatten=spectatten, pcoeff=pcoeff
endif

-----
:--- Loop of iterations and subsets
-----
for i = 1, nriter do begin
  subsetnum = 0
  for s = 0, nrsubsets - 1 do begin
    subset = NIsino_subset(nrsubsets, nrangles, subsetnum, $
      subsetmask, previoussubset)
    if keyword_set(norm_per_subset) and nrsubsets gt 1 then $
      backatten = 0
    if (onlysubset eq -1) or (s eq onlysubset) then begin
      NIm1, recon, sino, startangle, deltaangle, likeli = lik, $
      pcoeff = pcoeff, calc = calcsino, subset = subset,$
      spectatten=spectatten, backatten = backatten
      lik = lik / maxlik
      if iter eq 0 and likelihood[0] eq -1 then $
        likelihood = [lik] $
        else likelihood = [likelihood, lik]
      iter = iter + 1
    endif
  endfor
endfor
return, recon

end
:*****
:+
: NAME:
:   NIm1
:
: PURPOSE:
:   Apply a single ML-EM iteration, possibly restricted to a single subset.
:
:
: CALLING SEQUENCE:
:   NIm1, recon, sino, firstangle, deltaangle
:
: INPUTS:
:   RECON
:     The initial reconstruction image, which may be the result of a previous
:     iteration. Note that ML-EM is unable to convert zeros in something else,
:     since it is a multiplicative algorithm. Do not supply initial images
:     with pixels set to zero, unless you want them to stay zero.
:
:   SINO
:     The sinogram: first coordinate points to the detector or line of
:     response, the second to the projection angle.
:
:   FIRSTANGLE

```

```

: First projection angle. Zero for vertical projection.
:
: DELTAANGLE
: Angle between the projections (in radians)
:
:
: KEYWORD PARAMETERS:
: LIKELIHOOD
: If this array exists, the likelihood of the initial reconstruction image
: is appended. The likelihood of the resulting image is only calculated
: in the next iteration. The likelihood for subiterations is always an
: underestimation. For an accurate calculation of the likelihood, a
: complete projection of the image must be calculated. It is the goal
: of Ordered Subsets to avoid this calculation.
:
:
: CALCULSINO
: Provides and receives the calculated sinogram. If subsets are used,
: the calculation of the likelihood needs the previously calculated
: sinogram to compute a decent value. If you don't provide it, an internal
: one filled with zeros is generated. It then takes one iteration using
: all subsets before the likelihood value is meaningful.
:
:
: SUBSET
: An array indicating the rows of the sinogram that are included in the
: subsets. The routine NIsino_subset generates subsets.
:
:
: ATTENUATION
: An image of the same size as sino, containing the attenuation factors,
: and any other factor affecting the sensitivity of a LOR.
: For the ECAT 931 PET, this is the inverse (pixel by pixel) of the atn-file,
: which contains the attenuation correction.
: Originally designed for PET-applications. For SPECT, however, one may
: may use it to apply uniformity correction.
:
:
: SPECTATTEN
: An image of the same size as the reconstruction image, containing an
: attenuation map. The pixels must contain linear attenuation coefficients
: per pixelsize. (See also NIprouj.)
:
:
: PCOEFF
: If the keyword is not set or equal to zero, (back)projections are
: computed with the RIEMANN command.
: If the keyword is set to the result of a call to NIKul_coeff, the
: (back)projections are computed by calling a routine from the
: c-library.
:
:
: BACKATTEN
: The backprojection of the weighting. This image must be computed when
: attenuation or spectatten or specified. If this variable is set to
: an existing image (more than one element), that image is reused.
: Otherwise, the image is computed.
:
:
: OUTPUTS:
: RECON is updated.
:
:
: OPTIONAL OUTPUTS:
: If provided, also CALCULSINO and LIKELIHOOD are updated.
:

```

```

; COMMON BLOCKS:
;   none
;
; SIDE EFFECTS:
;   none
;
; PROCEDURE:
;   Calls Niproj to calculate the projection and the backprojection.
;
; MODIFICATION HISTORY:
;   Written by:  Johan Nuyts, K.U.Leuven, Belgium
;               aug-1995
;
;-----
pro NIml, recon, sino, firstangle, deltaangle, $
  likelihood = likelihood, calculsino = calculsino, subset = subset, $
  spectatten=spectatten, pcoeff = pcoeff, $
  backatten = backatten

  small      = max(sino) / 1e6
  sinosize   = size(sino)
  nrangles   = sinosize[2]

;-----
;--- Default: 1 subset
;-----
if n_elements(subset) eq 0 then subset = indgen(nrangles)

;-----
;--- Project the current reconstruction
;-----
if n_elements(calculsino) eq 0 then calculsino = 0 * sino $
  else calculsino[* ,subset,*] = 0
Niproj, recon, calculsino, firstangle, deltaangle, nrangles, /bil, $
  subset = subset, spectatten = spectatten, pcoeff=pcoeff

;-----
;--- Divide measurement by reprojection
;-----
noemer = calculsino[* ,subset,*]
isnul = where(noemer le small)
if isnul[0] ne -1 then noemer[isnul] = small
ratio = sino
ratio[* ,subset,*] = ratio[* ,subset,*] / noemer

;-----
;--- Backproject the ratio-sinogram
;-----
back = recon * 0
Niproj, back, ratio, firstangle, deltaangle, nrangles, /bil, /back, $
  subset = subset, pcoeff=pcoeff, spectatten = spectatten

;-----
;--- If SPECT-attenuation is required, compute the sum of all weights in
;--- every reconstruction pixel
;-----

```

```

if n_elements(spectatten) gt 1 and n_elements(backatten) le 1 then begin
    backatten = recon * 0
    allones = sino * 0 + 1
    Niproj, backatten, allones, firstangle, deltaangle, nrangles, /bil,$
        /back, subset = subset, spectatten=spectatten, pcoeff=pcoeff
endif

;-----
;--- If an image backatten has been generated, use it to normalize for
;--- the sum of weights.
;-----

if n_elements(spectatten) gt 1 $
    then back = back / (backatten > (max(backatten) / 1000.))

;-----
;--- Multiply with current reconstruction
;-----

recon = recon * back

if n_elements(likelihood) ne 0 then begin
    isnul = where(calculsino le 0)
    if isnul[0] ne -1 then calculsino[isnul] = 1e-15
    likelihood = total(-calculsino + sino * alog(calculsino))
endif

end

;*****
;+
; NAME:
;     NIfilterfunction
;
; PURPOSE:
;     Calculate the 1D frequency representation for the specified
;     filter function. The filter can be directly multiplied
;     applied to the result of a forward FFT. The function is
;     designed to be used for filtered backprojection (nifbp.pro).
;
; CALLING SEQUENCE:
;     filterarray = NIfilterfunction(filter, nrelements)
;
; INPUTS:
;
;     FILTER: 'rect' : an array of ones is returned.
;            'hann' : Hann low pass filter
;            'but'  : Butterworth low pass filter
;
;     NRELEMENTS: The number of elements in the returned
;                 filterarray. This value equals the number of elements
;                 of the array that you want to filter.
;
; KEYWORD PARAMETERS:
;
;     CUTOFF_FREQ: The interpretation depends on the filter.
;                 For 'rect': all frequencies > cutoff_freq are set to
;                 zero, the others to 1.
;                 For 'hann': the filter becomes zero at the
;                 cutoff_freq (with zero derivative)

```

```

/           For 'but' : the filter amplitude equals 0.5 at the
/           cutoff_freq.
/
/ POWER:
/           The power of the Butterworth filter. Ignored when an other
/           filter is selected. Default is 10.
/
/ RAMP:
/           When set, the specified low-pass filter is multiplied by a
/           ramp filter.
/
/ TWOD:
/           When set, a filter image is returned, which can be directly
/           multiplied with the FFT of an image.
/           Otherwise, the filter is returned as a one dimensional array,
/           to be multiplied with the FFT of a 1D array.
/
/ OUTPUTS:
/
/           FILTERARRAY: a 1D array of NRELEMENTS elements, containing the filter
/           amplitude. The first element is the DC point,
/           frequencies then increase up to the Nyquist
/           frequency. The second half of the array is a mirrored
/           version of the first half.
/
/ MODIFICATION HISTORY:
/           written by: Stefaan Vandenberghe en Swana Vanacker, dec 1995
/           modification:
/           jan 1996, Johan Nuyts: several bugs fixed
/           mar 1996, Johan Nuyts: adding small constant to the ramp filter,
/           to avoid over-attenuation of low frequencies.
/
/*****
function NIfilterfunction, filter, nrelements, cutoff_freq = cutoff_freq, $
    power = power, ramp = ramp, twoD= twoD

;-----
;--- An array with frequencies: starting from zero to Nyquist, followed by
;--- -Nyquist to zero. (Same as after FFT).
;--- Note that the sign of the frequencies is irrelevant, the filter is
;--- always a function of the absolute value. So for the two-D frequency
;--- image, we don't care restoring the correct sign as is done in the 1-D
;--- frequencyarray.
;-----

frequencyarray = findgen(nrelements)
middle          = fix((nrelements - 1)/2)
frequencyarray[middle +1:nrelements-1] = $
    -reverse(frequencyarray[0:(nrelements-1)-(middle +1)])
if keyword_set(twoD) then begin
    kwadfreq = frequencyarray^2 # (fltarr(1,nrelements)+1)
    frequencyarray = sqrt(kwadfreq + transpose(kwadfreq))
endif

if n_elements(cutoff_freq) eq 0 then cutoff_freq = 0.5
cutoff = nrelements * cutoff_freq

```

```

-----
;--- calculation of the filterarrays for the different filters
-----

case filter of
  'rect': begin
    filterarray = frequencyarray*0 + 1
    daar = where(abs(frequencyarray) gt cutoff)
    if daar[0] ne -1 then filterarray[daar] = 0
  end

  'hann': begin
    filterarray = 0.5 + 0.5 * cos(!pi * frequencyarray/cutoff)
    daar = where(abs(frequencyarray) gt cutoff)
    if daar[0] ne -1 then filterarray[daar] = 0
  end

  'but': begin
    if n_elements(power) eq 0 then power = 10
    filterarray = 1.0 / (1+ (abs(frequencyarray)/ cutoff)^power)
  end

  else: begin
    print, 'Illegal filter function: ', filter
    filterarray = -1
  end
end

encase
;-----
;--- The DC-amplification should not be set to zero. In the analogue
;--- case, there are an infinite number of projections, and the
;--- DC-amplification of the backprojection goes to infinity. In the
;--- digital case, the number of projections is limited, and the
;--- DC-amplification of the backprojection is a finite value. Hence, the
;--- ramp-filter must be adapted. There is a paper about this, but I
;--- don't have it at the moment, so I solved the problem by adding a
;--- small value, determined heuristically on a simulation. The result is
;--- that decent reconstructions are obtained without having to use large
;--- zeropadding values in the reconstruction (to increase the sampling in
;--- the frequency domain). The influence of the term decreases when the
;--- number of frequency samples is increased. The tests suggest that in all
;--- cases superior reconstructions are obtained with this term, but the
;--- difference becomes negligible for large zeropadding. 0.37
;-----

if keyword_set(ramp) then $
  filterarray = filterarray * (abs(frequencyarray) + 0.) / nrelements

return, filterarray

end
;*****
;+
; NAME:
;   Nifbp
;
; PURPOSE:
;   Computes the reconstruction from a sinogram using filtered backprojection.
;

```

```

: CALLING SEQUENCE:
:   Nifbp, recon, sinogram
:
: INPUTS:
:
:   SINOGRAM
:     the sinogram image to be reconstructed.
:     The dimensions are:
:       fltarr(nrcols, nrrows)
:     or, for multiple slices:
:       fltarr(nrcols, nrrows, nrplanes)
:
: KEYWORD PARAMETERS:
:
:   FILTER
:     The low pass filter to be applied (in combination with the ramp
:     filter) for noise suppression. See NIfilterfunction for the
:     possible values. Default is 'rect', a rectangular filter, with
:     transition from 1 to 0 at the frequency CUTOFF_FREQ.
:
:   CUTOFF_FREQ
:     The cut-off frequency of the filter, expressed in cycles/pixel:
:     the sample frequency is 1, the Nyquist is 0.5. The
:     interpretation depends on the filter. See NIfilterfunction for
:     further comments.
:
:   POWER
:     See NIfilterfunction.
:
:   STARTANGLE
:     the angle of the first projection in radians.
:
:   DELTAANGLE
:     angle, in radials, between two consecutive projections.
:     Filtered backprojection is designed for reconstruction of 180
:     degrees projection data. The routine accepts 360 degrees data,
:     but it is more efficient to add opposite projections (mirroring
:     one of them) and apply a 180 degrees reconstruction. FBP of
:     360 degrees data is mathematically identical to FBP of the
:     added (not averaged!) opposite projections. Divide by 2 if you
:     want the effect of averaging opposite projections. Default is
:     pi / number-of-projections.
:
:   ZEROPADDING
:     Number of zeros that must be appended to both sides of the
:     sinogram, to improve the Fourier-decomposition of the sinogram.
:     Default=0
:
:   PCOEFF
:     When set to 0 or not provided, the RIEMANN command is used to
:     compute the backprojection.
:     When set to the value returned by NIKul_coeff, the routine NIKul_proj
:     is used to compute the backprojection. This routines contains a
:     call to the backprojector in our C-library.
:
:   SUBSET
:     When set, only the projection lines belonging to this subset are
:     used. A subset is defined as an array of row indices for the sinogram.

```

```

:
: SHOWIMG
:   When set, each plane is displayed as soon as it has been reconstructed.
:
: OUTPUTS
:
:   IMAGE
:     The image that is reconstructed from the sinogram
:
: MODIFICATION HISTORY:
:   written by:   Swana Vanacker, Stefaan Vandenberghe dec 1995
:   Modification:
:     jan 1996, Johan Nuyts: several bugs fixed
:     apr 1996, Johan Nuyts: addition of keyword PCOEFF.
:
:=-
:*****
pro NIfbp, recon, sinogram, zeropadding = zeropadding, filter = filter,      $
    power = power, cutoff_freq = cutoff_freq, startangle = startangle, $
    deltaangle = deltaangle, pcoeff=pcoeff, subset = subset,              $
    showing = showing, demo=demo

:-----
:--- Default values
:-----
sinosize = size(sinogram)
nrdet    = sinosize[1]
nrangles = sinosize[2]
if sinosize[0] eq 3 then nrplanes = sinosize[3] else nrplanes = 1
pi = acos(-1)
if n_elements(deltaangle) eq 0 then deltaangle = pi / nrangles
if n_elements(startangle) eq 0 then startangle = 0.
if n_elements(power) eq 0 then power = 10
if n_elements(cutoff_freq) eq 0 then cutoff_freq = 0.5
if n_elements(zeropadding) eq 0 then zeropadding = 20
if n_elements(filter) eq 0 then filter = 'rect'
if n_elements(subset) eq 0 then subset = indgen(nrangles)
n_subset = n_elements(subset)

:-----
:--- Allocate a reconstruction image if not available
:-----
if n_elements(recon) le 1 then recon = ftarr(nrdet, nrdet, nrplanes)
tmprecon = ftarr(nrdet, nrdet)

:-----
:--- Definition of frequencyvector as an array of the frequencies where the
:--- filter must be calculated
:-----
newnrdet = nrdet + 2*zeropadding
filtervector = NIfilterfunction(filter, newnrdet, cutoff_freq=cutoff_freq,$
    power = power, /ramp)

for plane = 0, nrplanes-1 do begin
:-----
:--- A new sinogram is created by adding zeros at both sides of the
:--- old sinogram.
:-----
newsinogram = ftarr(newnrdet, nrangles)

```

```

newsinogram[zeropadding:zeropadding+nrdet-1,*] = sinogram [0:nrdet -$
    1, *, plane]

;-----
;--- 1D.Fouriertransformation for every angle (row) of the sinogram.
;-----
fouriersin = complexarr(newnrdet, n_subset)
for i=0, n_subset -1 do fouriersin[* ,i]= FFT(newsinogram[* ,subset[i]])

;-----
;--- Filtering of the Fouriertransformation of the sinogram
;-----
for i = 0,n_subset-1 do fouriersin[* ,i] = fouriersin[* ,i] * $
    filtervector

;-----
;--- 1D inverse fouriertransformation of the sinogram for each angle
;-----
filteredrsinogram = fltarr(newnrdet, nrangles)
for i = 0,n_subset-1 do filteredrsinogram[* ,subset[i]] = $
    FFT(fouriersin[* ,i], /inverse)

;-----
;--- Reduction of the sinogram to its original size
;-----
filteredrsinogram = filteredrsinogram[zeropadding : nrdet+zeropadding $
    -1,*]

if not keyword_set(demo) then begin
;-----
;--- Backprojection of the filtered sinogram
;-----
NIproj, tmprecon, filteredrsinogram, startangle, deltaangle, $
    /new,/bilinear, /backproject, pcoeff=pcoeff,
subset=subset
;-----
;--- Multiply with deltaangle, which is the equivalent of d
;--- theta in the analogue integral expression.
;-----
if keyword_set(showimg) then NIimage, tmprecon
endif else begin
    tmprecon[*] = 0
    teller = 0.0
    for i = 0, n_elements(subset)-1 do begin
        NIproj, tmprecon, filteredrsinogram, startangle, $
            deltaangle, /bilinear, /backproject,
            pcoeff=pcoeff,$
            subset=subset[i]
        teller = teller + 1.0 / float(n_elements(subset))
        if teller gt 1/40. then begin
            NIimage, tmprecon, /noerase
            teller = 0.0
        endif
    endfor
endif
recon[* ,*,plane] = tmprecon * !pi
endifor

```

```

end
:*****
function NIconvolgauss, img, fwhm=fwhm, sigma=sigma, showit=showit, $
    nrsigma=nrsigma, dimensions= dimensions, maskonly=maskonly

    if n_elements(dimensions) eq 0 then dimensions = [0,1,2]

    if n_elements(sigma) eq 0 then begin
    if n_elements(fwhm) eq 0 then sigma = 0 else sigma = fwhm / sqrt(8 * alog(2))
    endif
    if sigma eq 0 then return, img
    if n_elements(nrsigma) eq 0 then nrsigma = 2
    if n_elements(showit) eq 0 then showit = 0
    nrel = round(sigma * nrsigma) > 1

    x = findgen(2 * nrel + 1) - nrel
    masker = Nigauss(x, 0, sigma)
    masker = masker / total(masker)

    if showit then print, masker
    if keyword_set(maskonly) then return, masker

    imsize = size(img)
    if imsize[0] lt 3 then nrplanes = 1 else nrplanes = imsize[3]

    if nrplanes eq 1 then begin

        if total(dimensions eq 0) gt 0 $
            then begin
                if 2*nrel+1 gt imsize[1] then begin
                    eraf = nrel - fix((imsize[1]-1)/2)
                    tmpmask = masker[eraf:2*nrel-eraf]
                    tmpimg = convol(img, reform(tmpmask,2*(nrel-eraf)+1,1), /edge_t)
                endif else begin
                    tmpimg = convol(img, reform(masker,2*nrel+1,1), /edge_t)
                endelse
            endif $
        else tmpimg = img

        if total(dimensions eq 1) gt 0 $
            then begin
                if 2*nrel+1 gt imsize[2] then begin
                    eraf = nrel - fix((imsize[1]-1)/2)
                    tmpmask = masker[eraf:2*nrel-eraf]
                    tmpimg = convol(tmpimg, transpose(tmpmask), /edge_t)
                endif else begin
                    tmpimg = convol(tmpimg, transpose(masker), /edge_t)
                endelse
            endif
        return, tmpimg
    endif

    center = nrel

    if showit then niwin
    tmpimg = fltarr(imsize[1], imsize[2], imsize[3])
    for plane= 0, nrplanes-1 do begin
        totcoeff = 0.

```

```

if total(dimensions eq 2) gt 0 then begin
  for j= -center, center do begin
    curplane = plane + j
    maski = j + center
    if (curplane ge 0) and (curplane lt nrplanes) then begin
      tmpimg[*,*,plane] = tmpimg[*,*,plane] + masker[maski] * $
        img[*,*,curplane]
      totcoeff = totcoeff + masker(maski)
    endif
  endfor
endif else begin
  totcoeff = 1.
  tmpimg[*,*,plane] = img[*,*,plane]
endif
dummy = tmpimg[*,*,plane] / totcoeff
if total(dimensions eq 0) gt 0 then $
  dummy = convol(dummy, reform(masker,2*nrel+1,1), /edge_t)
if total(dimensions eq 1) gt 0 $
  then tmpimg[*,*,plane] = convol(dummy, transpose(masker), /edge_t) $
  else tmpimg[*,*,plane] = dummy
if showit then niimage, tmpimg[*,*,plane], /noerase
endifor

return, tmpimg

end
:*****

```

References

1. <http://www.cdc.gov/heartdisease> – last accessed on 14 February 2012.
2. http://www.who.int/cardiovascular_diseases/en/ – last accessed on 10 February 2012.
3. <http://www.womensheart.org/index.htm> – last accessed on 14 February 2012.
4. <http://www.nhs.uk/conditions/coronary-heart-disease/Pages/Introduction.aspx> – last accessed on 10 February 2012.
5. Loong CY, Anagnostopoulos C. Diagnosis of coronary artery disease by radionuclide myocardial perfusion imaging. *Heart*. 2004; 90:v2-v9.
6. Udelson JE, E J Flint EJ. Radionuclide imaging in risk assessment after acute coronary syndromes. *Heart* 2004; 90 (Suppl V): v16–v25.
7. Dahlberg S, Leppo J. Risk stratification of the normal perfusion scan: Does normal stress perfusion always mean very low risk? *J Nucl Cardiol* 2003; 10:87-91.
8. Rigo P, Benoit T. Myocardial ischaemia. In: *Clinical Nuclear Medicine* (Maisey MN, Britton KE, Collier BD, eds). 3rd ed. Chapman & Hall Medical, London. 1998:167-171.
9. Seminars in Nuclear Cardiology. (<http://www.nuclearcardiologyseminars.net/index.htm>)
10. Fowler MS, Heller G. Indications for Nuclear Cardiology Procedures: Suspected Coronary Artery Disease. In: *Nuclear Cardiology: Practical Applications* (Heller G, Hendel RC, eds). McGraw-Hill. New York. 2004:1-8.
11. Hendel RC, Berman DS, Cullom SJ, et al. Multicenter clinical trial to evaluate the efficacy of correction for photon attenuation and scatter in SPECT myocardial perfusion imaging. *Circulation*. 1999; 99:2742–2749.
12. Ficaro EP, Fessler JA, Shreve PD, Kritzman JN, Rose PA, Corbett JR. Simultaneous transmission/emission myocardial perfusion tomography: diagnostic accuracy of attenuation-corrected 99mTc-sestamibi single-photon emission computed tomography. *Circulation*. 1996; 93:463–473.
13. Kluge R, Sattler B, Seese A, Knapp WH. Attenuation correction by simultaneous emission-transmission myocardial single-photon emission tomography using a technetium-99m-labelled radiotracer: impact on diagnostic accuracy. *Eur J Nucl Med*. 1997; 24:1107–1114.
14. Bugiardini R, Manfredi O, Pizzi C, Fontana F, Morgagni G. Endothelial function predicts future development of coronary artery disease: a study of women with chest pain and normal coronary angiograms. *Circulation*. 2004; 109:2518–2523.
15. Noto JR Jr, Johnson LW, Krone R, et. al. Cardiac catheterization 1990: A report of the registry of the Society for Cardiac Angiography and Interventions (SCA&I). *Cathet Cardiovasc Diagn* 1991; 24:75-83.
16. Nakagawa Y, Nakagawa K, Sdringola S, Mullani N, Gould KL. A precise, three-dimensional atlas of myocardial perfusion correlated with coronary arteriographic anatomy. *J Nucl Cardiol*. 2001; 8:580–590.
17. Ahmed AH, Shankar KJ, Eftekhari H, Munir MS, Robertson J, Brewer A, Stupin IV, Casscells SW. Silent myocardial ischemia: Current perspectives and future directions. *Exp Clin Cardiol*. 2007 Winter; 12(4): 189–196.
18. Ficaro EP, Fessler JA, Shreve PD, Kritzman JN, Rose PA, Corbett JR. Simultaneous transmission/emission myocardial perfusion tomography. Diagnostic accuracy of attenuation-corrected Tc-99m sestamibi single-photon emission computed tomography. *Circulation*. 1996; 93:463-473.
19. Berman DS, Kiat HS, van Train KF, Germano G, Maddahi J, Friedman JD. Myocardial Perfusion Imaging with Technetium-99m-Sestamibi: Comparative Analysis of Available Imaging Protocols. *J Nucl Med*. 1994; 35:681-688.

20. Baggish AL, Boucher CA. Radiopharmaceutical Agents for Myocardial Perfusion Imaging. *Circulation*. 2008; 118: 1668-1674.
21. Kelly JD, Forster AM, Higley B, Archer CM, Booker FS, Canning LR, et. al. Technetium-99m-Tetrofosmin as a New Radiopharmaceutical for Myocardial Perfusion Imaging. *J Nucl Med*. 1993; 34:222-227.
22. DePuey EG, Rozanski A. Using gated technetium-99m-sestamibi SPECT to characterize fixed myocardial defects as infarct or artifact. *J Nucl Med*. 1995; 36:952-955.
23. Mahmarian JJ. State of the art for coronary artery disease detection: thallium-201. In: *Nuclear Cardiology: State of the Art and Future Directions* (Zaret BL, Beller GA, eds). 2nd ed. St Louis, Mo. Mosby. 1999:237-272.
24. Gerson MC. Test Accuracy, Test Selection, and Test Result Interpretation in Chronic Coronary Artery Disease. In: *Cardiac Nuclear Medicine* (Gerson MC. Ed.). 3rd ed. McGraw-Hill, New York. 1997:527-579.
25. Verzijlbergen JF, van Oudheusden D, Cramer MJ, Ascoop CAPL, Zwinderman AH, Niemeyer MG, van der Wall EE, Pauwels EKJ. Quantitative analysis of planar Technetium-99m Sestamibi myocardial perfusion images: Clinical application of a modified method for the subtraction of tissue crosstalk. *Eur Heart J*. 1994; 15:1217-1226.
26. Guidelines for Clinical Use of Cardiac Radionuclide Imaging: A Report of the American College of Cardiology/American Heart Association Task Force on Practice Guidelines. (Committee on Radionuclide Imaging). *J Am Coll Cardiol*. 1995; 25:521-547.
27. Berman DS, Kiat HS, van Train KF, Germano G, Maddahi J, Friedman JD. Myocardial Perfusion Imaging with Technetium-99m-Sestamibi: Comparative Analysis of Available Imaging Protocols. *J Nucl Med*. 1994; 35:681-688.
28. Matsunari I, Fujino S, Taki J, Senma J, Aoyama T, Wakasugi T, Hirai J, Saga T, Tonami N, Hisada K. Comparison of defect size between thallium-201 and technetium-99m tetrofosmin myocardial single-photon emission computed tomography in patients with single-vessel coronary artery disease. *Am J Cardiol*. 1996; 77:350-354.
29. Najm YC, Maisey MN, Clarke SM, Fogelman I, Curry PVL, Sowton E. Exercise myocardial perfusion scintigraphy with technetium-99m methoxy isobutylisonitrile: a comparative study with thallium-201. *Int J Cardiol*. 1990; 26:93-102.
30. Fowler MS, Heller G. Indications for Nuclear Cardiology Procedures: Suspected Coronary Artery Disease. In: *Nuclear Cardiology: Practical Applications* (Heller G, Hendel RC, eds). McGraw-Hill. New York. 2004:1-8.
31. DePuey EG III. How to detect and avoid myocardial perfusion SPECT artifacts. *J Nucl Med*. 1994; 35:699-702.
32. Cullom SJ, Case JA, Bateman MD. Electrocardiographically gated myocardial perfusion SPECT: technical principles and quality control considerations. *J Nucl Cardiol*. 1998; 5:418-425.
33. DePuey EG, Rozanski A. Using gated technetium-99m-sestamibi SPECT to characterize fixed myocardial defects as infarct or artifact. *J Nucl Med*. 1995; 36:952-955.
34. Lima RS, Watson DD, Goode AR, et al. Incremental value of combined perfusion and function over perfusion alone by gated SPECT myocardial perfusion imaging for detection of severe three-vessel coronary artery disease. *J Am Coll Cardiol*. 2003; 42:64-70.
35. Bailey IK, Griffith LS, Rouleau J, Strauss W, Pitt B. Thallium-201 myocardial perfusion imaging at rest and during exercise. Comparative sensitivity to electrocardiography in coronary artery disease. *Circulation*. 1977; 55:79-87.
36. Brindis RG, Douglas PS, Hendel RC, Peterson ED. ACCF/ASNC Appropriateness Criteria for Single-Photon Emission Computed Tomography Myocardial Perfusion Imaging (SPECT MPI). A Report of the American College of Cardiology Foundation Quality Strategic Directions Committee Appropriateness Criteria Working Group and the American Society of Nuclear Cardiology Endorsed by the American Heart Association. *J. Am. Coll. Cardiol*. 2005; 46:1587-1605.

37. Emmett L, Iwanochko RM, Freeman MR, Barolet A, Lee DS, Husain M. Reversible regional wall motion abnormalities on exercise technetium-99m-gated cardiac single photon emission computed tomography predict high-grade angiographic stenoses. *J. Am. Coll. Cardiol.* 2002; 39:991-998.
38. Jaszczak RJ, Coleman RE, Whitehead FR. Physical factors affecting quantitative measurements using camera-based single photon emission computed tomography (SPECT). *IEEE Trans Nucl Sci.* 1981; 28:69-80.
39. Tsui BMW, Frey EC, Zhao X, Lalush DS, Johnston RE, McCartney WH. The importance and implementation of accurate three-dimensional compensation methods for quantitative SPECT. *Phys Med Biol.* 1994; 39:509-530.
40. Rosenthal MS, Cullom J, Hawkins W, Moore SC, Tsui BMW, Yester M. Quantitative SPECT imaging: a review and recommendations by the focus committee of the Society of Nuclear Medicine Computer and Instrumentation Council. *J Nucl Med.* 1995; 36:1489-513.
41. Da Silva, AJ, Tang HR, Wong KH, Wu MC, Dae MW, Hasegawa BH. Absolute quantification of regional myocardial uptake of 99mTc-sestamibi with SPECT: experimental validation in a porcine model. *J Nucl Med.* 2001; 42:772-779.
42. Patterson R, Horowitz S, Eisner R. Comparison of modalities to diagnose coronary artery disease. *Semin Nucl Med.* 1994; 24:286-310.
43. Beller G. Myocardial perfusion imaging with thallium-201. *J Nucl Med.* 1994; 35:674-680.
44. Van Train KF, Garcia E, Maddahi J, Areeda J, Cooke CD, Kiat H, Silagan G, Folks R, Friedman J, Matzer L, Germano G, Bateman T, Ziffer J, DePuey EG, Darlene Fink-Bennett D, Cloninger K, Berman DS. Multicenter trial validation for quantitative analysis of same-day rest-stress technetium-99m-sestamibi myocardial tomograms. *J Nucl Med.* 1994; 35:609-618.
45. DePuey E, Garcia E. Optimal specificity of thallium-201 SPECT through recognition of imaging artifacts. *J Nucl Med.* 1989; 30:441-449.
46. Dunn R, Wolff D, Wagner S, Botvinick E. The inconsistent pattern of thallium defects: a clue to the false-positive perfusion scintigram. *Am J Cardiol.* 1981; 48:224-232.
47. Garver PR, Wacnich RD, Shibuya AM, Yeh F. Appearance of breast attenuation artifacts with thallium myocardial SPECT imaging. *Clin Nucl Med.* 1985; 10:694-696.
48. Eisner R, Tamas M, Cloninger K, Shonkoff D, Oates JA, Gober AM, Dunn DW, Malko JA, Churchwell AL, Patterson RE. Normal SPECT thallium-201 bull's-eye display: gender differences. *J Nucl Med.* 1988; 29:1901-1909.
49. Da Silva, AJ, Tang HR, Wong KH, Wu MC, Dae MW, Hasegawa BH. Absolute quantification of regional myocardial uptake of 99mTc-sestamibi with SPECT: experimental validation in a porcine model. *J Nucl Med.* 2001; 42:772-779.
50. El Fakhri G, Buvat I, Péligrini M, Benali H, Almeida P, Bendriem B, Todd-Pokropek A, Di Paola R. Respective roles of scatter, attenuation, collimator response and partial volume effect in cardiac SPECT quantitation: a Monte Carlo study. *Eur J Nucl Med.* 1999; 26:437-446.
51. Rosenthal MS, Cullom J, Hawkins W, Moore SC, Tsui BMW, Yester M. Quantitative SPECT imaging: a review and recommendations by the Focus Committee of the Society of Nuclear Medicine Computer and Instrumentation Council. *J Nucl Med.* 1995; 36:1489-1513.
52. Bailey DL. Quantitative procedures in 3D PET. In: *The Theory and Practice of 3D PET* (Bendriem B, Townsend DW, eds). Dordrecht, The Netherlands. Kluwer Academic Publishers. 1998:55-109.
53. Pitman A. Myocardial perfusion imaging. A validated and mature cardiac imaging modality. *Australian Family Physician.* 2006; 35:288-292.
54. Hutton BF. Cardiac single-photon emission tomography: is attenuation correction enough? *Eur J Nucl Med.* 1997; 24:713-715 (editorial).
55. de Vries DJ, King MA. Window selection for dual photopeak window scatter correction in Tc-99m imaging. *IEEE Trans Nucl Sci.* 1994; 41:2771-2778.

56. Hademenous GJ, King MA, Ljungberg M, Zubal G, Harrell CR. A scatter correction method for Tl-201 images: a Monte Carlo investigation. *IEEE Trans Nucl Sci.* 1993; 30:1179-1186.
57. Beekman FJ, Kamphuis C, Frey EC. Scatter compensation methods in 3D iterative SPECT reconstruction: A simulation study. *Phys Med Biol.* 1997; 42: 1619-1632.
58. Kadrmaz DJ, Frey EC, Tsui BMW. Application of reconstruction-based scatter compensation to thallium-201 SPECT: implementations for reduced reconstruction image noise. *IEEE Trans Med Imag.* 1998; 17:325-333.
59. Ogawa K, Harata Y, Ichihara T, Kubo A, Hashimoto S, A practical method for position dependent Compton scatter correction in single photon emission CT, *IEEE Trans Nucl Med*, 10:408-412 1991
60. Beekman FJ, de Jong HWAM, van Geloven S. Efficient fully 3-D iterative SPECT reconstruction with Monte Carlo-based scatter compensation. *IEEE Trans Med Imag.* 2002; 21 867-877.
61. Xiao J, de Wit TC, Staelens SG, Beekman FJ. Evaluation of 3D Monte Carlo-based scatter correction for 99mTc cardiac perfusion SPECT. *J Nucl Med.* 2006; 47:1662-1669.
62. Kadrmaz DJ, Frey EC, Karimi SS, Tsui BMW. Fast implementations of reconstruction-based scatter compensation in fully 3D SPECT image reconstruction *Phys Med Biol.* 1998; 43 857-873.
63. Sohlberg A, Watabe H, Iida H. Acceleration of Monte Carlo-based scatter compensation for cardiac SPECT. *Phys Med Biol.* 2008; 53:277-285.
64. DePuey GE, Garcia EV, Berman DS. Cardiac SPECT imaging. p4. Lippincott Williams & Wilkins, 2001.
65. Links JM, Zubieta JK, Meltzer CC, Stumpf MJ, Frost JJ. Influence of spatially heterogeneous background activity on "hot object" quantitation in brain emission computed tomography. *J Comput Assist Tomogr.* 1996; 20:680-687.
66. Videen TO, Perlmutter JS, Mintun MA, Raichle ME. Regional correction of positron emission tomography data for the effects of cerebral atrophy. *J Cereb Blood Flow Metabol.* 1998; 8:662-670.
67. Rousset OG, Ma Y, Léger GC, Gjedde AH, Evans AC. Correction for partial volume effects in PET using MRI-based 3D simulations of individual human brain metabolism. In: Quantification of brain function, tracer kinetics and image analysis in brain PET (Uemura K, Lassen NA, Jones T, Kanno I, eds). Amsterdam. Elsevier Science. 1993 :113-25.
68. Labbe C, Koepp M, Ashburner J. Absolute PET quantification with correction for partial volume effects within cerebral structures. In: Quantitative functional brain imaging with positron emission tomography (Carson C, Daube-Witherspoon M, Herscovitch P, eds). San Diego, Academic Press. 1998:59-66.
69. Kosugi Y, Sase M, Suganami Y, Momose T, Nishikawa J. Dissolution of partial volume effect in PET by an inversion technique with the MR-embedded neural network model. In: Quantification of Brain Function Using PET (Myers R, Cunningham V, Bailey D, Jones T, eds). San Diego, Academic Press. 1996:166-169.
70. Ma Y, Rousset O, Evans AC. A Generalized Methodology For Partial Volume Correction In Emission Tomography. *IEEE Nuclear Science Symposium and Medical Imaging Conference.* Toronto, Ontario, Canada; 8-14 November 1998.
71. Buvat I, Bartlett ML, Kitsiou AN, Dilsizian V, Bacharach SL. A "hybrid" method for measuring myocardial wall thickening from gated PET/SPECT images. *J Nucl Med.* 1997; 38:324-329.
72. Shannon CE. Communication in the presence of noise, *Proc. Institute of Radio Engineers*, vol. 37, no. 1, pp. 10-21, Jan. 1949. Reprint as classic paper in: *Proc. IEEE*, vol. 86, no. 2, (Feb. 1998)
73. Erlandsson K, Hutton BF. Partial Volume Correction in SPECT Using Anatomical Information and Iterative FBP. *Tsin Sci & Techn.* 2010; 15:50-55.
74. Bruyant PP. Analytic and Iterative Reconstruction Algorithms in SPECT. *J Nucl Med.* 2002; 43:1343-1358.

75. Metz CE, Atkins FB, Beck RN. The geometric transfer function component for scintillation camera collimators with straight parallel holes. *Phys Med Biol.* 1980; 25:1059-1070.
76. Tan P, Bailey DL, Meikle SR, Eberl S, Fulton SRR, Hutton BF. A scanning line source for simultaneous emission and transmission measurements in SPECT. *J Nucl Med.* 1993; 34:1752-1759.
77. Tsui BMW. Collimator design, properties and characteristics. In: *The Scintillation Camera* (G. H. Simmons, ed). The Society of Nuclear Medicine, New York, 1988:17-45.
78. Xia W, Lewitt RM, Edholm PR. Fourier correction for spatially variant collimator blurring in SPECT. *IEEE Trans Med Imag.* 1995; 14:100-115.
79. Pan TS, Luo DS, Kohli V, King MA. Influence of OSEM, elliptical orbits and background activity on SPECT 3D resolution recovery. *Phys Med Biol.* 1997; 42:2517-29.
80. Fessler JA. Penalized weighted least-squares image reconstruction for positron emission tomography. *IEEE Trans Med Imag.* 1994; 13(2); 290-300.
81. Borges-Neto S, Pagnanelli RA, Shaw LK, Honeycutt E, Shwartz SC, Adams GL, Coleman RE. Clinical results of a novel wide beam reconstruction method for shortening scan time of Tc-99m cardiac SPECT perfusion studies. *J Nucl Cardiol.* 2007; 14:555-565.
82. DePuey EG, Gadiraju R, John Clark J, Thompson L, Anstett F, Shwartz SC. Ordered subset expectation maximization and wide beam reconstruction "half-time" gated myocardial perfusion SPECT functional imaging: A comparison to "full-time" filtered backprojection. *J Nucl Cardiol.* 2008; 15:547-63.
83. De Lorenzo A, Fonseca LMB, Landesmann MCPP, Lima RSL. Comparison between short-acquisition myocardial perfusion SPECT reconstructed with a new algorithm and conventional acquisition with filtered backprojection processing. *Nucl Med Commun.* 2010; 31:552-557.
84. Ali I, Ruddy T, Almgrahi A, Frank Anstett F, Wells RG. Single photon emission computer tomography perfusion imaging in half the time. *J Nucl Med.* 2008; 49 (Supplement 1):72P.
85. Maddahi J, Mendez R, Mahmarian JJ, Thomas G, Babla H, Bai C, Arram S, Maffetone P, Conwell R. Prospective multicenter evaluation of rapid, gated SPECT myocardial perfusion upright imaging. *J Nucl Cardiol.* 2009; 16:351-357.
86. Vija AH, Zeintl J, Chapman JT, Hawman EG, Hornegger J. Development of rapid SPECT acquisition protocol for myocardial perfusion imaging. *IEEE Nucl Sci Symp Conf Rec.* 2006; 3:1811-6.
87. Venero CV, Ahlberg AW, Bateman TM, Katten D, Courter SA, McGhie AI, Philips RD, Case JA, Golub RJ, Cullom SJ, Heller GV. Enhancement of nuclear cardiac laboratory efficiency—Multicenter evaluation of a new post-processing method with depth-dependent collimator resolution applied to full and half-time acquisitions. *J Nucl Cardiol.* 2008; 15:S4.
88. Bateman TM, Heller GV, McGhie AI, et al. 2.04: Multicenter investigation comparing a highly efficient half-time stress-only attenuation correction approach against standard rest-stress Tc-99m SPECT imaging. *J Nucl Cardiol.* 2008; 15:S3-S3.
89. Tsui BMW, Hu HB, Gilland DR, Gullberg GT. Implementation of simultaneous attenuation and detector response correction in SPECT. *IEEE Trans Nucl Sci.* 1988; 35:778-83.
90. DePuey EG, Bommireddipalli S, Beletsky I, et al. 2.01: Quarter-time myocardial perfusion SPECT wide beam reconstruction. *J Nucl Cardiol.* 2008; 15:S2-S2.
91. McCarthy AW, Miller MI. Maximum likelihood SPECT in clinical computation times using mesh-connected parallel computers. *IEEE Trans. Med Imag.* 1991; 10:426-436.
92. Sorenson JA. Quantitative measurement of radioactivity in vivo by whole-body counting. In: *Instrumentation in Nuclear Medicine* (Hine G, Sorenson JA, eds). Vol 2. New York, NY. Academic Press. 1974:311-348.
93. Chang LT. A method for attenuation correction in radionuclide computed tomography. *IEEE Trans Nucl Sci.* 1978; 25:638-643.

94. Michel C, Sibomana M, Boi A, Bernard X, Lonneux M, Defrise M, Comtat C, Kinahan PE, Townsend DW. Preserving Poisson characteristics of PET data with weighted OSEM reconstruction. Conference Record of IEEE Nuclear Science Symposium and Medical Imaging Conference. Toronto, Ontario, Canada; 8–14 November 1998; 2:1323–1329.
95. Blankespoor S. C., Xu, X., Kaiki, K. et al., Attenuation correction of SPECT using X-ray CT on an emission-transmission CT system: myocardial perfusion assessment. *IEEE Trans Nucl Sci* 43: 2263-2274 (1996).
96. Kinahan P. E., Hasegawa, B. H. and Beyer, T., X-ray-based attenuation correction for positron emission tomography/computed tomography scanners. *Semin Nucl Med* 33: 166-179 (2003)
97. Koral KF, Zasadny KR, Kessler ML, Luo JQ, Buchbinder SF, Kaminski MS, Francis I, Wahl RL. CT-SPECT fusion plus conjugate views for determining dosimetry in iodine-131-monoclonal antibody therapy of lymphoma patients. *J Nucl Med*. 1994; 35:1714–1720.
98. Fleming JS. A technique for using CT images in attenuation correction and quantification in SPECT. *Nucl Med Commun*. 1989; 10:83–97.
99. Kinahan PE, Townsend DW, Beyer T, Sashin D. Attenuation correction for a combined 3D PET/CT scanner. *Med Phys*. 1998; 25:2046–2053.
100. Nickoloff EL, Perman WH, Esser PD, Bashist B, Alderson PO. Left ventricular volume: physical basis for attenuation corrections in radionuclide determinations. *Radiology*. 1984; 152:511–515.
101. Patton JA, Delbeke D, Sandler MP. Image fusion using an integrated, dual-head coincidence camera with x-ray tube-based attenuation maps. *J Nucl Med*. 2000; 41:1364–1368.
102. Kalki K, Blankespoor SC, Brown JK, Hasegawa BH, Dae MW, Chin M, Stillson C. Myocardial perfusion imaging with a combined x-ray CT and SPECT system. *J Nucl Med*. 1997; 38:1535–1540.
103. Beyer T, Townsend DW, Brun T, Kinahan PE, Charron M, Roddy R, Jerin J, Young J, Byars L, Nutt R. A combined PET/CT scanner for clinical oncology. *J Nucl Med*. 2000; 41:1369–1379.
104. Seo Y, Wong KH, Sun M, Franc BL, Hawkins RA, Hasegawa BH. Correction of photon attenuation and collimator response for a body-contouring SPECT/CT imaging system. *J Nucl Med* 2005; 46(5):868–877
105. Goetze S, Wahl RL. Prevalence of misregistration between SPECT and CT for attenuation-corrected myocardial perfusion SPECT. *J Nucl Cardiol* 2007; 14(2):200–206.
106. Utsunomiya D, Nakaura T, Honda T, et al. Object-specific attenuation correction at SPECT/CT in thorax: optimization of respiratory protocol for image registration. *Radiology* 2005; 237(2):662–669.
107. Bybel B, Brunken RC, DiFilippo FP, Neumann DR, Wu G, Cerqueira MD. SPECT/CT Imaging: Clinical Utility of an Emerging Technology. July 2008, *RadioGraphics*, 28, 1097-1113.
108. Gustav Konrad von Schulthess. *Molecular anatomic imaging: PET-CT and SPECT-CT integrated modality imaging*. Lippincott Williams & Wilkins. p267-268.
109. J. Friedman J, D.S. Berman, K. Van Train, et al, "Patient motion in thallium-201 myocardial SPECT imaging: An easily identified frequent source of artifactual defect," *Clin Nucl Med*, vol. 13, pp.321-324, 1988.
110. J. Friedman, K. Van Train, J. Maddahi, et al, "'Upward creep" of the heart: A frequent source of false-positive reversible defects during thallium-201 stress redistribution SPECT," *J Nucl Med*, vol. 30, pp. 1718-1722, 1989.
111. M.M. Ter-Pogossian, S.R. Bergmann and B.E. Sobel, "Influence of cardiac and respiratory motion on tomographic reconstructions of the heart: Implications for quantitative nuclear cardiology," *J Comp Ass Tomogr*, vol. 6, pp. 1148-1154, 1982.
112. K. Cho, S-I Kumiata, S. Okada and T. Kumazaki, "Development of respiratory gated myocardial SPECT system," *J Nucl Cardiol*, vol. 6, pp. 20-28, 1999.

113. Friedman J, Van Train K, Maddahi J, Rozanski A, Prigent F, Bietendorf J, Waxman A, Berman DS. "Upward creep" of the heart: a frequent source of false-positive reversible defects during thallium-201 stress-redistribution SPECT. *J Nucl Med.* 1989 Oct; 30(10):1718-22.
114. Patton JA, Turkington TG. SPECT/CT Physical Principles and Attenuation Correction. *J Nucl Med Technol* 2008; 36:1-10.
115. Ichihara T, Motomura N, Ogawa K, Hasegawa H, Hashimoto J, Kubo A. Evaluation of SPET quantification of simultaneous emission and transmission imaging of the brain using a multi detector SPET system with the TEW scatter compensation method and fan-beam collimation. *Eur J Nucl Med.* 1996; 23:1292-1299.
116. Van Laere K, Koole M, Kauppinen T, Monsieurs M, Bouwens L, Dierck R. Nonuniform transmission in brain SPECT using 201Tl, 153Gd, and 99mTc static line sources: anthropomorphic dosimetry studies and influence on brain quantification. *J Nucl Med.* 2000; 41:2051-2062.
117. Watson CC, Schaefer A, Luk WK, Kirsch CM. Clinical evaluation of single photon attenuation correction for 3D whole-body PET. *IEEE Trans Nucl Sci.* 1999; 46:1024-1031.
118. Tung C-H, Gullberg GT, Zeng GL, Christian PE, Datz FL, Morgan HT. Non-uniform attenuation correction using simultaneous transmission and emission converging tomography. *IEEE Trans Nucl Sci.* 1992; 39:1134-1143.
119. Watson CC, Eriksson L, Casey ME, Jones WF, Moyers JC, Miller S, Hamill J, Van Lingen A, Bendriem B, Nutt R. Design and performance of collimated coincidence point sources for simultaneous transmission measurements in 3-D PET. *IEEE Trans Nucl Sci.* 2001; 48:673-679.
120. Smith RJ, Karp JS, Muehlechner G, Gualtieri E, Benard F. Single transmission scans performed post-injection for quantitative whole body PET imaging. *IEEE Trans Nucl Sci.* 1997; 44:1329-1335.
121. Gilland DR, Jaszczak RJ, Greer KL, Coleman RE. Transmission imaging for nonuniform attenuation correction using a three-headed SPECT camera. *J Nucl Med.* 1998; 39:1105-1110.
122. Bailey DL, Hutton BF, Walker PJ. Improved SPECT using simultaneous emission and transmission tomography. *J Nucl Med.* 1987; 28:844-851.
123. Ficaro EP, Fessler JA, Rogers WL, Schwaiger M. Comparison of americium-241 and technetium-99m as transmission sources for attenuation correction of thallium-201 SPECT imaging of the heart. *J Nucl Med.* 1994; 35:652-663.
124. King MA, Tsui BMW, Pan TS. Attenuation compensation for cardiac single photon emission computed tomographic imaging. Part 1. Impact of attenuation and methods of estimating attenuation maps. *J Nucl Cardiol.* 1995; 2:513-524.
125. Cao Z, Tsui BMW. Performance characteristics of transmission imaging using a uniform sheet source with parallel-hole collimation. *Med Phys.* 1992; 19:1205-1212.
126. Zaidi H, Hasegawa BH. Attenuation Correction Strategies in Emission Tomography. *J Nucl Med.* 2003; 44:291-315.
127. Celler A, Sitek A, Stoub E, Hawman P, Harrop R, Lyster D. Multiple line source array for SPECT transmission scans: simulation, phantom and patient studies. *J Nucl Med.* 1998; 39:2183-2189.
128. Beekman FJ, Kamphuis C, Hutton BF, van Rijk PP. Half-fanbeam collimators combined with scanning point sources for simultaneous emission-transmission imaging. *J Nucl Med.* 1998; 39:1996-2003.
129. Zeng GL, Gullberg GT, Christian PE, Gagnon D, Tung C-H. Asymmetric cone-beam transmission tomography. *IEEE Trans Nucl Sci.* 2001; 48:117-124.
130. Wackers FJTh. Attenuation correction, or the emperor's new clothes? *J Nucl Med.* 1999; 40:1310-1312.
131. Wackers FJTh. Attenuation correction, or the emperor's new clothes? *J Nucl Med.* 1999; 40:1310-1312.

132. Zaidi H. Scatter modelling and correction strategies in fully 3D PET. *Nucl Med Commun.* 2001; 22:1181–1184.
133. Natterer F. Determination of tissue attenuation in emission tomography of optically dense media. *Inverse Probl.* 1993; 9:731–736.
134. Andersson JLR, Vagnhammer BE, Schneider H. Accurate attenuation correction despite movement during PET imaging. *J Nucl Med.* 1995; 36:670–678.
135. Panin VY, Zeng GL, Gullberg GT. Reconstructions of truncated projections using an optimal basis expansion derived from the cross-correlation of a "knowledge set" of a priori cross-sections. *IEEE Trans Nucl Sci.* 1998; 45:2119–2125.
136. Welch A, Gullberg GT, Christian PE, Datz FL, Morgan HT. A transmission-based scatter correction technique for SPECT in inhomogeneous media. *Med Phys.* 1995; 22:1627–1635.
137. Gourion D, Noll D, Celler A, Esquerre JP. Attenuation correction using SPECT emission data only. *IEEE Trans Nucl Sci.* 2002; 49:2172–2179.
138. Censor Y, Gustafson D, Lent A, Tuy H. A new approach to the emission computerized tomography problem: simultaneous calculation of attenuation and activity coefficients. *IEEE Trans Nucl Sci.* 1979; 26:2275–2279.
139. Nuyts J, Dupont P, Stroobants S, Benninck R, Mortelmans L, Suetens P. Simultaneous maximum a posteriori reconstruction of attenuation and activity distributions from emission sinograms. *IEEE Trans Med Imag.* 1999; 18:393–403.
140. Krol A, Bowsher JE, Manglos SH, Feiglin DH, Tornai MP, Thomas FD. An EM algorithm for estimating SPECT emission and transmission parameters from emissions data only. *IEEE Trans Med Imag.* 2001; 20:218–232.
141. Kaplan MS, Haynor DR, Vija H. A differential attenuation method for simultaneous estimation of SPECT activity and attenuation distributions. *IEEE Trans Nucl Sci.* 1999; 46:535–541.
142. Dicken V. A new approach towards simultaneous activity and attenuation reconstruction in emission tomography. *Inverse Probl.* 1999; 15:931–960.
143. Hosoba M, Wani H, Toyama H, Murata H, Tanaka E. Automated body contour detection in SPECT: effects on quantitative studies. *J Nucl Med.* 1986; 27:1184–1191.
144. Stodilka RZ, Kemp BJ, Prato FS, Kertesz A, Kuhl D, Nicholson RL. Scatter and attenuation correction for brain SPECT using attenuation distributions inferred from a head atlas. *J Nucl Med.* 2000; 41:1569–1578.
145. Segars WP, Lalush DS, Tsui BMW. A realistic spline-based dynamic heart phantom. *IEEE Trans on Nucl Sci.* 1998; 46:503-506.
146. Slomka PJ, Patton JA, Berman DS, Germano G. Advances in technical aspects of myocardial perfusion SPECT imaging. *J Nucl Cardiol.* 2009; 16:255–76.
147. Lewin HC, Hyun MC. A clinical comparison of an upright triplehead digital detector system to a standard supine dual-head gamma camera (abstract). *J Nucl Cardiol.* 2005; 12(4):S113.
148. O'Connor M. Evaluation of the CardiArc dedicated cardiac system (unpublished independent evaluation). Rochester, MN: Mayo Clinic; 2005.
149. Sharir T, Ben-Haim S, Merzon K, et al. High-speed myocardial perfusion imaging Initial clinical comparison with conventional dual detector anger camera imaging. *J Am Coll Cardiol Cardiovasc Imag.* 2008; 1:156-163.
150. Ben-Haim S, Hutton B, van Gramberg D, Waddington W, Prvulovich E, Bomanji J, Groves A, Kacperski K, Roth N, Ell P. Simultaneous dual isotope myocardial perfusion scintigraphy (DI MPS) - Initial experience with fast D-SPECT (abstract). *J Nucl Cardiol.* 2008; 15:S2.
151. Jaszczak RJ, Li J, Wang H, Zalutsky MR, Coleman RE. Pinhole collimation for ultra-high-resolution, small-field-of-view SPECT. *Phys Med Biol.* 1994; 39:425-37.
152. Schramm NU, Ebel G, Engeland U, Schurrat T, Behe M, Behr TM. High-resolution SPECT using multipinhole collimation. *IEEE Trans Nucl Sci.* 2003; 50:315-320.

153. Beekman FJ, Vastenhouw B. Design and simulation of a high resolution stationary SPECT system for small animals. *Phys Med Biol*. 2004; 49:4579-4592.
154. Funk T, Kirch DL, Koss JE, Botvinick E, Hasegawa BH. A novel approach to multipinhole SPECT for myocardial perfusion imaging. *J Nucl Med*. 2006; 47:595-602.
155. Metzler SD, Bowsher JE, Smith MF, Jaszczak RJ. Analytic determination of pinhole collimator sensitivity with penetration. *IEEE Trans Med Imag*. 2001; 20:730-741.
156. Steele PP, Kirch DL, Koss JE. Comparison of simultaneous dual isotope multipinhole SPECT with rotational SPECT in a group of patients with coronary artery disease. *J Nucl Med*. 2008; 49:1080.
157. Volokh L, Hugg J, Blevis I, Asma E, Jansen F, Manjeshwar R. Effect of detector energy response on image quality of myocardial perfusion SPECT. Paper presented at IEEE nuclear science symposium and medical imaging conference, 19–26 October 2008; Dresden, Germany.
158. Blevis I, Tsukerman L, Volokh L, Hugg J, Jansen F, Bouhnik J. CZT gamma camera with pinhole collimator: Spectral measurements. Paper presented at IEEE 2008 nuclear science and medical imaging conference, 19–26 October 2008; Dresden, Germany.
159. Garcia EV, Tsukerman L, Keidar Z. A new solid state, ultra fast cardiac multi-detector SPECT system. *J Nucl Cardiol*. 2008; 15:S3-S3.
160. Hawman PC, Haines EJ. The cardiofocal collimator: A variable focus collimator for cardiac SPECT. *Phys Med Biol*. 1994; 39:439-450.
161. Singh B, Bateman TM, Case JA, Heller G. Attenuation artifact, attenuation correction, and the future of myocardial perfusion SPECT. *J Nucl Cardiol*. 2007; 14:153-64.
162. Doucet A, de Freitas N, Gordon N. *Sequential Monte Carlo methods in practice*. Springer Science + Business Media. 2001, ISBN 0-387-95146-6.
163. MacKeown PK. *Stochastic Simulation in Physics*. Springer-Verlag, Singapore. 1997, ISBN 981-3083-26-3.
164. Harrison RL, Vannoy SD, Haynor DR, et al. Preliminary experience with the photon history generator module of a public-domain simulation system for emission tomography. *Conf Rec Nucl Sci Symp*. 1993; 2:1154-1158.
165. http://depts.washington.edu/simset/html/news/news_index.html. Accessed on 17 June 2010.
166. ¹⁶⁶ El Fakhri G, Buvat I, Péligrini M, Benali H, Almeida P, Bendriem B, Todd-Pokropek A, Di Paola R. Respective roles of scatter, attenuation, collimator response and partial volume effect in cardiac SPECT quantitation: a Monte Carlo study. *Eur J Nucl Med*. 1999; 26:437-446.
167. <http://www.ittvis.com/ProductServices/IDL.aspx>. Accessed on 10 June 2010.
168. <https://perswww.kuleuven.be/~u0015224/>. Accessed on 10 June 2010.
169. Tamaki N, Mukai T, Ishii Y, et al: Comparative study of thallium emission myocardial tomography with 180° and 360° data collection. *J Nucl Med* 23:661-666, 1982.
170. Garcia EV, Van Train K, Maddahi J, Prigent F, Friedman J, Areeda J, Waxman A, Berman DS. Quantification of Rotational Thallium-201 Myocardial Tomography. *J Nucl Med* 1985 26:17-26.
171. Draper, N. R., and H. Smith. *Applied Regression Analysis*. 3rd ed. Hoboken, NJ: Wiley-Interscience, 1998.
172. Levenberg, K. "A Method for the Solution of Certain Problems in Least Squares." *Quarterly of Applied Mathematics*. 1944; 2:164–168.
173. Field A (2007). *Discovering Statistics Using SPSS*. 2nd edition, p285 – 295. Sage Publications Ltd, London.
174. Rosenthal, R (1991). *Meta-analytic procedures for social research*. p19. Sage Publications Ltd, Newbury Park, CA.
175. http://www.nlm.nih.gov/research/visible/visible_human.html. Accessed 10 June 2010.

176. Banvard RA. The Visible Human Project® Image Data Set From Inception to Completion and Beyond, Proceedings CODATA: Frontiers of Scientific and Technical Data, Track I-D-2: Medical and Health Data. Montréal, Canada, October 2002.
177. Horowitz SF, Machac J, Levin H, and Matza D. Effect of Variable Left Ventricular Vertical Orientation on Planar Myocardial Perfusion Images. *J Nuc Med.* 1986; 27:694-700.
178. Garcia EV, Van Train K, Maddahi J, et al. Quantification of rotational thallium-201 myocardial tomography. *J Nucl Med.* 1985; 26:17-26.
179. Martin W, Tweddel AC, Hutton I. Balanced triple-vessel disease: enhanced detection by estimated myocardial thallium uptake. *Nucl Med Commun.* 1992; 13:149-153.
180. Fakhri GE, Buvat I, Benali H, Todd-Pokropek A, Paola RD. Relative Impact of Scatter, Collimator Response, Attenuation, and Finite Spatial Resolution Corrections in Cardiac SPECT. *J Nucl Med.* 2000; 41:1400-1408.
181. Ami E, Iskandrian, Mario S, Verani. New developments in cardiac nuclear imaging. *US Cardiology* (2005).
182. Fricke E, Fricke H, Weise R, Kammeier A, Hagedorn R, Lotz N, Lindner O, Tschoepe D, Burchert W. Attenuation Correction of Myocardial SPECT Perfusion Images with Low-Dose CT: Evaluation of the Method by Comparison with Perfusion PET. *J Nucl Med.* 2005; 46:736-744.
183. Bai C, Zeng GL, Kadmas DJ, Gullberg, GT. A Study of the Apparent Apical Defects in Attenuation Corrected Cardiac SPECT. *IEEE Trans. Nucl. Sci.* 1999; 40:2104-2110.
184. DePuey EG, Garcia EV. Optimising specificity of thallium-201 SPECT through recognition of imaging artifacts. *J Nucl Med.* 1989; 30:441-449.
185. Manglos SH, Thomas FD, Gagne GM, Hellwig BJ. Phantom Study of Breast Tissue Attenuation in Myocardial Imaging. *J Nucl Med.* 1993; 34:992-996.
186. Bellemare F, Jeanneret A, Couture J. Sex Differences in Thoracic Dimensions and Configuration. *Am J Respir Crit Care Med.* 2003; 168:305-312.
187. Germano G, Kavanagh PB, Su H, Mazzanti M, Kiat H, Hachamovitch R, Van Train KF, Areeda JS, Berman DS. Automatic Reorientation of Three-Dimensional, Transaxial Myocardial Perfusion SPECT Images. *J Nucl Med.* 1995; 36:1107-1114.
188. Manglos SH, Thomas FD, Gagne GM, Hellwig BJ. Phantom study of breast tissue attenuation in myocardial imaging. *J Nucl Med.* 1993; 34(6):992.
189. Eisner RL, Tamas MJ, Cloninger K, Shonkoff D, Oates JA, Gober AM, Dunn DW, Malko JA, Churchwell AL, Patterson RE. Normal SPECT thallium-201 bull's-eye display: gender differences. *J Nucl Med.* 1988; 29(12):1901.
190. Wackers, F. Diagnostic pitfalls of myocardial perfusion imaging in women. *J Myocard Ischemia* 1992; 4:23.
191. Horowitz SF, Machac J, Levin H, Matza D. Effect of Variable Left Ventricular Vertical Orientation on Planar Myocardial Perfusion Images. *J Nucl Med.* 1986; 27:694-700.
192. http://www.nlm.nih.gov/research/visible/visible_human.html. Accessed 10 June 2010.
193. Banvard RA. The Visible Human Project® Image Data Set From Inception to Completion and Beyond, Proceedings CODATA: Frontiers of Scientific and Technical Data, Track I-D-2: Medical and Health Data. Montréal, Canada, October 2002.
194. Singh B, Bateman TM, Case JA, Heller G. Attenuation artifact, attenuation correction, and the future of myocardial perfusion SPECT. *J Nucl Cardiol.* 2007; 14:153-64.
195. Bateman TM, Heller GV, McGhie AI, McGhie MI, Courter SA, Golub RA, Case JA, Cullom S. Multicenter investigation comparing a highly efficient half-time stress-only attenuation correction approach against standard rest-stress Tc-99m SPECT imaging. *J Nucl Cardiol.* 2008; 15:726-735.
196. Borges-Neto S, Pagnanelli RA, Shaw LK, Honeycutt EF, Shwartz SC, Trimble MA, Adams GL, Coleman RE. Clinical results of a novel wide beam reconstruction method for shortening scan time of Tc-99m cardiac SPECT perfusion studies. *J Nucl Cardiol.* 2007; 14:555-556.

197. Sohlberg A, Watabe H, Iida H. Acceleration of Monte Carlo-based scatter compensation for cardiac SPECT. *Phys Med Biol*. 2008; 53:277–285.
198. Vija AH, Zeintl J, Chapman JT, Hawman EG, Hornegger J. Development of rapid SPECT acquisition protocol for myocardial perfusion imaging. *IEEE Nucl Sci Symp Conf Rec*. 2006; 3:1811-6.
199. Venero CV, Ahlberg AW, Bateman TM, Katten D, Courter SA, McGhie AI, Philips RD, Case JA, Golub RJ, Cullom SJ, Heller GV. Enhancement of nuclear cardiac laboratory efficiency—Multicenter evaluation of a new post-processing method with depth-dependent collimator resolution applied to full and half-time acquisitions. *J Nucl Cardiol*. 2008; 15:S4.
200. MacDonald, Matthew (2009). *Your Body: The Missing Manual*. Sebastopol, CA: Pogue Press. ISBN 0-596-80174-2.
201. Chuanyong B, Zeng GL, Kadmas DJ, Gullberg GT. A study of apparent apical defects in cardiac SPECT images when performing attenuation compensation. *IEEE Tran. on Nucl Sci*. 1999; 46:2104-2110.
202. Piłachcińska A, Siennicki J, Kovacevic-Kuśmierk K, Bieńkiewicz M, Kuśmierk J. Effect of attenuation correction on normal (99m)Tc-MIBI myocardial perfusion scintigrams acquired with a hybrid SPECT/CT camera. *Nucl Med Rev Cent East Eur*. 2008; 2:59-66.
203. McQuaid SJ, Hutton BF. Sources of attenuation-correction artefacts in cardiac PET/CT and SPECT/CT. *Eur J Nucl Med Mol Imag*. 2008; 35:1117-1123.
204. Linda G. Shapiro and George C. Stockman (2001): "Computer Vision", pp 279-325, New Jersey, Prentice-Hall, ISBN 0-13-030796-3
205. Shepp LA, Vardi Y. Maximum likelihood reconstruction for emission tomography. *IEEE Trans Med Imaging* 1982; 1: 113-122.
206. Marais J, Taylor DN, Denman AR, Philips CA, Picton PD, D Monk D. Automatic segmentation of the left ventricle for image registration in an emission-based attenuation correction technique. Spring Scientific Meeting of the British Nuclear Medicine Society, Edinburgh, May 2008.
207. Marais J, Taylor DN, Denman AR, Philips CA, Picton PD, D Monk D. Automatic segmentation of the left ventricle for image registration in an emission-based attenuation correction technique. *Nucl Med Commun*. 2008; 29:P21.
208. <http://www.itvis.com/ProductServices/IDL.aspx>. Accessed on 9 June 2010.
209. MacKay DJC. *Information Theory, Inference, and Learning Algorithms*. Cambridge University Press. 2003:284.
210. Gonzalez RC, Woods RE. *Digital image processing*, 2nd ed. Upper Saddle River, N.J.: Prentice Hall, 2002.
211. http://www.dfanning.com/ip_tips/fit_ellipse.html. Accessed 12 June 2010.
212. <http://bishopw.loni.ucla.edu/air5>. Accessed on 15 September 2011.
213. Edelsbrunner H. *Algorithms in Combinatorial Geometry*. Springer-Verlag, New York. 1987:303.
214. Marais J, van Staden JA, Lötter MG. A 3D edge detection algorithm to be used in cardiac image registration. 42th SAFGB Congress, Mount Amanzi Lodge, Hartebeespoort, South Africa. May 2002.
215. <http://www.kilvarock.com/user/image/ellipsefitting.pdf>. Accessed on 9 June 2010.
216. Germano G, Kiat H, Kavanagh PB, et al. Automatic quantification of ejection fraction from gated myocardial perfusion SPECT. *J Nucl Med*. 1995; 36:2138–2147.
217. Germano G, Kavanagh PB, Berman DS. An automatic approach to the analysis, quantitation and review of perfusion and function from myocardial perfusion SPECT images. *Int J Card Imag*. 1997; 13:337–346.
218. Green PJ. Bayesian Reconstructions From Emission Tomography Data Using a Modified EM Algorithm. *IEEE Trans Med Imag*. 1990; 9:84-93.
219. Lee MM. Bayesian Reconstruction In Emission Tomography Using Gibbs Priors. A Dissertation Presented to the Faculty of the Graduate School of Yale University. May 1994.